Dipl. Ing. Thomas Ganner

Enzymatic Cellulose Degradation Visualized by Atomic Force Microscopy

Doctoral Thesis

For obtaining the academic degree

Doktor der technischen Wissenschaften

Doctoral Programme of technical Sciences

Technical Physics

Graz University of Technology

Supervisor:

Univ. Doz. Dipl. -Ing. Dr. techn. Harald Plank

Institut für Elektronenmikroskopie und Nanoanalyse

Co-Supervisor:

Ao. Univ. Prof. Dipl. -Ing. Dr. techn. Gerald Kothleitner

Institut für Elektronenmikroskopie und Nanoanalyse

Graz, April 12th, 2016

EIDESSTATTLICHE ERKLÄRUNG

AFFIDAVIT

Ich erkläre an Eides statt, dass ich die vorliegende Arbeit selbstständig verfasst, andere als die angegebenen Quellen/Hilfsmittel nicht benutzt, und die den benutzten Quellen wörtlich und inhaltlich entnommenen Stellen als solche kenntlich gemacht habe. Das in TUGRAZonline hochgeladene Textdokument ist mit der vorliegenden Dissertation identisch.

I declare that I have authored this thesis independently, that I have not used other than the declared sources/resources, and that I have explicitly indicated all material which has been quoted either literally or by content from the sources used. The text document uploaded to TUGRAZonline is identical to the present doctoral dissertation.

_____   _____
       Datum / Date   Unterschrift / Signature

Acknowledgments

This thesis is the result of 3 and half years of constant research, work and cooperation between me, colleagues, friends and collaborators. It was an interesting and absolutely unforgettable journey through different scientific fields and collaborations. Herein, I want to thank these people for their support, their suggestions and their friendship. I am sincerely grateful to be given the opportunity to work in such a positive and eager environment. For that, I want to gratefully acknowledge the help and supervision of Univ. Doz. Dr. Harald Plank as my supervisor and mentor. In all this time, his suggestions and valuable support guided me through hard times or complicated scientific problems and his part in this thesis cannot be emphasized enough. I want to thank him for his amicable form of cooperation which allowed us to cooperate and work on an uncomplicated basis. I also want to thank my co-supervisor Prof. Dr. Gerald Kothleitner for his support and important suggestions. Furthermore, I want to thank all my colleagues from the work group S3: Their support helped me to learn new techniques and tricks to encounter some trivial and some more complicated problems. Here, I want to gratefully acknowledge the help of Robert Winkler and Roland Schmied for the FIB introduction and Sebastian Rauch for the help with the physical vapor deposition. I want to thank my colleagues Timothy Aschl, Stefanie Rošker and Jürgen Sattelkow for the help with experiments and AFM measurements. Some of the work shown in this thesis is based on their support and help. I also want to thank all other colleagues of the FELMI-ZFE for their help. Herein, I want to especially acknowledge my kind and always amusing office colleague Angelina Orthacker but also all other good friends and colleagues in the doctoral school as Daniel Knez, Johanna Kraxner, Georg Haberfeldner, Manfred Nachtnebel, Harald Fitzek and Lukas Konrad. I sincerely thank Dr. Ferdinand Hofer as the head of the institute. He provided advice whenever needed and he decided to invest in a new AFM which helped tremendously in the experiments. He also decided to extend my contract for a few months. I am also sincerely grateful for the collaboration with the Institute of Biotechnology and Biochemical Engineering. Here, the help of Manuel Eibinger and the supervision of Prof. Dr. Bernd Nidetzky laid part of the foundation of this thesis. Without their knowledge and contributions this work wouldn't have been possible and fruitful. I want to emphasize that Manuel and I did most of the measurements together and that he provided the knowledge of microbiology and chemistry.

The review of this thesis was conducted by Prof. Dr. Christian Teichert which not only made valuable and important suggestions but also read the thesis thoroughly and comprehensively. For this I am sincerely thankful and grateful as his suggestions led to a significant improvement of the thesis.

Most important, I want to thank a few more persons, which are of paramount importance to me and my life. Here I want to thank my family for their financial and personal support. Their kindness has guided me through hard and stressful times and they have always supported me. I cannot possibly describe how important they are. Here grateful appreciation goes to my father Peter Paul and my mother Margarethe as well as my sister Johanna and my brother Simon. I'm sincerely grateful to have you in my life.

Last but not least I want to thank the most important person in my life Verena, which has traveled this way by my side and I am so glad that we made this journey together. Thank you for your support, your suggestions and your love.

Abstract

Fundamental research on enzymatic cellulose degradation is one of today's key scientific fields in microbiology. The reason is that cellulose is the most abundant and almost inexhaustible bio-polymer on earth and utilization of this vast resource for sustainable production of energy is the driving force behind the ever growing interest on this topic. Bio-catalytic degradation of cellulose to glucose as its monomeric unit is from bio-chemical view well understood. However, it turns out, that special effects and in particular synergism, which is the cooperative activity of multiple enzyme-types acting together, cannot be clarified satisfactory by the known models. To gain a deeper and comprehensive understanding of the underlying processes, researches have already in the past used high-resolution microscopy methods. Important findings were achieved by transmission electron microscopy, however, were mostly based on end-point analyses where bio-catalytic activity was no more observable in a direct manner. Therefore, over the past years, atomic force microscopy methods gained increasing interest as they are able to operate in liquids and natural enzyme environments. Hereby, not only lateral resolutions are comparable to electron microscopy methods, but also allow *in-situ* high-speed observation of biochemical processes. Nevertheless, to exploit the full potential of atomic force microscopy methods, special demands on the investigated substrate have to be fulfilled. Here, the overall flat topology is of particular relevance to allow molecular resolution. For the investigation of enzymatic cellulose disintegration, there are additional requirements in respect to the used substrate. From a chemical point of view, natural cellulose is highly polymorphic, which means that crystalline (parallel arranged polymer chains) and unordered amorphous regions are found side-by-side. To unravel individual effects on different material phases, it is therefore inevitable to have a cellulose substrate in hand, which allows a controllable polymorphism and high reproducibility. Based on these challenges, this thesis focused on different strategies to develop such ideal model substrates. Development was accompanied by careful analysis of the corresponding substrates. This knowledge proved to be decisive in later applied dedicated atomic force microscopy experiments to answer still open questions on enzymatic cellulose degradation. Substrate development is covered by the introduction of different preparation protocols enabling the fabrication of fully amorphous, fully crystalline and tunable, polymorphic cellulose substrates with flat topology for high-resolution, *in-situ* experiments. The latter revealed the significant role of polymorphism and allowed the direct assignment of individual enzyme activities to different cellulose phases (crystalline or amorphous). This is of particular relevance if enzymes of different type are combined in synergistic cellulose cocktails. We showed that this is a pivotal aspect in the efficient degradation of polymorphous celluloses. The achieved results expanded the fundamental understanding of the related mechanisms and enabled the development of new models for the description of enzymatic degradation. By that, the findings of this thesis contribute to the challenge of an industrial application concerning the efficient cellulose disintegration towards a competitive basis against crude oil, which further should allow the production of sustainable and carbon dioxide free bio-fuels.

Kurzfassung

Grundlagenforschung im Bereich des enzymatischen Zelluloseabbaus ist eines der interessantesten Gebiete der heutigen Mikrobiologie. Der Grund ist, dass Zellulose das am meisten vorkommende und nahezu unerschöpfliche Biopolymer auf unserer Erde ist und somit die Nutzbarmachung dieser Ressource zur nachhaltigen Energiegewinnung beitragen könnte. Die bio-katalytische Zersetzung der Zellulose zu ihrem Grundbaustein Zucker und weiteren molekularen Bauteilen ist von biochemischer Seite bereits gut verstanden. Es zeigt sich jedoch, dass gewisse Effekte – im Speziellen die des Synergismus, welcher die kooperative und vorteilhafte Zusammenarbeit verschiedener Enzyme beschreibt – mit den zugrundeliegenden Modellen nicht vollständig erklärt werden können. Um ein tieferes Verständnis zu erlangen, wurde schon in der Vergangenheit auf hochauflösende Mikroskopie gesetzt. Wichtige Erkenntnisse wurden mittels Transmissions-Elektronenmikroskope erzielt. Diese basierten jedoch auf Endpunktanalysen bei denen die katalytische Aktivität der Enzyme nicht direkt beobachtet werden kann. In den letzten Jahren wurde daher immer mehr auf die Anwendung von Rasterkraftmikroskopie gesetzt, welche in der natürlichen flüssigen Umgebung der Enzyme angewandt werden kann. Hierbei sind bei gleicher Auflösung *in-situ* Versuche möglich, die mit heutigen schnellen Mikroskopen sogar den Einblick in die relevanten Prozesse in Echtzeit ermöglichen. Jedoch sind, um Auflösungen im molekularen Bereich mittels Rasterkraftmikroskopie zu erzielen, spezielle Anforderungen zu erfüllen. Hierzu zählen insbesondere ein absolut flaches Substrat und eine hohe Reinheit der Zellulose. Zusätzlich müssen für die Untersuchung des enzymatischen Zelluloseabbaus zusätzliche Anforderungen erfüllt werden. Zellulose ist ein hochgradig polymorphes Polymer bei dem kristalline (parallel verlaufende Ketten) und ungeordnete Bereiche einander abwechseln. Es ist daher notwendig Substrate zu entwickeln, die sowohl den Anforderungen der Rasterkraftmikroskopie als auch der speziellen Zellulosestruktur genügen. In dieser Doktorarbeit werden Strategien gezeigt um ideale Zellulosesubstrate herzustellen. Begleitend zur Entwicklung werden verschiedene Analysetechniken vorgestellt, um diese Substrate genau zu charakterisieren. Dieses Wissen über die Substratzusammensetzung stellt sich als entscheidend in den später durchgeführten AFM Experimenten heraus, um ungelöste Probleme dieses interessanten Prozesses beantworten zu können. Die Substratentwicklung beinhaltet Protokolle, um vollständig amorphe, kristalline oder polymorphe Substrate mit einstellbarer Kristallinität zu erzeugen und in *in-situ* Experimenten zu nutzen. Diese zeigen die wichtige Rolle des substratspezifischen Polymorphismus und erlauben die exakte Zuordnung von spezifischen Enzymaktivitäten zu den zugehörigen Phasen (kristallin oder amorph). Dieser Effekt ist im Speziellen interessant, wenn verschiedene Enzymtypen zu einem synergistisch aktiven Zellulasesystem zusammengefasst werden, welche – wie gezeigt werden konnte – einen zentralen Aspekt in der enzymatischen Zersetzung von Zellulose einnehmen. Die dadurch gewonnenen Resultate erweitern das vorliegende fundamentale Verständnis der zugrundeliegenden Mechanismen und erlauben die Entwicklung neuer Modelle, um den enzymatischen Abbau zu beschreiben. Somit tragen die Ergebnisse dieser Arbeit dazu bei, die Herausforderungen des effektiven Abbaus von Zellulose zu meistern und folglich einen kohlendioxidfreien Biokraftstoff zu erhalten, welcher nachhaltig und dem Erdöl ebenbürtig ist.

"With his five senses, man explores the universe around him and calls the adventure Science"

Edwin Hubble, May 1929

Devoted to my family, Peter Paul, Margarethe, Johanna, Simon and Verena

Table of Contents

Preface

This thesis comprises fundamental research on enzymatic degradation of cellulose structures by the use of atomic force microscopy. Its content is separated into 6 *chapters*. The first three will deal with fundamental concepts of atomic force microscopy, cellulose structures and cellulose degrading enzymes, called cellulases. The first *chapter* is specifically designed to give a short but comprehensive overview on basic atomic force microscopy related concepts. The second *chapter* deals with cellulose and its structure and shows further important concepts for the analysis of such structures as wide angle x-ray scattering (WAXS) or Raman microscopy. The last introductory *chapter* will deal with enzymes and their functionality. Here basic concepts in bio-chemistry will be shown, which will be important for the understanding of bio-chemical measurements. Please note, due to the vast range of these research fields, *chapters* are designed to give a basic understanding. For deeper understanding and more details, each *chapter* is equipped with its own references including comprehensive reviews ore books.

Following these introductory *chapters*, the next two *chapters* deal with model cellulose substrates and AFM based visualization of their enzymatic decomposition. Here, *chapter IV* will be used to show the need of model substrates, which allow super flat topology and a corresponding polymorphism in close correlation to natural celluloses. The preparation of such substrates will be shown alongside with a full and detailed analysis via electron microscopy, atomic force microscopy (AFM), wide angle X-ray scattering (WAXS) and Raman microscopy. With the precise knowledge of these substrates, *chapter V* deals with the application of these substrates in *in-situ* AFM measurements and shows the impressive capabilities which may be associated with the combination of biochemical and AFM based methods.

The last *chapter* is designed to show future prospects and research activities associated with thin cellulose model substrates.

At the end of the thesis, a comprehensive conclusion will be given. The presented results here were topic of independent publications which will be listed on page 14. The corresponding sections are designed to give a summary of the corresponding publications with extended sections on methodology and preparation. Specific sections were, with kind permission of the respective journal, reused under the consideration that the main text was written by the author of this thesis. If sections were taken from a publication or comprehensively summarized, a specific point "Publication Summary" will specify precisely the contribution of each author. Each *chapter* begins with an overview and introduction to the specific topic and ends with a comprehensive conclusion. Digital media as movies will be available on USB sticks attached to the backside of this thesis. Movies will also be reused with kind permission of the journal. Reuse within another thesis or manuscript requires permission of the author or the corresponding journal.

List of Abbreviations

AFM………………………… Atomic Force Microscopy

AM-AFM………………… Amplitude Modulated – Atomic Force Microscopy

ATFC……………………… Amorphous Thin Film Cellulose

BMIMCl…………………… 1-Butyl-3-Methylimidazolium Chloride

C1…………………………… Cellulose I

C2…………………………… Cellulose II

CAZy……………………… Carbohydrate Active Enzymes; www.cazy.org

CBH……………………… Cellobiohydrolase

CBM……………………… Carbohydrate Binding Module

DMSO…………………… Dimethyl Sulfoxide

DNA……………………… Deoxyribonucleic Acid

DP………………………… Degree of Polymerisation

DS………………………… Degree of Substitution

DT………………………… Dwelltime

EFM……………………… Electrostatic Force Microscopy

EG………………………… Endoglucanase

FEBIC…………………… Focused Electron Beam Induced Cellulose Regeneration

FEBID…………………… Focused Electron Beam Induced Deposition

FIB………………………… Focused Ion Beam

FM-AFM………………… Frequency Modulated – Atomic Force Microscopy

FWHM…………………… Full Width at Half Maxium

GH………………………… Glycoside Hydrolase

HV………………………… High Vacuum

IL…………………………… Ionic Liquid

KPFM…………………….. Kelvin Probe Force Microscopy

L-AFM…………………… Atomic Force Microscopy in Liquids

LPMO…………………… Lytic Polysaccharide Monooxidase

LV………………………… Low Vacuum

MACS…………………… Mixed Amorphous Crystalline Cellulose Substrate

MFM…………………….. Magnetic Force Microscopy

NCC……………………… Nano-crystalline Cellulose

NCTFC………………… Nano-crystalline Thin Film Cellulose

OTS……………………….	Octadecyltrichlorosilane
PP…………………………….	Point Pich
RMS………………………….	Root Mean Square Roughness
RS…………………………….	Raman Spectroscopy
SAXS………………………….	Small Angle X-ray Scattering
SCTFC……………………….	Semicrystalline Thin Film Cellulose
SEM………………………….	Scanning Electron Microscopy
STM………………………….	Scanning Tunneling Microscope
SVG 17……………………….	Catalog name of a strain of the fungus *Hypocrea jeronica*
TEM………………………….	Transmission Electron Microscopy
THF………………………….	Tetrahydrofuran
TMSC………………………..	Trimethlysilyl-Cellulose
UM…………………………….	Ultramicrotomy
WAXS……………………….	Wide Angle X-ray Scattering

List of Publications

Chapter IV	**Section IV.2**	Ganner, T.; Aschl, T.; Eibinger, M.; Bubner, P.; Meingast, A.; Chernev, B.; Mayrhofer, C.; Nidetzky, B.; Plank, H. Tunable Mixed Amorphous–crystalline Cellulose Substrates (MACS) for Dynamic Degradation Studies by Atomic Force Microscopy in Liquid Environments. *Cellulose* **2014**, *21* (6), 3927–3939.
Chapter IV	**Section IV.3**	Ganner, T.; Roŝker, S.; Eibinger, M.; Kraxner, J.; Sattelkow, J.; Rattenberger, J.; Fitzek, H.; Chernev, B.; Grogger, W.; Nidetzky, B.; et al. Tunable Semicrystalline Thin Film Cellulose Substrate for High-Resolution, *In-situ* AFM Characterization of Enzymatic Cellulose Degradation. *ACS Appl. Mater. Interfaces* **2015**, acsami.5b09948.
Chapter V	**Section V.2.1-V.2.4**	Ganner, T.; Bubner, P.; Eibinger, M.; Mayrhofer, C.; Plank, H.; Nidetzky, B. Dissecting and Reconstructing Synergism: In Situ Visualization of Cooperativity among Cellulases. *J. Biol. Chem.* **2012**, *287* (52), 43215–43222.
Chapter V	**Section V.2.5**	Eibinger, M.; Bubner, P.; Ganner, T.; Plank, H.; Nidetzky, B. Surface Structural Dynamics of Enzymatic Cellulose Degradation, Revealed by Combined Kinetic and Atomic Force Microscopy Studies. *FEBS J.* **2014**, *281* (1), 275–290.
Chapter V	**Section V.3**	Eibinger, M.; Ganner, T.; Bubner, P.; Roŝker, S.; Kracher, D.; Haltrich, D.; Ludwig, R.; Plank, H.; Nidetzky, B. Cellulose Surface Degradation by a Lytic Polysaccharide Monooxygenase and Its Effect on Cellulase Hydrolytic Efficiency. *J. Biol. Chem.* **2014**, *289* (52), 35929–35938.
Chapter VI		Ganner, T.; Sattelkow, J.; Rumpf, B.; Eibinger, M.; Reishofer, D.; Winkler, R.; Nidetzky, B.; Spirk, S.; Plank, H. Direct-Write Fabrication of Cellulose Nano-Structures via Focused Electron Beam Induced Nanosynthesis. *In Submission.* **2016**.

Chapter I   Atomic Force Microscopy in Microbiology
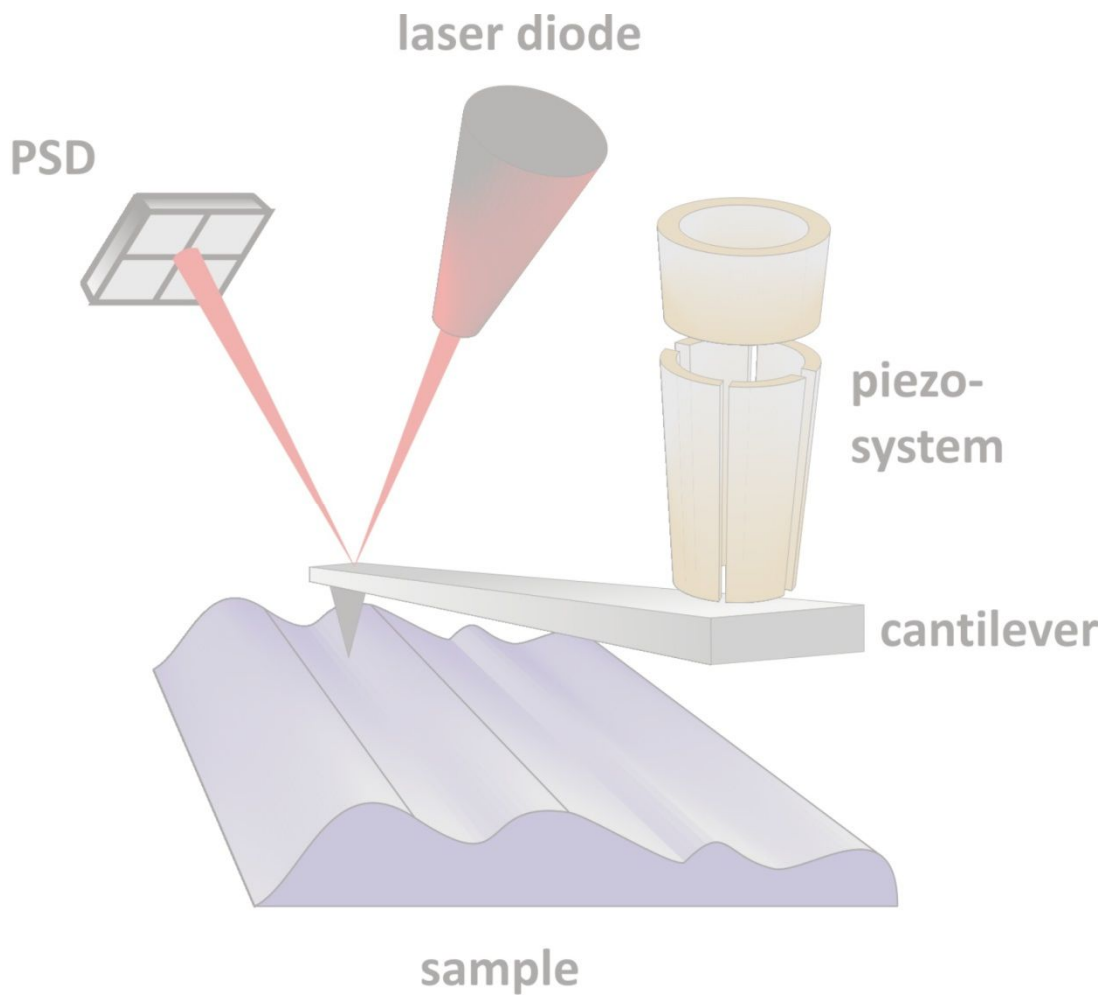
I.1 Introduction

In the past decade, Atomic Force Microscopy (**AFM**) has proven to be a feasible method to investigate dynamic enzymatic processes on surfaces down to molecular levels. By that, a fundamental insight in biological systems under natural conditions is available. The method itself was invented in 1986 by Binnig, Quate and Gerber[1] as an extension to the former developed scanning tunneling microscope (**STM**)[2] which is restricted to conductive specimens. Based on a similar principle, the AFM uses a sharp tip mounted on a cantilever to scan the surface by detection of physical quantities of the cantilever system, which may be the deflection of the cantilever due to the interaction with the sample. The latter is called contact mode and was the starting point in a series of novel inventions over the years, which are still in progress. Soon thereafter dynamic modes like amplitude modulated AFM (**AM-AFM**)[3] and frequency modulated AFM (**FM-AFM**)[4] were introduced. Tapping mode AFM (AM-AFM) proved to be the basis for many modes used today, covering the detection of electrostatic[5], electric[6], magnetic[7] and other properties[8]. The basic principle as a force sensitive microscopy method soon also offered the possibility to measure and quantify molecular forces in the pN regime[9]. The expansion of AFM to liquid environments using contact[10],tapping[11] or force quantification methods[9] was another milestone towards real bio-microscopy. First attempts include the visualization of whole cellular bodies[12] and DNA strands[13]. Since then, progress has consequently been made towards smaller biological specimens as antibodies[14], membrane proteins[15] and single enzymes[16]. Just recently, Igarashi and coworkers showed the enzymatic degradation of cellulose by direct visualization of the movement of single enzymes with the help of a laboratory build high speed AFM[16,17]. The visualization of such processes is extremely challenging, as small macromolecules (enzymes) are active on soft materials and on short time scales. Today, fluid AFM operation may be seen as state-of-the art, however, at relative low scanning speeds. Current developments focus on faster systems which will allow to image samples in the sub-second regime, thus unraveling biological processes in real time. To exploit the full potential of this technique, it is important to understand the theoretical background. In this *chapter* a summary of theoretical principles will be given alongside with the basic operation principles which apply for all closed loop controlled AFM scanners.

I.2 Atomic Force Microscopy

I.2.1 Instrumental Concept

The instrumental concept of AFM is closely related to the former invented STM, where a sharp tip is scanned over the surface and the tunneling current between probe and conducting specimen is monitored as feedback. The requirement of conducting samples is a strong restriction and usually excludes soft not metallic materials. Binnig, Quate and Gerber[1] thought about another concept, where the probe is mounted on a long flexible cantilever. At low tip-surface separations, short and long range atomic forces (Van der Waals, electrostatic, magnetic, Pauli-repulsion) couple to the cantilever system and generate measurable changes in, for instance, the deflection. This first mode was called contact mode AFM and led the foundation for all AFM modes known today. A disadvantage of contact mode is that full contact operation is prone to either tip-wear or sample

damage[18]. Thus, alternative methods with strongly reduced energy dissipation to the sample were required. So, soon after contact mode, the tapping or amplitude modulated AFM was developed[3]. In principle, both methods rely on the same system requirements in terms of detection system and control electronics as depicted Figure I-1 by a schematic diagram of a conventional AFM.
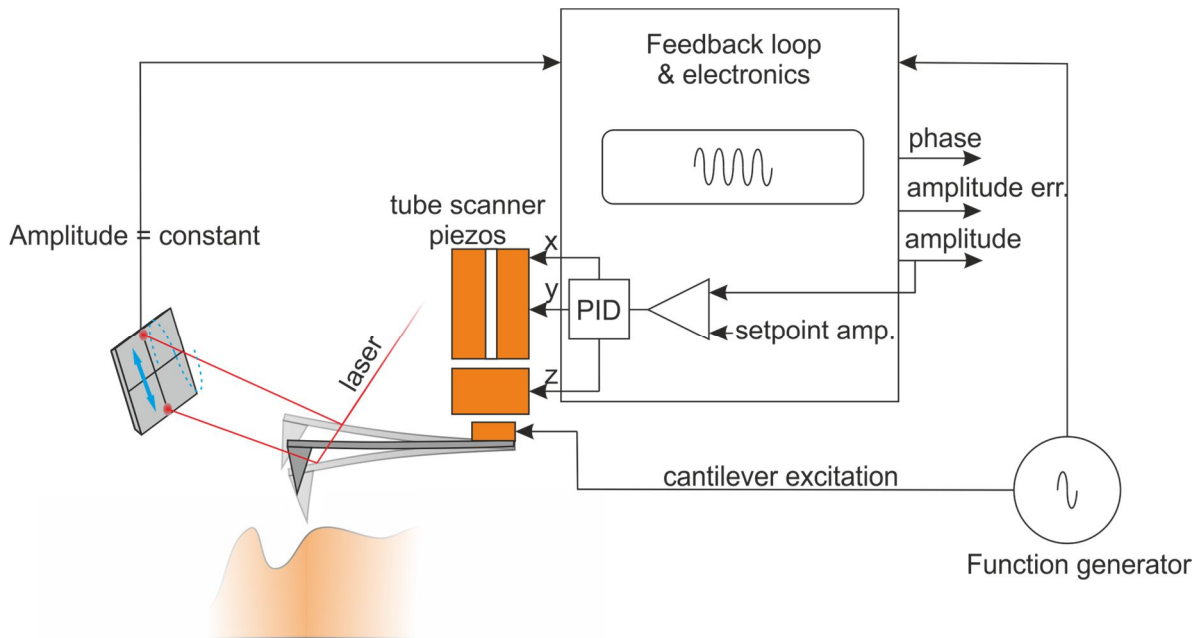
Figure I-1: Schematic drawing of an amplitude modulated AFM with feedback electronics, an optical detection system (laser and a four segment photodetector) and a tube piezo scanner. For contact mode, the feedback parameter is the deflection of the cantilever, while for tapping mode the oscillation-amplitude of the cantilever is used.

A typical system can be divided into 3 main components, including either a probe or sample piezo-electrical actuator system for modulation, movement (x,y) and topography scanning (z); a detection system, which in this case is the so called optical method and an electronic system with PC, feedback loop, function generator and PID controller. The following sections will deal with these systems in detail.

I.2.2 Probe-Actuator System

The probe actuator system may be associated with our tactile sense. In this form, it may be seen as our finger (probe), the arm (cantilever) and the muscles to move it (piezo actuators). Despite this vivid description, the size and shape of the AFM system is considerably smaller and mechanical as well structural components are extremely important for image interpretation. Thus, at first the cantilever has to be considered in more detail.

I.2.2.1 Cantilever

Most commercially available cantilevers have dimensions ranging from a few µm to hundreds of µm, while the width mostly stays below a few tens of µm. Tips are usually a few µm high, but have only a few nm in tip radius. In order to produce cantilevers reproducibly and precisely, new preparation protocols had to be found and quickly led to the use of silicon (Si) or silicon nitride (Si_4N_3)[8]. The reason is, that existing procedures were already known from semiconductor industry[19]. Most cantilevers either have a rectangular or trapezoidal shape (Figure I-2) which mainly depends on the applied operation mode and imaging media (gas, liquid). For optical detection enhancement, backsides are often coated with gold or aluminum.
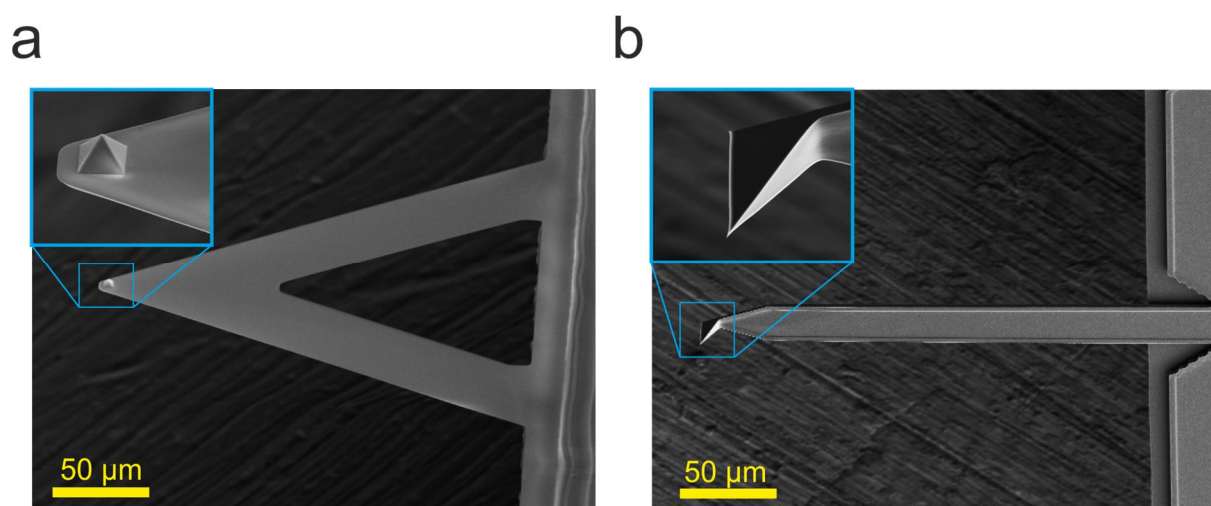
Figure I-2: SEM images of a triangular (a) and rectangular (b) cantilever with the probe in front. The triangular cantilever has a pyramidal Si_4N_3 tip and the rectangular a half-symmetric tetragonal tip. Please note, tip shape as seen in (b) is not typical for rectangular cantilevers but a consequence of the fabrication process. Other shapes may be achieved by different processes.

Reconsideration of the instrumental concept (see I.2.1) shows that important parameters of the probe cantilever system are associated with its mechanical properties and dimensions. These parameters determine the response in either contact (deflection, friction force) or tapping mode (resonance frequency, phase mapping). This becomes important when thinking about the interaction of tip and specimen. It is evident, that mapping of weak interaction forces or soft materials would require a lower stiffness as mapping of hard materials like silicon or ceramics. As a good rule of thumb, hard specimens require stiffer cantilevers and softer materials more flexible ones. In liquid, stiff cantilevers are seldom used, as materials are most of the time soft anyway. Best results may be acquired by using spring constants between k = 0.05 N/m to 1 N/m. If used in contact mode, spring constants are usually exceptionally low to prevent scratching of the sample or tip wear. The parameters introduced here will be needed for a mathematical description of AM-AFM shown in section I.4.2 .

I.2.2.2 Probe

It is important to consider the probe shape and the tip radius as it considerably influences imaging. Perfect images would require infinite aspect ratios and tip radii approaching zero. As this is not the case in real systems (see Figure I-2), images are always a convolution between tip and surface (see

section I.2.5). Another aspect is that etched silicon tips often do not have fully symmetric shapes which would lead in special cases to differences in images when the scanning angle is alternated (Figure I-3). An example demonstrating this is shown in Figure I-3. A detailed description of imaging artefacts is given in section I.2.5 .
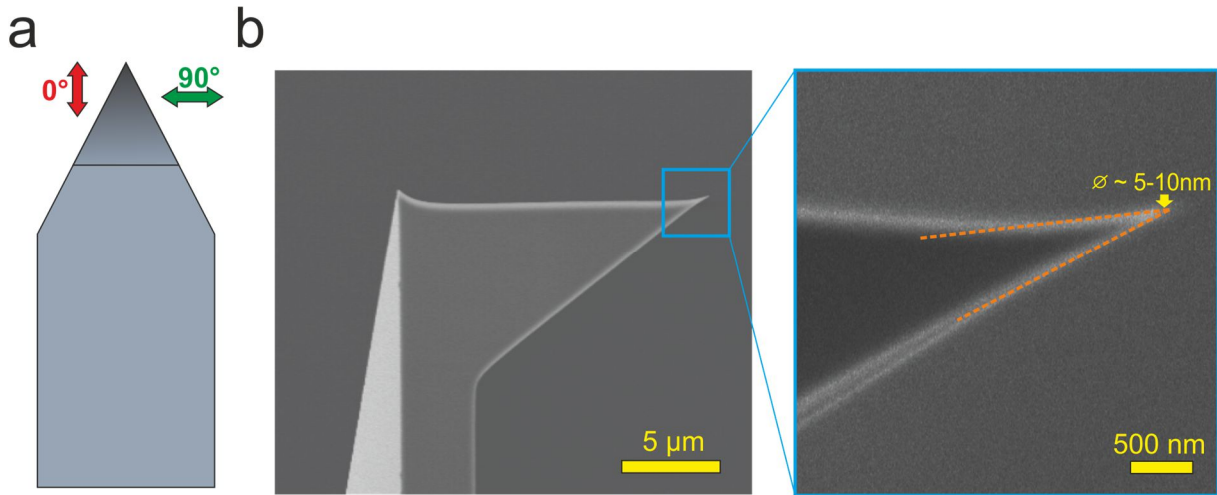
Figure I-3: (a) Schematic drawing of conventional probe (Olympus AC160-TS) seen from the top. Arrows red (0° scan angle) and green (90° scan angle) demonstrate that in the case of 0°, scanning symmetry is not given and may led to artifacts on large features (>200 nm). (b) Similar probe visualized by SEM showing the tip with a tip radius usually around 5-10 nm and an opening angle of about 35° and 15° on back- and side-angle (orange envelope).

Although most commercially produced tips have now tip radii below 10 nm, high aspect ratio tips like single carbon nanotubes are still not widely available[8]. This simply results from a complicated fabrication, high fabrication costs and limited reproducibility. However, advanced AFM modes have triggered the development of modified probes like in, e.g., magnetic force microscopy[20] with cobalt chrome (CoCr) coatings. Further examples include scanning thermal microscopy with thermocouple tips or scanning nearfield optical microscopy[21] with probes with aperture connected to an optical waveguide. In conclusion, a lot of different imaging modes are now available, but tip shape, opening angle and aspect ratio should be kept in mind in all AFM investigations.

I.2.2.3 Piezo Actuators

In a conventional AM-AFM as in Figure I-1 piezo-actuators are used to excite cantilever oscillations and scan the tip over the surface. Typically, maximum nominal lateral scan areas are found between 150 x 150 µm^2 to a few µm, depending on different concepts used. For vertical resolution the range is typically a few micrometers but can be as high as 15 µm. As a rule of thumb, the reachable minimal resolution correlates with the maximum scan range (small maximum scan rates allows higher resolution). The reason is that piezo-actuator suffer from a series of problems as creep, aging, hysteresis and thermal drift[8]. Creep, hysteresis, non-linearity and thermal drift can be compensated by software implemented algorithms or so called closed loop scanners. Here, displacements of the piezos during scanning are measured by magnetic, capacitive or optical systems and are corrected towards their nominal values[8]. The mechanical implementation of the actuators differs between microscopes. In most commercial AFMs so called table scanners are found for high-resolution

imaging (maximum image size is a few tens of µm) and tube scanners for large maximum scan ranges (Figure I-1; scan sizes up to 150 x 150 µm^2 and larger). The microscopes used in this study were all equipped with tube scanners and ongoing description will focus on this type. As one of the major advantages, tube scanners allow larger movements (scales) of the cantilever simply by the fact that piezo-movement is not longitudinal but rather lateral as shown in Figure I-4. Here, two piezos for x and y, respectively, are arranged to form a tube with another smaller tube attached to the bottom for the z-direction. Applying opposite voltages to e.g. both x-piezos will result in distortion of the tube which results in a spherical calotte movement or so called "scanner bow". This in turn has to be compensated by the z-piezo to allow imaging and may be seen as the disadvantage of this method. However, the strong deflection associated with the tube length allows way larger scan scales to common table scanners coupled with the advantage of extreme space below and to the side of the scanner. Moreover, the fact that specimens are below the scanner allows saver liquid operation as spilling of liquid will not cause problems due to short circuits at the piezos. In Figure I-4, a schematic drawing of the tube scanner system is given.
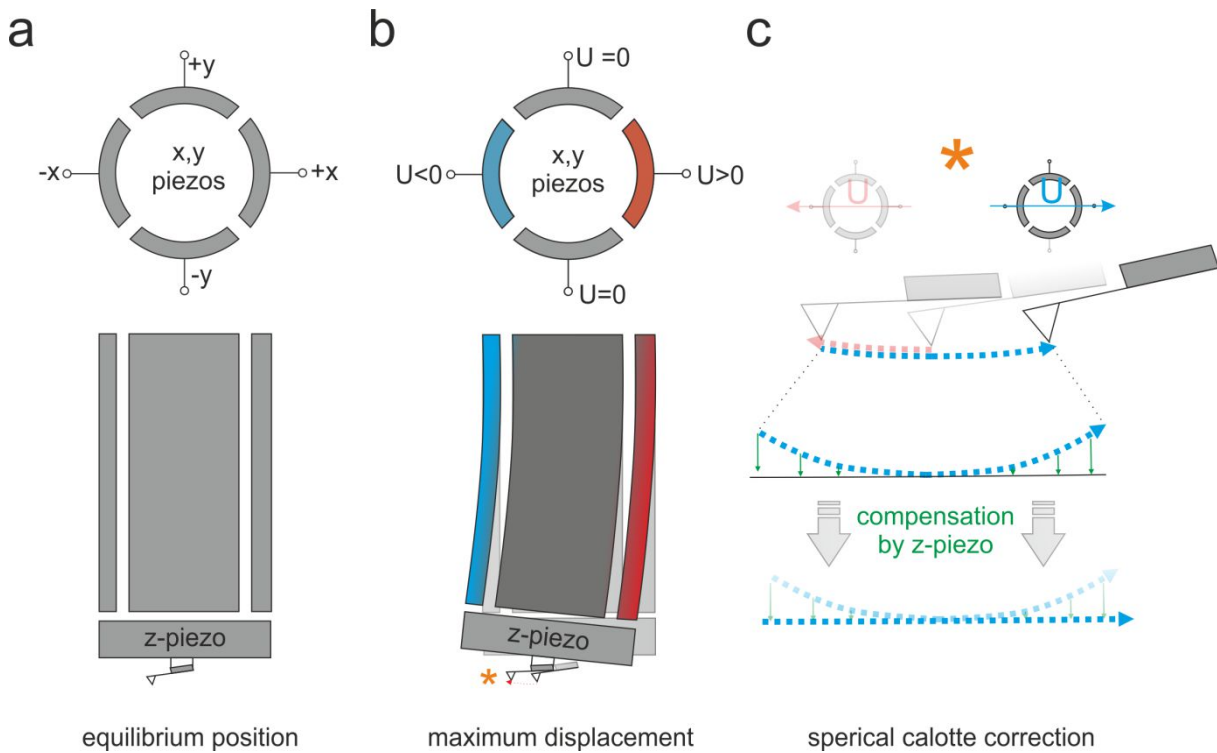
Figure I-4: Schematic illustration of tip movement in a tube scanner when a voltage is applied (a, b) to the z-piezos. The tip follows a spherical calotte (c) and this must be compensated by the z-piezo for every line to allow proper scanning. The maximum scan size can be adjusted simply by changing the tube length.

It is noteworthy, that one should remember to calibrate the microscope every 2-3 months as differences in piezo sensitivity will lead to changes in topographic accuracy. With proper calibration, vertical resolution of a few hundred picometers may be achieved. Lateral minimal resolutions depend on the nominal maximum scan range and tip dimensions (shape and size) but typically are found below two nm.

I.2.3 Detection Systems

Accurate measurement of cantilever deflection or amplitude is the foundation to successful AFM operation, as this provides the "sense" to the microscope. Different methods have been used so far, basically divided in direct or indirect methods. Direct methods are, e.g., piezo-resistive detection. Here, two contacts at the backside of the cantilever are connected through a thin deposited piezo on the backside of the cantilever which produces different voltages at different deflections. Other methods use piezo-based tuning forks[22] with attached tip to measure amplitudes in AM-AFM. The most common indirect technique goes back to the first AFMs [23] and uses optical detection by reflecting a laser beam of the cantilever onto a photodiode. It is the simplicity of this method, coupled with its high sensitivity, high signal to noise ratio and stability which led to the common use in commercially available AFMs[8]. All AFMs used in this study were equipped with this detection method and further description will only apply to this method. In Figure I-5 a schematic drawing of the optical method shows the main elements, with laser diode, mirrors and the 4-segment photodetector. A laser beam is reflected at the backside of the cantilever and detected by a 4-segment photodiode. Mirrors are used to focus and position the laser on the cantilever due to the fact that no cantilever can be positioned at the exact same spot during probe mounting.
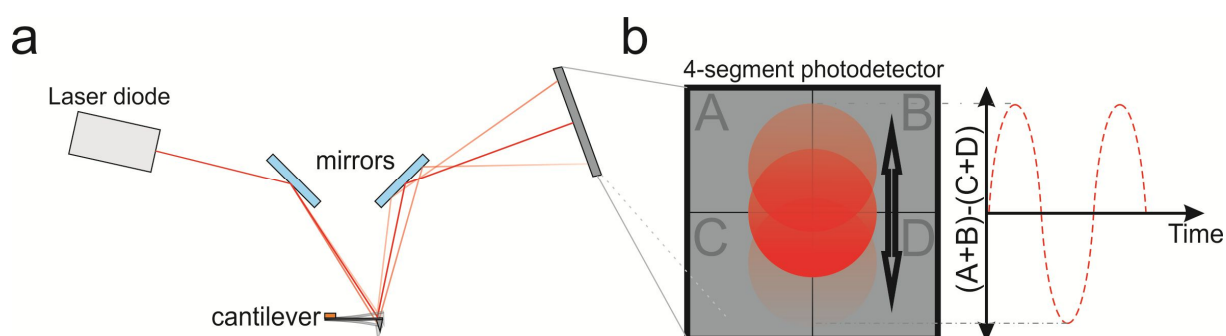
Figure I-5: The optical detection system of a convetional AFM. (a) The laser follows an optical path determined through mirrors and is detected at a 4-segment photodetector where the signal of, e.g., amplitude modulation AFM is generated by subtracting segments AB from CD yielding the waveform in (b).

Detection of amplitude or deflection is realized by electronic subtraction of the intensity values of the different segments. A simple mathematical consideration by Garcia[8] shows that the amplification of the cantilever amplitude (Δz) on the photodetector is proportional to the ratio of the cantilever-photodiode distance D and the cantilever length L (see equation (1.1)).

$$A_{photodetector} \propto \frac{2D}{L} \Delta z \qquad (1.1)$$

I.2.4 Feedback Loop

The feedback loop is a pivotal point of any modern AFM and should therefore be considered comprehensively. It allows the operator to adjust the imaging in a way that minimal energy dissipation to the sample and highest spatial resolution is provided. In feedback loop operation, the

actual measured amplitude (A_{act}) is compared to a user specified set-point amplitude (A_{sp}) and, if necessary, corrected to resemble the set-point amplitude (see Figure I-1 and Figure I-6). At each sampling point in **time, the actual amplitude A_{act} is measured and the difference ΔA is calculated by equation (1.2).**

$$\Delta A(t) = A_{sp}(t) - A_{act}(t) \qquad\qquad (1.2)$$

Thereby, an error signal commonly called "amplitude signal", is generated and stored in a separate channel and usually recorded as amplitude image. The amplitude image contains valuable information on the tracking conditions. Improper feedback loop parameters or controller gains will lead to either large error signals (response time is to long) or noisy images (response time is to short) in the amplitude channel. In a perfect controller this signal should always be zero. However, as controllers are not infinitely fast, this signal is only zero on flat parts of the sample. The error amplitude (ΔA) is fed to a PID (**P**roportional-**I**ntegral-**D**ifferential) controller and correction is applied by moving the z-piezo up and down. The correlation of piezo voltage and piezo-expansion – which is called the calibration – allows topographic image recording. It is absolutely essential that the PID controlling parameters are set properly to gain images with lowest noise and energy dissipation to the sample. This is usually applied by adjusting P and I gains which basically determine the reaction speed of the feedback loop to changes ΔA. D gains are most of the time zero or not accessible as these are very sensitive and tend to destabilize the controlling.

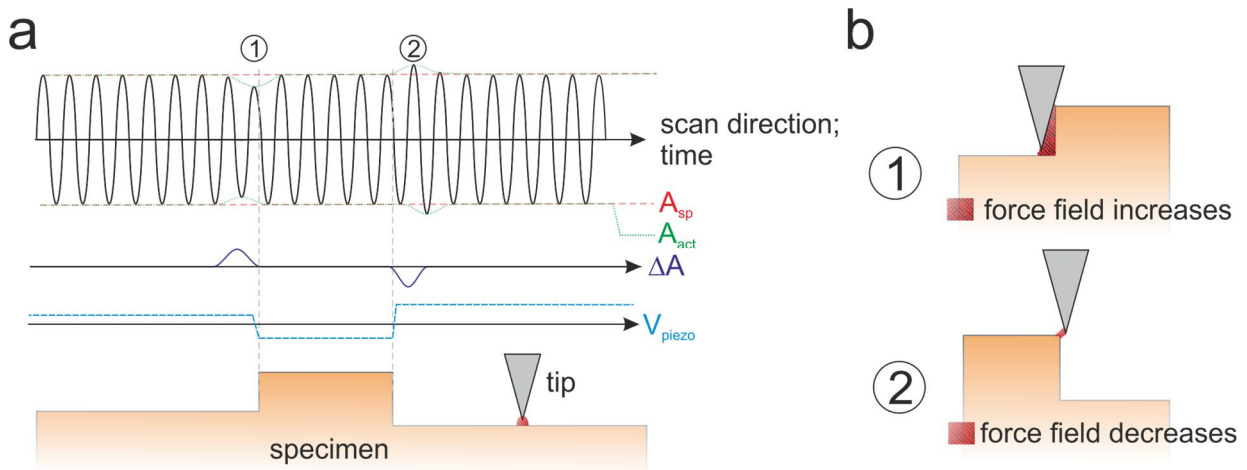*Figure I-6: (a) Schematic representation of the measured amplitude in an AM-AFM (section I.3) in dependence of topographic features. At steps, a different impact of forces on the tip reduces (b;1) or increases (b;2) the amplitude. The amplitude error is then used to correct the piezo voltage V_{piezo} through equations (1.3) to (1.6).*

The parameter P-gain, or proportional gain, is responsible for the instantaneous correction of the piezo voltage as denoted in equation (1.3).

$$V_{piezo}^{P} \propto P_{gain} * \Delta A(t) \tag{1.3}$$

Although fast, this parameter alone would amplify cantilever noise, so the following parameter, the integral gain is used to correct for this disadvantage. As the name already specifies the integral gain is used in an integrative way where the mean value of the amplitude error $\Delta \bar{A}$ is used for correction (see equation (1.4)). By that, noise is canceled out and proper scanning is ensured. Both gains may be seen in as opposing factors where the proportional gain is responsible for a fast response and the integral gain ensures that the response is not caused by noise.

$$\Delta \bar{A} = \frac{1}{T_I} \int_{t1}^{t1+T_I} A(t)dt \tag{1.4}$$

$$V_{piezo}^{I} \propto I_{gain} * \Delta \bar{A} \tag{1.5}$$

$$V_{piezo} \propto V_{piezo}^{P} + V_{piezo}^{I} \propto P_{gain} * \Delta A(t) + I_{gain} * \frac{1}{T_I} \int_{t1}^{t1+T_I} A(t)dt \tag{1.6}$$

Most software implementations will use the factor $I_{gain}*1/T$ as I-gain. By that, higher gains will cause shorter integration times and lower gains higher ones. By adjusting these parameters carefully, image quality can be increased dramatically. However, care should be taken as choosing integration times too long will cause the AFM to react too slow, thus causing damage to the tip. There are several more parameters associated with electronics and software which will help to enhance image quality, but a full explanation would be beyond the scope of this thesis.

I.2.5 Imaging Artifacts

At the end of this short introduction to AFM and its main components the important topic of imaging artifacts remains to be explained. The reason to do this at this point is simply that here, a fundamental property of AFM is given with strong impact on image interpretation which is independent from the applied imaging mode. Artifacts may have multiple causes, whereas probe-specimen convolution may be the most observed one, resulting from tip wear, tip damage and pickup of specimen material. Although also present on non-contaminated probes, the term artifact may not be appropriate for these convolutions, as these are inevitable and fundamental aspect in any AFM image (Figure I-7). Other artifacts, like scanner hysteresis or scanner nonlinearity will not be part of this thesis, as these result from false calibration which applies differently to each AFM. A comprehensive insight is given in most AFM manuals and in the book of Braga and Ricci[24]. As the

basis to the usual observed tip shape related artifacts, understanding probe convolution is essential and demonstrated in Figure I-7. Here a clean and perfect AFM tip is producing an image, which is the convolution of specimen feature (e.g., spike) and the conical tip. This image is different from reality and should be kept in mind. While this plays minor role on small features and non-spiked objects, this has to be considered on sharp high walls, spikes and deep trenches. In summary, care must be applied on image interpretation if the hole or trench opening angles are comparable to tip angles.

On the other hand, contaminated probes or broken tips produce artifacts which are not always easily distinguishable against real data and care should be taken upon analysis of every image. In Figure I-8 the two most common artifacts are shown resulting from a broken "double" tip and a contaminated tip. In summary, these images (Figure I-8) show that image generation and interpretation by the use is not always an easy task and that care should be applied.
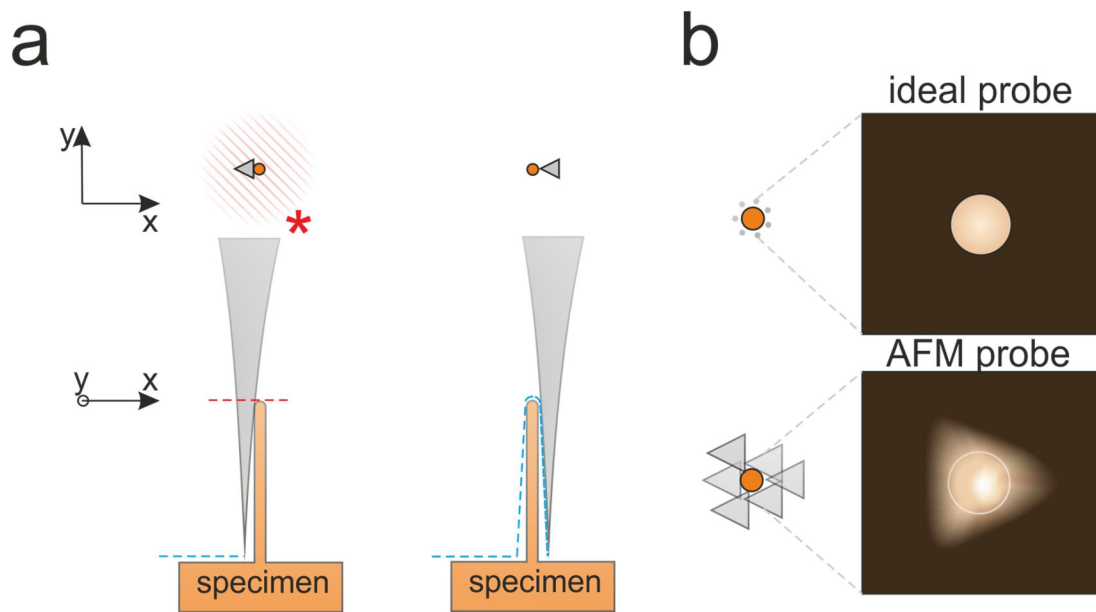
Figure I-7: Images acquisition by a conventional AFM tip (a; b, AFM probe) leading to convolution effects of surface feature and tip. (b) Difference of an ideal probe with infinite aspect ratio and a conventional AFM tip. The effect is considerable large on pointed large objects (e.g high-aspect ratio spikes), should, however, be taken into account in any image.
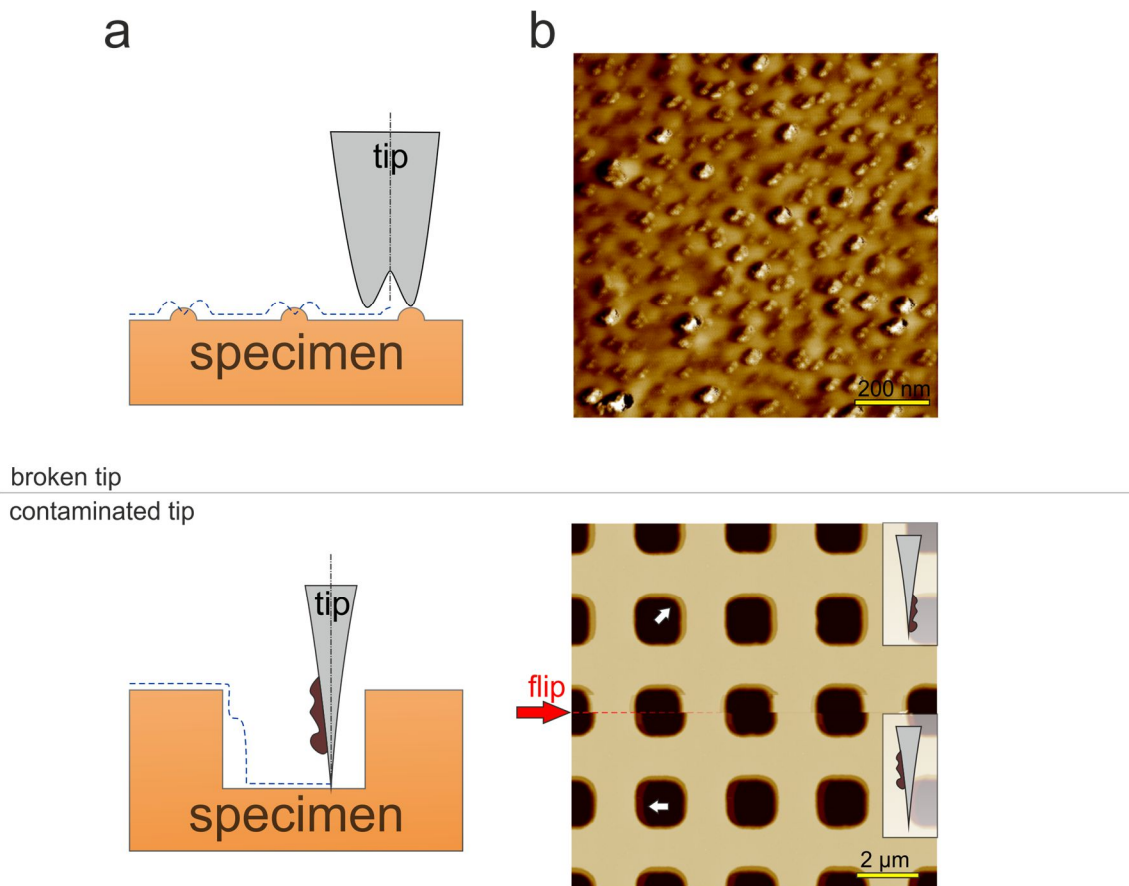
Figure I-8: (a) Schematic representation of the two most common artifacts: broken multi-tip and contaminated tip with real data in (b). (b) For the broken tip, a so called double tip is observed, which results in double features on every particle as seen in the schematics. A contaminated tip produces an additional step at steep etches. Here by coincidence the contamination flips in the middle of the image to the other side of the tip. This causes non-real data and should be carefully considered.

I.3 Amplitude Modulated AFM

Often denoted as dynamic atomic force microscopy, amplitude modulated AFM (AM-AFM) is the common method used due reduced tip load, longer tip lifetime and additional phase modes (EFM, KPFM, MFM)[5–7]. However, understanding the theory behind AM-AFM is a complex matter, as tip-sample interactions are highly non-linear (see next section I.4) and coupled with a complex 3-dimenional shape of the tip, cantilever and specimen. This complexity is reflected by 20 years of development to establish the theory of AM-AFM following its invention[8]. As a full description is beyond this thesis, a short and concise introduction to the theoretical basis behind AM-AFM in air as well liquid will be given. Most of the presented theoretical explanations are based on the book of Garcia[8].

I.4 Tip Surface Interaction – Forces in Air

AFM imaging and operation is closely related to the tip-sample nanoscale forces when scanned over the surface. A simple approximation of the forces observed by the tip are shown in Figure I-9 and

discussed in more detail in the following *chapter*. The super-positioned potential (blue) is well known as the Lennard-Jones potential.
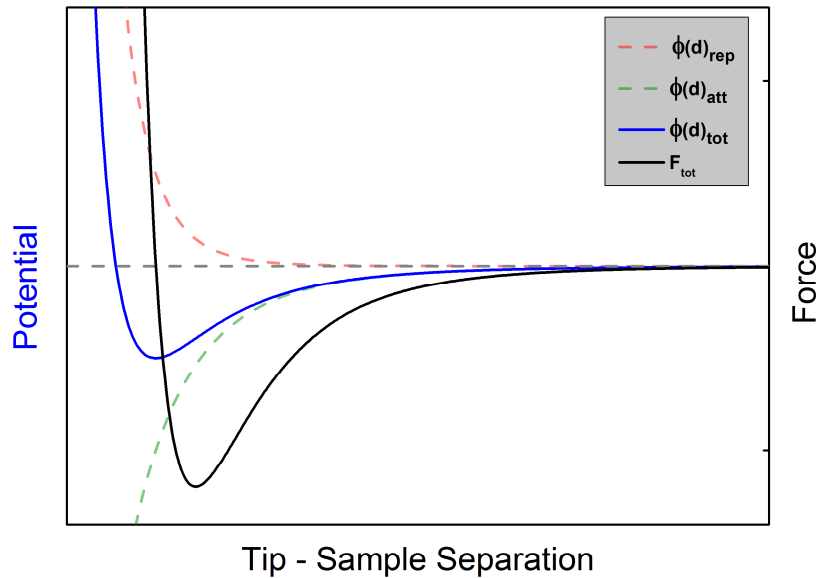
Figure I-9: A typical potential between the highest specimen atom and the tip atom. The total potential (blue) corresponds to the sum of an attractive (e.g. Van der Waals; green) and repulsive (e.g. Pauli exclusion principle; red) potential. The negative derivative of the potential yields the force in black with the attractive (F_{tot}<0) and the repulsive part (F_{tot}>0).

In reality however, the shown potential can only be seen as an approximation since the 3-dimensional geometry of the tip and specimen has to be considered. A detailed description of forces involved in tip–sample interactions is given by Israelachvili or Butt and coworkers[25,26]. To understand the implications of forces described later in this section, one must know, that AM-AFM operation usually is characterized through two force regimes: the attractive regime where the overall force is positive (F<0; Figure I-9) and the repulsive regime where the overall force is negative (F>0; Figure I-9). Both forces are mainly described through two contributions, the long range attractive Van der Waals force and the repulsive forces resulting from ion-ion or Pauli repulsion. A short description of these contributions will be given in the following.

I.4.1.1 Van der Waals Forces

Long range interaction of the Van der Waals type arises from fluctuations in the electromagnetic field of two particles (Figure I-9; Attractive Force). Usually applied for molecules, the situation in AFM is different, since the 3-dimensional shapes of tip and the specimen have to be considered. The Van der Waals force for a sphere-flat geometry, as good approximation for AFM operation, can be given by equation (1.7)[27].

$$F_{vdW} = -\frac{A_H R}{6d^2} \tag{1.7}$$

Here A_H is the Hamaker constant including the physio-chemical information of the system[26], R the radius of the tip and d the tip-sample instantaneous separation. It may be worth mentioning that although this force usually is attractive, there is the exception of two surfaces brought together in liquid where this force can be repulsive (see also Israelachvili[25]).

I.4.1.2 Contact Mechanic Forces

The repulsive forces in AFM are the result of Pauli and ionic repulsion, formed by the interaction of thousands of atoms or ions between 3 dimensional objects, like tip and specimen. The best theoretical description of this problem is by contact mechanic models. So far multiple models were developed[28], each using different parameters of elasticity and load as well as limitations. In the beginning of contact mechanics, Hertz based the mathematical description on a simple assumption of an infinite sharp and absolutely repulsive interaction[29] which obviously is not true in reality. Once the tip comes into contact with the sample, there will be contribution from attractive forces, still acting on parts of the tip not in contact with the specimen, as well as deformation of the probe or sample. One commonly used method implementing long range attractive interaction forces outside the contact region is the Derjaguin-Muller-Toporov model (DMT-Model)[30]. The full theory is beyond the scope of the thesis but comprehensively described in literature[28,30,31]. Briefly, the interaction is summarized in an attractive and repulsive contribution and given by the following equation (1.8),

$$F_{DMT} = F_a + F_r = -4\pi R\gamma + 4/3E^*\sqrt{R}(\alpha)^{\frac{3}{2}} \qquad (1.8)$$

$$E^* = \left(\frac{1 - v_t^2}{E_t} + \frac{1 - v_s^2}{E_s}\right) \qquad (1.9)$$

where R is the tip's radius, γ the surface energy, E^* the effective Young's modulus and α a parameter describing the deformation of specimen and tip[30]. Equation (1.9) shows the relationship of the effective Young's modulus with v_t and v_s and E_t and E_s corresponding to the Poisson ratio and Young's modulus of tip and specimen, respectively. In the case of a hard tip and a soft specimen, as usually the case in AFM, α is the indentation of the spherical probe which can be measured and used to map the nano-mechanical properties of the sample. This is used today in novel force mapping modes as, e.g., PeakForce® nanomechanical mapping (Bruker AXS, Santa Barbara, California/USA) where soft samples can be analyzed according to their mechanical spatial confined mechanical properties. However, the theory applies to contact mechanics in general by describing tapping mode AFM considerably well.

I.4.1.3 Capillary force

Under ambient conditions, water vapor present in ambient air can condensate on hydrophilic surfaces forming a thin water layer (often referred to as wetting layer). This is especially relevant in pores, cracks and other obstacles and might considerably influence imaging. The reason is that from

theoretical calculation under high humidity, capillary forces may take values of about 1-100 nN[8]. This is a significant force and may dominate all other forces in the AM-AFM. The nature of the meniscus formed at the tip apex would then decrease image quality, stability and resolution to a major extent. Solutions to this problem might be found by controlled environment systems (glove box) where water concentration is held at absolute minimum (ppm). Using AC controlled environment and careful drying procedures (heating, silica beds) is, however, in most cases sufficient to render capillary forces negligible. Note, for some techniques which are performed in non-contact intermitted mode (KFM, MFM, EFM), glovebox environment is decisive. For detailed description see[8,26].

I.4.2 Theory of AM-AFM in Air

The starting point of any theory is to establish a model of the involved structures and parts and their physical behavior. For AFM, the cantilever-probe system is of main relevance as it is the transducer of the interactions of specimen and tip. For a rectangular cantilever the partial differential equation of motion is described by the Euler-Bernoulli beam equation (1.10) with some additional dissipative elements [8].

$$EI\frac{\partial}{\partial x^4}\left[w(x,t) + a\_1\frac{\partial w}{\partial t}\right] + \rho Wh\frac{\partial^2 w}{\partial t^2} = -a_0\frac{\partial w}{\partial t} + \delta(x - L)[F_{exc}(x,t) + F_{ts}(d)] \quad (1.10)$$

In equation (1.10) E, I and ρ are the Young modulus, mass of inertia and mass density; L, W and h the length, width and thickness of the cantilever; a_0 and a_1 external and internal damping parameters and F_{exc} and F_{ts} the applied external force and the tip-specimen interaction force, respectively. The equation in this form is difficult to solve and should only provide a demonstration of the complexity behind AM-AFM operation. Fortunately there are straight-forward simplifications of this problem which describe some of the phenomena observed in AM-AFM considerably well. A good example is the point mass model.

I.4.2.1 The Point-Mass Model

A good and valid simplification may be given by the point mass model where the geometric and intrinsic properties (E, I, W, L, h, ρ, etc.) are concentrated into a spring with spring constant k and a pointed mass m. By that, the motion of the cantilever may be described by a driven damped harmonic oscillator with non-linear forces (equation (1.11)) [8,32].

$$m\ddot{z} + kz + \frac{m\omega_0}{Q}\dot{z} = F_0\cos(\omega t) + F_{ts}(z,\dot{z}) \; ; \; \omega_0 = \sqrt{\frac{k}{m}} \quad (1.11)$$

In equation (1.11) Q is the so called quality factor which is defined as the ratio between stored energy at resonance against the energy loss per cycle. High Q factors thereby denote a low damping

or high resonance frequency. Consideration of the tip-specimen interaction forces F_{ts} which are (section I.4) non-linear, makes analytical solutions to this problem difficult. However, far from the sample F_{ts} equals to zero and the movement of the cantilever follows the laws of a forced harmonic oscillator with damping [3,33] yielding equation (1.12)-(1.14).

$$\omega_r = \omega_0 \left(1 - \frac{1}{4Q^2}\right)^{\frac{1}{2}} \tag{1.12}$$

$$A(\omega) = \frac{F_0}{m\left[(\omega_0^2 - \omega^2)^2 + \left(\frac{\omega\omega_0}{Q}\right)^2\right]^{\frac{1}{2}}} \tag{1.13}$$

$$\Phi = \tan^{-1}\left(\frac{\omega\omega_0}{Q(\omega_0^2 - \omega^2)}\right) \tag{1.14}$$

In equation (1.12)-(1.14) ω_r, $A(\omega)$ and φ are the resonance frequency, amplitude and the corresponding phase shift, respectively.

Now, upon approach to the surface F_{ts} changes to attractive and subsequently repulsive interactions as already shown in section (Figure I-9). In a first approximation under the requirement that the amplitude and corresponding cantilever displacement is small we may linearize F_{ts} by Taylor expansion to the first order (equation (1.15)).

$$F_{ts}(z, \dot{z}) = F_{ts}(0) + \left(\frac{dF_{ts}}{dz}\right)_0 z = F_{ts}(0) + k_{ts}z \tag{1.15}$$

Per definition, this linearization, if substituted to equation (1.11), yields again a forced and damped harmonic oscillator with an effective spring constant $k_{eff} = k \pm k_{ts}$. Consider Figure I-9 where dF_{ts}/dz is either negative (repulsive) or positive (attractive) yielding $k_{eff}=k+k_{ts}$ or $k_{eff}=k-k_{ts}$, respectively. This situation is schematically depicted in Figure I-10. Also by taking equation (1.12)-(1.14) one observes that the resonance frequency is shifted to lower values or higher values for the attractive and repulsive situation, respectively. However, although the ansatz presented here shows principles which are found in real operation, like lower resonance frequencies upon attractive forces, it lacks a full description of AFM dynamics. This is expectable by the considerable large simplification done in equation (1.11) compared to equation (1.10).

In particular, the simplification in (1.15) cannot demonstrate the observed non-linear dynamics observed in AM-AFM (e.g. bistability etc.). Following the force in Figure I-9 would suggest a continuous change from the attractive to the repulsive force regime, reflected also in a continuous change from the phase from about -90 degrees to +90 degrees as seen in Figure I-10. However, this is not observed in AM-AFM imaging where change from attractive to repulsive regime is discontinuous. In the next section a refinement to this method will be discussed which accounts for this problem by the application of numerical methods to calculate an approximated solution
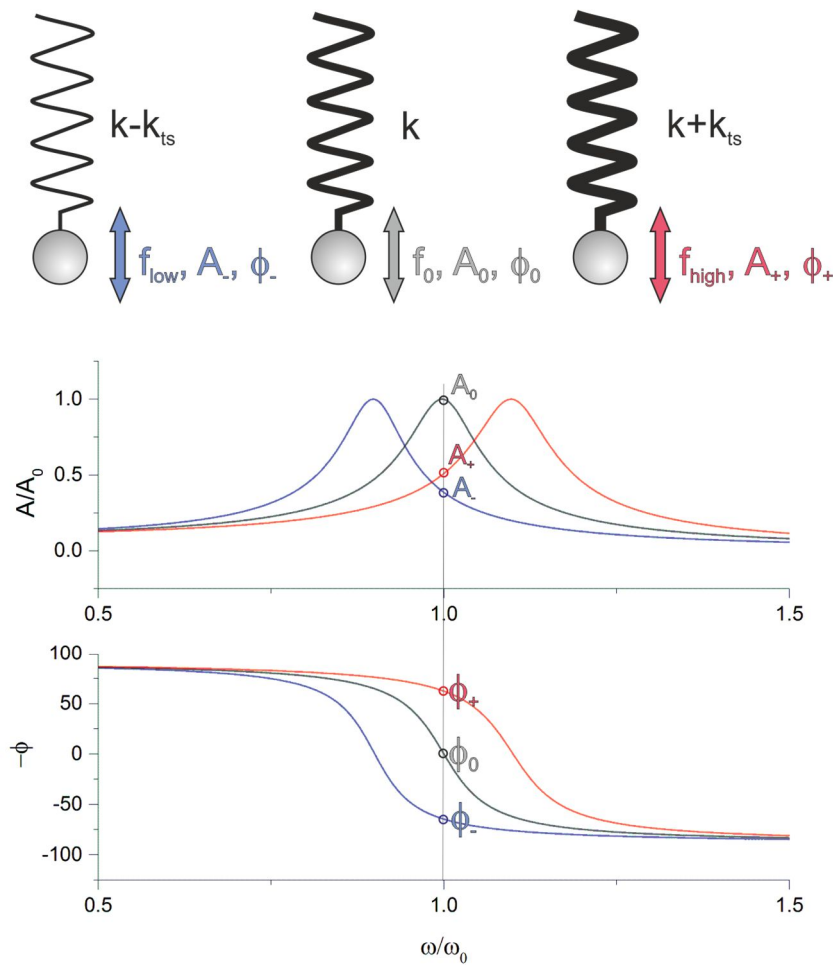
Figure I-10: Calculation of the amplitude and phase of the weakly perturbed oscillator from equation (1.13), (1.14) and (1.15) showing the impact of attractive (blue) and repulsive (red) forces.

I.4.2.2 Numerical Treatment of the Point-Mass Model

Numerical calculations by a fourth-order Runge-Kutta algorithm of equation (1.11) and corresponding forces (1.7)-(1.9) offer a more comprehensive insight into the complex non-linear dynamics observed for AM-AFM. The numerical treatment does not rely on a linearization of $F_{ts}(z, \dot{z})$ as in equation (1.15) and thus show also a different non-linear behavior. In Figure I-11 numerical simulations of the equation of motion (1.11) yield the possibility of two stable solutions[27] denoted further as high amplitude (**HiA**) and low amplitude (**LoA**) solution. As a matter of fact, only one solution can be present at one point in time. This behavior is exactly which is observed in AM-AFM operation by the presence of two regimes which are called the attractive and repulsive regime. Again from numerical solutions[27], it is found that the HiA-solution is characterized through overall negative force gradients and the LoA-solution through positive force gradients. Furthermore, in the HiA-solution the tip is in intermitted contact with the sample and may in this case really be denoted as tapping mode AFM. However, in the LoA-solution the tip is usually not in contact with the sample and the term non-contact amplitude modulated AFM may be more appropriate. This has significant consequences as the force of the tip exerted onto the specimen is much lower in the attractive (LoA)

regime as in the repulsive regime. However, resolution in phase and also in topography may be less prominent as one may map the always present water layer on the sample. Decision whether to stay in attractive or repulsive mode is a question of specimen sensitivity. Nevertheless, in order to reach highest possible contrast in phase mode one usually operates in the repulsive regime, if possible. In any case there is one regime which should be avoided, denoted as bi-stable regime, characterized by jumps between the HiA and LoA-solution. These jumps are reflected in the phase which simply originate from the relation in Figure I-10 where the phase difference between the attractive (ϕ_-) and repulsive (ϕ_+) regime is reflected by a difference of about 150 degrees (see Figure I-11 b and section I.4.2.3). Bi-stability is given, because on edges, force fields acting on the tip shortly differ (see Figure I-6) leading to instability and cyclic movement in the observed hysteresis between the HiA and LoA solution. This not only causes insufficient phase data but also may affect topographic imaging and should therefore be avoided.

In summary, the point mass model shows good correlation with the observed behavior in a real AM-AFM and can prove important properties of the non-linear dynamics. However, in order to get a deeper understanding of cantilever dynamics and vibrational modes one is forced to solve equation (1.10) which will not be part of this thesis. A good description of the method is given in the book of Garcia [8].
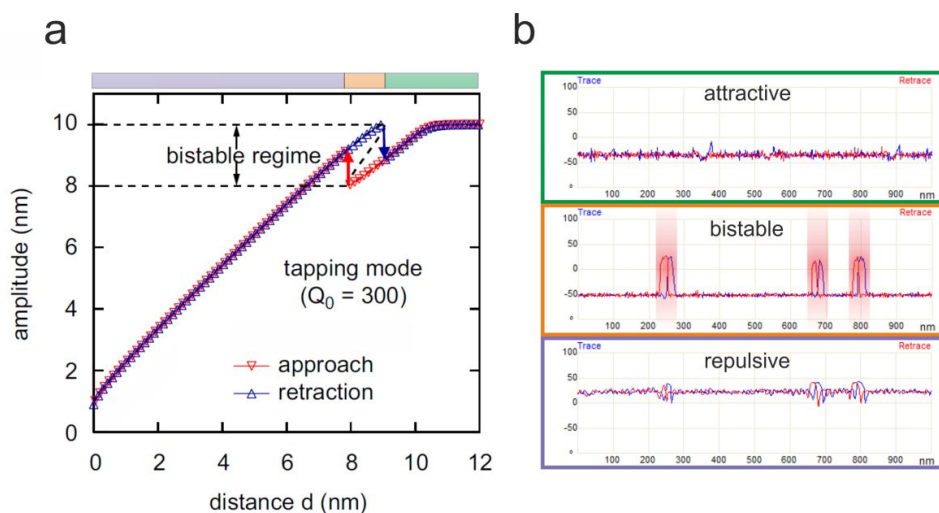
Figure I-11: (a) Numerical simulation of the oscillation amplitude in dependence of the mean tip-sample distance; Adapted from[32] with kind permission from Elsevier. Colors at the top of the figure illustrate the corresponding regimes shown in (b) by real phase data, observed on a Fastscan Bio AFM (Bruker AXS, Santa Barbara, California/USA).

I.4.2.3 Phase Imaging

Conventional AM-AFM usually provide 3 channels to the user which show topographic, amplitude and phase information. While topographic information may be understood quite easily by the description given above and amplitude information or in better terms amplitude error information is simply the difference of the set-point-amplitude to the real amplitude, phase imaging, in particular the theory behind it, places higher demands. Therefore, only a quick summary will be given here and a more detailed description can be found in the book of Garcia and literature[8,34].

It can be shown[8] that the sinusoidal motion of the tip cantilever system can be expressed as

$$z = z_0 + A cos(\omega t - \varphi) \tag{1.16}$$

Now as a matter of fact, a steady motion of the tip-cantilever system requires that energy dissipated to the sample (E_{dis}) and by hydrodynamic damping in the medium (E_{med}) must be compensated by the exiting force. Thus, we may write

$$E_{exc} = E_{med} + E_{dis} \tag{1.17}$$

The above quantities are defined as follows:

$$E_{exc} = \oint F_{exc} \dot{z} \, dt = \oint F_0 \cos(\omega t) \frac{dz}{dt} dt = \frac{\pi k A_0 A(\omega) \sin(\varphi)}{Q} \tag{1.18}$$

$$E_{med} = \oint \frac{m\omega_0}{Q} \frac{dz}{dt} dt = \frac{\pi k A^2}{Q} \frac{\omega}{\omega_0} \tag{1.19}$$

$$E_{dis} = \oint F_{ts} \frac{dz}{dt} dt = \langle F_{ts}\dot{z} \rangle = P_{ts} \tag{1.20}$$

Substitution of equation (1.18)-(1.20) into equation (1.17) yields:

$$\sin(\varphi) = \frac{A\omega}{A_0\omega_0} + \frac{2QP_{ts}}{k_c A A_0 \omega} = \frac{A\omega}{A_0\omega_0}\left(1 + \frac{E_{dis}}{E_{med}}\right) \tag{1.21}$$

Numerical simulations and experiments[35,36] have shown the validity of equation (1.21). This result allows to draw important conclusions: The first term in equation (1.21) is associated with the **elastic deformation between tip and sample** and the second term includes **dissipation of energy** by the nanoscale forces and the hydrodynamic damping in the medium[37]. Furthermore, by consideration that AM-AFM by definition shows constant Amplitude *A,* we can state that the phase information is only dependent on the viscoelastic properties of the material. For **elastic properties, P_{ts}** (see equation (1.20)) **equals zero** and therefore no phase change would be observable.

As an example of phase contrast Figure I-12 shows a hexagonal Boron Nitride (BN) flake, visualized by AM-AFM. Despite topography and amplitude error information, phase contrast is striking and offers

valuable information. In proximity of a central dome, originating from preparation, darker stripes are seen in the flake (red arrows) and residuals on the side of the flake (blue arrow) which most likely originate from preparation. While residuals are definitely a different material, the stripes are open for speculation: It may be that stress introduced through the dome formation is causing local changes in the viscoelastic properties which yields differences in the phase signal. In summary, phase imaging gives additional information on substrate composition which may be extremely helpful in image interpretation. Images were taken in repulsive mode.

Now, with this brief introduction of AM-AFM the basic principles behind this method are clear. Furthermore, through additional information obtained by phase imaging, valuable information is gathered on the specimen nature. In fact, most advanced techniques such as FMF, EFM and Kelvin-Force microscopy do use phase information, however, originating from a different interaction force. To understand liquid AFM operation one must develop a different and even deeper understanding of forces and mechanics which will be described shortly in the next section.
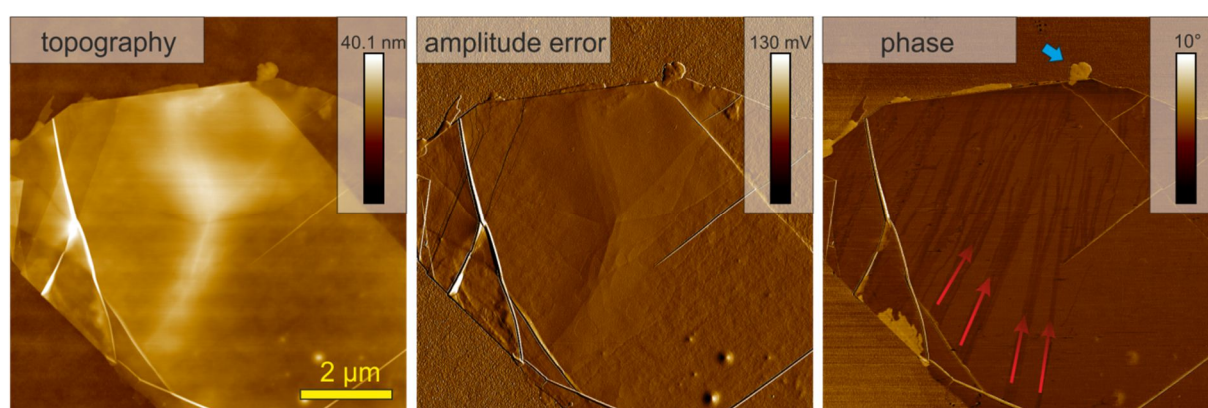
Figure I-12: Ultrathin hexagonal Boron Nitride (BN) flakes (approx. 3 nm thickness) visualized in AM-AFM. The topography shows a flat flake with a dome in the center, probably originating from preparation. Debris on the side walls of the flake shows a different phase signal and corresponds to a different material most likely originating from preparation (blue arrow). Darker strips in proximity of the dome may result from internal stress which causes variation of the viscoelastic properties (red arrows). Although additional investigations would be required to test this hypothesis the images show the importance of phase information in AFM imaging.

I.5 Amplitude Modulated AFM in Liquid

AM-AFM in liquids offers one of the most stunning and striking advantages of AFM over conventionally available high-resolution microscopy methods such as Transmission Electron Microscopy (**TEM**) or Scanning Electron Microscopy (**SEM**) which all rely on vacuum conditions and partly harsh probing conditions (high energy electrons and / or electric currents). The possibility to operate in liquid, even with atomic resolution is unattainable by these methods, leaving liquid AM-AFM the only candidate to study dynamic molecular processes *in-situ* and at this scale. The special character of cantilever dynamics in liquid with parasitic resonances from the liquid itself, additional high damping and liquid based forces increases the complexity of the matter. Therefore, the theoretical description of liquid AM-AFM is still in progress[8]. Here, a quick overview over the theoretical background, but also the resulting behavior will be given. A detailed description may be found in literature [38–43].

I.5.1 Tip Surface Interaction – Forces in Liquids

Forces in liquid environment differ significantly from forces observed in gaseous or vacuum conditions due to missing capillary force and additional electrostatic interactions between liquid and bulk materials as tip and specimen. The two most relevant forces are shown in Figure I-13 and are: *1)* The **double layer force** originating from surface charging in liquid and its interaction with counter-ions present in the liquid; and *2)* the **solvation force** which is based on the gap between liquid and surface where the liquid bulk ordering is altered due to molecular interactions of liquid and surface molecules[25,26].
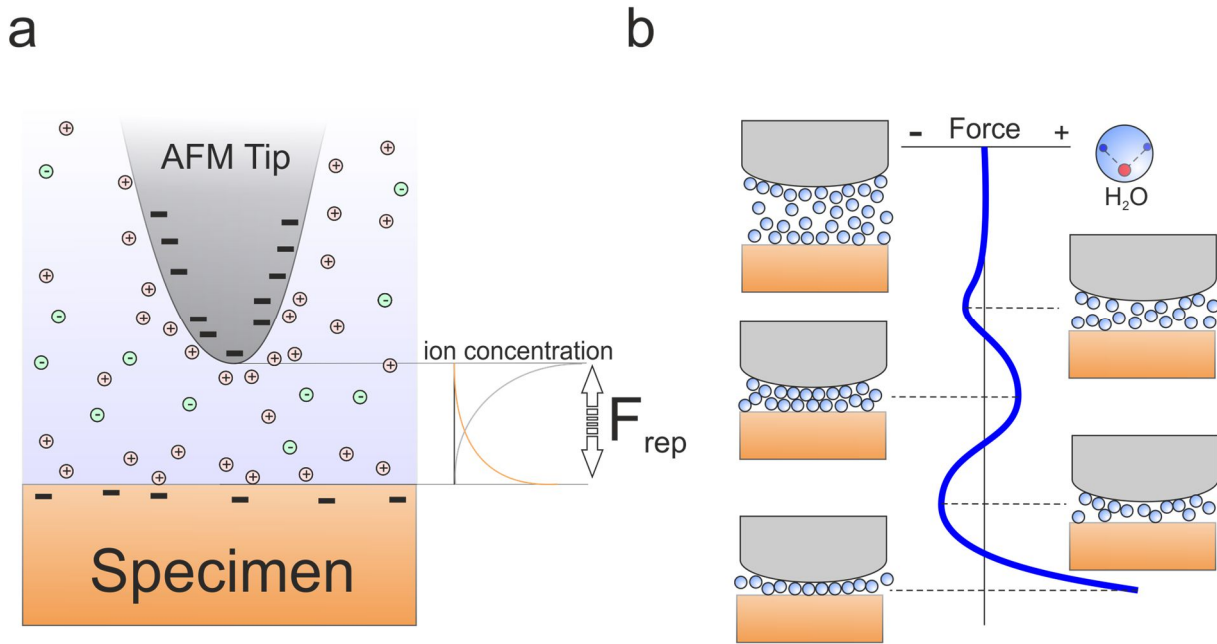
Figure I-13: (a) The double layer force between tip and specimen originates from a charging of the surfaces and the interaction with counter-ions from the liquid. (b) The solvation force originates from the fact that the liquid structure is usually different to the bulk structure at a surface boundary. Squeezing these boundary layers upon approach of two surfaces leads to an oscillatory force with a period in the range of the molecule size.

Apart from double layer and solvation force, hydration forces or monotonic hydration forces may also be present. However, all these forces are usually dominated by the double layer and solvation force [8].

I.5.1.1 The Double Layer Force – DLVO Theory

In the early years of the 20th century the theory behind electrostatic forces between materials and solutions evolved[44]. The investigations were driven by observations and experiments showing that colloidal solutions show high stability depending on the solvent and pH value. These are the forces that prevent the conglomeration of particles which otherwise would aggregate quickly under the influence of attractive Van der Waals interaction. It is important to know that in solutions, surfaces may be charged by 3 effects: *1)* **dissociation of surface groups** (e.g -COOH $\rightarrow$ COO$^-$ + H$^+$); *2)* **adsorption of ionic species** from the liquid; and *3)* c**harge transfer between very close surfaces** leading to attractive forces between the oppositely charged surfaces[25]. In the DLVO theory by

Derjaguin-**L**andau-**V**erwey-**O**verbeek[45,46] the electrostatic interaction between particles separated by a distance *d* and the corresponding Van der Waals force are combined[25]. Although the theory is based on several assumptions including a continuous charge distribution without discrete entities (ions), no consideration of non-coulomb interactions, a neglected finite size of the ions and a continuous solvent with constant permittivity[26], it describes experimental data in an exceptional good way. The reason is that uncertainties associated with these assumptions cancel each other out. For instance, neglecting non-coulomb interactions (e.g., Van der Waals), decreases the ion concentration at the surface which increases the potential. In turn, neglecting the finite ion size increases the ion concentration and thus decrease the potential[26]. So both contributions, if neglected, also cancel the resulting disadvantages. Note, similar effects are present for the charge distribution and the continuous solvent with constant permittivity.

In summary, the DLVO theory has proven to be feasible to describe liquid AFM operation to reasonable detail. However, mastering the theoretical background is rather complicated and requires extensive knowledge in thermodynamics and electrodynamics. In principle, the solution to the problem is given by the combination of the Boltzmann distribution (Nernst equation; equation (1.22)) with the Poisson equation (equation (1.23)) which gives the Possion-Boltzmann (PB-) equation (1.24).

$$\rho = \rho_0 e^{\left(-\frac{ze\psi}{kT}\right)} \tag{1.22}$$

$$ze\rho = -\varepsilon_0 \varepsilon \left(\frac{d^2\psi}{dx^2}\right) \tag{1.23}$$

$$\frac{d^2\psi}{dx^2} = -\frac{ze\rho}{\varepsilon_0\varepsilon} = -\frac{ze\rho_0}{\varepsilon_0\varepsilon} e^{-\frac{ze\psi}{kT}} \tag{1.24}$$

Here *z* is the valence of the ion, *e* the elementary charge, *ρ* the charge density, *ε* the dielectric constants and *Ψ* the potential. The PB-equation is a nonlinear second order differential equation and solutions require suitable and physical boundary conditions. It is quite clear that mastering this equation requires considerable mathematical skills and will therefore not be done in this thesis. However, the book of Israelachvili gives and excellent introduction into this matter[25]. Briefly, applying suitable boundary conditions like a **vanishing field at the midplane** in equilibrium ($d\Psi/dx_{midplane}$ = 0) (which must be the case as the system is otherwise not in equilibrium) and the assumption that the number of ions and counter-ions must show **electroneutrality**, important equations ((1.25)-(1.28)) may be derived. It is quite strait forward by differentiating equation (1.22) to *x* and following integration that charge densities must fulfill:

$$\rho_x = \rho_0 + \frac{\varepsilon\varepsilon_0}{2kT}\left(\frac{d\psi}{dx}\right)_x^2 = \rho_0 + \frac{\varepsilon\varepsilon_0}{2kT}\sigma_x^2 \tag{1.25}$$

$(d\Psi/dx)_x$ is the electric field at position x. Solving to σ_x and using equation (1.22) for ρ_0 and ρ_x, one can calculate *(dΨ/dx) with the help of relation sinh(x) = e^x-e^-x/2* yielding equation (1.26). Note the corresponding formula is only valid for a 1:1 electrolyte. For different electrolytes, similar equations can be deduced, however, with additional terms at the end. The formalism is known as the Grahame equation[25].

$$\frac{d\psi}{dx} = \sigma = \sqrt{\frac{8kT\rho_{\infty,i}}{\varepsilon\varepsilon_0}}\sinh(\frac{e\psi_x}{2kT}) \qquad (1.26)$$

Integration leads to[25]:

$$\psi_x = \frac{2kT}{e}log\left[\frac{1 + \tanh\left(\frac{e\psi_0}{4kT}\right)e^{-\kappa x}}{1 - \tanh\left(\frac{e\psi_0}{4kT}\right)e^{-\kappa x}}\right] \approx \frac{4kT}{e}\tanh\left(\frac{e\psi_0}{4kT}\right)e^{-\kappa x} \qquad (1.27)$$

In equation (1.27) κ is the Debey length with:

$$\kappa = \sqrt{\frac{\rho_{\infty,i}e^2z_i^2}{\varepsilon\varepsilon_0 kT}} \qquad (1.28)$$

<u>This is a remarkable result:</u> it shows that **the potential**, and with it the force, **decays exponentially** with a **characteristic length** and that the latter is **only dependent on the type of solvent and its ionic interaction** ($\rho_{\infty,i}$...Bulk concentration of the solvent, **ε**...Dielectric constant, z_i...charge of the ion species). This is valid for all geometries[25] with separations beyond more than one Debye length. For smaller separations, numerical results to solve (1.24) must be found and show a different behavior[25]. However, this is not of concern for the DLVO theory as the Van der Waals force leads to attractive interaction anyway when small separations are chosen. This follows quite simply from the fact that the Van der Waals force decays on a power law against the electrostatic double layer force. Now, expanded by the corresponding Van der Waals interaction one may derive the following equation for a flat specimen and a spherical tip[8]:

$$F_{DLVO} = \frac{4\pi R}{\varepsilon\varepsilon_0\kappa}\sigma_t\sigma_s e^{-\kappa d} - \frac{A_H R}{6d^2} \qquad (1.29)$$

Here, σ_t and σ_s are the respective surface charge densities of tip and specimen, R the radius, ε the dielectric constant, d the separation and A_H the Hamaker constant (see I.4.1.1). In summary, the DLVO theory shows **that changing the pH** of the solvent will **alter κ** and thus the characteristic length which as a result will lead to different force fields and further a screening of electrostatic interaction. Thus the pH value is essential for image resolution in liquid AFM. **Calculating κ for deionized water**

shows an extremely large Debye length of approximately 1µm and is therefore not recommended for high-resolution imaging in liquid tapping mode AM-AFM. For NaCl at 1 mM in water κ drops to 0.96 nm which shows the significant impact of the solvent and pH.

I.5.1.2 Solvation Force

As shown in Figure I-13 b solvation forces arise from density fluctuations in between approaching surfaces in close proximity to each other. The force can only be understood by the fact that liquids are composed of discrete entities (molecules). During the approach of the tip to the specimen, the liquid and therefore the molecules are squeezed in between the gap. As the gap diminishes, more and more molecules are squeezed out which leads to density fluctuations as depicted in Figure I-13. Usually this force is only relevant in a distance of a few molecule diameters apart from the surfaces. For example force curves measured by Yamada and coworkers[47] in water showed an oscillation period of 0.2 nm which correlates with the bonding length of H_2O proving that the period is roughly defined by the molecule size which is expectable by considering Figure I-13. The forces arising from solvation may be described well by an oscillating exponentially decaying formalism as in equation (1.30)[26].

$$f_{sv} = f_0 \cos\left(\frac{2\pi d}{a_m}\right) e^{-\frac{x}{\lambda_{sv}}}$$

(1.30)

Here a_m is the molecular diameter and λ_{sv} the decay length of the oscillation. For a sphere with radius R (tip) and a planar surface and separations being small compared to the tips radius we may use Derjaguins approximation (1.31)[25,26,48].

$$F_{sv} = F_0 \cos\left(\frac{2\pi d}{a_m} + \varphi\right) e^{-\frac{d}{\lambda_{sv}}}$$

(1.31)

$$F_0 = \frac{R f_0}{\sqrt{(2\pi\lambda_{sv})^{-2} + a_m^{-2}}}$$

(1.32)

$$\tan\varphi = \frac{\lambda_{sv}}{a_m}$$

(1.33)

Thus the total force may be simply calculated knowing the molecular/atomic diameter and the decay length. In summary, both double layer force and solvation force prove to be significantly different from forces in air or vacuum. The fact that ionic strength, concentration and pH have important consequences for the imaging should be kept in mind. For more information see Israelachvili[25]. With this short and concise introduction to forces in liquid we may now proceed to the theory of the AM-AFM in liquid.

I.5.2 Theory of AM-AFM in Liquid

I.5.2.1 Liquid vs. Gaseous Environment

The operation in liquid is, if compared to air or vacuum conditions, a challenging task as it implies significant differences by forces and cantilever dynamics. This immediately becomes obvious by comparing frequency curves between both media as shown in Figure I-15 calculated from (1.13) by altering Q. The shown curves demonstrate the change in resonance behavior for different media which results from the following: *1)* In liquid the hydrodynamic damping increases dramatically (low Q) which obstructs cantilever movement; *2)* At the cantilever, a liquid boundary layer is formed which usually differs to the bulk liquid. This boundary layer has to be moved at any cycle, thereby decreasing the spring constant of the cantilever. For magnetic actuation where a coated cantilever is excited by a coil below the specimen, the curves presented in Figure I-15 are valid. However, for piezo actuated resonance curves the signals differ significantly due to the following: Piezo active excitation induces parasitic resonances[49] in the liquid which are induced by the cantilever holder (see Figure I-14). This leads to resonances in the liquid, the cell and the scan head. This yields resonance curves which usually show a significant number of peaks and choosing the correct resonance can be quite challenging. However, so called thermal tuning, where the excitation of the cantilever due to Brownian motion is measured, can be used to find the resonance. In Figure I-14, a real tune curve and the thermal tune are shown. The applied cantilever was a FastScan D cantilever (Bruker AXS, Santa Barbara, California/USA) with a nominal spring constant of 0.3 N/m. The curve was recorded in liquid. Thermal tune is done by switching off the piezo, detecting the Brownian motion induced resonance and plotting it below the former recorded parasitic resonance plot[40]. Thermal tuning is usually available on commercial microscopes nowadays.

Considerations so far, have been done far from the specimen surface, and cantilever response changes again significantly upon approach. In close proximity to the surface, the quality factor is decreased even further and the frequency shifts further to lower values [50]. A simple explanation is that the movement of the cantilever (e.g., sinusoidal) has to remove the liquid between tip and specimen which gets more difficult at closer distances due to fluid shear. Another significant change is observed when the movement of the cantilever is considered. Here, the oscillation gradually changes towards non-sinusoidal wave forms[49,51] during the approach procedure. This has the implication that a mathematical treatment, in contrast to air or vacuum operation where a sinusoidal movement was assumed, must be different. The reason for the non-sinusoidal wave form is that low Q factors facilitate contribution of higher eigenfrequencies, especially at the bottom of the oscillation period. To account for these differences, a different theory, as for the case in air or vacuum, has to be developed. It is noteworthy that this procedure is still in research and still not completed. The reason is simply that the liquid states additional problems which have to be accounted for. However, there are again simplifications which can be used to get a qualitative understanding of cantilever dynamics in liquids.
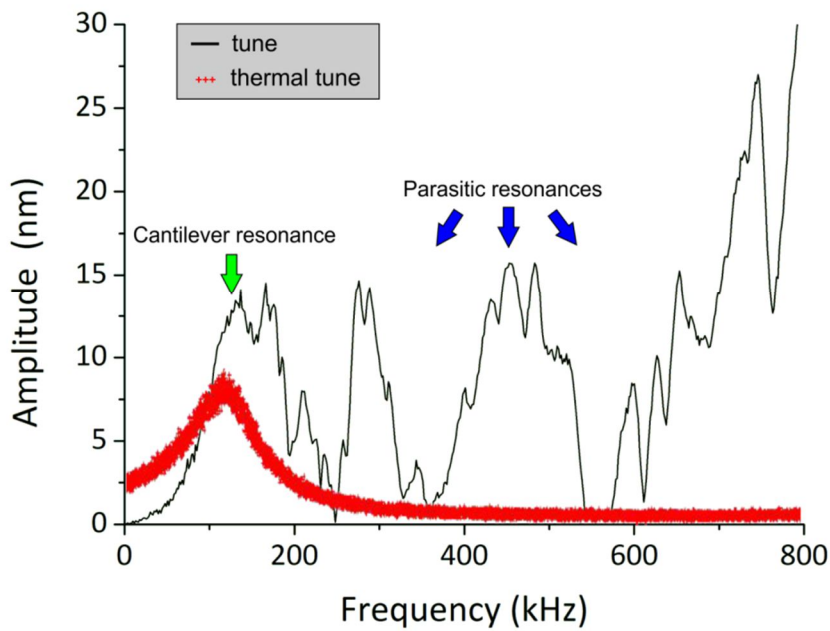
Figure I-14: Cantilever tune curve of a FastScan D cantilever with nominal spring constants of 0.3 N/m (black). Multiple peaks appear due to parasitic resonances originating from resonances in the liquid, the cell and the scan head. The thermal tune is shown in red and demonstrates that the cantilever actually has one resonance. The thermal tune is recorded from the Brownian motion of the cantilever. Without the help of thermal tuning, finding the correct resonance can be quite challenging. Presented curves were recorded on a Fastscan Bio-AFM (Bruker AXS, Santa Barbara, California/USA) equipped with FastScan C (Bruker AXS, Santa Barbara, California/USA) cantilevers in 50 mM sodium citrate buffer (pH 5.0) at 22°C.
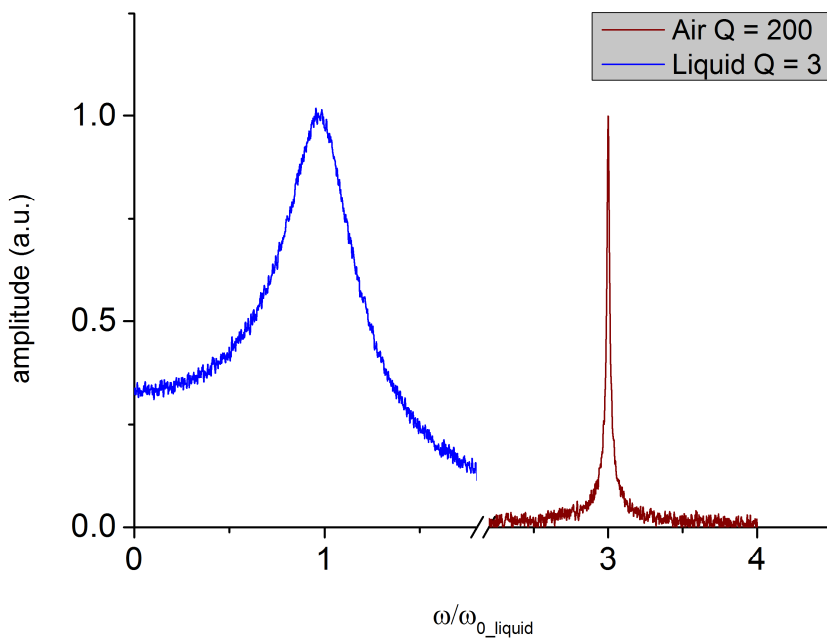
Figure I-15: A schematic representation of observed resonance curves (Matlab simulation) calculated from (1.13) with a Q of 200 (red resonance curve; air) and Q of 3 (blue curve, liquid). Please note, the curve in blue still holds for ambient conditions. Liquid conditions require a different treatment of the mathematics and show a different behavior.

I.5.2.2 The Point Mass Model in Liquid

In analogy to section I.4.2.1 the point mass model may be described by a spring with spring constant k, a pointed mass m and must fulfil equation (1.11). The theory is valid and a good description of the dynamics far from the surface[8] and provides some semi-analytical and numerical results. However, equation (1.11) is only valid in this form when magnetic excitation is used. For acoustic excitation, the low Q factors and high damping demand considerably higher driving voltages of the exciting piezo and thus facilitate also a stronger movement of the cantilever base. This may be well neglected in the case of operation in air, however, has to be considered in liquid. This implies, that the measurable movement (photodiode) of the cantilever (z(t)) differs from the cantilever movement (S(t)) (see Figure I-16).
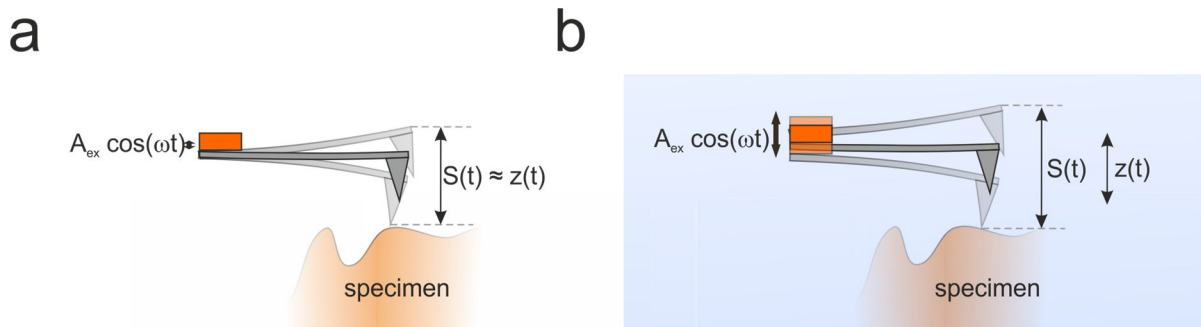
Figure I-16: Acoustic excitation in air (a) and liquid (b). Higher driving amplitudes (A_{ex}) lead to a significant cantilever movement which differs from the measurable movement (z(t)).

From Figure I-16 we may deduce an equation of motion which is slightly different[8]:

$$\ddot{S}(t) + \frac{b}{m_{eff}}\dot{S}(t) + \omega_0 z(t) = 0 \qquad (1.34)$$

The measurable movement of the cantilever $z(t)$ is related to $S(t)$ by[8]:

$$S(t) = z(t) + A_{ex}\cos(\omega t) = z_0 + A_z \cos(\omega t + \varphi) + A_{ex}\cos(\omega t) \qquad (1.35)$$

The solution to equation (1.34) is then given by:

$$A_z(\omega) = \frac{\frac{F_0}{k}\sqrt{\omega^4 + \left(\frac{\omega\omega_0}{Q}\right)^2}}{\sqrt{(\omega_0^2 - \omega^2)^2 + \left(\frac{\omega\omega_0}{Q}\right)^2}} \qquad (1.36)$$

The result obtained by equations (1.34)-(1.36) is different to equation (1.13) derived for the harmonic oscillator in air. For $\omega \to 0$, A_z goes to zero and at $\omega \to \infty$ approaches F_0/k which is the exact opposite from the case in air. So, the implication of the piezo movement has significant impact on the amplitude at low and high frequencies, and this has therefore to be considered in semi-analytical and numerical simulations.

I.5.2.3 Semi-Analytical and Numerical Calculations

The point mass model for measurements in liquids is representative for the dynamics far from the surface. In a first approximation, one may use the same method as in section I.4.2.1 by assuming a linearization of the total tip specimen force F_{ts} corresponding to the ansatz in equation (1.15). However, we have to include an additional term accounting for the higher interaction damping in proximity of the surface due to the description given above.

$$F_{ts}(z, \dot{z}) = F_{ts}(z_c) - k_{int}(z_c)z - \gamma_{int}(z_c)z \qquad (1.37)$$

Using equation (1.37) and (1.34) the following values for amplitude A may be derived [8]:

$$A_{z(\omega)} = \frac{A_{ex}\sqrt{\left(m_{eff}\omega^2 - k_{int}\right)^2 + \omega^2\left(\left(\frac{m_{eff}}{Q}\right) + \gamma_{int}\right)^2}}{\sqrt{\left(k + k_{int} - m_{eff}\omega^2\right)^2 + \omega^2\left(\left(\frac{m_{eff}}{Q}\right) + \gamma_{int}\right)^2}} \qquad (1.38)$$

Although, the assumptions and the complex nature of cantilever dynamics in liquid are not well described by this model, some effects, especially the response of the cantilever in force distance curves may be used in well agreement to describe the phase and amplitude response to solvation forces as shown by Mugele and coworkers[40]. Here the oscillatory force response changing from attractive (Figure I-13; b; F<0) to repulsive interaction (Figure I-13; b; F>0) may be represented by k_{int} yielding phase responses which correlate well to the observed experimental curves[40]. Nevertheless, description of dynamic behavior, as contribution of higher harmonics, reduction of Q and ω_0 in close proximity of the surface and the phase response require a more sophisticated theory which includes the implementation of a Navier-Stokes equation for the fluid surrounding the cantilever and the Euler Bernoulli equation (1.10). Mastering the theory behind it is a considerable hard task and still under progress. So far the most advanced theories are based on finite element simulations[42] and will not be further described in this thesis but are described in detail by Garcia[8].

I.6 Liquid AM-AFM in Microbiology

Understanding the theory behind liquid AFM is one way to understand cantilever dynamics during experiments. However, successful operation in liquid includes a considerable higher amount of knowledge concerning specimen preparation, specimen sensitivity and behavior under specific temperatures and liquid environments which simply results from the fact that most applications aim on biological and living specimens. In the following a short introduction in the preparation of different specimens will be given. A good and comprehensive description of applications in biology is given in the book of Morris[52].

I.6.1 Specimen Preparation – Fundamental Aspects

Substrate preparation is a fundamental part for successful liquid AFM as the liquid environment usually gives rise to detachment of molecules, macromolecules or cells. Therefore, basic knowledge about substrates and its properties is absolutely essential to immobilize the specimens. There are multiple methods for immobilization, each with its advantages and disadvantages and in the following sections a basic consideration of these methods will be provided. However, according to the topic of the thesis, the focus lies on cellulose and cellulose degrading enzymes.

I.6.1.1 Substrates

In liquid AFM science, the most common substrates are mica, glass or graphite/graphene which are discussed briefly. All of them feature extremely flat surfaces, as a basic requirement for high-resolution AFM, and allow easy cleaning or delamination to form atomically flat surfaces. If properly delaminated, mica and graphite do not need further surface cleaning steps. Glass however, should be carefully cleaned by appropriate organic solvents such as isopropanol or acid solutions to remove any biological contamination[52].

Mica is a group of mineral silicates with a sheet like crystal structure which may be cleaved several times to form atomically flat (over several microns) and clean substrates. The specific properties include a strongly hydrophilic surface which allows the efficient covering with particles from an aqueous solution. However, in liquid, care has to be taken that the surface is negatively charged at neutral pH[52] which should be remembered in any application. For example, in the course of this thesis, nanocrystalline cellulose whiskers were prepared from microcrystalline cellulose by acid hydrolysis resulting in negatively charged nanoparticles [53]. To observe reactions on these particles in liquids, immobilization on mica would not have been possible due to repulsion between particles and substrate. In strong contrast, DNA immobilization is observed on mica which is counterintuitive as DNA is also strongly negatively charged. However, the reason is the used buffer which facilitates, if containing Ca^{2+} or Mg^{2+}, an ion exchange process thereby screening the negative charge of the surface and leading to a strong binding of the DNA. In summary, accurate knowledge about substrate, buffer and specimen is essential for successful experiments.

Glass is quite analogous to mica (although not as flat), negatively charged and averagely hydrophilic providing high suitability for cells and bacteria. Moreover, it is a cheap and readily available substrate which can be found in most laboratories. As a disadvantage one may see that glass cover slides

usually are not very clean and preparation should always include careful cleaning. As a good rule of thumb, one may use the following procedure: To remove all organic contamination usually different acids may be used which include sulfuric acid and hydrogen peroxide (piranha solution). As alternative ozone etching in oxygen plasma is common and easy to use. As last step wiping with acetone and CO_2 spray drying followed by ultrasonic assisted isopropanol cleaning again finished by CO_2 spray drying is recommended to provide chemically clean surfaces. .

Graphene and Graphite are frequently used and important substrate materials. Most of the time highly oriented pyrolytic graphite (HOPG) is used and may be purchased in different purities. The properties of the substrate differ from glass and mica by a strongly hydrophobic surface which is inhibiting uniform dispersion of particles from aqueous solution. However, it has its advantages considering a special set of binding forces which is the hydrophobic-hydrophobic interaction [25]. This interaction is an attractive force formed between two hydrophobic surfaces in aqueous solutions. The driving force is that excess of water is energetically favorable. In this thesis, this has an important experimental implementation as we immobilized nanocrystalline celluloses that way. Here, the hydrophobic sides of the cellulose bind to the hydrophobic graphene.

If the specified properties for the above given substrates do not fit to the experimental problem there is a variety of coatings to change the surface charge, the topology and hydrophobic /hydrophilic interactions. A given example may be the immobilization of bacteria by gelatin or poly-L-lysine coated mica slides[54]. The application of coatings allows to facilitate physisorption, chemisorption, covalent binding or biological binding (antibodies). The huge variety of biological species generates the same variety in coatings which doesn't allow a comprehensive full description in this thesis. A good overview of the complexity can be found in a review by Pelton[55] on paper based bioactive sensors. Here cellulose is modified to act as an immobilization substrate for various biological active proteins which is basically the same to the AFM required immobilization.

I.6.2 Imaging of Macromolecules

The most stunning and persuasive argument for AFM in liquid is the possibility to visualize and study biological reaction *in-situ* and real time. No other technique is known today which satisfies the same resolution and imaging speed in liquids. The development of high speed AFM for the real time investigation of, e.g., biocatalytic degradation of cellulose[16,17] or the movement of myosin V[56], an important transport protein on actin filaments, proved the impressive possibilities which are now available. However, imaging of enzymes as very soft and "living" objects states a challenge as the load, speed and amplitude of the oscillation strongly impact the behavior. Thus this section should give some basic ideas how proper imaging of enzymes or proteins may be achieved.

I.6.2.1 Cantilever-Forces

As the transducer of atomic forces during the oscillating movement in AM-AFM, cantilever stiffness has a significant impact on image as well specimen stability and speed. As a rule of thumb, cantilevers for liquid operation should be soft (k=0.01-1 N/m) and triangular shaped which may prevent torsional movement of the cantilever at scan angles of 90°. However, current developments focus on high speed probes which usually are short and small to drive the resonance frequency to

higher values without increasing the spring constant. Therefore, the triangular shape is no longer common for fast scan probes (tip velocities up to 3000 µm/s) and should only be considered for conventional "slow" scan probes (tip velocities up to 50µm/s). The stiffness has significant impact on specimens as high force loads may distort specimens and lead to force related artifacts. A nice example is given by the work of Garcia and San Paulo[14] where antibodies where imaged under different force loads in air (Figure I-17) with cantilevers featuring spring constants of about 25-50 N/m. Although, not comparable to liquid operation where amplitude and phase response differs significantly, it proofs the high sensitivity of such structures.
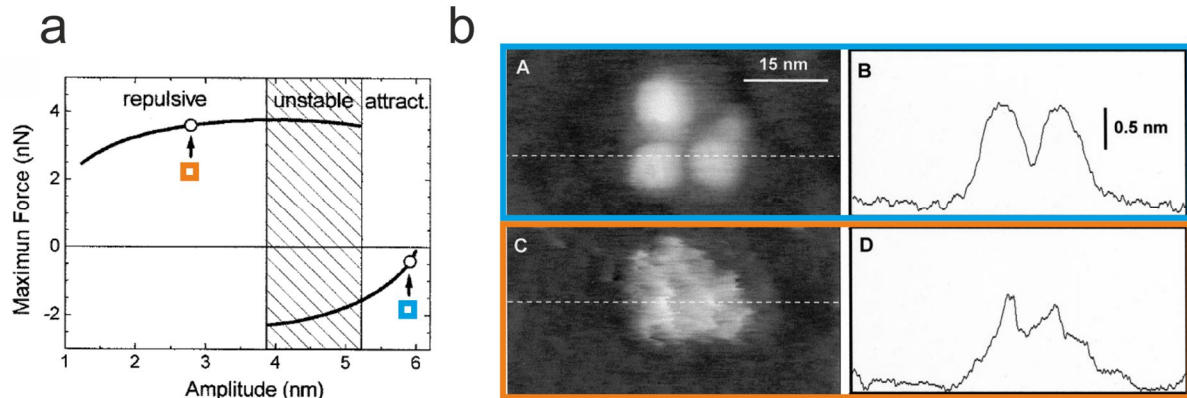
Figure I-17: Maximum force curves (a) calculated from model in literature [14] showing that the attractive and repulsive regime apply different forces. (b) AFM image of α-HSC molecules (Y-shaped antibody) proofing the high sensitivity to forces. Forces loads as low as 4 nN lead to complete disruption of the antibody yielding disrupted and artefact rich images. Adapted and reprinted with kind permission from Elsevier [14].

In liquids the situation is even more aggravated as forces due to the low Q factor and thus low sensitivity of the cantilever tend to be higher. Simulations have shown that even with low spring constants in the range of a few 100 mN/m forces of about up to 80 nN are reached (Figure I-18) which is about the factor of 20 more than in the case of air. Under this load, proteins like antibodies are expected to be distorted. In order to reduce the average force load exerted on the sample, Q-control may be used to decrease it as shown in literature [32].
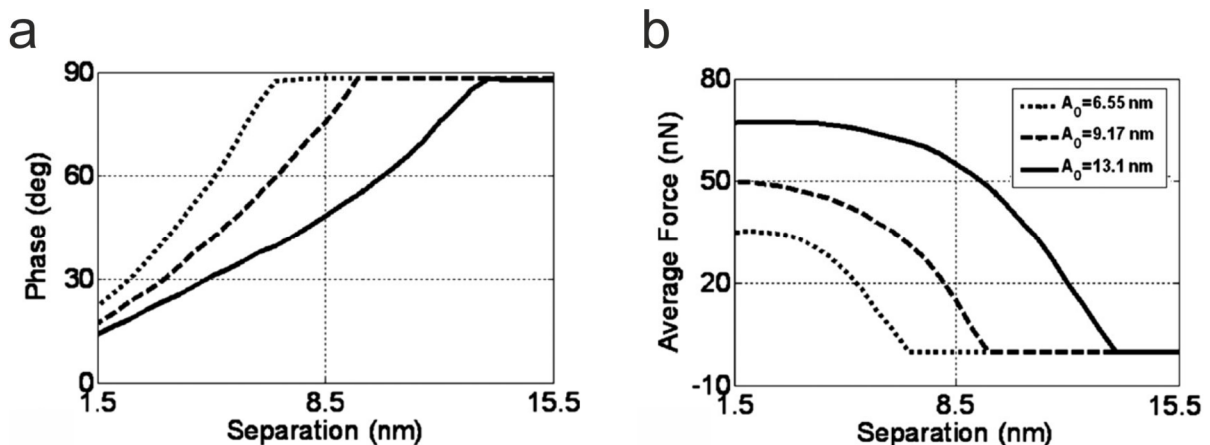
Figure I-18: Phase responce (a) and average force plots (b) of a soft cantilever in liquid calculated by the model given by Korayem and coworkers [57] for amplitudes in the range of 6.55-13.1 nm. Reprinted and adapted with permission from AIP Publishing LLC. [57]

In summary there are two precautions which should be fulfilled for imaging in liquid:

1. The cantilever **spring constant should be as low as possible** in order to not damage the specimen but still high enough to allow excitation by the piezo actuators.
2. The **amplitude should be as low as possible** in order to decrease the average force onto the specimen (see Figure I-18). If this is not sufficient, Q-control may be used to further decrease force loads[32].

I.7 Chapter Summary

In conclusion, this *chapter* has given some of the basic ideas and concepts behind AFM operation in air and liquids. It is clear that this section cannot provide a full description which simply results from the complexity behind cantilever dynamics and forces. However, the *chapter* summarized some valuable information how to use AFM and how to prepare the specimens. Furthermore, by understanding quite simple theoretical concepts one may understand how, e.g., changing the pH of a solution may alter the resolution. For deeper understanding please refer to the presented books and references.

I.8 References

[1]   G. Binnig, C. Quate, C. Gerber, *Phys. Rev. Lett.* **1986**, *56*, 930.

[2]   G. Binnig, H. Rohrer, C. Gerber, E. Weibel, *Phys. Rev. Lett.* **1982**, *49*, 57.

[3]   Y. Martin, C. C. Williams, H. K. Wickramasinghe, *J. Appl. Phys.* **1987**, *61*, 4723.

[4]   T. R. Albrecht, P. Grütter, D. Horne, D. Rugar, *J. Appl. Phys.* **1991**, *69*, 668.

[5]   J. E. Stern, B. D. Terris, H. J. Mamin, D. Rugar, *Appl. Phys. Lett.* **1988**, *53*, 2717.

[6]   I. Tanaka, I. Kamiya, H. Sakaki, N. Qureshi, S. J. Allen, P. M. Petroff, *Appl. Phys. Lett.* **1999**, *74*, 844.

[7]   C. Schönenberger, S. F. Alvarado, S. E. Lambert, I. L. Sanders, *J. Appl. Phys.* **1990**, *67*, 7278.

[8]   R. Garcia, *Amplitude Modulation Atomic Force Microscopy*, Whiley, 69469 Weinheim, **2010**.

[9]   W. Baumgartner, P. Hinterdorfer, H. Schindler, *Ultramicroscopy* **2000**, *82*, 85.

[10]   B. Drake, C. Prater, A. Weisenhorn, S. Gould, T. Albrecht, C. Quate, D. Cannell, H. Hansma, P. Hansma, *Science (80-.).* **1989**, *243*, 1586.

[11]   P. K. Hansma, J. P. Cleveland, M. Radmacher, D. a. Walters, P. E. Hillner, M. Bezanilla, M. Fritz, D. Vie, H. G. Hansma, C. B. Prater, J. Massie, L. Fukunaga, J. Gurley, V. Elings, *Appl. Phys. Lett.* **1994**, *64*, 1738.

[12]   E. Henderson, *Prog. Surf. Sci.* **1994**, *46*, 39.

[13]   M. Hegner, P. Wagner, G. Semenza, *FEBS Lett.* **1993**, *336*, 452.

[14]   A. San Paulo, R. García, *Biophys. J.* **2000**, *78*, 1599.

[15]   T. Uchihashi, R. Iino, T. Ando, H. Noji, *Science* **2011**, *333*, 755.

[16]   K. Igarashi, T. Uchihashi, A. Koivula, M. Wada, S. Kimura, T. Okamoto, M. Penttilä, T. Ando, M. Samejima, *Science* **2011**, *333*, 1279.

[17]   K. Igarashi, A. Koivula, M. Wada, S. Kimura, M. Penttilä, M. Samejima, *J. Biol. Chem.* **2009**, *284*, 36186.

[18]   F. Moreno-Herrero, J. Colchero, J. Gómez-Herrero, a. M. Baro, *Phys. Rev. E - Stat. Nonlinear, Soft Matter Phys.* **2004**, *69*, 1.

[19]   A. Boisen, O. Hansen, S. Bouwstra, *J. Micromechanics Microengineering* **1996**, *6*, 58.

[20]   Y. Martin, H. K. Wickramasinghe, *Appl. Phys. Lett.* **1987**, *50*, 1455.

[21]   R. J. Pylkki, P. J. Moyer, P. E. West, *Jpn. J. Appl. Phys.* **1994**, *33*, 3785.

[22]   F. J. Giessibl, *Appl. Phys. Lett.* **2000**, *76*, 1470.

[23]   G. Meyer, N. M. Amer, *Appl. Phys. Lett.* **1988**, *53*, 1045.

[24]   P. C. Braga, D. Ricci, *Atomic Force Microscopy*, Humana Press, Totowa, New Jersey 07512, **2004**.

[25]   J. N. Israelachvili, *Intermolecular and Surface Forces*, **2011**.

[26]   H. J. Butt, B. Cappella, M. Kappl, *Surf. Sci. Rep.* **2005**, *59*, 1.

[27]   R. García, A. San Paulo, *Phys. Rev. B* **1999**, *60*, 4961.

[28]   B. Luan, M. O. Robbins, *Phys. Rev. E - Stat. Nonlinear, Soft Matter Phys.* **2006**, *74*, 1.

[29]   K. L. Johnson, *Contact Mechanics*, Cambridge University Press, **1987**.

[30]   B. V. Derjaguin, V. M. Muller, Y. P. Toporov, *Prog. Surf. Sci.* **1994**, *45*, 131.

[31]   S. Hu, A. Raman, *Appl. Phys. Lett.* **2007**, *91*, 2005.

[32]   H. Hölscher, U. D. Schwarz, *Int. J. Non. Linear. Mech.* **2007**, *42*, 608.

[33]   A. P. French, *Vibrations and Waves*, CRC Press, **1971**.

[34]   Á. Paulo, R. García, *Phys. Rev. B* **2001**, *64*, 1.

[35]   G. Bar, L. Delineau, R. Brandsch, M. Bruch, M. H. Whangbo, *Appl. Phys. Lett.* **1999**, *75*, 4198.

[36]   J. Tamayo, R. García, *Appl. Phys. Lett.* **1998**, *73*, 2926.

[37]   N. F. Martínez, R. García, *Nanotechnology* **2006**, *17*, S167.

[38]   E. T. Herruzo, R. Garcia, *Appl. Phys. Lett.* **2007**, *91*, 27.

[39]   J. Kokavecz, a. Mechler, *Appl. Phys. Lett.* **2007**, *91*, DOI 10.1063/1.2753104.

[40]   S. De Beer, D. Van Den Ende, F. Mugele, *Appl. Phys. Lett.* **2008**, *93*, 2006.

[41]   J. Legleiter, T. Kowalewski, *Appl. Phys. Lett.* **2005**, *87*, 1.

[42]   S. Basak, A. Raman, *Appl. Phys. Lett.* **2007**, *91*, 064107.

[43]   D. Kiracofe, A. Raman, *J. Appl. Phys.* **2010**, *107*, DOI 10.1063/1.3284206.

[44]   H. R. Kruyt, J. T. G. Overbeek, *Trans. fo Faraday Soc.* **1940**, *35*, 110.

[45]   B. Derjaguin, L. Landau, *Prog. Surf. Sci.* **1993**, *43*, 30.

[46]   E. J. W. Verwey, J. T. G. Overbeek, *J. Phys. Chem. Chem.* **1947**, *51*, 631.

[47]   T. Fukuma, K. Kobayashi, K. Matsushige, H. Yamada, *Appl. Phys. Lett.* **2005**, *86*, 1.

[48]   R. G. Horn, J. N. Israelachvili, *J. Chem. Phys.* **1981**, *75*, 1400.

[49]   M. Lantz, Y. Liu, X. Cui, H. Tokumoto, S. Lindsay, *Surf. Interface Anal.* **1999**, *27*, 354.

[50]   S. Basak, A. Raman, S. V. Garimella, *J. Appl. Phys.* **2006**, *99*, DOI 10.1063/1.2202232.

[51]   C. a J. Putman, K. O. Van Der Werf, B. G. De Grooth, N. F. Van Hulst, J. Greve, *Appl. Phys. Lett.* **1994**, *64*, 2454.

[52]   V. J. Morris, A. R. Kirby, A. P. Gunning, *Atomic Force Microscopy for Biologists*, Imperial College Press, **2010**.

[53]   D. Bondeson, A. Mathew, K. Oksman, *Cellulose* **2006**, *13*, 171.

[54]   M. J. Doktycz, C. J. Sullivan, P. R. Hoyt, D. a. Pelletier, S. Wu, D. P. Allison, *Ultramicroscopy* **2003**, *97*, 209.

[55]   R. Pelton, *TrAC - Trends Anal. Chem.* **2009**, *28*, 925.

[56]   N. Kodera, D. Yamamoto, R. Ishikawa, T. Ando, *Nature* **2010**, *468*, 72.

[57]   M. H. Korayem, N. Ebrahimi, *J. Appl. Phys.* **2011**, *109*, 084301.

Chapter II **Cellulose – Abundant Raw Material for Biofuel Fabrication**
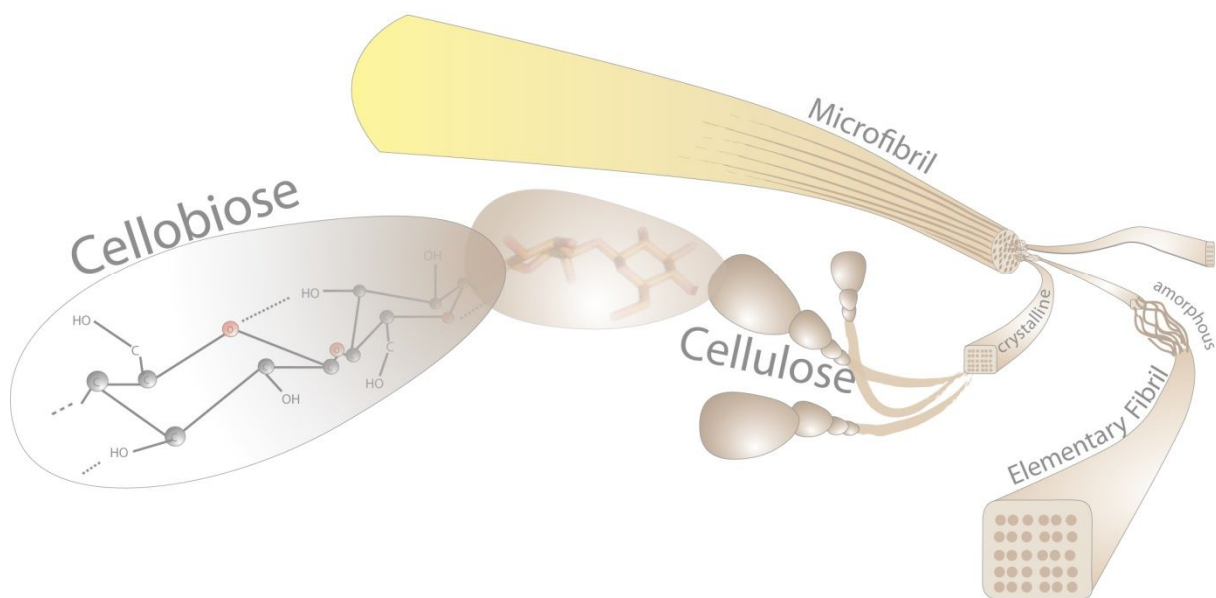
II.1 Introduction

Cellulose is the most abundant bio-synthesized polymer in our hemisphere and found in the cell wall of plants, algae, and bacteria[1]. It was in 1838 that the French chemist Anselme Payen discovered a white and solid remaining after treatment of various plants with ammonia and acid and subsequent extraction with water, alcohol and ether[2]. By elemental analysis, he determined the formula with $C_6H_{10}O_5$ and soon thereafter the term "cellulose" was formed by the French academy[3]. It took another 80 years to discover that cellulose is merely composed of covalently linked D-glucose[4] units forming long linear molecular chains. With an estimated annual synthesis rate of 1.5×10^{12} dry tons it may be seen as an almost inexhaustible raw material for utilization[5]. The linear structure of cellulose has significant influence on the structure and mechanical properties of cellulose as it facilitates parallel packing of chains stabilized through inter- and intra-molecular H-bonding. This specific structure as a crystalline and chemically highly stable polymer elucidates its main purpose as a structure giving and stabilizing element in higher plants, where cellulose content usually ranges from 40% (softwood) to about 55 % (hardwood)[6]. However, imperfect crystalline structures with regions of less order are found between subsequent crystallites denoted as amorphous cellulose. An alternating sequence of crystallites and amorphous intermediate regions forms the so called elementary fibril (1.5 - 3.5 nm) which is further packed into micro-fibrils (10 - 30 nm), macro-fibrils and then structured, according its mechanical purpose, complexly into the cell wall[5]. Micro-fibrils are usually encapsulated by a layer of hemicellulose and lignin, which act as glue towards other micro-fibrils, thus increasing the flexibility[7]. It is the combination of these molecular and supra-molecular structures which elucidates the strength and stability of cellulose components against other polymers. Not only that these beneficial properties of cellulose elucidate the use as building and clothing material since the beginning of humane culture, it also triggered constant technical development since the Egyptian papyri to high-tech and nano-materials nowadays[8]. The range of use today spans from laboratory filters (cellulose nitrate)[9] to composite materials[10] and even bioactive and bio-compatible sensors and active elements[8]. Despite its value in material research, another interesting application, which is heavily researched today, is based on utilization of cellulose as carbohydrate source for so called second generation biofuels. The technique relies on the decomposition of cellulose to D-glucose which is followed by fermentation to ethanol or related high energy liquids for transportation fuels[7,11,12]. Early attempts pointed at depolymerizing cellulose by acid based hydrolysis under harsh chemical conditions to its 5- and 6-chain[7,13] sugars. However, these methods are relatively inefficient, prone to produce unwanted byproducts and expensive, which quickly demonstrated the need for alternatives. It was soon thereafter that a highly effective cellulose degrading fungus was detected by the U.S. Army Natick Laboratory due to significant problems of quickly rotting canvas equipment in the tropics during World War Two[11]. The fungus was identified as *Trichoderma viride* or *Trichoderma reesei* (today *Hypochrea jeronica*) and produces high amounts of specialized enzymes denoted as cellulases capable of degrading cellulose to D-glucose as an energy resource of the organism. In the next *chapter* a comprehensive description of cellulases and enzymology will be given. To understand the basic working mechanisms of the cellulases comprehensive knowledge of cellulose structures and morphologies is absolutely required.

II.2 Cellulose Structure

Properties of cellulose materials are mainly defined by the supra-molecular hierarchical structures of cellulose fibers and composites. In turn, the structure as a linear polymer pre-defines properties to show a high degree of crystallinity, linearity and tendency to form long fibers. The stabilizing elements in this structure are physically defined through a strong and ordered network of H-bonds between adjacent cellulose chains and within an individual chain[5,14,15] which further are strengthened by Van der Waals forces[16]. These structures are, not unexpected, an essential part in cellulose hydrolysis and comprehensive understanding of the structure is key in the following *chapters* of this thesis. Complementary, the most reliable and used method of crystal structure determination, namely X-ray diffraction will be shortly discussed.

II.2.1 Hierarchical Structure

Figure II-2 shows a schematic representation of the hierarchical structure of cellulose found in all woody plants, some bacteria or algae. The monomeric unit of cellulose denoted as cellobiose is a dimer of β-1,4 linked D-glucose molecules. Multiple cellobiose molecules are synthesized and subsequently linked together in the cell wall, thus forming long linear chains. The linkage between cellobiose and D-glucose within this conformation is known to be present between the first and forth carbon atom leading to a strong and linear covalent bond. Thus, linear chains with a repeating value of cellobiose units (= degree of polymerization; **DP**) in the range of 300 up to 10000 units are formed [5]. The DP is typically decreased upon chemical treatment but is still in the range of 300 - 1700 for wood pulp and 250 – 500 for regenerated cellulose (from cellulose solutions)[5].

The chains are terminated by a C4-OH group denoted as non-reducing end and a C1-OH group in equilibrium with an aldehyde structure denoted as reducing end. These end groups are thought to be important for the later enzymatic degradation as they act as marker molecules for the attachment and chain loading of processive exo-glucanases. In between, multiple hydroxyl groups participate to H-bonding, thus facilitating the observed crystalline structure of cellulose. Here, the linear conformation together with a network of H-bonds forms highly orientated and parallel aligned structures **further denoted as crystalline cellulose**. However, different arrangement of the H-bonds allow 4 different today known allomorphs, which will be comprehensively described in the next section. It is important to notice that the arrangement is not perfect and usually after a varying length[14] or nano-crystallite **less ordered amorphous areas are found connecting two adjacent crystallites**. This structure is forming the so called **elementary fibril** which is a basic element of cellulose structures. Elementary fibrils are further aggregated into micro-fibrils, which further are packed together with lignin and hemicelluloses to form the cellulose fiber observable in wood structures[1] (see Figure II-2). The latter are thought to increase biological and mechanical resistivity by introducing a protecting layer against microorganisms (e.g. cellulase producing fungi) and glue between adjacent micro-fibrils. In summary, the **supramolecular structure** implements **high strength materials (crystalline cellulose)** with **flexible elements (amorphous cellulose, lignin and hemicelluloses)** and offers plants the ability to build high structures (e.g mammoth tree) which are capable to absorb most of the lateral (e.g. wind) and vertical energy.

In summary the hierarchical structure which schematically is depicted in Figure II-2, is responsible for the strength but also the recalcitrance of cellulose structures form the viewpoint of degradation. Here, lignin, hemicellulose and other components state major limitations for degradation. Not only that the components are highly complexed in form of a fibrillary intertwining but also the protection through chemically different materials (lignin, hemicellulose) is problematic. It is possible to visualize these structures by AFM. However, at first a disintegration to some extend is necessary. We employed sulfuric acid which hydrolysis primarily amorphous regions as well as lignin and hemicellulose and visualized fibers after a 15 min treatment in 64 vol.% sulfuric acid at 45°C. The data is shown in Figure II-1.
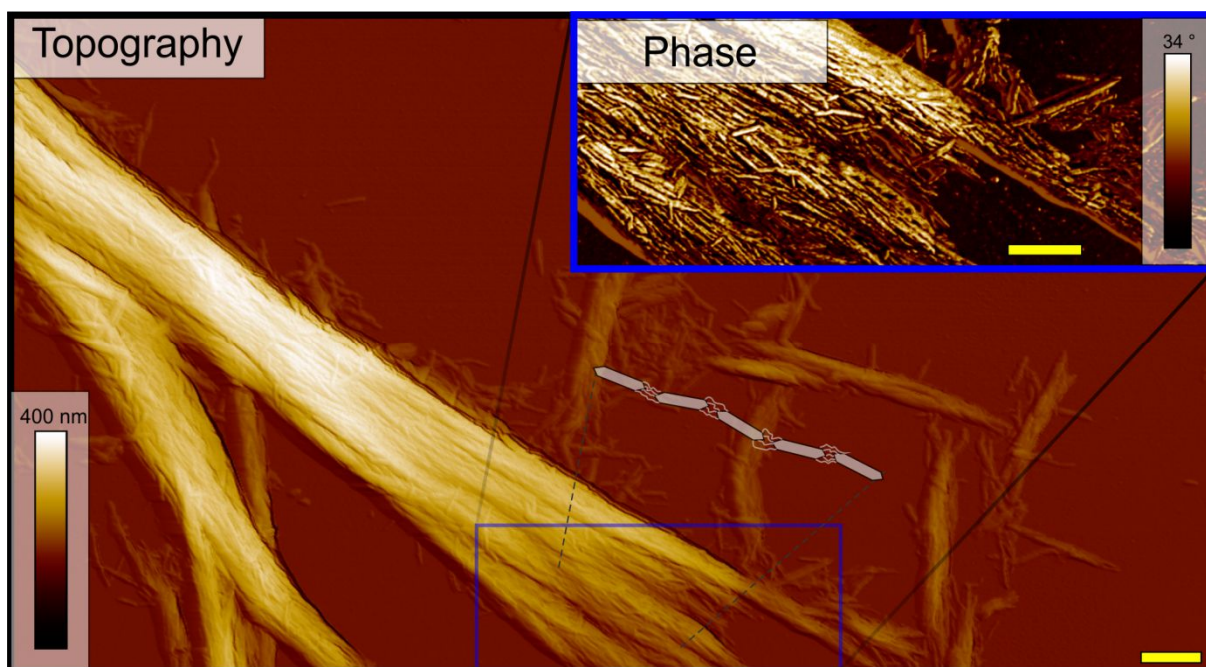
Figure II-1: An AFM topography image of a partly hydrolyzed fiber (sulfuric acid) with a corresponding phase image in the highlighted area (blue rectangle). The intrinsic structure is visible by the AFM image: 1) Small nanocrystals are visible, which are an essential part of cellulosic structures as depicted in Figure II-2. Additionally, the acid treatment leads primarily to degradation of the amorphous areas which leads to fragmentation of the fiber (see side walls of fiber). A model of the cellulose microfibril is schematically shown and highlighted by dotted lines. Scale bars represent 400 nm.
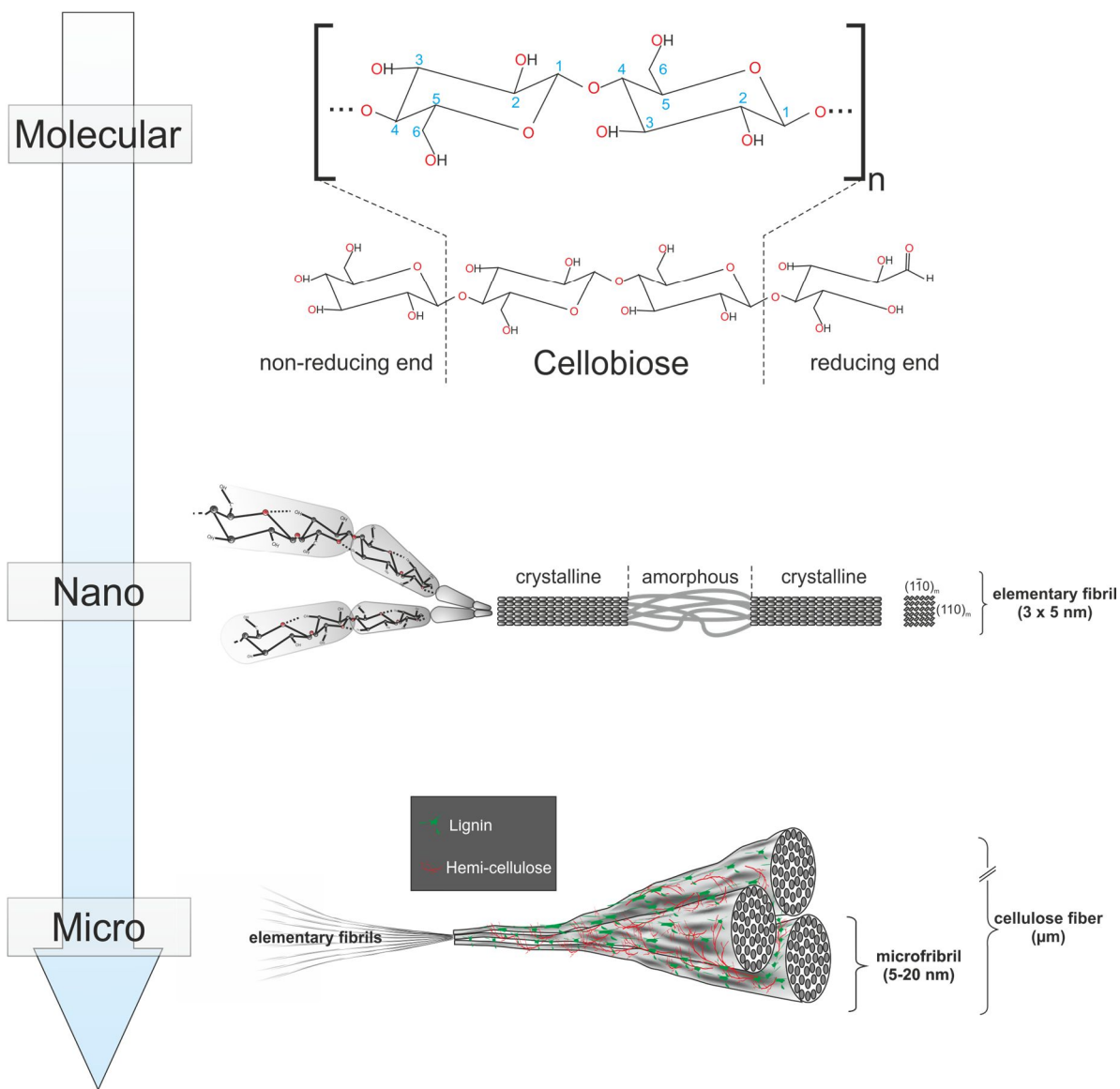
Figure II-2: Hierarchical cellulose structures found in natural cellulose sources (e.g wood). The structure comprises molecular, supramolecular and microscopic superstructures defined through the properties of cellulose as a linear polymer and the biological synthesis strategy. The molecular level is defined through a linear polymer of covalently β-1,4 linked D-glucose dimers (Cellobiose) forming long linear chains called cellulose. The linearity facilitates linear packing of chains leading to high density and crystalline cellulose crystals intercepted by less ordered or amorphous regions together forming the so called elementary fibril. Multiple elementary fibrils are then again packed in a twisted manner forming the micro-fibrils which are embedded in a matrix of lignin and hemi-cellulose acting as flexible and gluing components. In a final step cellulose fibers (multiple micro-fibrils) are arranged in different layers of the cell wall to meet the desired strength and stability requirements.

II.2.2 Crystal Structures

Crystalline structure of cellulose is caused by the ability to form different networks of hydrogen bonds. Today, 4 main crystalline allomorphs with some subgroups are identified. Here, cellulose-I is the only one found in nature. Treatment of this natural allomorph may lead to other crystal structures, which have significant impact on various parameters, as for instance the degradability. Here the work of Igarashi and coworkers [17] may be taken as example where cellulose-III was degraded at much faster rate compared to cellulose-I_α.

In Figure II-3 today known crystal structures are shown from the (a, b) plane of the unit cell. All structures feature triclinic or monoclinic unit cells and are despite cellulose-I only found after chemical treatment. An interesting point is, that cellulose-I and II show a different chain conformation in respect of non-reducing and reducing ends. For cellulose-I non-reducing and reducing ends are accumulated on one side of the elementary crystallite, which may be attributed to biosynthesis where chains are packed directly after synthesis with ends aligned[14]. Cellulose-II was found to show antiparallel conformation with respect to non-reducing and reducing ends by X-ray diffraction techniques[18]. Although this concept is commonly accepted by most research groups[1], there is still some controversy on the structural rearrangement of cellulose-I to cellulose-II, which has to implement a back folding of chains or complicated rearrangement between elementary crystallites of different orientation[19]. So far also MD simulations[20] showed the possibility of parallel cellulose-II which is in conflict with X-ray diffraction and neutron diffraction data[21–23]. A final answer is, to the best knowledge of the author, not available. So far the antiparallel model is the most accepted and valid one and will be further used in this thesis. The implication on the enzymatic degradation is significant, as some cellulases are end-group specific. Here, loading occurs at either the non-reducing or reducing end group, which will be important for *chapters IV* and *V*. Subsequent crystal structures as cellulose-III and cellulose-IV are indicated by suffixes with I and II corresponding their origin or their parallel and antiparallel chain conformation, respectively. It is thought that the parallel or antiparallel conformation is conserved in the cellulose-I (III_I, IV_I) line and cellulose-II (III_{II}, IV_{II}) line. Calculation showed also that cellulose-II is the energetically most favorable form which explains the irreversible transformation upon regeneration or mercerization. Crystal structure and knowledge about it, is crucial upon interpretation of AFM data obtained during *in-situ* observation of enzymatic activity as end-group specific chain loading, substrate density and hydrogen bonding network play a significant role[17]. For the next *chapter*s, however, only knowledge about cellulose-I and cellulose-II will be necessary.
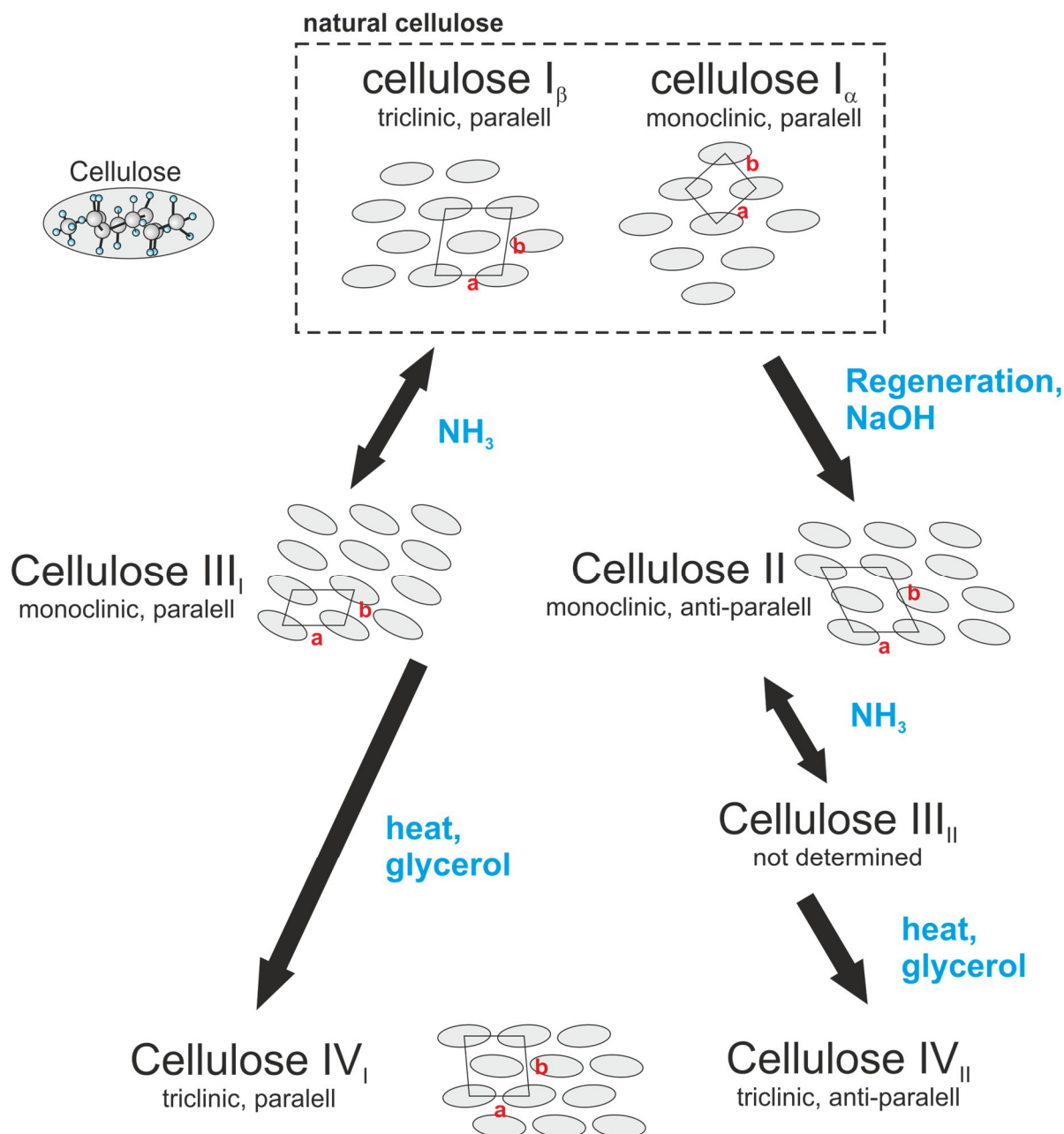
Figure II-3: Cellulose crystal structures (allomorphs) seen from the (a, b) plane of the unit cell. Natural cellulose sources show a combination of cellulose-I_β and I_α structures whereas I_β dominates in higher plants and I_α in bacteria[5]. Cellulose-II is formed after regeneration from solution or if cellulose-I is treated with sodium hydroxide. Calculations show that cellulose-II is the energetically most favorable structure[1,5]. Cellulose-III may be obtained by treatment of either cellulose-I or II with ammonia[24] and cellulose-IV is obtained by following heat treatment in glycerol[25]. Cellulose IV_I and Cellulose IV_{II} differ only in their chain orientation (parallel or antiparallel) while the crystalline structure is similar. Cellulose-III and IV are of minor technical relevance.

II.2.3 Crystal Structure, Crystallinity & X-ray Diffraction Analysis

Determination of crystal structure is, at least from enzymatic perspective, not important as natural cellulose is only found in the cellulose I allomorph. However, there are differences in the sub-classes cellulose-I$_\alpha$ and cellulose-I$_\beta$. Although, in principle both allomorphs are found in most resources, plants and microbial derived celluloses usually show cellulose-I$_\beta$ and cellulose-I$_\alpha$ rich structures, respectively. Beside crystal structure, crystallinity, which is the ratio of crystalline phase to amorphous phase, is of significant impact as degradation is effected to a significant part as demonstrated by numerous studies[26–29]. Thus methods to evaluate crystallinity are highly anticipated and should be considered more closely. In the following, X-ray diffraction will be described briefly as the most common and reliably used method. An exact description of X-ray techniques and corresponding analysis methods is beyond this thesis and may be found in a book by Warren [30]. Briefly, the technique is based on the interaction of electromagnetic waves (X-rays) with matter. A simple explanation is given in Figure II-4 and corresponds to the Bragg formalism to describe constructive interference of incoming electromagnetic waves with atomic planes in a crystal. The principle is rather simple and says: If an incoming wave (X-rays) is reflected at a certain angle Θ, constructive interference is going to occur when the path difference (green line; Figure II-4) corresponds to an integer number times the wavelength. This is a very simplified picture of X-ray diffraction but states the basic principle behind it. In reality the situation is usually more complicated as diffraction is influenced by thermal motion, crystallite size, crystal orientation and the interaction of a huge number of atoms which leads to varying intensities in the diffraction pattern. A deeper description may be found in literature [30].

A typical powder diffraction pattern for cellulose-I$_\beta$ is shown in Figure II-5. The pattern was created by simulation[31] and shows a spectrum for fully polycrystalline cellulose-I$_\beta$.

Although, the technique of X-ray diffraction is a powerful tool to determine crystal structure and morphology it may also be used in the case of polymorphism to determine the crystallinity. The crystallinity index is defined as the ratio of the crystalline phase to its amorphous phase and is applicable to polymorphous pure materials. In the case of cellulose, this is a formidable hard task which is reflected by a large variance of the crystallinity index for a given material[29]. Part of the discrepancy may be attributed to different methods of analysis and corresponding models. Moreover, it is thought that the crystal structure is small and prone to imperfections which exacerbate conclusions on crystal lattice, size and crystallinity. A simple example may be given by the use of Avicel (Avicel PH101®, Sigma Aldrich, St. Lois, Missouri, USA) which is the most common model substrate in cellulase science. Here, crystallinities are found in a broad range of 60 to 90% in respect to the applied method [29]. In Figure II-6 an exemplary diffraction pattern is shown as the sum of a crystalline (cellulose-I$_\beta$) and amorphous pattern. The problem now is: In reality, diffraction patterns cannot simply be separated to an amorphous and crystalline part (like in Figure II-6) as their exact form is elusive. However, there are approximation methods which will be described briefly in the following.

$$n\lambda = 2d\sin(\Theta)$$
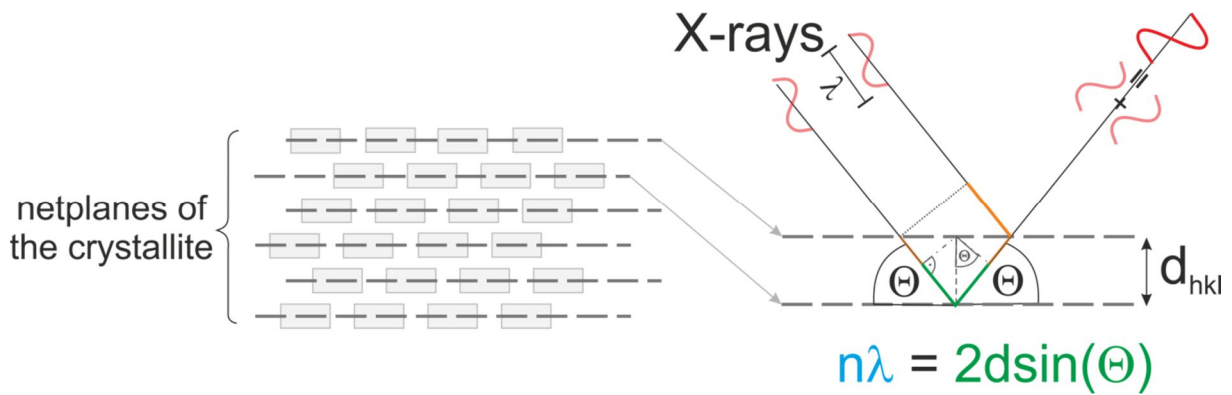
Figure II-4: Bragg condition for a given set of net-planes. Incoming waves will interfere constructively if the path difference (green line) is equal to an integer number times the wavelength. In this case maxima and minima of two waves add up and form a diffraction peak.
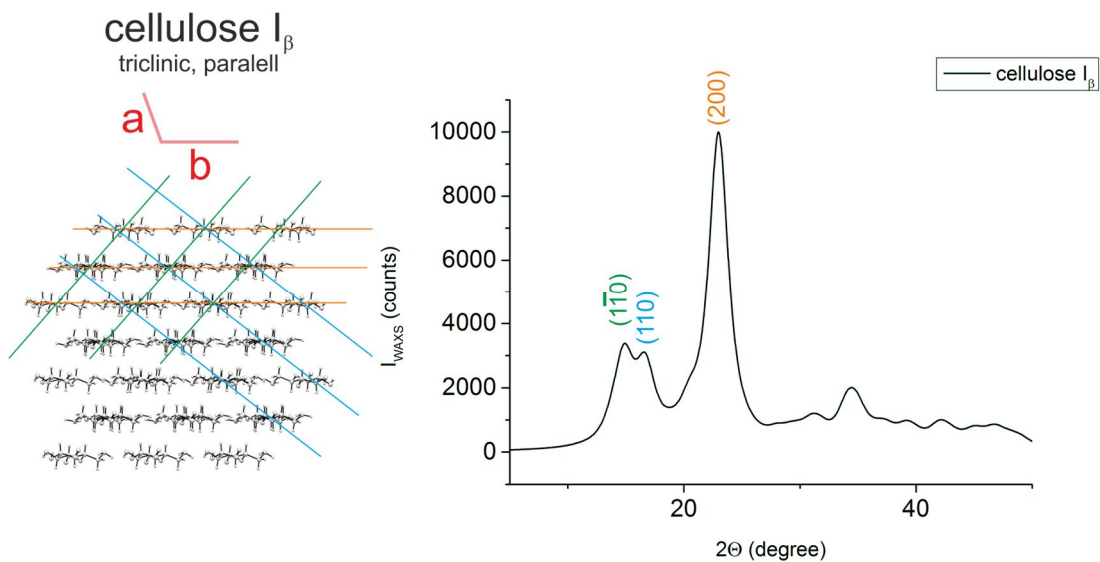
Figure II-5: Crystal structure with net-planes and the corresponding simulated diffraction pattern[31] of cellulose-I$_\beta$. Miller indices and colors correspond to the net-plane colors. Crystallite is seen perpendicular to the a-b plane of the unit cell.
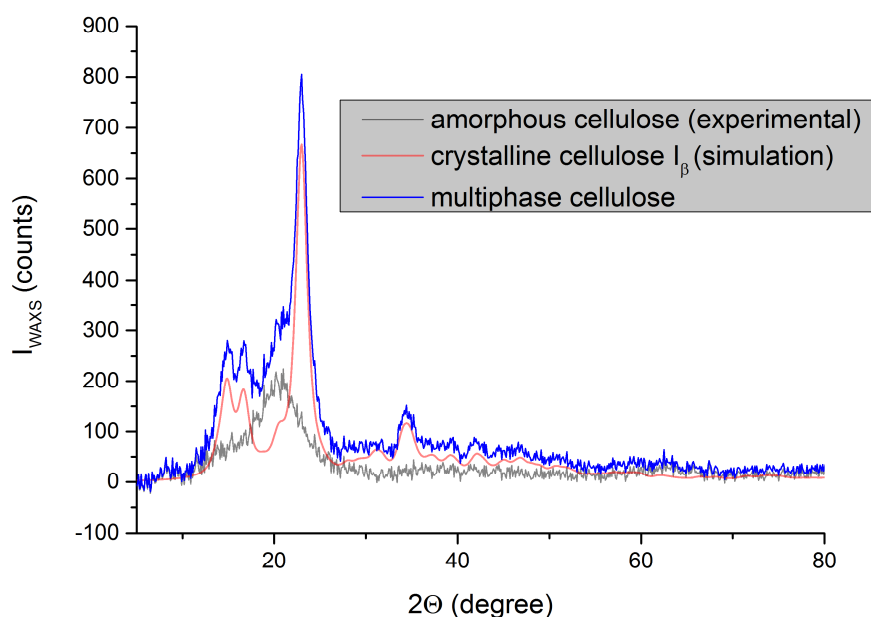
Figure II-6: X-ray diffraction pattern of a multiphase cellulose substrate (blue) as the sum of a crystalline (red[31]) and amorphous (grey) part.

Multiple methods have so far been tested but show different results which causes interpretation to be difficult. A good overview over methods which may be used to determine crystallinity are summarized in the work of Park and coworkers[29]. Probably, the most sophisticated and theoretical based method was used by Ruland[32] by introducing lattice vibrations as well imperfections to the calculation of the crystallinity index. As mastering this method requires fundamental and comprehensive understanding of X-ray methods, a complete description is not shown. Although Rulands method is based on reliable theoretical concept, we applied a different method throughout this thesis due to the following: As all of our substrates are controllable in crystallinity, we could produce pure amorphous cellulose and a corresponding spectrum. Once we had recorded the X-ray diffraction pattern of such an amorphous substrate, we knew the form and could fit this pattern to the later polycrystalline diffraction pattern. By that a separation of crystalline and amorphous part was reliably possible. Integration over the specific intensities delivers a ratio which represents the crystallinity. Note, this method is only available when a corresponding amorphous diffraction patterns are available. Other methods may be used as well, as for instance Raman spectroscopy[33] to test the crystallinity, however, are less appropriate than X-ray diffraction.

II.3 Cellulose – Chemistry

The aspect of insolubility of cellulose in water and many other common solvents poses one of the major problems which are encountered in cellulose chemistry. Moreover, this has significant implications on enzymatic cellulose degradation. In both cases, the strong hydrogen bonding network of hydroxyl groups prevents dissolution as well chemical reactions due to the inaccessibility of these most reactive groups. Therefore, most reactions are today carried out in more or less swollen states and are determined by activation steps to break the hydrogen bond network[5]. Such

reactions are not easy to control, and effective synthesis is thus hard to achieve. Through the use of specific cellulose solvents the reactivity of cellulose may be increased together with an effective control over the reaction (e.g. the grade of substitution by derivatives). So far, the interest in cellulose chemistry was mainly triggered by the clothing and paper industry. However, new applications now focus on hi-tech materials on cellulose basis like bio-active elements and sensor[34,35]. A good summary of this highly interesting applications can be found in the review of Credou and Berthelot[8]. These applications are based on the given knowledge of cellulose chemistry, and a good introduction is given in the review by Klemm and coworkers[5]. The description in this thesis will be limited to used solvents as the ionic liquid 1-butyl-3-methlyimidazolium chloride **(BmimCl)** and the cellulose derivative trimethylsilyl-cellulose **(TMSC)**.

II.3.1.1 Cellulose Solvent – 1-Butyl-3-Methlyimidazolium Chloride

Today various specific cellulose solvents are known as lithium-chloride in N,N-dimethylacetamide or tetrabutylammodnium fluoride trihydrate dissolved in dimethyl sulfoxide (**DMSO**). In recent years a new class of solvents, so called ionic liquids, has drawn the attention in the field of cellulose utilization. Ionic liquids are organic salts which are liquid below 100°C or at even room temperature. These liquids are capable to disrupt the hydrogen bond network of cellulose and thus dissolve it. Furthermore, they show beneficial properties as immeasurable low vapor pressure and low toxicity, together with the ability to recover the solvent, which have led to the name of green solvents[36]. A good description of applicable and known ionic liquids may be found in a review of Mäki-Arvela and coworkers[37]. In this thesis the main application was to bring cellulose in a malleable form, which in term of AFM has the following reasons*: 1)* Cellulose structures from **natural resources often do not show** the **topographic requirements** for AFM investigations with deep holes, trenches, large features and all-in-all non-flat surfaces*. 2)* The **reproducibility for natural cellulose cannot be guaranteed** as in nature growth conditions vary and thus cellulose structure. Therefore, solution of cellulose and further recovery in a different, flat and reproducible form was intended. For this purpose the ionic liquid 1-butyl-3-methylimidazolium chloride (BMIMCl; Figure II-7) was used, as it shows one of the highest dissolution capabilities of cellulose with approximately 10-20 wt.% depending on the used cellulose source.
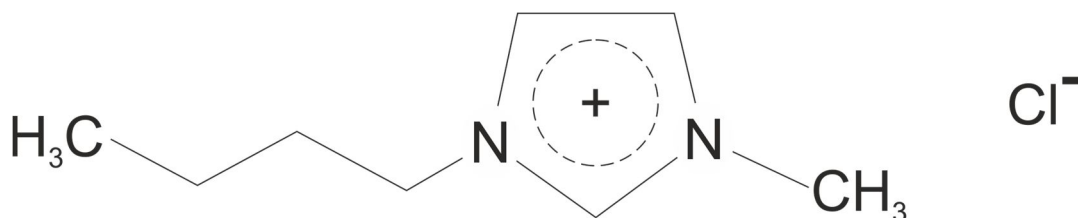

Figure II-7: 1-butyl-3-methylimidazolium chloride

So far the exact mechanism of solution has been evaluated only in view studies. Here, the chloride anion interacts with a 1:1 stoichiometry of the hydroxyl groups in cellulose which causes disruption of the hydrogen bond network and further dissolution[37]. The exact preparation-process used in this study to dissolve cellulose will be given in a following *chapter* of this thesis.

II.3.1.2 Cellulose Derivatives – Trimethylsilyl-Cellulose

Another interesting concept to dissolve cellulose, is to use derivatives by substitution of the hydroxyl groups[5]. Thus the interaction by hydrogen bonding is prevented and dissolution capabilities are increased. Other applications are the protection of selected hydroxyl groups of cellulose in chemical reactions. However, all these application require the possibility to re-substitute the derivative with the hydroxyl group. In this study we used trimethylsilyl-cellulose (TMSC) as a precursor to form thin films of cellulose which include two advantages: *1)* The layer **may be produced extremely flat** without further treatment*; 2)* The cellulose substrates are chemically **pure and reproducible** and may even be combined with lignin, hemicelluloses, crystalline nano-cellulose or other components. This makes the approach to form cellulose thin films via TMSC to one of the hot topics in cellulose science[38–42]. Synthesis of TMSC shown in Figure II-8 again implies ionic liquids as reaction media and may be achieved by a protocol from literature[5,43] with a degree of substitution of up to 2.89.
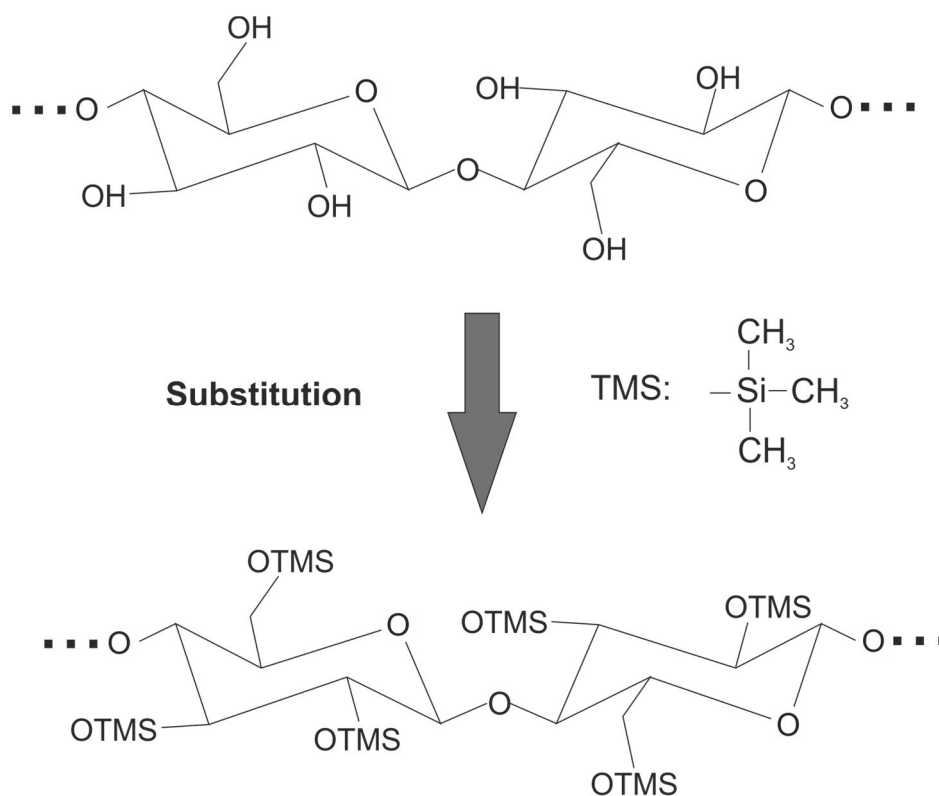

Figure II-8: Cellulose (top) and Trimethylsilyl-cellulose (bottom). The TMS groups prevent H-bonding between oxygen and hydrogen, thus increasing the solvability.

The resulting TMSC, as shown in Figure II-8, is then solvable in most non-polar solvents and may be used for electrospinning or spin coating processes as shown schematically in Figure II-9.
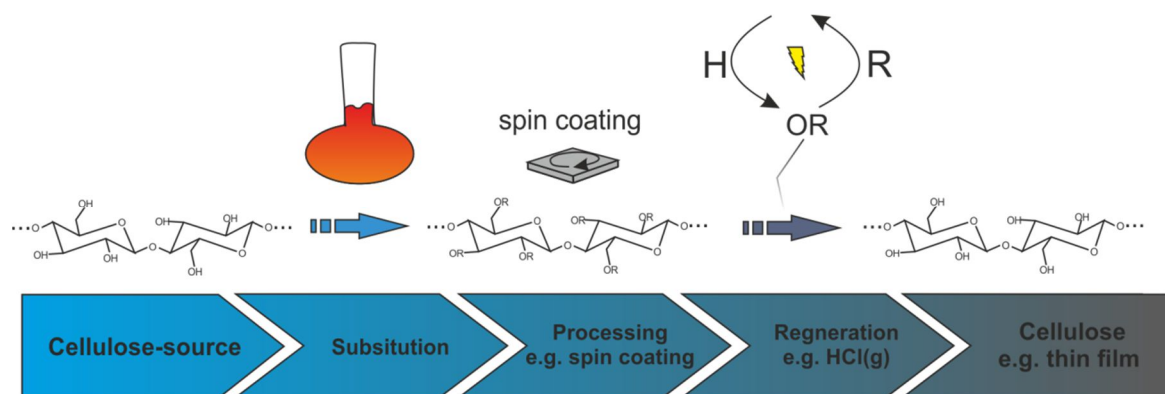
Figure II-9: Processing of TMSC from the cellulose source to the final cellulose product. First substitution is performed by protocol from literature[9,43] and dissolved, further processed and in a final step regenerated. The regeneration step (yellow lightening bold) is usually achieved by application of acids. Here, the protonation of the acid allows re-substitution with hydrogen and cleavage of the Si-O bond. The resulting cleaved species is usually volatile or later removed by careful rinsing with water. In the final state pure, amorphous cellulose (e.g. thin film) is again present.

The processing of trimethylsily-cellulose includes the dissolution in a non-polar solvent and further processing by electrospinning, Langmuir Blodgett dip casting or spin coating to yield thin cellulose fibers or films, respectively[41,44,45]. In a final step, the back transformation may be simply performed by using gaseous hydrochloric acid vapors ($HCl_{(g)}$) which hydrolyze the oxygen silicon bond back to the cellulose structure. The simplicity of this process educates the success of this method.

II.3.2 Cellulose Chemistry – Raman Spectroscopy

Raman spectroscopy and associated microscopy is a very powerful tool to analyze the chemistry of a given material. The method is based on the inelastic scattering of coherent light (laser) on a sample which produces a characteristic fingerprint for a specific molecule. By that, purity and compositions of different materials may be quickly revealed. Again, Raman spectroscopy and a comprehensive theory behind it are beyond this thesis, and the reader may refer to the book of Long[46] for further information. Briefly, if coherent light from a laser source is transmitted through a material scattering events may occur. In contrary to infrared spectroscopy, where the light energy is in the range of vibrational and rotational energies of the molecule, the photon energy in Raman scattering does not allow such a transition as it usually lies in the energy range between two electronic states. In this case, the ground energy of the molecule $E_0^{V/P}$ and the energy of the incoming light $\hbar\omega_P$ may create a so called virtual state. This state is the quantum mechanical representation of the scattering process between the incoming light and the molecule energy and exists only for a very short time. The virtual state is immediately de-occupied and relaxation to the former energy $E_0^{V/P}$ is the most probable transition and denoted as classical Rayleigh scattering. However, there are more possibilities: *1)* The relaxation may be performed in a way that an vibrational or rotational molecule state $E_1^{V/P}$ is the end product which is **higher than the ground state**. This is called Raman Stokes scattering and yields an inelastic scattering with the photon energy $\hbar(\omega_P-\omega_{V/P})$. *2)* The photon energy may hit **an already excited state $E_1^{V/P}$** yielding a different virtual level (virtual levels are not quantized which allows occupation in any case) and relaxation may then lead to the ground state. This is called Raman anti-

Stokes scattering and produces a photon with energy $\hbar(\omega_P+\omega_{V/P})$. A schematic of the process is shown in Figure II-11. Please note, although this introduction may suggest that a Raman-effect is always observable, classical theory proves the opposite. Raman-scattering is the inelastic scattering of a photon at molecules by interaction with its polarizable electron density. In a classical description one must consider the oscillation of a molecule and in particular its polarizability at passage of the equilibrium state. If the polarizability changes at passage, Raman scattering is the result. Otherwise, only Rayleigh scattering occurs. This result may be achieved by using a Taylor expansion to the first term of the polarizability and a sinusoidal electric field excitation. The complete theory may be found in literature[46]. However, as a rule of thumb for molecules with a center of symmetry, usually infrared spectroscopy observed bands are not Raman active and vice versa. Therefore these methods are seen as complementary. Note, Raman operates at higher photon energies (usually visible light) which allows using conventional optics and less sample preparations. Therefore in this thesis, this method was chosen.

Now considering a complex molecule with 3N (N is the number of atoms) degrees of freedom, a complex spectrum is the result, which is characteristic for a given molecule. Such Raman spectra show a characteristic fingerprint for every molecule and thus chemical analysis is available. In the case of cellulose, the spectrum not only shows the presence of cellulose but also gives valuable information on the crystal structure. The reason is that, hydroxyl groups involved in hydrogen bonding are unavailable for Raman scattering due to the missing vibrational and rotational freedom. So different networks of hydrogen bonds produce different Raman spectra and thus show the crystal structure as shown in Figure II-10.

In summary, it is essential to note that that X-ray diffraction is more appropriate for crystal determination while Raman gives more information on chemical purity of the material. Combination of both is therefore highly anticipated in the analysis of cellulose materials which will be comprehensively shown in the following *chapters*.
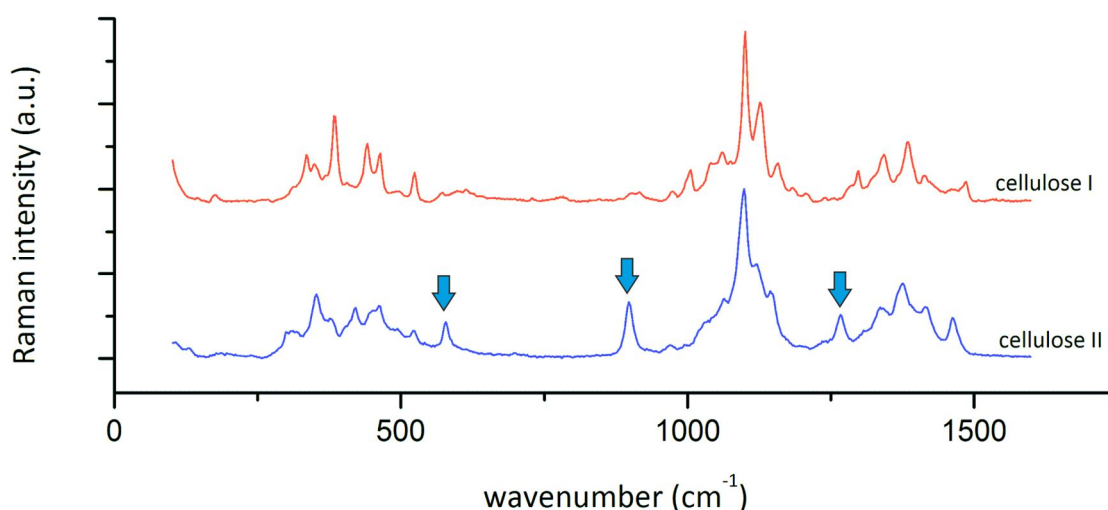

Figure II-10: Raman fingerprint region of cellulose-I (red) and cellulose-II (blue). Characteristic differences originating from the different hydrogen binding network in both allomorphs are marked with blue arrows. An exact assignment of bands to atomic movement (vibrational, rotational) are given by the work of Atalla and Wiley[47].
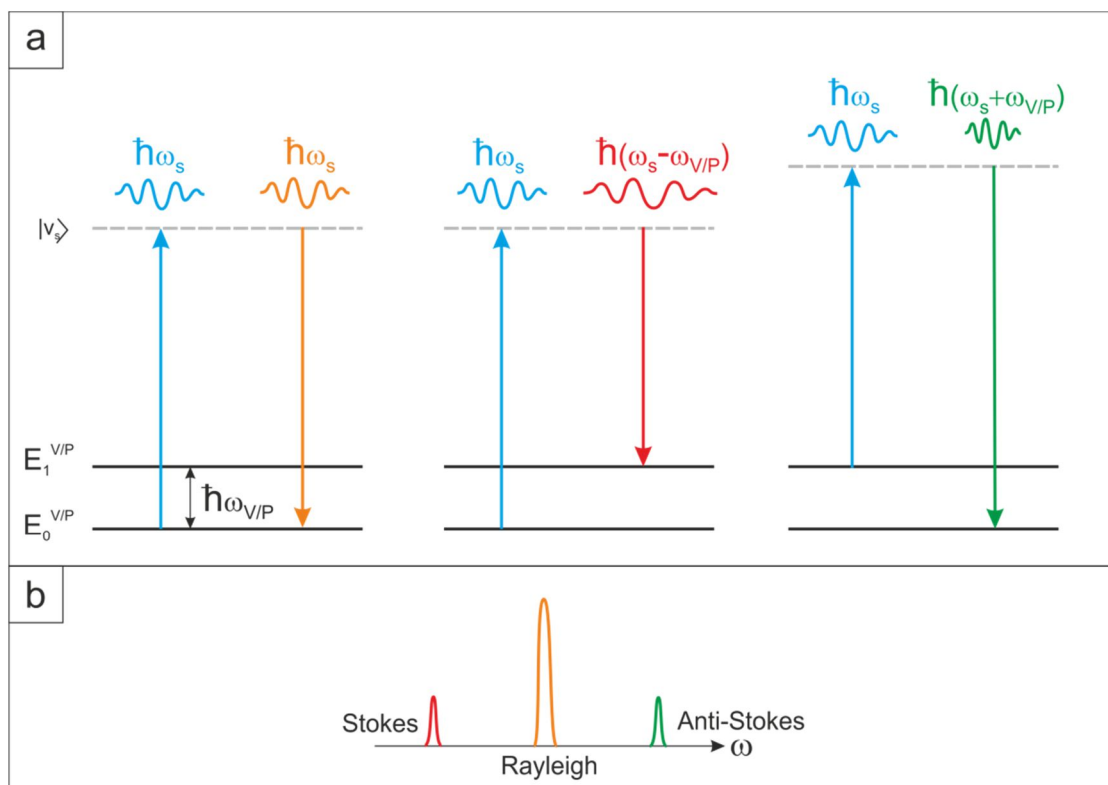
Figure II-11: (a) Simple model of Raman scattering. $E_0^{V/P}$ is the ground energy $E_1^{V/P}$ the next higher energy state and v_s denotes the virtual state in quantum mechanical notation and the energy of the incident light is $\hbar\omega_P$. (b) The observed spectrum in Raman scattering: Beside a multiple times stronger Rayleigh line Raman Stokes and Anti-Stockes Lines are found from the inelastic scattering process as shown in (a).

II.4 Nano-Cystalline Cellulose

The structure of cellulose as a composite material of different cellulose allomorphs, lignin, hemicelluloses and proteins, all linked and structured on a nano-scopic level (that is below 100nm) elucidate the common interest in the special properties of nano-cellulose-composites. The scientific interest ranges from a combination of cellulose nanocrystals with other polymers to increase strength, flexibility and resistivity to cellulose structures artificially created[48–52]. Nano-cellulose may rather simply be created by using bacterial cellulose or by treatment of other cellulose sources with strong acids (see Figure II-1). By that, primarily amorphous intermediate regions of the elementary fibril are hydrolyzed and degraded resulting in a colloidal solution of cellulose nanocrystals (see Figure II-12 and Figure II-13). Shape, size and aspect ratio may be altered by using different cellulose sources or by alternating the time of acid hydrolysis[10,14,53] as visualized by Figure II-13. The colloidal stability of nano-crystalline cellulose (**NCC**) is largely triggered by charged surface groups, primarily introduced by the use of sulfuric acids [14]. Other acids like hydrochloric acid do not produce such groups and colloidal stability is reduced.
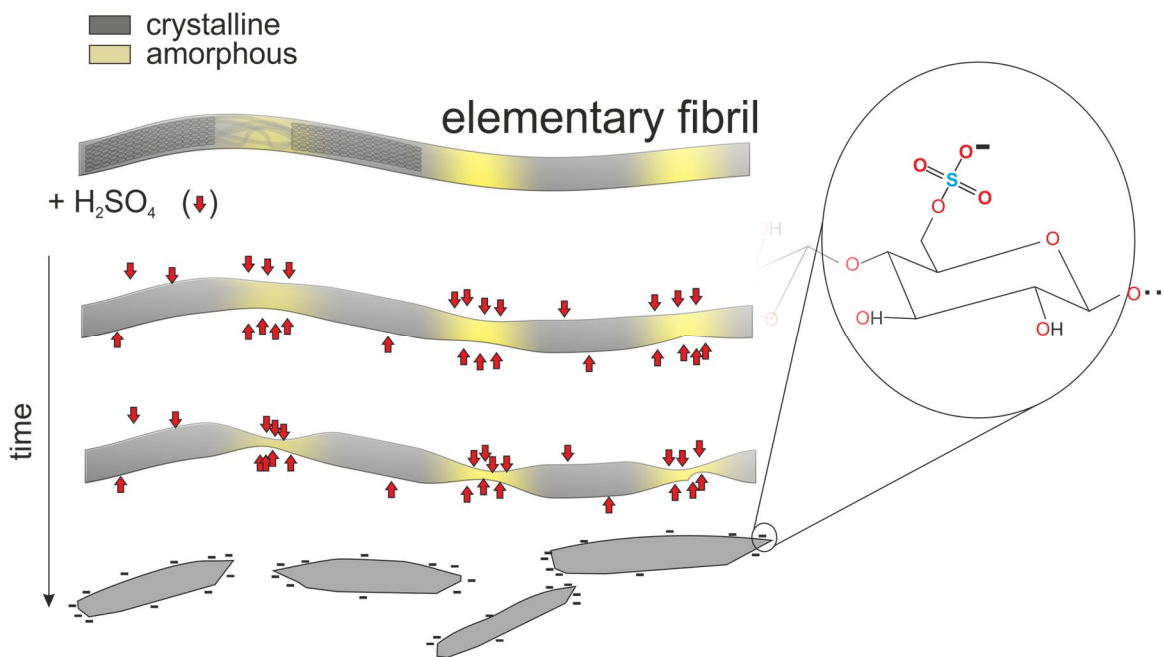
Figure II-12: A schematic model of the acid driven hydrolysis of cellulose. Upon addition of sulfuric acid, amorphous parts are quickly attacked and crystalline regions are not, due to their higher resistivity (red arrows). Over time the small nano-crystalline whiskers are separated from the less ordered regions and a solution of nano-crystallites is the result, stabilized to a colloid by acid induced sulfonic esters (inset).

Colloidal stability is highly important for the intermixing with other solvents and further use as agglomeration is largely irreversible due to hydrogen bonding and Van der Waals forces. Analysis shows a high index of crystallinity[54] and a shape similar to needles as would be expected considering the above mentioned model.
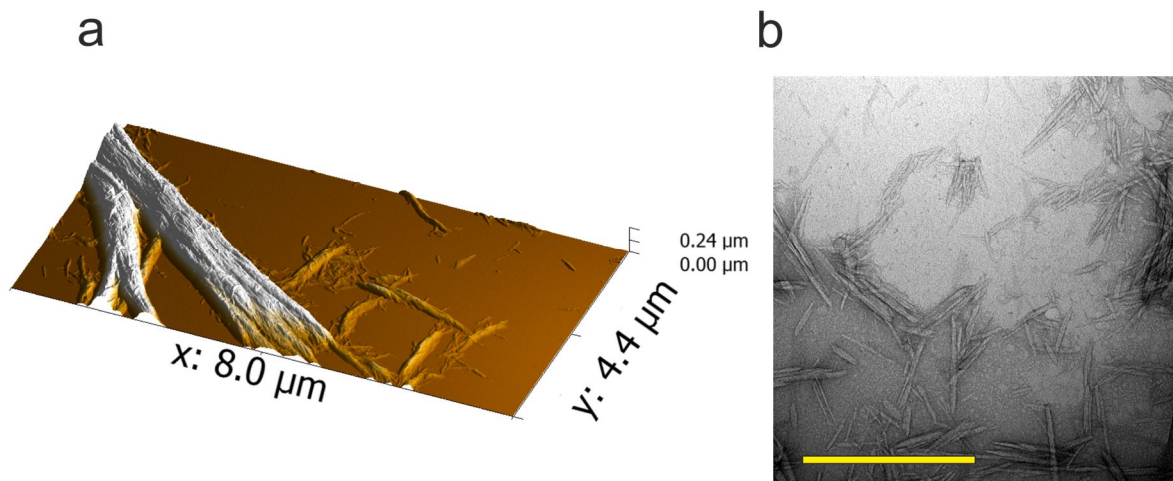
Figure II-13: (a) AFM 3D image of a cellulose fiber after 15 min sulfonic acid (64 wt.% at 45°C) showing nicely that whiskers are separated from the structure due to the acid (see Figure II-1). (b) Nano-crystalline cellulose visualized by TEM imaging showing the elongated shape of the crystallites. Analysis of dimensions reveals approximately 120 nm and 17 nm in length and width, respectively. Scale bar represents 500 nm.

Interestingly, NCC in solution shows liquid crystallinity forming a chiral nematic phase under special conditions[14]. Despite these properties, the exceptional high crystallinity and the purity of such crystallites, together with the fact that the smallest unit of the cellulose superstructure is now at hand, offers interesting capabilities for the investigation of cellulose degradation by enzymes. The reason is that upon degradation, enzymes will encounter these crystallites of highest crystallinity and that high ordering and strong binding network of hydrogen bonds will affect cellulose degradation significantly. It is thought that this may play a role in the rate limitation during hydrolysis caused by inhibition of enzymes due to the strong linkage of cellulose chains or obstacles in the crystallites. So, the understanding of the effects of cellulose degradation on such small scales is essential for the deeper understanding of enzymatic cellulose degradation.

II.5 Chapter Summary

This *chapter* has provided a basic introduction to cellulose, its structure and chemistry. Additionally at relevant sections basic analysis methods were shortly discussed as wide angle X-ray scattering and Raman spectroscopy. The reason is that these methods will be used in *chapters IV* and *V*. Cellulose is, as depicted in Figure II-2, a highly complex material and poses different obstructive elements for the efficient degradation by cellulases. The complete picture of cellulase interdependence with its substrate is far from complete. However, from fundamental considerations and recent studies it is clear that part of the difficulties to efficiently degrade cellulose may be found within its complex intrinsic structure. Here, crystallinity is of particular interest. In terms of AFM, the complex structure is further problematic as standardized substrates are rarely given by nature itself. The reason is that in nature cellulose structures are built in dependence of the growth conditions (see year rings in trees) which renders reproducibility to be low. Moreover, substrate fabrication requires extensive pretreatment to gain sufficiently flat and pure substrates. Thus, artificially fabricated substrates allowing good control over the composition are required. So far, most substrates featured either amorphous or crystalline celluloses, which at some point, is disadvantageous considering substrate affinities of different cellulases. We therefore will, in *chapter IV,* describe methods to fabricate such substrates which allow introducing crystalline and amorphous celluloses in standardized model substrates. Here, concepts focus on implementation of large crystalline features (as the fiber in Figure II-1) and nano-crystalline celluloses within an amorphous matrix (see section II.4). To understand these concepts, the basic knowledge introduced here is absolutely required. However, preparation of standard substrates, at least in some cases, is depending on the cellulase system to be investigated itself. Therefore, a basic introduction to enzymatic systems and cellulases in particular is so far still missing. The next *chapter* will deal with basic concepts of enzymology and the corresponding cellulases.

II.6 References

[1]   A. C. O. Sullivan, *Cellulose* **1997**, *4*, 173.

[2]   A. Payen, *C. R. Hebd. Seances Acad. Sci* **1838**, *7*, 1052.

[3]   A. Brongniart, T. T. Pelouze, A. B. Dumas, *Comptes Rendus* **1839**, *8*, 51.

[4]   H. Staudinger, *Berichte der Dtsch. Chem. Gesellschaft* **1920**, *53*, 1073.

[5]   D. Klemm, B. Heublein, H.-P. Fink, A. Bohn, *Angew. Chem. Int. Ed. Engl.* **2005**, *44*, 3358.

[6]   Y. Sun, J. Cheng, *Biorecource Technol.* **2002**, *83*, 1.

[7]   E. M. Rubin, *Nature* **2008**, *454*, 841.

[8]   J. Credou, T. Berthelot, *J. Mater. Chem. B* **2014**, *2*, 4767.

[9]   D. Klemm, B. Heublein, H. H.-P. Fink, A. Bohn, *Angew. Chemie* **2005**, *117*, 3422.

[10]   Y. Habibi, L. a Lucia, O. J. Rojas, *Chem. Rev.* **2010**, *110*, 3479.

[11]   S. P. S. Chundawat, G. T. Beckham, M. E. Himmel, B. E. Dale, *Annu. Rev. Chem. Biomol. Eng.* **2011**, *2*, 121.

[12]   L. R. Lynd, P. J. Weimer, W. H. van Zyl, I. S. Pretorius, *Microbiol. Mol. Biol. Rev.* **2002**, *66*, 506.

[13]   F. B. Laforge, C. S. Hudson, *J. Ind. Eng. Chem.* **1918**, *89*, 925.

[14]   R. J. Moon, A. Martini, J. Nairn, J. Simonsen, J. Youngblood, *Chem. Soc. Rev.* **2011**, *40*, 3941.

[15]   S. Y. Oh, I. Y. Dong, Y. Shin, C. K. Hwan, Y. K. Hak, S. C. Yong, H. P. Won, H. Y. Ji, *Carbohydr. Res.* **2005**, *340*, 2376.

[16]   T. Huber, J. Müssig, O. Curnow, S. Pang, S. Bickerton, M. P. Staiger, *J. Mater. Sci.* **2012**, *47*, 1171.

[17]   K. Igarashi, T. Uchihashi, A. Koivula, M. Wada, S. Kimura, T. Okamoto, M. Penttilä, T. Ando, M. Samejima, *Science* **2011**, *333*, 1279.

[18]   F. J. Kolpak, J. Blackwell, *Macromolecules* **1976**, *9*, 273.

[19]   T. Okanot, A. Sark, *J. Appl. Polym. Sci.* **1985**, *30*, 325.

[20]   L. M. J. Kroon-Batenburg, B. Bouma, J. Kroon, *Biomacromolecules* **1996**, *9297*, 5695.

[21]   P. Langan, Y. Nishiyama, H. Chanzy, *Cellulose* **2001**, *2*, 410.

[22]   P. Langan, Y. Nishiyama, H. Chanzy, *J. Am. Chem. Soc.* **1999**, *121*, 9940.

[23]   P. Langan, N. Sukumar, Y. Nishiyama, H. Chanzy, *Cellulose* **2005**, *12*, 551.

[24]   M. Wada, H. Chanzy, Y. Nishiyama, P. Langan, *Macromolecules* **2004**, *37*, 8548.

[25]   A. Isogai, M. Usuda, T. Kato, T. Uryu, R. H. Atalla, *Macromolecules* **1989**, *22*, 3168.

[26]   T. Ganner, T. Aschl, M. Eibinger, P. Bubner, A. Meingast, B. Chernev, C. Mayrhofer, B. Nidetzky, H. Plank, *Cellulose* **2014**, *21*, 3927.

[27]   P. Bansal, B. J. Vowell, M. Hall, M. J. Realff, J. H. Lee, A. S. Bommarius, *Bioresour. Technol.* **2012**, *107*, 243.

[28]   M. Eibinger, T. Ganner, P. Bubner, S. Rošker, D. Kracher, D. Haltrich, R. Ludwig, H. Plank, B.

Nidetzky, *J. Biol. Chem.* **2014**, *289*, 35929.

[29]   S. Park, J. Baker, M. Himmel, P. Parilla, D. Johnson, *Biotechnol. Biofuels* **2010**, *3*, 10.

[30]   B. E. Warren, *X-Ray Diffraction*, Addison-Wesley Pub. Co., **1990**.

[31]   C. F. Macrae, I. J. Bruno, J. A. Chisholm, P. R. Edgington, P. McCabe, E. Pidcock, L. Rodriguez-Monge, R. Taylor, J. van de Streek, P. A. Wood, *J. Appl. Cryst.* **2008**, *41*, 466.

[32]   W. Ruland, *Acta Crystallogr.* **1961**, *14*, 1180.

[33]   K. Schenzel, S. Fischer, E. Brendler, *Cellulose* **2005**, *12*, 223.

[34]   R. Pelton, *TrAC - Trends Anal. Chem.* **2009**, *28*, 925.

[35]   M. Kavruk, V. C. Özalp, H. A. Öktem, *J. Anal. Methods Chem.* **2013**, *2013*, DOI 10.1155/2013/932946.

[36]   J. Vitz, T. Erdmenger, C. Haensch, U. S. Schubert, *Green Chem.* **2009**, *11*, 417.

[37]   P. Mäki-Arvela, I. Anugwom, P. Virtanen, R. Sjöholm, J. P. Mikkola, *Ind. Crops Prod.* **2010**, *32*, 175.

[38]   T. Mohan, R. Kargl, A. Doliška, A. Vesel, S. Köstler, V. Ribitsch, K. Stana-Kleinschek, *J. Colloid Interface Sci.* **2011**, *358*, 604.

[39]   T. Mohan, R. Kargl, A. Doliška, H. M. A. Ehmann, V. Ribitsch, K. Stana-Kleinschek, *Carbohydr. Polym.* **2013**, *93*, 191.

[40]   R. Kargl, T. Mohan, S. Köstler, S. Spirk, A. Doliška, K. Stana-Kleinschek, V. Ribitsch, *Adv. Funct. Mater.* **2013**, *23*, 308.

[41]   E. Kontturi, P. C. Thüne, J. W. Niemantsverdriet, *Polymer (Guildf).* **2003**, *44*, 3621.

[42]   E. Kontturi, et al., *Biomacromolecules* **2011**, *12*, 770.

[43]   S. Köhler, T. Liebert, T. Heinze, *J. Polym. Sci. Part A Polym. Chem.* **2008**, *46*, 4070.

[44]   F. F. Rossetti, P. Panagiotou, F. Rehfeldt, E. Schneck, M. Dommach, S. S. Funari, A. Timmann, P. Müller-Buschbaum, M. Tanaka, *Biointerphases* **2008**, *3*, 117.

[45]   T. Mohan, S. Spirk, R. Kargl, A. Doliška, H. M. A. Ehmann, S. Köstler, V. Ribitsch, K. Stana-Kleinschek, *Colloids Surfaces A Physicochem. Eng. Asp.* **2012**, *400*, 67.

[46]   D. A. Long, *The Raman Effect: A Unified Treatment of the Theory of Raman Scattering by Molecules*, **2002**.

[47]   H. Wiley, R. H. Atalla, *Carbohydr. Res.* **1987**, *160*, 113.

[48]   S. K. Mahadeva, J. Nayak, J. Kim, *Smart Mater. Struct.* **2013**, *22*, 075011.

[49]   T. Zhang, W. Wang, D. Zhang, X. Zhang, M. Yurong, Y. Zhou, L. Qi, *Adv. Funct. Mater.* **2010**, *20*, 1152.

[50]   M. Peresin, Y. Habibi, J. Zoppe, J. Pawlak, O. Rojas, *Biomacromolecules* **2010**, *11*, 674.

[51]   I. Siró, D. Plackett, *Cellulose* **2010**, *17*, 459.

[52]   S. J. Eichhorn, A. Dufresne, M. Aranguren, N. E. Marcovich, J. R. Capadona, S. J. Rowan, C. Weder, W. Thielemans, M. Roman, S. Renneckar, W. Gindl, S. Veigel, J. Keckes, H. Yano, K. Abe, M. Nogi, A. N. Nakagaito, A. Mangalam, J. Simonsen, A. S. Benight, A. Bismarck, L. A. Berglund, T. Peijs, *Review: Current International Research into Cellulose Nanofibres and*

Nanocomposites, **2010**.

[53]   M. a. Hubbe, O. J. Rojas, L. a. Lucia, M. Sain, *BioResources* **2008**, *3*, 929.

[54]   F. Jiang, Y. Lo Hsieh, *Carbohydr. Polym.* **2013**, *95*, 32.

Chapter III **Cellulases – Biocatalytic Hydrolysis of Cellulose to Glucose**
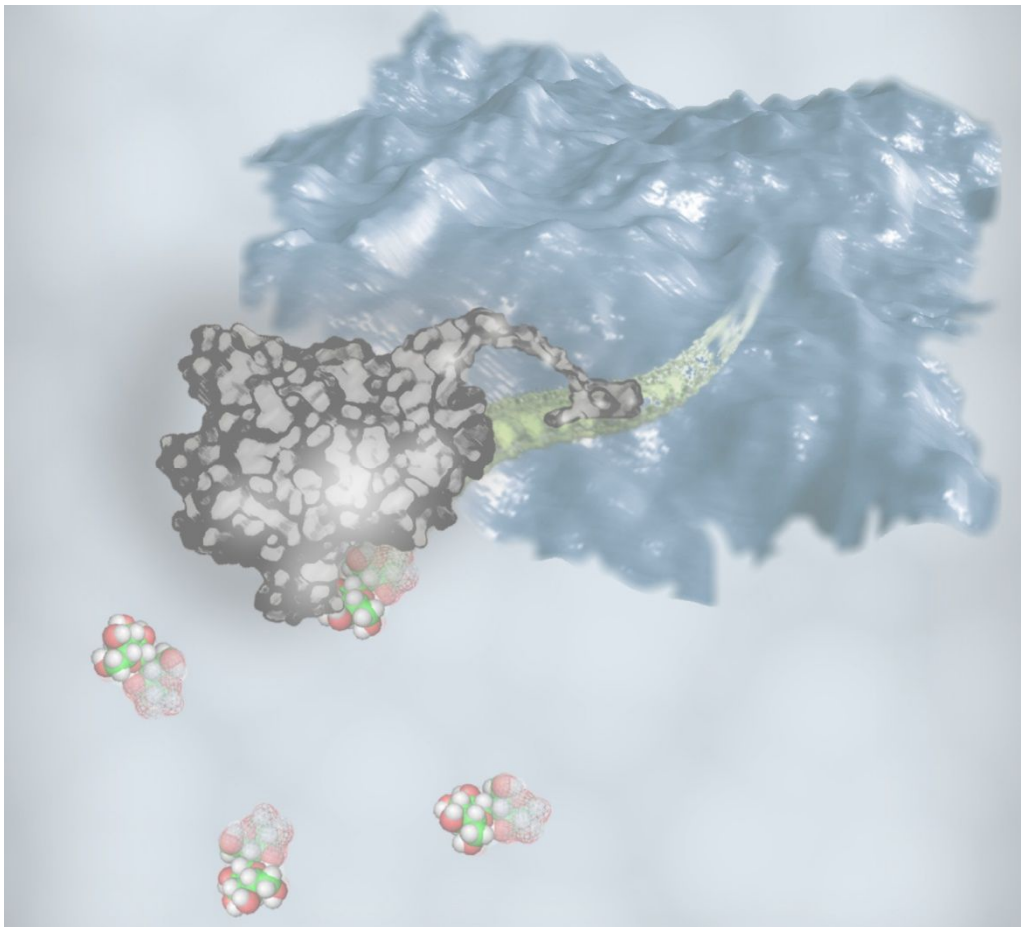
III.1 Introduction

Biochemistry is the science of chemical reactions, which are required for "life". Although we observe a vast diversity of life-forms and organisms, the majority of these reactions and contributing macromolecules share several similar features. One class of macromolecule is used by all organisms and is denoted as enzyme. These large macromolecules are bio-catalytic units which are constructed out of 20 different building blocks called amino-acids[1]. Here, all organisms share the same pool of available amino-acids, be it algae, bacteria or mammals. In this thesis, the focus will lie on a specific class of enzymes called cellulases. Cellulases are enzymes produced by various microorganisms to utilize cellulose as an energy resource. This is achieved by the decomposition of cellulose, which yields glucose as the basic construction element of the polymer. Organisms thereby are able to utilize cellulosic materials as food or energy resource (e.g. tree fungus). Since the discovery of cellulose degrading enzymes by the US Army during World War Two decades have past[2] and although the idea of using these mechanisms for energy production in technical scale processes were shortly developed thereafter, we still have no complete picture of the complex underlying processes. The reasons for this are manifold and lie certainly in the complex structure of cellulose and the complex interdependencies of multi cellulases cocktails but also in the inability to "see" these cellulases at work. At least from the point of resolution, this is not problematic, as we are able to see smaller scale objects fairly easily by applying electron microscopy. However, a high vacuum is definitely nothing what enzymes would enjoy and thus renders analysis to sequential or rather end-point specific experiments. Clearly, other methods allow visualizing living enzymes by, e.g., fluorescence microscopy but not with comparable resolution[3]. In recent years, Atomic Force Microscopy (**AFM**) has proven to be a versatile tool to investigate these processes *in-situ*. In this thesis, we have used the technique of *in-situ* liquid AFM to investigate complex interdependencies between cellulases and substrates. This requires a fundamental understanding of enzymatic reactions and its implications on cellulose. Previous *chapters* have dealt with a basic introduction to AFM, cellulose as a substrate and will be completed by the basic introduction to cellulases shown here. The huge variety of cellulases does not allow a complete discussion in the frame of a PhD thesis. However, the reader may refer to reviews of Payne and coworkers, Bornscheuer and coworkers or Lynd and coworkers[4–6]. In particular, cellulases applied in the framework of this thesis will be described in detail. At first, fungal cellulases will be described, followed by so called non-hydrolytic Lytic Polysaccharide Monooxignases (**LPMOs**) which have recently been discovered. At the end of this *chapter* Cellulosomes, a special class of bound multi-enzyme "machineries", will be described. All these systems will again appear in *chapter V* in the AFM investigations. Further information may be found in reviews of Bayer and coworkers, Hyeon and coworkers or Beeson and coworkers[7–9]. To begin with, we have to get a basic understanding what enzymes are and what the term bio-catalytic unit means. Enzymes – General Remarks

III.1.1 Basic Functionality – Thermodynamic Considerations

In chemistry, catalysis of reactions is one of the most important tools for selective and specific production of various substances. In biological systems, the same is true, and realized by bio-catalytic units denoted as enzymes. Enzymes are characterized through high efficiency and high selectivity to produce a product P from a substrate S. The latter is based on the so called "lock and key" model as

shown in Figure III-1 where the substrate (key) is specific for the respective enzyme (lock). This specificity for a substrate (substrate A, Figure III-1) is often pronounced in such a way that small changes to A (substrate B, Figure III-1) render the latter as inappropriate for catalytic cleavage as seen in Figure III-1. This is the former introduced selectivity and makes enzymes highly specialized tools to facilitate specific chemical reactions.
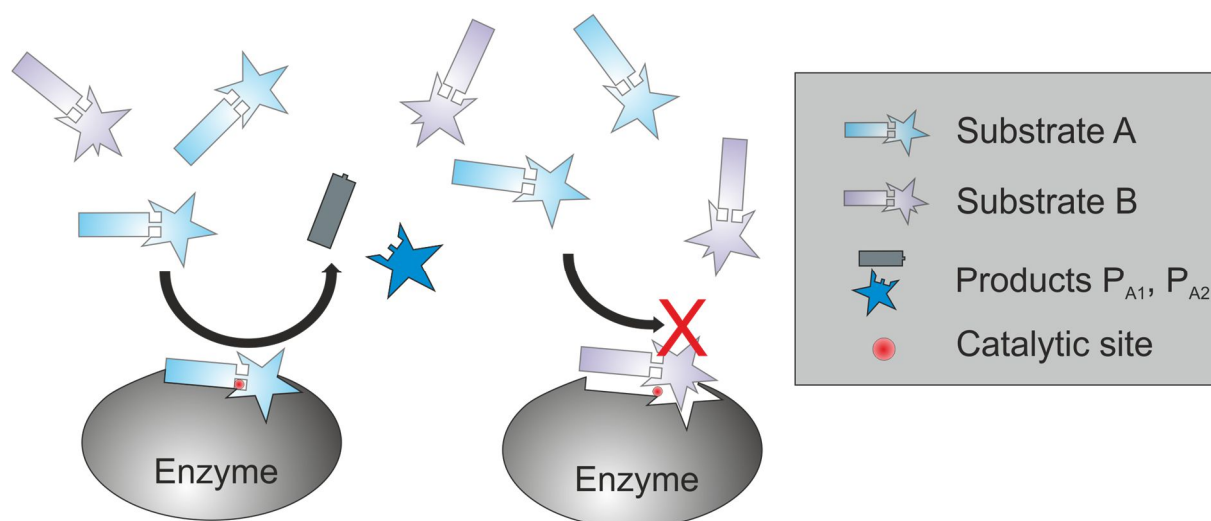

Figure III-1: The key lock model. Although substrate A and B are almost identical (look at the head), the enzyme only catalyzes substrate A to products P_{A1} and P_{A2}.

In their function as biocatalysts, enzymes are not different to other conventional, e.g., metal based catalysts. Both will accelerate reactions but will not change the reaction equilibrium. This is a pivotal aspect of any kind of catalysis. Thereby, concepts known from conventional catalysts apply to enzymes as well. In particular the catalytic effect is notably caused by a change in activation energy which is required to start the chemical reaction. However, there may be differences for enzymes against other conventional, e.g., metal catalysts. Structural conformation of the enzyme plays a decisive role in catalysis by, e.g., producing a favorable reaction environment insight the enzyme's body (e.g., hydrophobicity). Another difference may be found in the often found co-enzymes or co-factors which may be required to start the reaction. All in all, enzymes offer a wider bandwidth of possible reactions against normal catalysts. This is the reason, for the increasing interest in enzymology in technical applications.

Now, the reduction in activation energy is the key principle behind catalysis and a good example for this is the degradation of wood: While cellulose, if degraded without microbial, mechanical or chemical treatment, would at least require several million years[10] to depolymerize, enzymatic activity allows the de-polymerization of large amounts of cellulose within hours or days depending on their size and structural arrangement (smaller cellulose particles due to surface effects will degrade faster). The degradation product glucose is then used by the respective organism as energy resource. A common understanding of the effects behind can only be found by thermodynamic considerations.

To start with, we have to consider the free enthalpy. The difference in free energy ΔG is defined through the free energy of the substrate G_S and the products G_P. Please note that this is a universal relationship in chemistry and not limited to enzymes. While it determines if a reaction is, e.g., spontaneous ($\Delta G < 0$), it has no implication on the reaction speed. If we take a reaction as in (3.1) we get the following for the free enthalpy.

$$A + B \rightleftharpoons C + D \tag{3.1}$$

$$\Delta G = \Delta G_0 + RTln\left(\frac{[C][D]}{[A][B]}\right) \tag{3.2}$$

With ΔG_0 as the free standard-enthalpy, R the gas constant, T the temperature and $[X]$ the concentration of product/substrate X in mol L^{-1} or the corresponding activity. By that, the following definition is valid: ΔG is the **sum of ΔG_0** which refers to the enthalpy at standard values (T = 273.15 K, 101325 Pa) **and a logarithmic dependence on the actual concentrations**. In biochemistry, standard conditions imply a pH of 7.0 which turns ΔG_0 in $\Delta G_0'$. ΔG is zero in equilibrium and we get with a standard equilibrium constant $K' = [C][D]/([A][B])$ equation (3.3).

$$\Delta G_0' = -RTln(K') \tag{3.3}$$

Please note that the reaction form (exergonic ($\Delta G < 0$) or endergonic ($\Delta G > 0$)) is determined through ΔG. In contrast, $\Delta G_0'$ is a value related to the reaction partners and not the reaction. In other words ΔG may be endergonic (requires energy) or exergonic (spontaneous reaction) in the dependence of the concentrations while $\Delta G_0'$ stays constant. This principle holds in general and is not bound to enzymatic reactions. Equation (3.2) shows the direction of the equation, however, holds no information on the reaction velocity. Here considering of the activation energy is of help. The activation energy is the energy which is needed to bring the substrate molecule S in an activated state S^+ (that is a state where the reaction with, e.g., a specific other molecule is possible). The activation state is not part of equation (3.2) as the terms would cancel out due to the fact that the energy required for S^+ is immediately released upon transformation to P. In section III.2.2, this concept or consideration will be again needed. Now, to understand equation (3.2) and the here introduced thermodynamic considerations, one may draw the energy diagram as schematically depicted in Figure III-2.
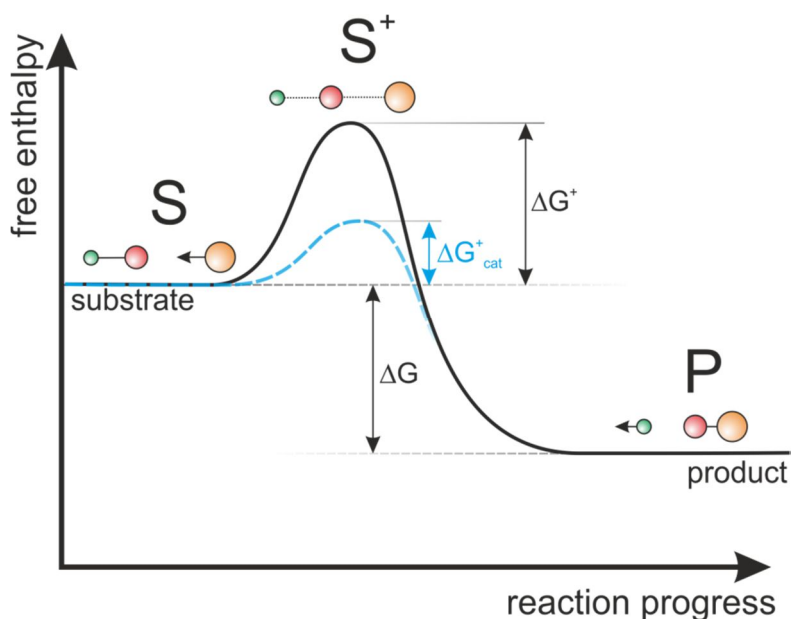
Figure III-2: Diagram of the free enthalpies during the reaction progress. Molecules with reaction partners (green, red and orange) are shown. The activated state is an intermediate and extremely short time state and quickly processes to the final product. If a catalyst like an enzyme is used the activation energy is reduced leading to less need of activation energy and thus faster reaction rates. The mathematical description of this will be shown in the following.

This – so far general description – holds for catalysts of any type and thus also for enzymes. It has to be emphasized that enzymes, despite their biological origin, show the same properties as other catalysts and their main properties are as follows: *1)* **Enzymatic activity will not change the thermodynamic equilibrium**. *2)* Enzymatic activity has **its only purpose in reducing the activation** energy and **thus the time needed to reach equilibrium**. So far, we have shown the first part by Figure III-2. If we want to understand the second part, we have to consider the activation state. For the velocities we may assume that S to S^+ is the limiting part and that S^+ to P is almost instantaneous (see equation (3.4)).

$$S \rightleftharpoons^{K^+} S^+ \longrightarrow^k P \tag{3.4}$$

If we further assume that the reaction from S to S^+ is in thermal equilibrium with the equilibrium constant K^+ we get from equation (3.2).

$$\Delta G_0^+ = -RTln(K^+) = -RTln\left(\frac{[S^+]}{[S]}\right) \tag{3.5}$$

Now, if we assume that the reaction velocity from S^+ to P is fast, which is feasible in most cases, we produce P in dependence on $[S^+]$ and thus may write:

$$V(S^+ \rightarrow P) \propto [S^+] \ or \ V = k[S^+] = k[S]e^{-\frac{\Delta G_0^+}{RT}} \tag{3.6}$$

The last term in equation (3.6) was obtained by using relation (3.5). A closer look on equation (3.6) now reveals the full nature of catalytic activity. A reduction in ΔG_0^+ immediately results in an increase of the reaction velocity. Thereby equilibrium of reaction (3.1) is reached in considerably shorter time while the **equilibrium is not changed**. In summary, the former introduced concept of enzymatic catalysis and increase in reaction velocity has now its theoretical basis. This concept is the same in enzymatic hydrolysis of cellulose. Here, cellulose de-polymerization is an exergonic reaction, which in principle will occur without any catalyst. However, without catalysis, the velocity to reach equilibrium (almost all cellulose is depolymerized) is achieved with almost immeasurable slow velocity (millions of years). This has its origin in the high energy barrier, which has to be surpassed to break the glycosidic bond. The enzyme now has its functionality in reducing this barrier by applying conformational changes and a different reaction environment, which leads to fast degradation (see Figure III-4). This is the reason why technological application of cellulases for cellulose utilization which, – as already described – is an almost inexhaustible material on earth, is so highly anticipated. The following section will deal with further and subtler description of enzyme kinetics. The change in concentration of reaction partners changes also ΔG and ΔG_0^+ (see equation (3.2) and (3.5)) which will lead to different reaction velocities in dependence of, e.g., the substrate concentration. It is noteworthy, that the following section is not absolutely essential for an empiric understanding of *chapter IV* and *V* but inherits further basic concepts of enzymatic activity. Special terms may appear in *chapter V* and are here briefly described.

III.1.2 Kinetics in Enzymatic Catalysis

Catalysis by enzymes is facilitated by their ability to form a complex with the substrate (ES-complex) which stabilizes the intermediate state S^+ and further reduces the activation free enthalpy. First hints for this complex were found by the asymptotic progression of the reaction velocity when the substrate concentration is increased at constant enzyme concentration (see Figure III-3). A simple explanation is a finite number of available active zones which contribute to the reaction by forming an ES-complex. The active zone is a 3-dimensional structure of amino-acid residues located inside a trench, tunnel or gap of the enzyme and usually is small compared to the whole structure (see Figure III-1). It is thought that the structure of the enzyme itself is used to bring the substrate in a favorable position for the later conversion. Another property is that the enzyme's body around the active zones creates a micro-environment to facilitating binding and reaction[1]. It is furthermore the release of binding energy which causes not only a stabilization of the intermediate ES-structure, but also provides the energy to reduce the activation energy. In the following terms in brackets (e.g. *[ES]*) represent concentrations.

The combination of respective properties of the ES-complex and Figure III-2 with corresponding equations (3.4)-(3.6) allows the following definition:

$$E + S \underset{k_{1-}}{\overset{k_{1+}}{\rightleftharpoons}} ES \underset{k_{2-}}{\overset{k_{2+}}{\rightleftharpoons}} E + P \tag{3.7}$$
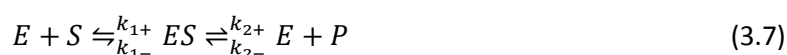
If we assume that a *[ES]* reaches quickly a steady state (George Briggs and John Haldane, 1925)[11] and that at *t*=0 k_{2-} can be neglected, we may write in analogy to (3.6) equation (3.8). This is feasible, because the binding of enzyme and substrate usually appears rather quickly and renders [ES] to stay constant (steady state). Furthermore $P_{(t=0)}$ equals to zero which immediately also determines k_{2-} to be zero.

$$V\big|_{t=0} = V_0 = k_{+2}[ES] \tag{3.8}$$

The steady state is characterized as the ES-complex in equilibrium with its environment (*P* and *S*) and we get[12]:

$$\frac{d[ES]}{dt} = 0 = V^{E+S \to ES} - V^{E+S \leftarrow ES \to E+P} = k_{1+}[E][S] - (k_{1-} + k_{2+})[ES] \tag{3.9}$$

In other words, the steady state is given in the case that complexation and de-complexation of *ES* are of the same rate (this is usually the case if *[S] >> [E]*). Furthermore, equation (3.9) includes the assumption $k_{2-} << k_{2+}$ which is also feasible considering Figure III-2. As we do not know *[E]* at *t=x* and neglect the change in *[S]* (*[S] >> [E]*) we may write for *[E][S] = ([E]_0-[ES])[S]* (*[E]_0* is the concentration of non-complexed enzymes at t = 0) and solve equation (3.9) for *[ES]*:

$$[ES] = \frac{k_{1+}[S][E]_0}{k_{1+}[S] + k_{1-} + k_{2+}} = \frac{[S][E]_0}{[S] + \dfrac{k_{1-} + k_{2+}}{k_{1+}}} = \frac{[S][E]_0}{[S] + K_M} \tag{3.10}$$

Now substituting equation (3.10) into equation (3.8) we get:

$$V_0 = \frac{k_{2+}[S][E]_0}{[S] + K_M} \tag{3.11}$$

If we now consider that V_{max} is reached when all substrate binding sites are saturated and thus *[ES] = [E]_0* we obtain:

$$V_{max} = k_{2+}[E]_0 \tag{3.12}$$

and

$$V_0 = V_{max} \frac{[S]}{[S] + K_M} \tag{3.13}$$

Equation (3.13) is the Michaelis-Menten equation with the Michaelis constant K_M and corresponds to kinetic behavior of the enzyme-substrate system. If *[S]* corresponds to K_M we get $V_0 = V_{max}/2$ and by evaluating V_{max} and K_M corresponding to Figure III-3, important characteristic of an enzyme are available.
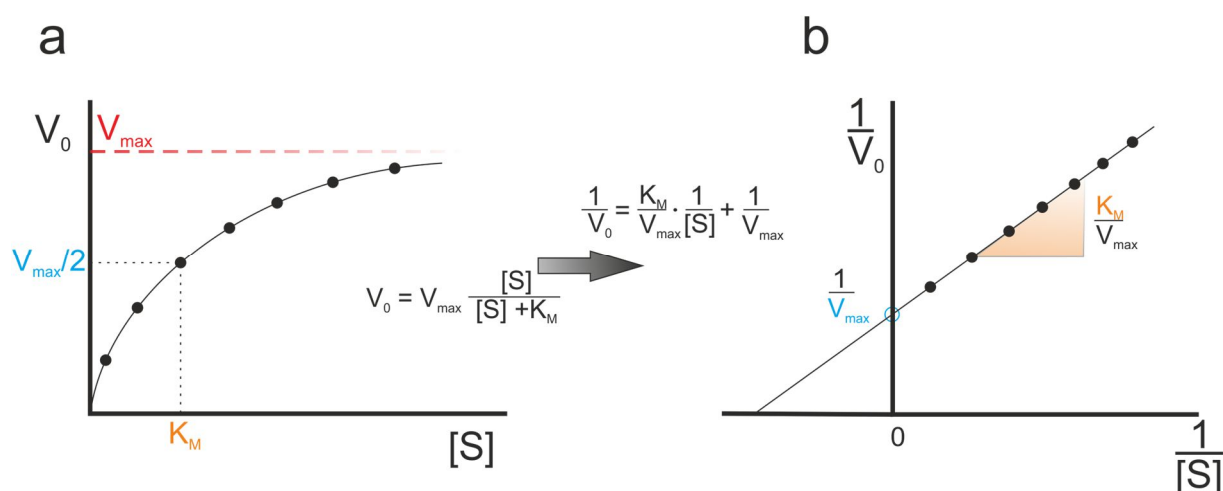

Figure III-3: Michaelis-Menten (a & b) kinetic of enzymatic catalysis and corresponding evaluation of important values V_{max} (blue) and K_M (orange) which may simply be found by inversion of equation (3.13) and following extrapolation.

If V_{max} and $[E]_0$ are known one can calculate k_+^2 as an important constant (equation (3.12)). It corresponds to the conversion of *S* into *P* at maximum binding of *S* to *E* and therefore denotes the catalytic efficiency of the enzyme which elucidates the conventional used term k_{cat}. Note, this term will appear in *chapter V*.

This brief introduction to enzymatic activity and kinetics is far from complete. Nevertheless, it shows the basic properties of enzymes. It shows that enzymes are effective and selective biocatalysts, which follow the rules of conventional catalysis. An introduction to enzyme kinetics led to the derivation of the Michaelis-Menten formalism revealing important properties as the maximum velocity V_{max}, the Michaelis constant K_M and k_{cat} as a factor of the catalytic efficiency. Now, in terms of AFM operation, these values may not seem to be important but are used in the later analysis of AFM data. Here, a cross correlation of degradation rate and observed visual effects with, e.g., k_{cat} is highly anticipated. Furthermore, additional terms like k_{on} and k_{off} which denote the adsorption and desorption of enzymes on a solid substrates may be easier to understand. These terms will appear at specific sections in *chapter IV* and *V* and are therefore necessary. A deeper introduction to enzymology may be found in the book of Stryrer, Tymoczko and Berg [1].

III.2 Cellulases – Cellulose Degrading Enzymes

III.2.1 Fungal Cellulases

Cellulose degrading enzymes are commonly found in various microorganisms, which utilize cellulose rich materials for their energy balance. The catalytic activity facilitates the degradation of cellulose to pure glucose, which then can be used for their living. Not surprisingly, imitation of this process is of technical relevance and already used to produce a second generation of biofuels. The enzymes or cellulases behind the degradation have been indirectly first discovered by the U.S. Army during World War Two due to their problems with the fast decomposition of cellulose rich materials (tents, clothing, sandbags etc.)[4]. Analysis in the U.S. Army Natick Laboratories identified the fungal organism *Trichoderma viride* (later classified as *Trichoderma reesei* in honor of Elwyn Reese and nowadays *Hypocrea jecorina*) as the cause of the problem. Up today, a huge variety of other organisms is known to produce cellulases[4,13]. However, *H. jecorina* is still the most important and studied model organism due to its capability to excrete extremely high amounts of the corresponding cellulase cocktail. This powerful enzyme cocktail of *H. jecorina* elucidates the still common interest in today's research. Strain QM6a (first discovered) of *H. jecorina* is known to produce at least 193 glycoside hydrolases (**GH**; cellulose hydrolyzing enzymes)[4]. The huge variety of such enzymes has led to the launch of the **C**arbohydrate-**A**ctive-en**Zy**mes (CAZy) database (http://www.CAZy.org) where cellulase and GH structures are collected and classified into families according to a scheme introduced by Henrissat and Davies[14]. Fungal cellulases are found in families 5-7, 12 and 45 and are denoted like *Hj*Cel7A (*H. jecorina* family 7 glycoside hydrolase).

In general, cellulases hydrolyze cellulose by two mechanisms: *1)* **Processive movement** along the chain which implements that the chain is somehow guided and fixed through the enzyme; *2)* **Cleavage in between,** which is only possible when the active center is directed outwards of the enzyme. Both forms are observed in nature[15–17] and classified as **exo-** and **endo-glucanases** with either **processive** or **random cleavage** of chains, respectively. In addition, most cellulases implement a so called carbohydrate binding module (**CBM**) which facilitates binding to the substrate. This is thought to be important due to the following: Stronger binding increases the **time which is available** for the enzyme for one catalysis step and it **facilitates 2-dimensional diffusion** causing higher efficiencies (no desorption – adsorption steps $k_{on} \gg k_{off}$). There is again a huge variety of CBMs and their exact role is still under discussion as the possibility of additional functionalities like crystal structure disruption might be relevant[4].

Although GH's appear in a huge variety in nature, the mechanisms to hydrolyze cellulose seem to be highly preserved. For the catalytic cleavage of cellulose, two mechanism have been suggested by Koshland in 1953[18] which are widely accepted today[4]. Both mechanisms are schematically shown in Figure III-4 with the chemical formalisms implemented.
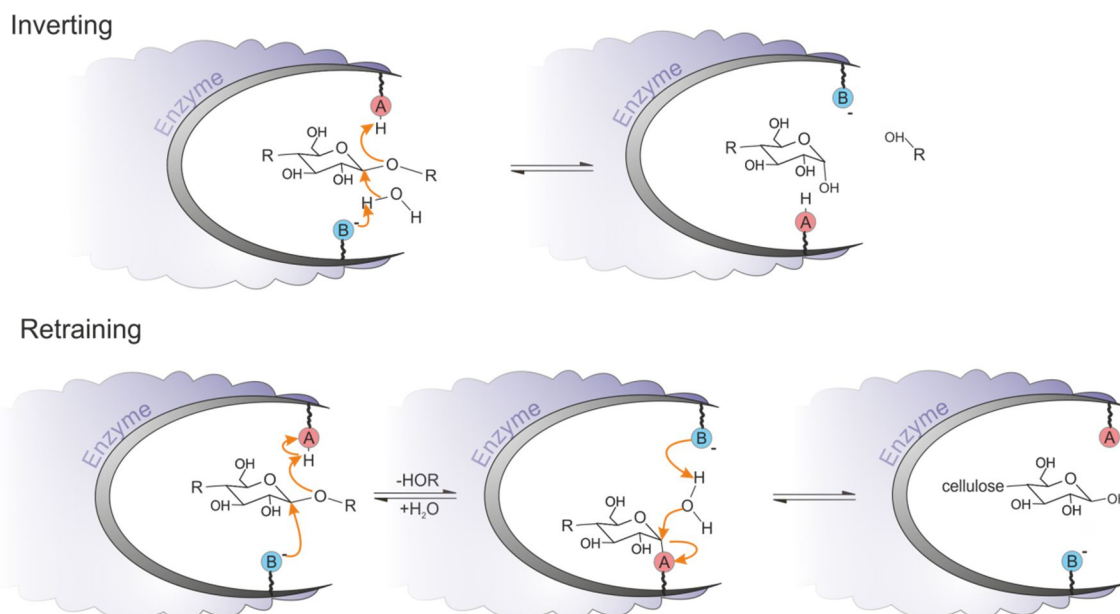
Figure III-4: Inverting and retraining mechanism of cellulose chain cleavage as suggested by Koshland[18]. Schematically depicted are the enzyme and the catalytic site (grey half-moon) with amino-acid residues featuring an acid or basic appearance, which corresponds to A and B, respectively. Catalysis happens on this acid and base residues of the enzyme (most of the time by aspartic acid (Asp) or glutamic acid (Glu)) featuring generally carboxyl groups. The inverting mechanism is achieved by electron and proton transfer and inversion of the chemical (acid or basic) state. The retraining mechanism achieves preliminary binding of the cellulose residual and changes conformation. The original state is restored by another water molecule as well as electron and proton transfer.

With a basic introduction on the role of the catalytic site, the catalyzing mechanism and the role of the CBM we can now proceed by considering the degradation mechanism itself, as it bears some interesting concepts, like synergism. It has to be emphasized that the corresponding formalism was developed for fungal cellulases originating from *H. jecorina*. However, it is feasible to assume similar behaviors for other cellulase cocktails. First of all, the 3-dimensional structure of the enzyme is relevant as it determines not only the maximum number of absorbable enzymes on one surface but also the influence of surface protrusions and obstacles generated by the enzymes. One of the first structural determinations were carried out by Abuja and coworkers[19] and showed that the shape of the exoglycanases *Hj*Cel7A (formerly CBH I) and *Hj*Cel6A (formerly CBH II) show a tadpole like shape with a larger catalytic domain, a linker region and the CBM module (see Figure III-5). They used Small Angle X-ray scattering (SAXS), a technique used to determine the structures of small molecules. Here, a highly monochromatic beam of X-rays is used and scattered off particles in a liquid phase. The pattern produced provides valuable information of the shape of the molecule. With theoretical models a structure can be fitted to the pattern which represents the rough molecule structure and shape.
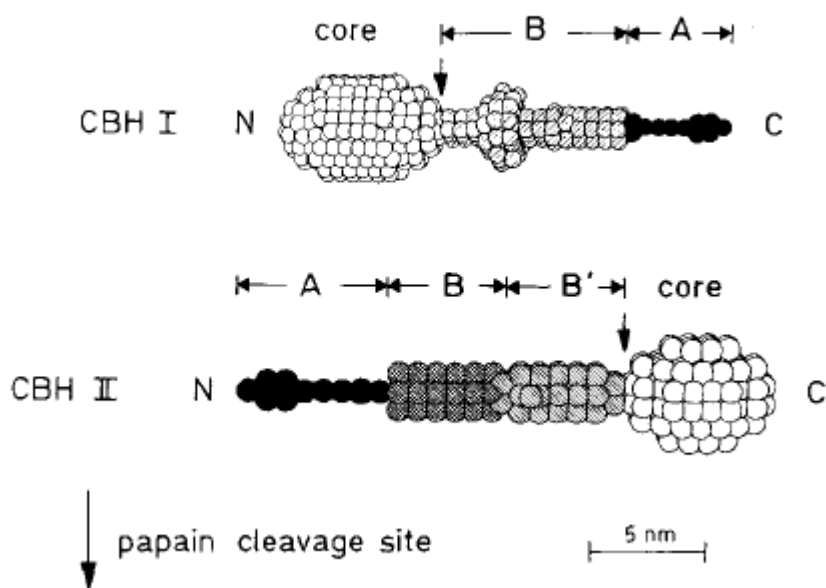
Figure III-5: 3-Dimensional model of exo-glucanases HjCel7A and HjCel6A revealed by SAXS. The core domain (with the catalytic center) is the largest part followed by the linker and the carbohydrate binding module (CBM, A). Additionally a papain cleavage site is indicated which was used to separate the catalytic domain and CBM to be evaluated by SAXS. Reprinted with kind permission of Elsevier[19].

Today, more accurate structures of both enzymes are known and available via the CAZy website (www.CAZy.org). For exo-glucanases (CBHs), most structures show a tunnel implemented in the catalytic domain (core). This is expectable, if we concern the processive movement of the enzyme. In Figure III-6 a molecular dynamic simulation shows the current structure of *Hj*Cel7A and its corresponding sliding mechanism[20]. For endoglucanases the mechanism is quite different, as no tunnel is present. Here, random cleavage of chains takes place, which has significant implications, as it bears the potential to produce more chain ends. This is the first and easy understandable concept of synergism. This cooperative activity is referred to as so called **synergism** meaning the cooperative activity when multi-enzyme complexes are used for degradation. It states that the activity of the multi-enzyme-system is far more effective than the sum of the individual activities. **Thus, synergism is a pivotal aspect of cellulose degradation and it is thought that it is required for an efficient degradation**[21]. Therefore, a comprehensive understanding of the process is absolutely essential which might help to improve the technical applications of such multi-enzyme systems. In this thesis, the current paradigm of the multi-enzyme degradation of cellulose by cellulases of *Hypocrea jecorina* will be demonstrated (Figure III-7).
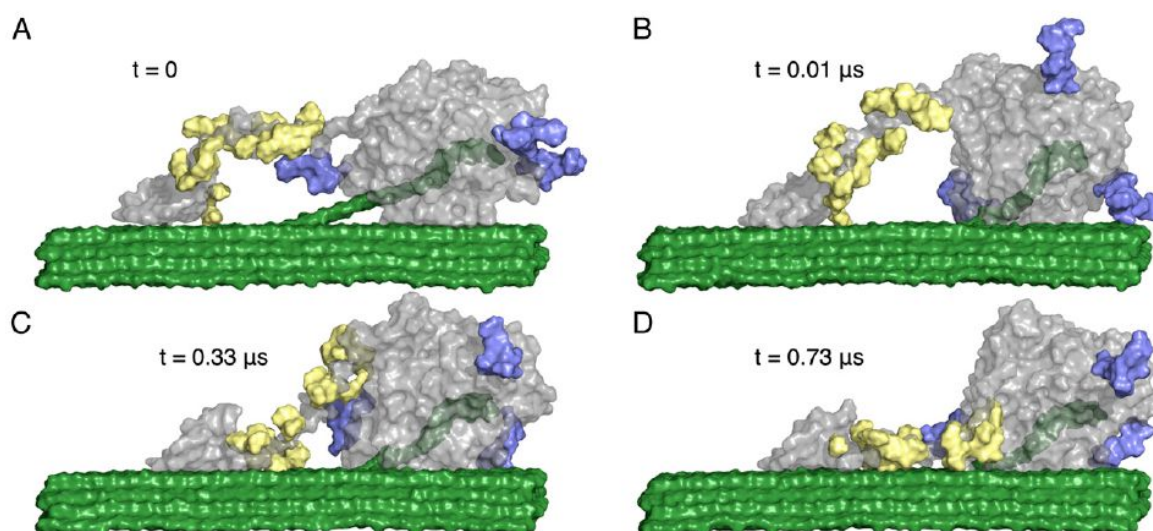
Figure III-6: Processive movement of HjCel7A on crystalline cellulose (green) simulated by molecular dynamics simulations. The chain is loaded in the internal core tunnel to immobilize the core to the direction of the chain. Each catalysis step is performed by elongation and contraction steps. Reprinted with kind permission of PNAS[20].
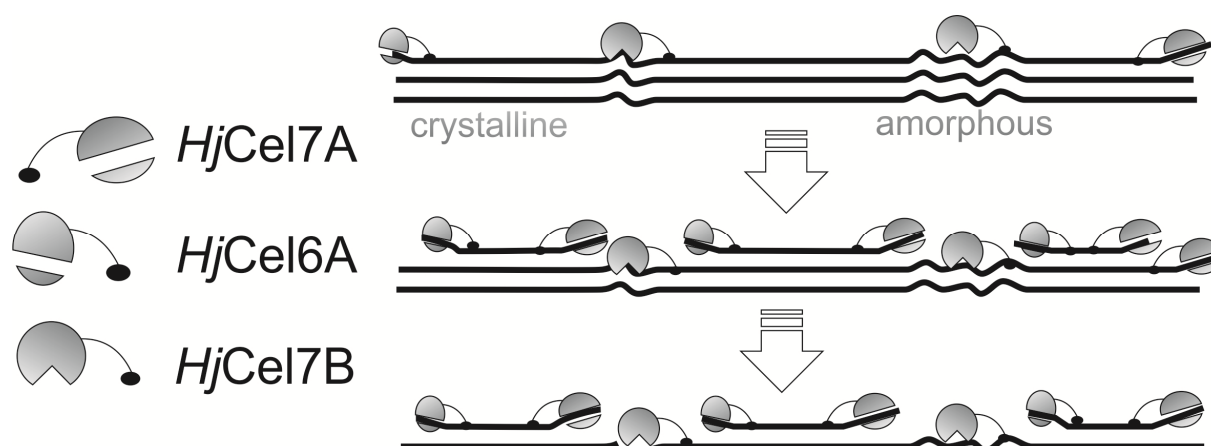

Figure III-7: Current paradigm of multi-enzyme degradation of a polymorphous substrate (amorphous/crystalline) by cellulases HjCel7A, HjCel7B and HjCel6A. Here endo-activity of HjCel6A yields more chain ends, which may be used for faster degradation by HjCel7A and HjCel6A. This in turn provides, after ablative activity a better accessibility of the underlying amorphous areas for HjCel7B.

Although current description models show good compliance with experimental observations, there are some controversies which still have to be solved. The above given model is a good description of so called endo-exo synergism where new chain ends and shorter chains lead to faster degradation. However, exo-exo synergism[21,22] is far from answered by this model. The problem is simple: A processive movement of *Hj*Cel7A and *Hj*Cel6A from each side of the crystallite must lead to collision events which rather should obstruct degradation than to boost it. While this is still under debate and multiple explanations have been proposed, a clear view is presumably only available by direct

visualization methods as demonstrated in this thesis. A review of these models in detail would be beyond the scope of this thesis and further information may be found in the reviews of Payne and coworkers and Bornscheuer and coworkers[4,5]. It is again clear that **direct visualization is an absolute essential part of any further and more comprehensive understanding** of the mechanisms behind synergistic degradation.

III.2.2 Lytic Polysaccharide Monooxygenase – a Non-Hydrolytic Cellulase

During the early years of the 1990s, a new class of enzymes was discovered with the potential to substantially contribute to enzymatic cellulose degradation[9]. These enzymes were first classified as family 61 endo-active GHs (GH61) due to their weak hydrolytic activity on crystalline cellulose[23]. However, soon thereafter first crystallographic data suggested a different form of action. Here, a highly conserved flat surface, a missing of the usual observed cleft or tunnel active site and a lack of conserved carboxy-methyl residues, which are required for catalysis led to a different sight. Furthermore, the combination with a metal binding site on the outpointing flat surface soon led to a dismissal of a hydrolytic active enzyme. DNA analysis also showed that GH61s are expressed in high amounts in various fungi emphasizing their importance for cellulose degradation. In 2010 Harries and coworkers[24] provided first biochemical evidence that the GH61 from *T. aurantacus* is synergistically active with endo- and exo-glucanases of *H. jecorina*. With this, the initiation of a high research effort was sealed and multiple studies were published over the last view years[9]. The mechanisms behind GH61 activity include metal-enzyme complexes with copper. The copper atom is bound at the exposed flat surface of the enzyme and catalyzes an oxidative reaction which further hydrolyses the glycosidic bond (see Figure III-8). Further evidence for this form of reaction was found by studies confirming that GH61 activity relies on electron donors required for oxidation[9]. Based on these findings the term lytic polysaccharide monooxidase (**LPMO**) was thought to be more appropriate than GH61. The structure and the exact chemical mechanisms behind the oxidation reaction by LPMO are still under debate. Although models anticipate C1, C4 and C6 oxidation, C1 and C4 are, so far, favored[9] (C_x: x denotes the Carbon atom position at the glucose ring). Further information on the chemical reaction may be found in the review of Beeson and coworkers[9]. Oxidation at the C1 and C4 of the glycoside ring are thought to cause disruption of the hydrogen-network of the cellulose crystallite, which in turn again facilitated degradation by exo- and endo-glucanases. A simple and refined schematic according to Figure III-7 is shown in Figure III-9.
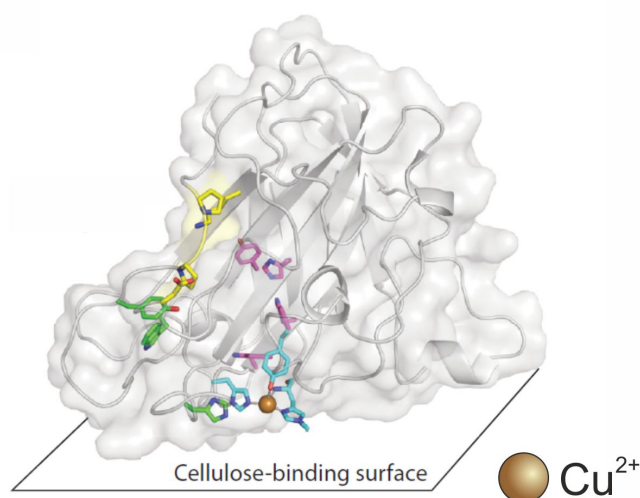
Figure III-8: LPMO from Neurospora crassa shown with the copper atom pointing at the cellulose binding surface. Adapted and reprinted with permission of Annual Reviews of Biochemistry[9].
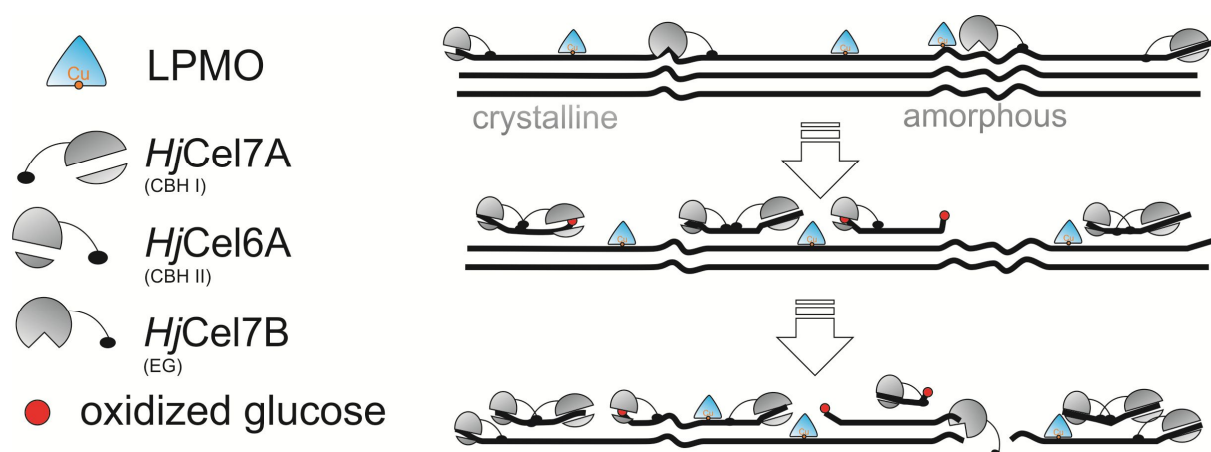

Figure III-9: LPMO catalyzed degradation in synergy with cellulases from H. jecorina (HjCel7A,6A and 7B)[9]. The oxidative cleavage opens again new chain ends for exo-glucanases.

Now, considering Figure III-9 and the depicted model, one can understand the preliminary classification of an endo-glucanase. LPMO shows from the point of the given model a similar activity as "classical" cellulose hydrolyzing endo-glucanases. However, the form of cleavage (oxidation) and the presumable disruption of the crystalline structure around the attack site differ significantly. Here, the oxidized intermediates are not stable and hydrolysis takes place after the oxidizing step without enzymatic activity. This may also account for **the overall efficiency on especially crystalline cellulose as disruption and accessibility of linear chains is here more pronounced**[25].

This brief introduction should provide an idea on the activity of LPMOs. However, it has to be emphasized that the complete understanding of enzymatic cellulose degradation by LPMOs is far from complete. Further information may be found in the review of Beeson and coworkers and Horn and coworkers[9,26]. The here given short introduction will be important for *chapter V* as a dedicated

experiment was conducted using this enzyme. The data introduced here should help the reader of this section to understand the sometimes complicated interdependencies between cellulases from H. jecorina and LPMOs. In the final section of this *chapter* the cellulosome, another interesting and complex multi-enzyme complex is described. This enzyme-complex was used also in this thesis and a concise and short introduction is important for the later understanding of respective sections in *chapter V*.

III.2.3 The Cellulosome – a Bacterial Multi-Enzyme Complex

It was in the early 1980s that Bayer, Lamed and colleagues[27,28] discovered a cellulose binding and degrading enzymatic complex in the bacteria *Clostridium thermocellum*. The identification as a molecular ordered complex of enzymes pointing at the deconstruction of cellulose, positioned at the outer wall of the bacterium, soon formed the term cellulosome. The complex is constructed by one long and flexible scaffolding protein with cohesin proteins attached. Cellulases with no CBM but dockerin proteins bind with cohesin proteins and form a multi-enzyme complex (see Figure III-10).
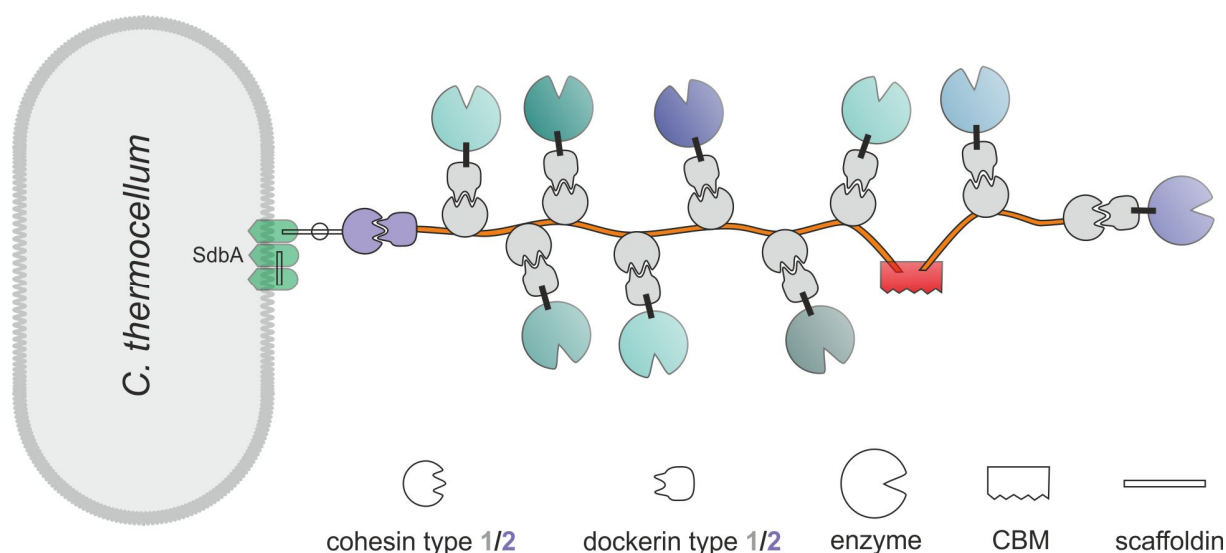

Figure III-10: Typical cellulosome complex of C. thermocellum with the scaffolding, cohesin and dockerin of type 1 and 2 and the enzymes which degrade cellulosic structures. The scaffolding is anchored to membrane proteins like SdbA. A CBM is used to bind the cellulosome to the substrate[29].

Initial investigations concluded that cellulosomes do not only comprise cellulases but also may contain hemicellulases and pectinases[29]. Therefore, the cellulosome may rather be seen as micro-machinery capable of degrading the full cell wall with its cellulose, pectin, lignin and hemicellulose components. The adaption to different substrates by varying the hydrolytic active contents of the cellulosome are presumable performed by the organism itself by varying the enzymatic species confined in one cellulosome. Here, we may shortly discuss the advantages of such an approach. Free cellulases are secreted to the extracellular space and there is no guarantee for the host cell that sugar produced is also available for its own benefit. Moreover, there is the possibility that the enzyme may get lost or stuck. Cellulosomes in turn are rather complex structures and losing them

might just be too costly for the host cell. So the cell anchors most of the cellulosomes to its own cell wall and thus eliminates the chance of loss and further also may free once stuck cellulosomes by mechanical strain. Additionally, produced glucoses have a greater change to be available for the host cell. Furthermore, confinement of different celluloses may increase the hydrolytic activity. While endo- and exo-glucanases are depending on lateral correlated activity (once new chain ends are opened, exo-glucanase must diffuse to this position by chance) the here confined structure presumably helps to speed up such reactions. The rate of degradation of cell wall polysaccharides is thought to be more efficient by that. However, the argumentation is still controversially with differences between different findings from different laboratories[30,31]. Nevertheless, the degradation of crystalline cellulose is, if compared to *H. jecorina* free cellulases, more efficient which explains the significant interest on the better understanding of this multi-enzyme machinery.

Here, we may point out once again, that the overall complexity of such cellulosomic systems is overwhelming and not within the scope of this thesis. However, the basic functionality is given with this short introduction and may again help the reader to understand concepts and analyses in *chapter V*. For further reading please refer to the comprehensive reviews of Fontes and coworkers, Bayer and coworkers or Demain and coworkers[7,29,31,32].

III.3 Chapter Summary

Mastering and understanding the mechanistic activity of cellulases is a challenging task and highly anticipated by science and industry for a save and clean utilization of cellulose waste products. An estimation by the US department of Energy stated that 1.3 billion tons of plant biomass are annually available for sustainable fuel production[33] in the U.S. which is in about 30% of the annual need. This shows the importance to proper master the technique for sustainable and environmental friendly production of transportation fuels. In this introduction *chapter,* basic properties of enzymes as well as a thermodynamic background was provided on fungal and bacterial cellulases. The huge variety of cellulases and their complex interdependence with cellulose and other substrates elucidate the need for deeper investigations, pointing at resolutions which until now where unreachable. AFM techniques are in combination with biochemical studies an invincible tool to unravel these complex interdependencies. To understand studies given in the following *chapter* it is important to have a basic understanding of current and well-studied models. For a more comprehensive introduction to individual cellulases, lytic polysaccharide monooxygenases and cellulosomes the reviews mentioned in this *chapter* are a good resource. At this point introductory *chapters* (*I-III*) are completed. In the following the results and AFM investigations (*chapter IV* & *V*) as well as substrate developments (*chapter IV*) will be shown.

III.4 References

[1]   J. M. Berg, J. L. Tymoczko, L. Stryer, *Stryer Biochemie*, **2007**.

[2]   M. K. Bhat, S. Bhat, *Biotechnol. Adv.* **1997**, *15*, 583.

[3]   P. Bubner, H. Plank, B. Nidetzky, *Biotechnol. Bioeng.* **2013**, *110*, 1529.

[4]   C. M. Payne, B. C. Knott, H. B. Mayes, H. Hansson, M. E. Himmel, M. Sandgren, J. Ståhlberg, G. T. Beckham, *Chem. Rev.* **2015**, *115*, 1308.

[5]   U. Bornscheuer, K. Buchholz, J. Seibel, *Angew. Chemie* **2014**, *126*, 11054.

[6]   L. R. Lynd, P. J. Weimer, W. H. van Zyl, I. S. Pretorius, *Microbiol. Mol. Biol. Rev.* **2002**, *66*, 506.

[7]   E. A. Bayer, J.-P. Belaich, Y. Shoham, R. Lamed, *Annu. Rev. Biochem.* **2004**, *58*, 521.

[8]   J. E. Hyeon, S. D. Jeon, S. O. Han, *Biotechnol. Adv.* **2013**, *31*, 936.

[9]   W. T. Beeson, V. V. Vu, E. a. Span, C. M. Phillips, M. a. Marletta, *Annu. Rev. Biochem.* **2014**, *84*, 150317182619002.

[10]   M. M. Askarieh, a. V. Chambers, F. B. D. Daniel, P. L. Fitzgerald, G. J. Holtom, N. J. Pilkington, J. H. Rees, *Waste Manag.* **2000**, *20*, 93.

[11]   G. E. Briggs, J. B. S. Haldane, *Biochem. J.* **1925**, 338.

[12]   C. Raymond, *Physical Chemistry for the Chemical and Biological Sciences*, University Science Books, Sausalito, CA 94965, **2000**.

[13]   U. Bornscheuer, K. Buchholz, J. Seibel, *Angew. Chem. Int. Ed. Engl.* **2014**, *53*, 10876.

[14]   B. Henrissat, G. Davies, *Curr. Opin. Struct. Biol.* **1997**, *7*, 637.

[15]   K. Igarashi, A. Koivula, M. Wada, S. Kimura, M. Penttilä, M. Samejima, *J. Biol. Chem.* **2009**, *284*, 36186.

[16]   K. Igarashi, T. Uchihashi, A. Koivula, M. Wada, S. Kimura, T. Okamoto, M. Penttilä, T. Ando, M. Samejima, *Science* **2011**, *333*, 1279.

[17]   A. G. Conjugates, R. A. Nieves, R. P. Ellis, R. J. Todd, J. A. Timothy, K. Grohmann, M. E. Himmel, *Appl. Environ. Microbiol.* **1991**, *57*, 3163.

[18]   D. Koshland, *Biol. Rev.* **1953**.

[19]   P. M. Abuja, I. Pilz, M. Claeyssens, P. Tomme, *Biochem. Biophys. Res. Commun.* **1988**, *156*, 180.

[20]   C. M. Payne, M. G. Resch, L. Chen, M. F. Crowley, M. E. Himmel, L. E. Taylor, M. Sandgren, J. Ståhlberg, I. Stals, Z. Tan, G. T. Beckham, *Proc. Natl. Acad. Sci. U. S. A.* **2013**, *110*, 14646.

[21]   B. Nidetzky, W. Steiner, M. Hayn, M. Claeyssens, *Biochem. J.* **1994**, *298*, 705.

[22]   P. Bubner, J. Dohr, H. Plank, C. Mayrhofer, B. Nidetzky, *J. Biol. Chem.* **2012**, *287*, 2759.

[23]   J. Karlsson, M. Saloheimo, M. Siika-Aho, M. Tenkanen, M. Penttilä, F. Tjerneld, *Eur. J. Biochem.* **2001**, *268*, 6498.

[24]   P. V Harris, D. Welner, K. C. McFarland, E. Re, J.-C. Navarro Poulsen, K. Brown, R. Salbo, H.

Ding, E. Vlasenko, S. Merino, F. Xu, J. Cherry, S. Larsen, L. Lo Leggio, *Biochemistry* **2010**, *49*, 3305.

[25]   M. Eibinger, T. Ganner, P. Bubner, S. Rošker, D. Kracher, D. Haltrich, R. Ludwig, H. Plank, B. Nidetzky, *J. Biol. Chem.* **2014**, *289*, 35929.

[26]   S. J. Horn, G. Vaaje-Kolstad, B. Westereng, V. G. Eijsink, *Biotechnol. Biofuels* **2012**, *5*, 45.

[27]   E. A. Bayer, R. Kenig, R. Lamed, **1983**, *156*, 818.

[28]   R. Lamed, E. Setter, R. Kenig, E. A. Bayer, in *Bio- Technol. Bioeng. Symp.*, **1982**, pp. 163–181.

[29]   C. M. G. A. Fontes, H. J. Gilbert, *Annu. Rev. Biochem.* **2010**, *79*, 655.

[30]   T. K. Ng, J. G. Zeikus, *Appl. Environ. Microbiol.* **1981**, *42*, 231.

[31]   A. L. Demain, M. Newcomb, J. H. D. Wu, A. L. Demain, M. Newcomb, J. H. D. Wu, **2005**, *69*, 124.

[32]   E. A. Bayer, L. J. Shimon, Y. Shoham, R. Lamed, *J. Struct. Biol.* **1998**, *124*, 221.

[33]   R. D. Perlack, B. J. Stokes, *U.S. Billion-Ton Update - Biomass Supply for a Bioenergy and Bioproducts Industry*, Oak Ridge National Laboratory, Oak Ridge, **2011**.

Chapter IV **Cellulose Model Substrates for Liquid Atomic Force Microscopy**
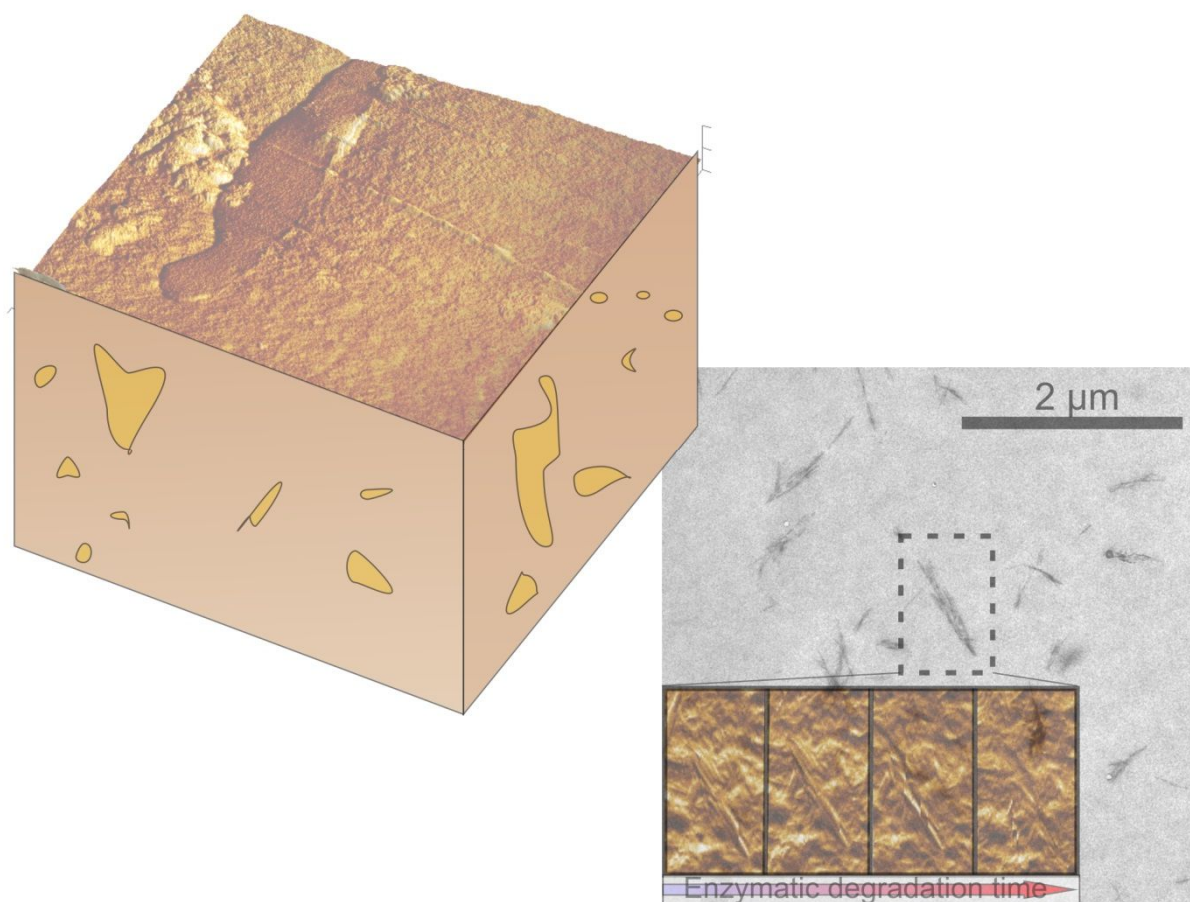
IV.1 Introduction

Considering *chapter I* and *II* it is clear that *in-situ* analysis of enzymatic cellulose degradation provides two main requirements to the substrate in order to allow successful investigation: **A defined cellulose material regarding their chemistry, structure and spatial phase distribution** (crystalline / amorphous) which furthermore reveal a **flat surface topology.** While the former is essential concerning the enzymatic activities (*chapter III*), the latter is decisive to allow high-speed, high-resolution AFM (*chapter I*). Fulfillment of both allows a comprehensive insight on fundamental biochemical mechanisms during enzymatic decomposition of cellulose. Therefore, a central part of this study was the development of such materials and related substrates via different approaches. Based on the introduction in *chapter II*, it is clear that substrates stemming from natural resources cause two main problems: *1)* **purity, tunable polymorphism, and reproducibility** are extremely **hard to establish** by natural cellulose from, e.g., plants, as growing conditions vary within one plant due to environmental effects; and *2)* the **flat topology is usually not readily available** which requires elaborate preparation and typically is very complicated. Thus, we have introduced two novel concepts each having distinct features allowing a more comprehensive and deep insight into enzymatic cellulose degradation. Both concepts are based on a bottom-up fabrication of celluloses with a considerable polymorphism. Please remember, this is important as natural celluloses usually feature both, amorphous and crystalline structures within one sample. To emulate this situation while being in "control" over the composition, we allow a reproducible route of substrate preparation. Here crystalline and amorphous materials are achieved by either dissolution in an appropriate solvent (see *chapter II*; BMIMCl) or by combination of cellulose precursors (see *chapter II*, TMSC) and nano-crystalline cellulose. While both feature similar polymorphism or crystallinity, there are significant differences. The first concept uses Avicel cellulose and a solvent to produce cellulose with a varying content of crystallinity. This may be achieved by oversaturating the solution. This leads to a cellulose substrate with crystalline and amorphous phases in one substrate. The second concept is based on the cellulose derivate TMSC, which may be easily dissolved in organic solvents and spin-coated on flat silicon specimens. A combination with nano-crystalline cellulose (see *chapter II*) allows again an adjustable polymorphism. However and most strikingly, we obtain flat samples for the second approach from the beginning while elaborate fabrication is needed for the first concept. Nevertheless, the first concept has its advantages by providing larger crystalline features (from nm to µm) while the second concept offers the true building entity of cellulose structures, the nano-crystal as shown in *chapter II*. So in summary, both concepts have advantages and disadvantages and may be **seen in this form complementary**. Larger structures which showed to have significant impact on degradability may be analyzed by **concept 1** and high resolution and speed imaging may be performed on the **fundamental crystals of concept 2**. In the following both concepts will be described in detail.

The first concept was published in CELLULOSE (Wiley)[1] whose content is part of section IV.2 . The second concept was re-submitted to ACS Applied Materials & Interfaces (American Chemical Society) after revisions and summarized in section IV.3 . Styling has been adapted to feature the thesis style (References, Image caption etc.). Author contributions will be described in detail before the text paragraphs. In the end of this *chapter* an extended summary will conclude the findings and give a short outlook. Both papers will, as a main part of this study, have an overlapping with enzymatic

degradation experiments. Therefore, it is recommended to read *chapters II* and *III* for complete understanding.

IV.2 Tunable Mixed Amorphous-Crystalline Cellulose Substrates (MACS) for Dynamic Degradation Studies by Atomic Force Microscopy in Liquid Environments[2]

IV.2.1 Publishing Information

Section IV.2 summarizes and expands the article *"Tunable mixed amorphous–crystalline cellulose substrates (MACS) for dynamic degradation studies by atomic force microscopy in liquid environments"* [2] in Cellulose (Wiley), submitted in June, 2014. The paper was published on August 2014 and the authors were Thomas Ganner*, Timothy Aschl*, Manuel Eibinger, Patricia Bubner, Arno Meingast, Boril Chernev, Claudia Mayrhofer, Bernd Nidetzky and Harald Plank†. Concept and idea for the manuscript was from TG and HP. TG and TA conducted the AFM experiments. TG and TA performed WAXS experiments and data analysis. TG, TA, ME and PB prepared the substrates. Embedding and ultramicrotomy was conducted by CM. TG made all figures and captions. AM performed TEM investigations and HP was responsible for TEM data analysis. BC performed Raman experiments while data was analyzed by TG. TG and HP wrote the paper including the revision. Briefly, the following sections give detailed description on substrate preparation and in-depth discussion concerning, structural and chemical analyses via AFM, Scanning Electron Microscopy (SEM), Transmission Electron Microscopy (TEM), Raman spectroscopy (RS) and microscopy and Wide Angle X-ray Scattering (WAXS). Please note, while the sections 2.2 – 2.4 are expanded compared to the manuscript, section 2.5 and 2.6 are reprinted from[2] with kind permission from Springer. **Reference style and figure captions are adapted to the style of this thesis. Note: Trichoderma reesei was exchanged to Hypocrea jecorina for consistency throughout the thesis.**

IV.2.2 Background

First reports of so called ionic salts which are capable to dissolve cellulose were given in 1934 by Graenacher[3,4]. The value of this discovery was not entirely recognized by the community, probably due to their relative high melting points of about 118°C[5]. Nevertheless, this discovery laid the foundation for today's applications using ionic salts (**IL**) as powerful systems to dissolve cellulose for various purposes. As already described in *chapter II*, the ionic liquid 1-butyl-3-methylimidazolium chloride (**BMIMCl**) was used to dissolve cellulose. This was followed by regeneration into the **mixed amorphous crystalline cellulose substrate** (**MACS**) discussed in detail in this section. The protocol includes the following steps: Dissolution of pure cellulose → fixation of the low viscous liquid between homogeneously separated glass plates → slow extraction of BMIMCl → thoroughly washing in ethanol solutions with varying concentrations → cutting and embedding in epoxy resin →

---

* Equally contributing authors.
† Corresponding author.

ultramicrotomy preparation and finally AFM investigations. For biochemical studies the last 2 steps are not required.

The concept of MACS therefore is the following: The **liquid state** allows bringing the cellulose solution with relative high viscosity in a **defined shape** (evenly thick, round sheets) which then can be subjected to a solvent exchange and further prepared in **epoxy embedded specimens** via ultramicrotomy. At last elaborate cutting procedures by Ultramicrotomy (UM) yield cellulose surfaces with RMS values below 10 nm over large areas[2]. Thus, the substrate is reproducible and appropriate for AFM investigations. Although preliminary experiments showed the presence of crystalline phases in MACS we can only speculate about their origin. There are two possibilities. Either, we see recrystallization processes in the material upon precipitation of BMIMCl or we have an oversaturation from the beginning. As both aspects may be related to some extent, we defined our experimental range roughly to data from literature[6]. Here, dissolution is achieved depending on the cellulose source, within a range of 1 to 20 wt.%. Our hypothesis was that the oversaturation yields both, larger crystallites and further also recrystallization. First experiments confirmed the validity of this hypothesis and MACS materials were used to study the synergistic activity of the cellulase system of *H. jeronica*[1]. The following section is the result of constant improvement of this approach and states an accurate **and** conceived analysis of the substrate MACS. This is important for the later application and interpretation of the substrate behavior in continuative experiments focusing on enzymatic cellulose degradation.

IV.2.3 Preparation of MACS

Preparation of MACS includes critical steps which are crucial for a successful preparation. Here a step by step instruction is given on MACS preparation to yield tunable crystallinity contents. Materials were always of highest available purity. Avicel PH-101® was used as pure cellulose source and BMIMICl was used as ionic salt. Both substances were purchased from Sigma-Aldrich (St. Louis, MO, USA).

IV.2.3.1 Dissolution of Cellulose

BMIMICl is a solid white powder at room temperature and has to be heated to a minimum Temperature of 100°C to allow mixing with cellulose. Note, higher temperatures are not recommended in order to prevent solvent induced de-polymerization of cellulose. It must be emphasized that the salt is extremely hydrophilic and exposure to ambient air should be as short as possible, as water will cause a reduction of cellulose miscibility[6,7]. This is especially important concerning the fact that the flask with BMIMICl is exposed multiple times and this will affect the future fabrication of cellulose materials. Usually one or two grams of BMIMICl were put into glass vials (4 ml, Rotilabo Ø 15 mm, Karlsruhe, Germany) and placed in a laboratory build heating container which was constructed to ensure a negligible heat gradient over the glass vials (see Figure IV-1).
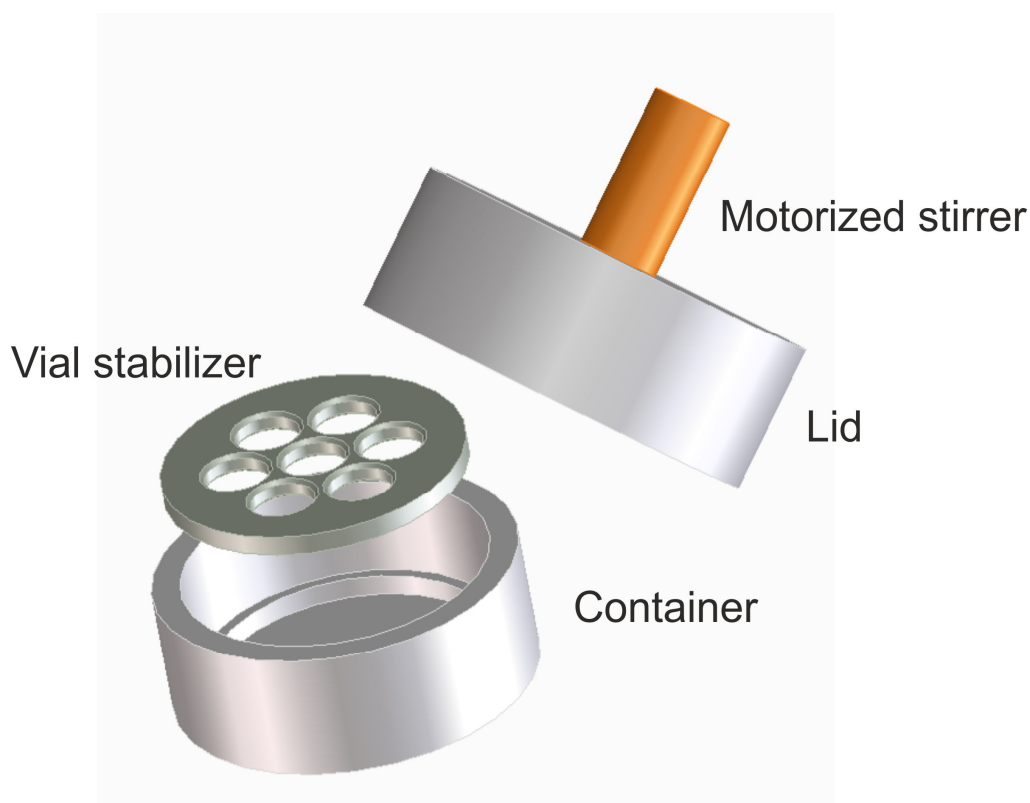
Figure IV-1: CAD drawing of the laboratory build heating container. A motorized stirrer is used to mix cellulose and BMIMICl over a certain period of time. The stirrer itself is produced out of glass as BMIMICl is highly corrosive for metal based stirrers.

The heating container shown in Figure IV-1 is first placed on a feedback controlled laboratory heating stage and temperature is set to 100°C. As soon as the temperature is reached and stabilized BMIMICl is filled into glass vials, placed in the center position, stabilized by the vial top plate and the motorized stirrer is lowered into the vial. BMIMICl is now mixed for about 15 minutes until all BMIMICl is melted. At this point it is necessary to emphasize that the motorized stirrer is absolutely necessary. Conventional stirring with magnetic stirrers is inappropriate as viscosity is significantly increased upon dissolution of cellulose. Therefore a laboratory build motorized stirrer with a glass stirrer was designed. The glass is needed as other materials, especially metals, are prone to corrosion which renders the resulting substrates to be contaminated with corrosion products. Subsequently to complete melting, the stirrer is removed from the fluid and the corresponding amount of Avicel is added (4 to 20 wt. %). Please note, that the next step is absolutely crucial: **Immediately after addition to the BMIMCl liquid** the solution and cellulose powder are mixed with a **carefully cleaned glass stick** to evenly distribute the cellulose. Failing this step results in a situation where larger rafts of cellulose stay on top of the fluid and once viscosity is increased are not dissolved in the liquid. This often results in useless films. A failure is visible after the transfer between evenly separated glass microscopy slides by visible precipitations of undissolved cellulose. The procedure is outlined schematically in Figure IV-2. The result of this process is seen in Figure IV-6 a.
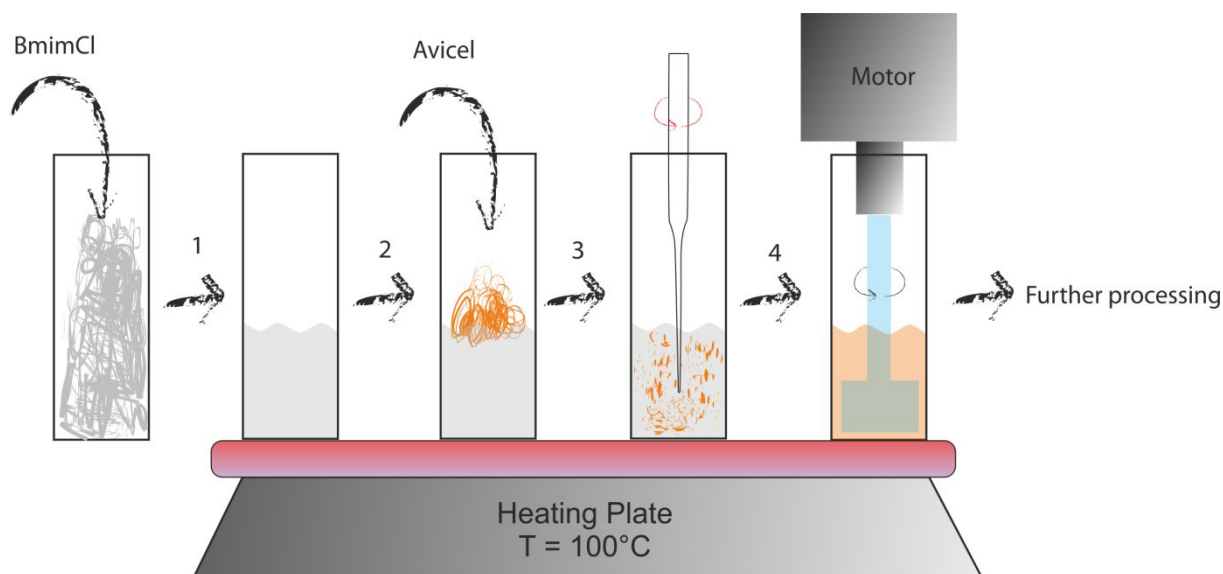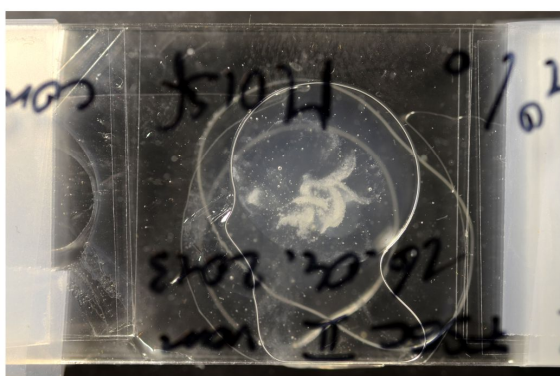
Figure IV-2: Schematic representation of solvation procedure of Avicel cellulose in BMIMICl.
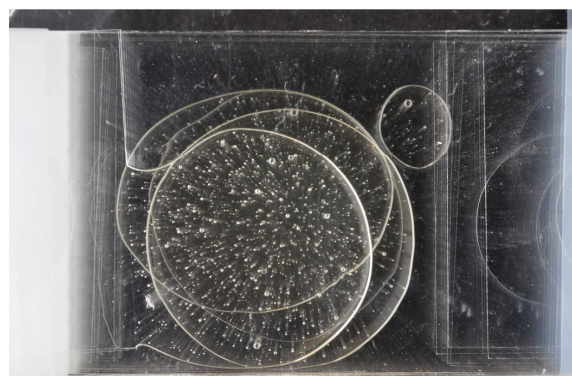

Figure IV-3: (a) Films between glass spacers shows white non-transparent impurities which result from incomplete dissolution of crystalline material. This appears when homogeneous distribution could not be established in the beginning of solvation (Step 3 → 4 in Figure IV-2). The resulting agglomeration forms capsules where no ionic liquid can enter and homogeneous dissolution is obstructed. (b) Appropriate films with no impurities, except gas bubbles, which are not problematic.

After 24 hours of mixing all crystalline parts are dissolved and a clear and viscous solution is obtained. Substrates used are denoted with **MACS-xx** whereas XX stands for the mass concentration (wt.%).

IV.2.3.2 Gelation of BMIMICl-Cellulose Solution

The next process step includes the transfer of small portions of the solution on microscopy glass slides which are used to bring the gels in a defined and reproducible shape. Here the following procedure is most accurate and yields the best results: Prior to the transfer, carefully cleaned

microscopy glass slides are prepared by placing two microscopy cover slips on one of the microscopy slides. These spacers are glued to the microscopy slides by hot-melt adhesive. In the following, the counter-slide is placed on a separate heating plate at 100°C and a small portion of the cellulose solution (approx. 200 µL) is placed on it. The microscopy slide with the spacers is then firmly pressed on the second slide, thus forming a round shaped gel lamella. A schematic representation is given in Figure IV-4. After finishing this step, slides are immediately placed in petri dishes and sealed with parafilm. The gelation starts upon cooling from the liquid by slow precipitation of BMIMICl due to uptake of the anti-solvent water. This is a result of the high hydrophilic nature of the IL[4]. Tests with entirely water free environment (desiccator with silica beads) proved this hypothesis. The gelation is performed over the period of one week. Thereafter gels are soft flexible lamellas with adsorbed water BMIMCl mixture.
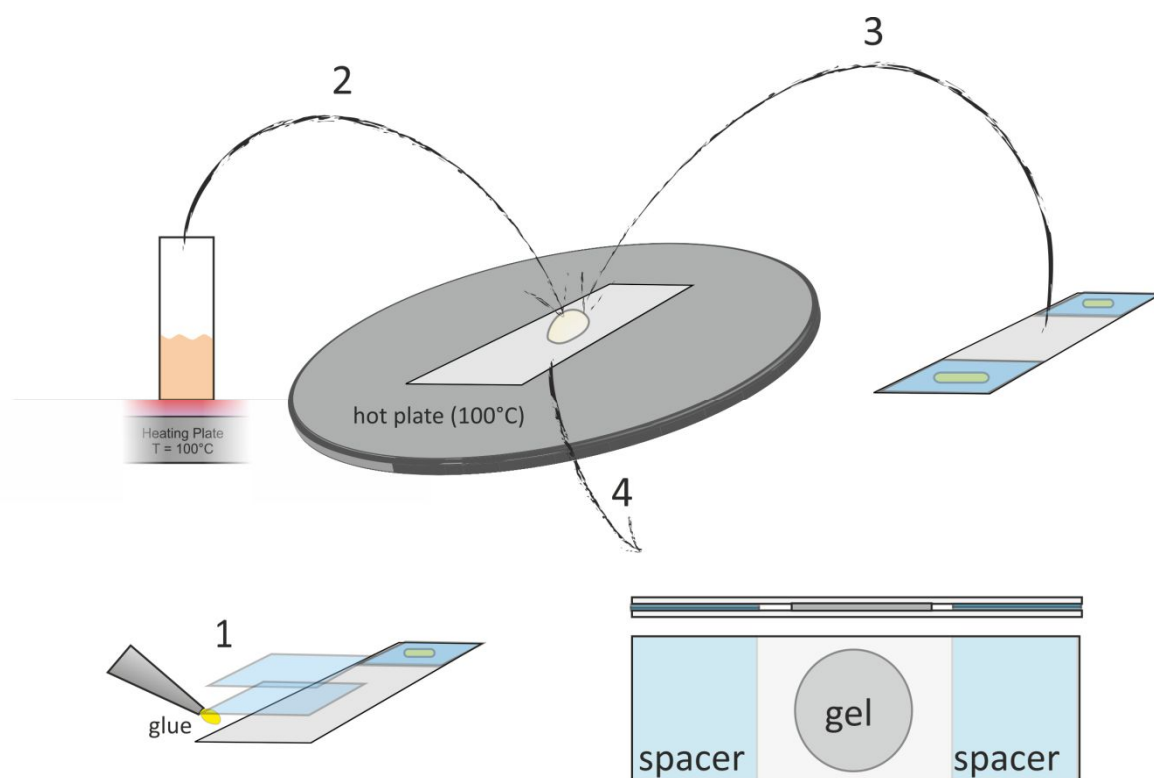

Figure IV-4: Schematic representation of the steps needed prior to gel formation. To get uniform thick gel lamellas, first microscope slides are prepared with spacers (2 x cover slides, approx. 150µm thick) (1) and then a droplet (approx. 200 µL) is removed from the solution and placed on another heated microscopy slide (2). Subsequently, the prior prepared microscopy slide (with spacers) is firmly pressed on top of the droplet (3) and removed (4) from the heating plate.

IV.2.3.3 Preparation of MACS

In a final step, MACS is transferred from a gel like state with contents of water and BMIMCl into pure cellulose lamellas via solvent exchange and drying. To perform this as carefully as possible, a well-known and often applied slow solvent exchange via bathing in increasing ethanol concentrations in water mixtures is applied. By that, all resulting water and BMIMICl is removed from the sample. This sequence is again shown by a schematic drawing.
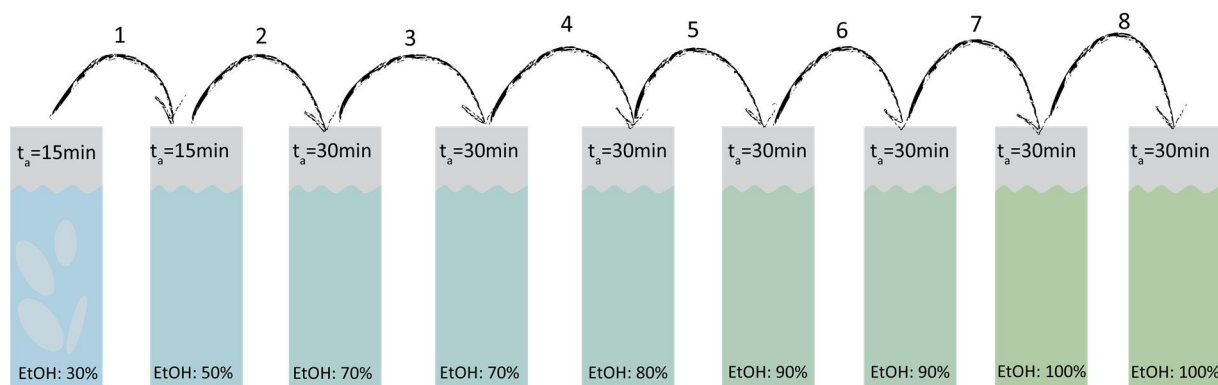
Figure IV-5: Solvent exchange by a sequence of increasing ethanol baths were all remaining BmimCl and water is washed out.

The sequence shown in Figure IV-5 is important as remaining BMIMICl residues would affect enzymatic activity. After this procedure, the lamellas can be stored in pure ethanol until further preparation. In this state, the substrate is now denoted as MACS. For biochemical studies, lamellas are removed from ethanol, dried between cellulose filter papers and cut to the desired size and weight. For AFM experiments additional and crucial preparation steps are required as discussed in the following section.

IV.2.3.4 MACS for AFM Experiments

In the following, the preparation procedure for MACS is discussed and summarized in a preparation scheme in Figure IV-6. The small MACS parts which are still stored in ethanol are placed in a glass petri dish and cut with razor blades into thin strips of ~ 5 mm length. These stripes are then removed and placed between weighted filter papers. Ethanol is removed by drying for 12 hours. Cellulose stripes are put into free slots of PELCO® flat embedding molds (Ted Pella, Redding, USA) and Specifix-40 epoxy resin is prepared by blending in a ratio of 5:2. Epoxy resin is mixed thoroughly for about 2 minutes and air bubbles are allowed to vanish over a period of 5 minutes. Immediately after, epoxy resin is filled into the slots with MACS within. Additionally a small paper sheet with the date of fabrication and the corresponding MACS-xx substrates is added for clear identification. The epoxy resin is hardened at 40°C for 4 hours. The specimens are now ready for ultramicrotome preparation.

Ultramicrotomy preparation starts by reshaping the epoxy embedded MACS specimens as seen in Figure IV-6 e. Specimens are then mounted in the ultramicrotome and a rough cut with a glass knife is performed. Subsequently, the specimens are placed in buffer for about 2 to 4 hours to saturate the cellulose with buffer. Note, without this step MACS will swell uncontrollably in the AFM liquid cell. After swelling, knife is changed to an ultrasonic diamond knife (Ultrasonic, Diatome, Biel, Switzerland) which is then used to perform the final cuts. Note, again this step is performed always in wet conditions with a droplet of water on the cutting plane. Performing this step in a careful manner allows the production of substrates with an RMS roughness below 10 nm, which is perfectly suited for AFM analysis. Specimens are immediately transferred to glass vials with buffer in it and are stored a maximum period of 48 hours before AFM investigation.
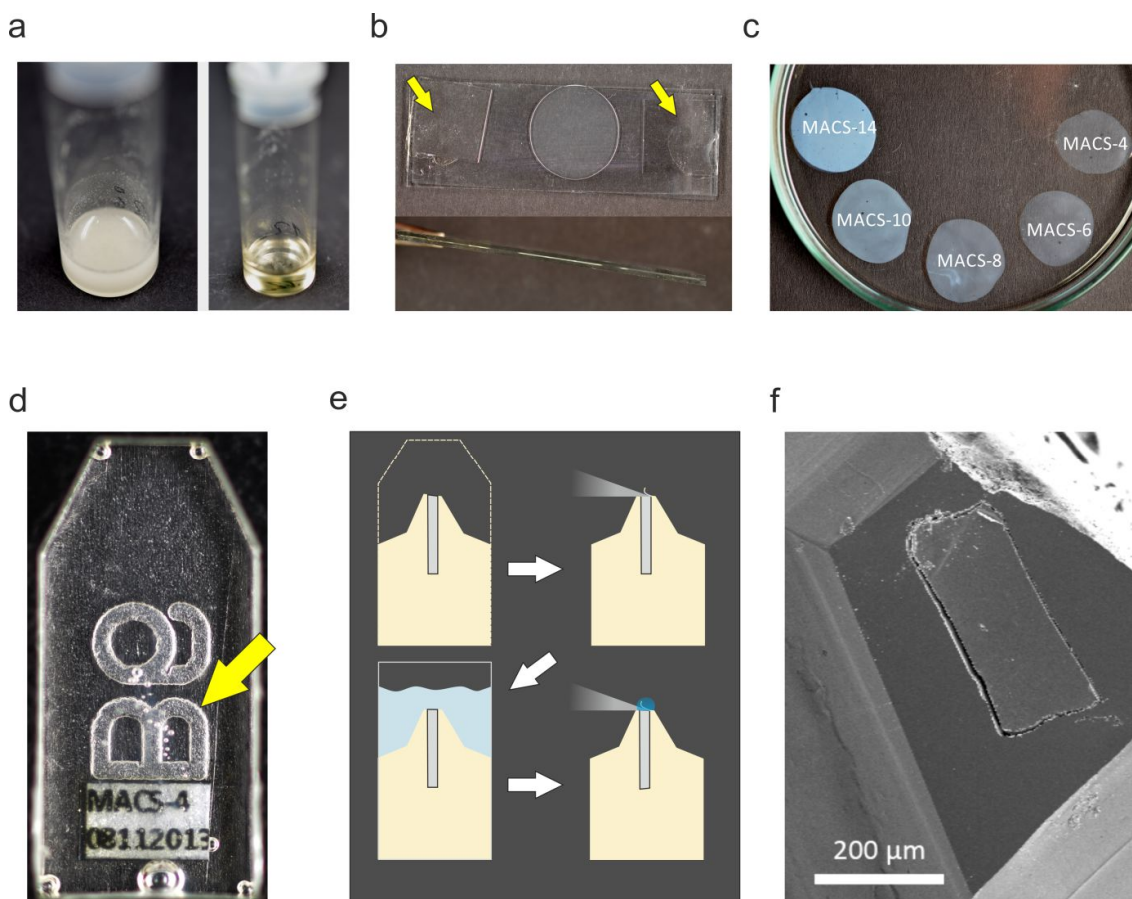
Figure IV-6: (a) Left image shows a solution of molten BMIMICl (primary gel) immediately after addition of Acivel and subsequent stirring with a glass stick. Solution is homogenous and milky in appearance. Right image shows the same solution after 24 h of constant mixing at 95 °C. Solution is now fully transparent and highly viscous. (b) Gel as prepared immediately after mixing. Yellow arrows indicate glass spacers, guaranteeing uniform gel thickness (approx. 300 µm). (c) MACS specimens after solvent exchange stored in pure ethanol. Increasing Avicel concentration upon mixing of the substrates leads to a decreasing transparency of the substrates, indicating concentration dependent change of internal morphology as demonstrated by WAXS, RS, AFM and TEM. (d) MACS-4 sample embedded in epoxy. The position of the specimen is highlighted by the yellow arrow. (e) Schematic representation of the UM preparation. See main text for detailed description. (f) Dried MACS-4 sample in the SEM. Reprinted with kind permission of Springer[2].

IV.2.4 Results and Discussion‡

The structural multiphase character of MACS is highly suitable for enzymatic synergism studies in the AFM with liquid environment (L-AFM) as described in our recent studies[1,8,9]. Although, presence of a multiphase substrate and characteristics were comprehensively analyzed for MACS-15, origin of the observed multiphase character stayed elusive[1,9]. Prior investigations suggested strong dependence on the concentration of Avicel used for fabrication. This study is aimed to give proof for this hypothesis by various methods described in the following. Considering solvability studies of cellulose in BMIMICl[4,6], we limited our experimental range to concentrations from 4 to 20 wt%, further denoted as MACS-4 to MACS-20. As a starting point, the structural properties of MACS were analyzed using wide angle X-ray diffraction.

---

‡ Section IV.2.4 is reprinted from [2] with kind permission from Springer[2]. Reference style is adapted.

IV.2.4.1 Wide Angle X-ray Diffraction

Figure IV-7a shows the WAXS diffraction patterns for all MACS specimens investigated. For reference purposes, WAXS patterns of crystalline $C1_\beta$ (Avicel) and C2 (mercerized) cellulose are shown at the top and at the bottom, respectively. Considering the trend from MACS-4 to MACS-20 it is evident that: (1) overall intensities are significantly increasing; and (2) that the central peak around 20° shifts towards higher diffraction angles as summarized in Figure IV-7b. Taking identical substrate areas and experimental WAXS conditions for all specimens into account, rising intensities either result from increasing density of cellulose material or from a superposition with an additional cellulose diffraction pattern. As a first step we consider the broad, diffuse peak at around 20° of 2Θ for MACS-4, which coincides with the angle position of amorphous cellulose[10]. Amorphous nature of MACS-4 is confirmed by dedicated AFM and TEM experiments (see Figure IV-10 - Figure IV-12). In order to investigate the diffraction patterns with respect to additional contributions from other cellulose structures, an amorphous MACS-4 diffraction pattern is subtracted from a MACS-8 and MACS-14 pattern as shown by the (green and red) top graphs in Figure IV-8 a, b, respectively. Remaining difference diffraction patterns can be interpreted as signal from additional cellulose allomorphs in MACS-8 and MACS-14. Compared to experimental WAXS data for pure C2 and $C1_\beta$ (dark green and dark red) in Figure IV-8a, b proof is given that additional allomorphs are present in MACS. To validate experimental data, simulations are given by the black curve (FWHM = 2.0) to show a 100 % crystalline diffraction pattern without other contributions. Simulations in gray (FWHM = 0.1) were used to index peaks by Miller indices.
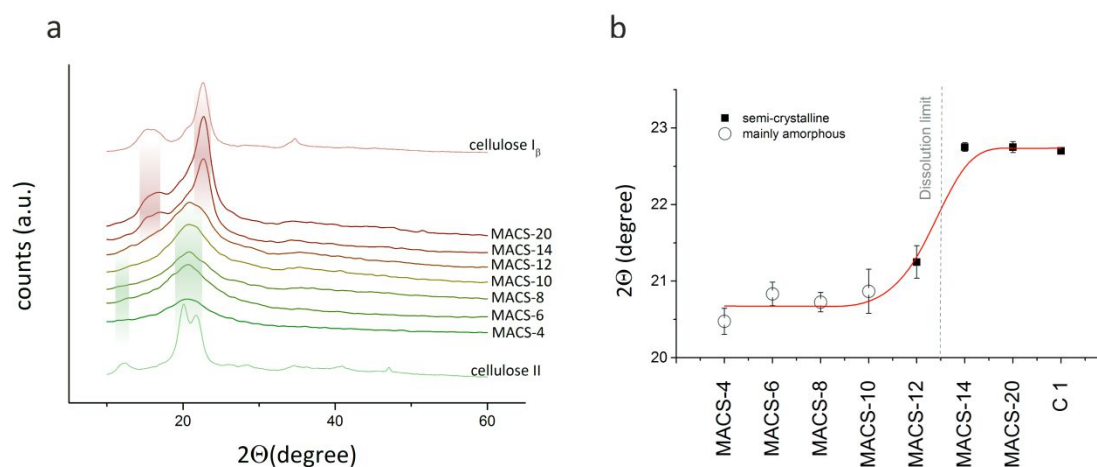

Figure IV-7: (a) Stacked WAXS diffraction patterns of MACS specimens from 4 to 20 wt% with the corresponding reference diffraction patterns of cellulose allomorph I_β (Avicel; red) and II (mercerized Avicel, green). Color transformation from green to red illustrates the change from amorphous to semi-crystalline cellulose. Specimens below 10 wt% cellulose show mainly amorphous contributions to the pattern with the possibility of small contributions from C2 (see Figure IV-8) as illustrated by a green shading. For MACS-12 or higher, additional peaks appear in the patterns in good correlation with $C1_\beta$ as shown by the red shading. (b) Plot of the main peak shift as seen in (a). Here peak shifts from 20.5 (amorphous) to 22.7 (crystalline (200), C1b) degrees of 2Θ. Circles and squares indicate amorphous and semi-crystalline cellulose. Error bars are calculated from multiple diffraction patterns. Reprinted with permission of Springer[2].

Please note that only peaks which were also identified in difference diffraction patterns are indexed. In more detail, for MACS- 14, difference pattern show reflections at 15.2°, 16.5°, 22,7° and 34,6° for the (1$\bar{1}$0), (110), (200) and (004) crystal plane of $C1_\beta$ which is in good correlation with simulation data

[11]. For MACS-8 not all peaks may be unequivocally identified in the difference diffraction patterns, which results from minor contribution and therefore low signal. However, the correlation between C2 and the difference signal is reflected in numerous resolved peaks, such as those at 20.7°, 22.8°, 27.3°, 29.9° and 35.0° for the (110), (020), (1$\bar{2}$2), (103) and (2$\bar{1}$3) reflection which, although slightly shifted to higher diffraction angles for the experiment, correlate well with simulated data. From these comparisons it can be concluded that MACS-8 consists of mainly amorphous cellulose with small amounts of C2. This is not fully unexpected, as cellulose polymers once dissolved recrystallize in allomorph C2. In addition, a rising concentration of cellulose must result in increased tendency to crystalize. This is reflected by an overall rising intensity in the diffraction patterns for MACS-4 to MACS-12 as seen in Figure IV-7a. However, the additional C2 contributions are small compared to the additional contribution found for MACS-14. Here a clear correlation to the C1$_\beta$ allomorph is found (see red and blue graphs in Figure IV-8b) stemming from incomplete dissolution of Avicel in MACS. This dissolution limit can be clearly seen in Figure IV-7b by the main peak shift from amorphous (and small C2 contributions) towards semi-crystalline cellulose around 12 wt%. This is in good agreement with literature[4]. Moreover, the observed changes in the diffraction patterns are in good agreement with the change of transparency on different concentrated MACS specimens as shown in Figure IV-6c. However, WAXS basically can only show the transformation to multiphasic substrates, but lacks any spatial information. To gather a more detailed view on MACS as prepared for L-AFM investigations, Raman Spectroscopy was used as described in the following.
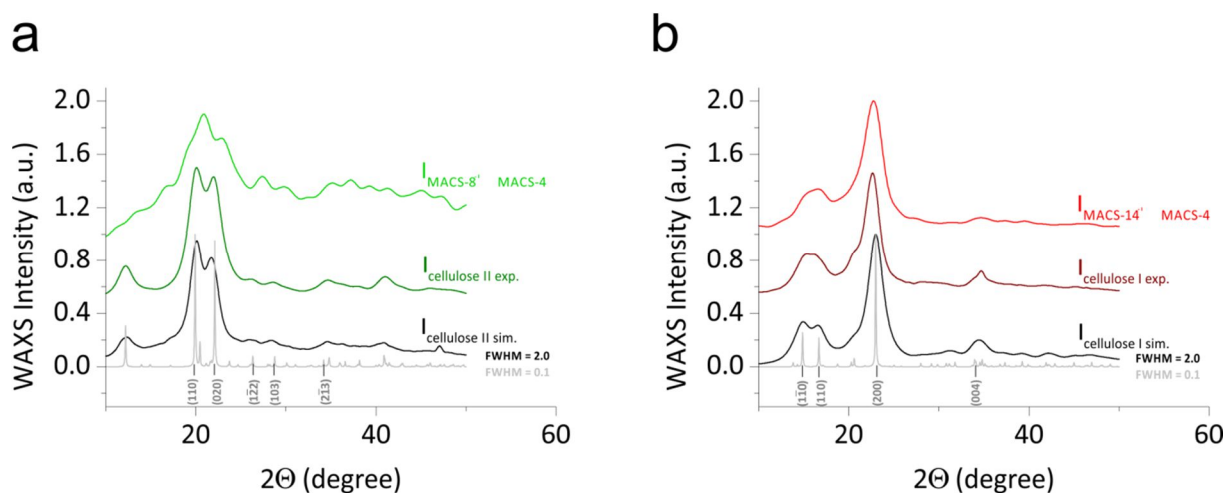

Figure IV-8: Difference diffraction patterns of MACS-8 minus MACS-4 (a; green) and MACS-14 minus MACS-4 (b; red) shows additional contributions from other cellulose allomorphs. Corresponding experimental data of C2 (dark green; mercerized Avicel) and C1$_\beta$ (dark red; Avicel) are shown together with simulation data (black, FWHM = 2.0; grey, FWHM = 0.1). Simulation parameters were carefully chosen accordingly to fit the experimental data. Most relevant peaks resolved in subtracted diffraction patterns and simulation data are indexed with Miller indices. Structures were kindly provided by Alfred D. French[11]. Reprinted and adapted with permission from Springer[2].

IV.2.4.2 Raman Spectroscopy

RS has proven to be a versatile tool to distinguish different cellulose allomorphs[12–14]. To provide comparability to our previous studies[1,8,9] and complementary techniques applied in this study, all specimens were prepared identical to the L-AFM investigations. Figure IV-9a shows two typical

spectra of a MACS-14 sample recorded on and off a crystallite (Figure IV-9b, c). Note, crystallites are found for concentrations higher than MACS-12 due to surpassed dissolution limit, as shown by WAXS. The bands for clear identification are indicated by (+) for $C1_\beta$ (crystalline, red) and (-) for C2/amorphous cellulose (green)[13]. Please note, it is well reported[13,15] that sole amorphous and crystalline cellulose of allomorph II show similar bands and distinction is difficult. However, in accordance with WAXS data the presence of $C1_\beta$ and amorphous cellulose is clear from both spectra. Figure IV-9b shows a SEM top view image with a representative micrometer sized particle in MACS-14, which can typically be found all over the samples for concentrations above 12 wt%. Figure IV-9c shows the RS map on the same particle with the color code according to the spectra in Figure IV-9a. Substrate in proximity of the crystalline particle shows an amorphous/C2 spectrum. In contrast the central crystallite can be clearly identified as $C1_\beta$ allomorph (red spectra), thus originating from undissolved Avicel residues. Please note that SEM was performed after RS investigations to prevent electron beam induced damage of the specimen. Average spectra of larger areas in MACS-4 to MACS-14 show same significant changes from amorphous to semi crystalline material as shown in Figure IV-9d. As reported by Schenzel et al.[15] analysis of multiphase spectra can be used to calculate the crystallinity index in respect to C1b and amorphous/C2 cellulose as described above. Figure IV-9d shows the relevant band range between 1,200 and 1,500 cm-1. Bands for calculations are indicated by the red (crystalline) and green arrow (amorphous/C2). Figure IV-9e shows the calculated crystallinity index plotted against the corresponding substrate. In accordance with WAXS data, the dissolution limit is revealed by a strongly increasing crystallinity around MACS-12. Combined evidence from RS and WAXS derived data clearly suggest that substrates above MACS-12 show a multiphasic spatial organization with increasing allomorph I_β content. To resolve fibrillar structures, as described in recent studies[1,9] high-resolution microscopy methods were applied.
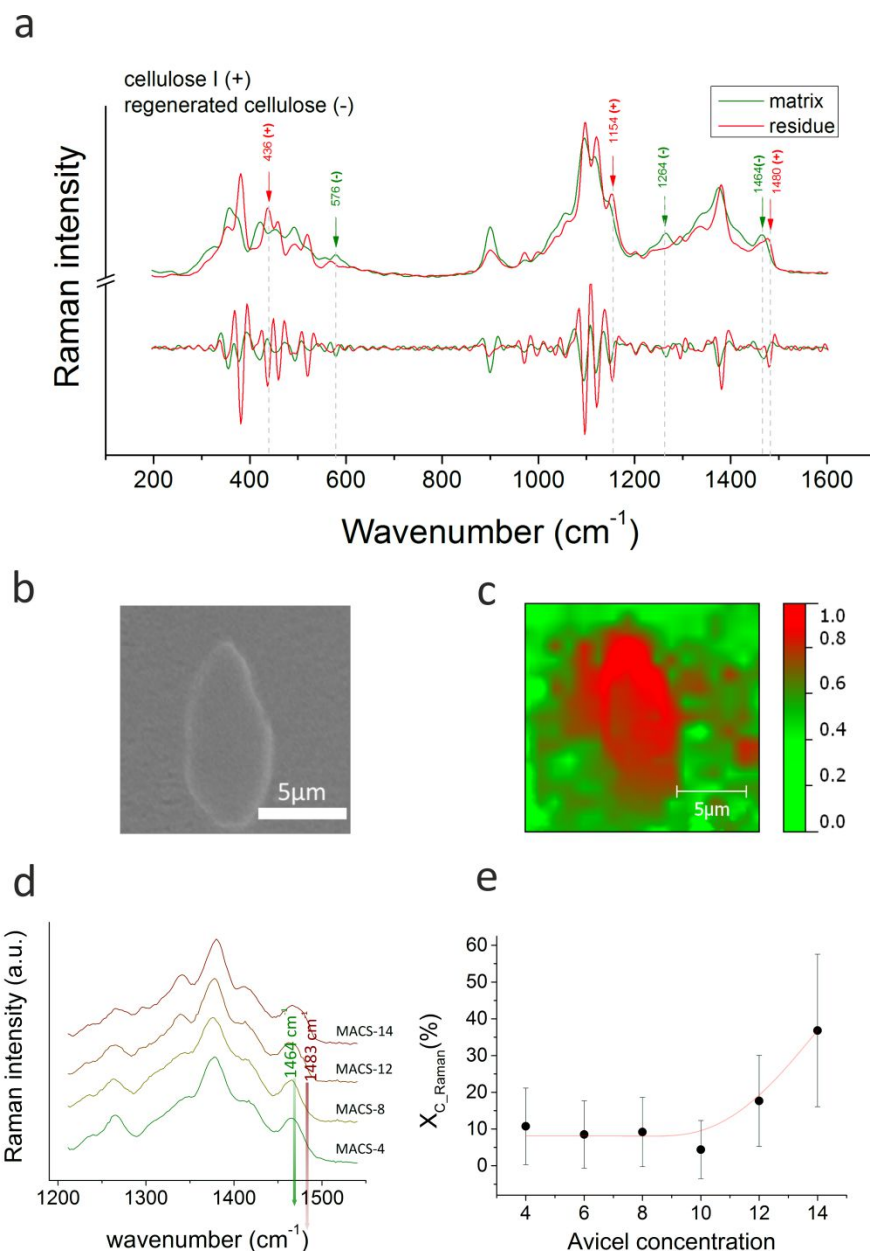
Figure IV-9: (a) Raman spectra (above) and corresponding second derivatives (below) of cellulose allomorphs as found in MACS- 14 or higher. Colors of the spectra correlate with the Raman color map in (c). Typical bands are illustrated by (+) for crystalline and (-) for amorphous/C2 cellulose. (b) SEM micrograph of a typical crystalline cellulose particle found in MACS-14, corresponding to the Raman image in (c). SEM investigation was performed after Raman mapping to prevent electron induced damage of the specimen. (c) Raman map for the same particle as in (b) with color scale according to (a). (d) MACS Raman spectra in the range of 250–1550 cm^{-1} showing the relevant bands for crystallinity index determination as shown in (e). Here the d(CH$_2$) bending vibration of regenerated cellulose at 1464 cm^{-1} and crystalline cellulose at 1483 cm^{-1} are used for the calculation as proposed by Schenzel et al.[15]. (e) Calculated crystallinity index for MACS 4 to MACS-14 form the bands as illustrated in (d). Error bars are calculated from Raman spectrometer accuracy of ±2cm^{-1}. Reprinted with kind permission from Springer[2].

IV.2.4.3 Atomic Force Microscopy in Liquid Environments

Multiple L-AFM investigations, probing the enzymatic degradation, uncovered the presence of different allomorphs by a non-uniform speed of deconstruction[1,8,9]. Surface changed from formerly flat to distinctive rough topology. RMS increase was several hundred percent in the first few hours of the experiment. Dedicated additional experiments showed, that beside residual large crystallites, fibers in the nanometer regime are found in the surrounding matrix. Moreover, these fibers were responsible for the pronounced increase of RMS in the AFM experiments. A protocol to resolve different synergistic activity of cellulase revealed a novel mechanism in multiphase substrate degradation[1,9]. While residual large crystallites stayed almost unchanged over the time investigated, nano-sized fibers showed significant impact on synergistic deconstruction from the beginning. Here internal structure, in particular the ordered crystalline packing and the small dimensions, triggered a controversial form of degradation. While amorphous substrate was degraded at uniform speed, areas with fibers embedded featured a slow and a fast phase of substrate removal[1,16]. First, crystalline fibers were excavated and cleaned from the surrounding material, followed by fast degradation from the ends. This fast removal of crystalline material is only possible due to small dimensions of the fibers (approx. 30 nm x 100 nm). Here, the low number of obstacles and high accessibility of fiber ends allows fast and linear processive movement of exo-glucanases. This however, showed that smaller crystalline features of similar dimension found in elementary fibrils are of high importance for synergistic degradation of cellulose. Despite the extensive knowledge from recent studies about the synergistic behavior of such fibers, proof of exact formation during preparation was not given. Therefore, we used the same preparation procedures as described above to investigate surface topography of MACS with varying Avicel concentration. Figure IV-10 shows representative 3-D AFM images of MACS-4 andMACS-14 with overlaid phase signal. Analysis on MACS-4 supports findings from WAXS with no evidence for fibrillar structures and numerous on MACS-14. In more detail, areas with pure crystalline nature (Figure IV-10; MACS-14, C) and pronounced semi crystalline appearance (Figure IV-10; MACS-14, SC) can be found in MACS-12 or higher. Fibers in the amorphous matrix as well as on highly crystalline areas correlate in diameter and length indicating similar formation mechanisms. In Figure IV-11a, a representative image of a fiber rich area on a MACS-14 specimen is shown by an AFM amplitude image revealing well pronounced fibers. Correlated AFM height, phase and amplitude cross sectional analysis is shown in Figure IV-11b (see white line in Figure IV-11a) revealing mean widths of 10–15 nm. A more detailed analysis reveals that regions with higher fiber density show slightly higher phase signals indicating stiffer regions. This is in good agreement to the observed phase signal on residual Avicel particles (see Figure IV-10; MACS-14, C). To gain statistically relevant data, numerous experiments were analyzed with respect to fiber widths as summarized in Figure IV-11c. Gaussian peak fitting reveals a fiber width of 9.5 ± 2.7 nm in good agreement with previous literature[17–19]. Please note that the asymmetric histogram distribution towards broader fibers in Figure IV-11c is caused by slightly increasing tip influences for rougher samples. As AFM is limited to surface structures, further TEM investigations have been conducted to access the internal MACS structure for a more comprehensive analysis as discussed in the following.
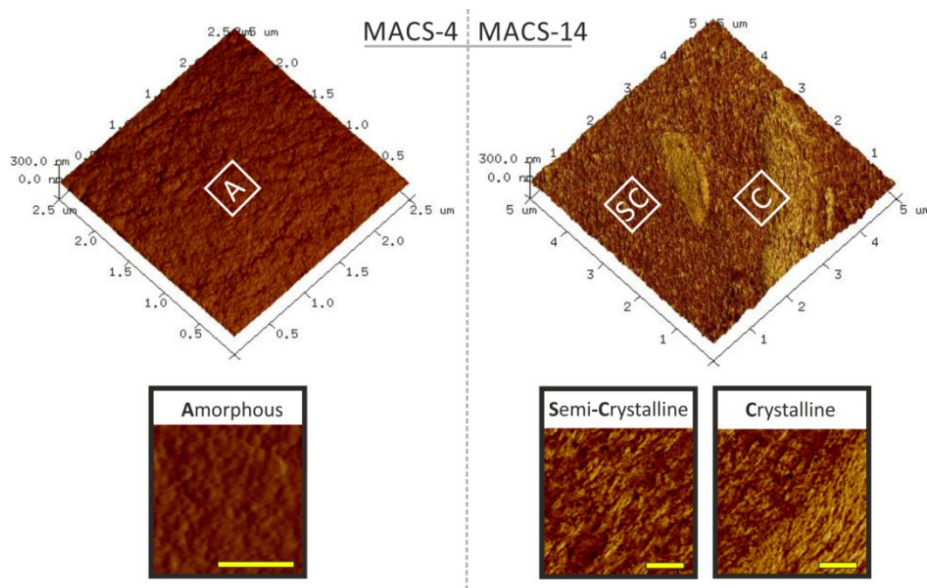
Figure IV-10: L-AFM 3D images of an amorphous MACS-4 and semi- crystalline MACS-14 specimen overlaid with phase information (repulsive). For MACS-4 smooth amorphous (A) cellulose surfaces are found without any pronounced features. MACS-14 reveals highly heterogeneous surface implementing a semi- crystalline (SC) phase and residual micron sized crystallites (C). Insets show close up images with featureless amorphous (MACS-4; A), semi-crystalline (MACS-14; SC) and highly packed crystalline substrate areas (MACS-14; C). Fibrillar structures are clearly visible for MACS-14 on crystalline as well semi-crystalline parts of the substrate. Scale bars (yellow) show 250 nm of the substrate. Reprinted with kind permission of Springer[2].
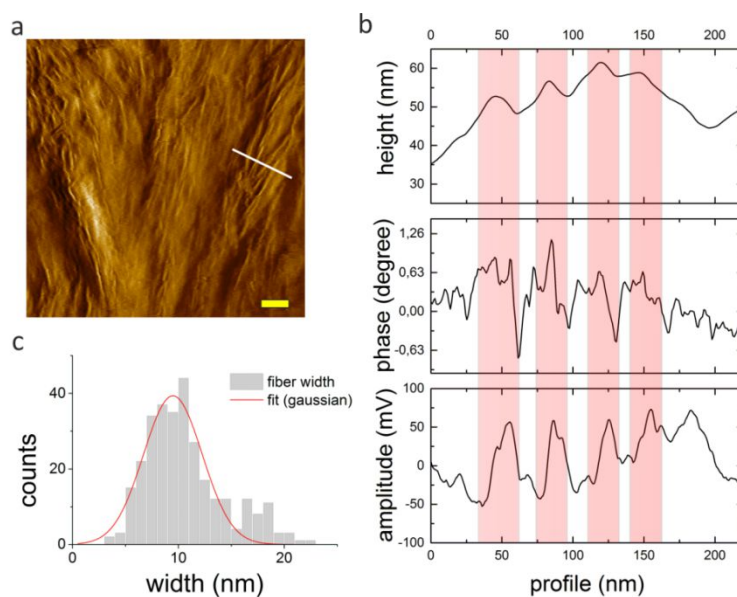
Figure IV-11: (a) Amplitude image of MACS-14 surface shows numerous fibrillar structures on a highly crystalline area of the substrate. Scale bar (yellow) is 100 nm. (b) Cross section profiles as seen in (a) (white line) showing height, phase and amplitude data. Areas with high density of fibers feature slightly higher phase signals indicating a higher stiffness of the material in agreement to the phase signal on Avicel residues (see Figure IV-10, MACS- 14, C). c Statistical analysis (N_f = 300) of fiber width on numerous MACS-14 specimens (N_e = 5) revealing 9.5 ± 2.7 nm of fiber diameter. Reprinted with permission of Springer[2].

IV.2.4.4 Transmission Electron Microscopy

TEM was performed on thin (<100 nm) MACS sections produced by UM. Contrast was enhanced by standard ruthenium tetroxide staining as described above. In Figure IV-12 a plot of the density of highly ruthenium stained areas is given against the corresponding specimen. TEM bright field images of MACS-4 and MACS-14 are given as inset. MACS-4 shows less structure compared to MACS-14, where staining shows a fibrous network. As ruthenium tetroxide staining is based on different diffusion velocities in crystalline and amorphous parts of polymers, darker areas are associated with denser and therefore crystalline material. Hence, fibers seen in the L-AFM are not confined to the surface of MACS and multiphasic properties are indeed intrinsic. Interestingly, density of fibers also shows the dissolution limit of MACS by a strong increase of ruthenium dense regions. Most likely, this is the result of increased tendency of the cellulose to recrystallize from an oversaturated solution upon cooling. Determination of exact allomorph of present nanofibrils however, remains elusive due to spatial resolution limitations of suitable techniques (Raman, WAXS). However, considering the missing local evidence for $C1_\beta$ in the amorphous matrix by Raman data and taking recrystallization processes into account[20,21], as indicated by WAXS, nanofibrils might be of allomorph II.
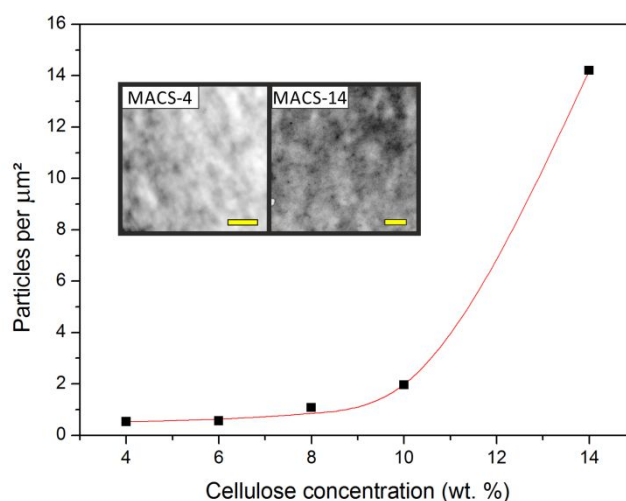

Figure IV-12: Areal density of highly ruthenium stained regions in MACS specimens as observed by TEM. Plot shows slightly linear trend below MACS-12 with low densities followed by a sharp increase around MACS-12 correlating with the proposed dissolution limit of 12 wt%. The insets show MACS-4 and MACS-14 TEM images which clearly proof the increased number of small stained particles for MACS-14. Scale bar is 500 nm. Note, ruthenium is accumulated around crystalline features due to a different diffusion velocity against amorphous parts, indicating highly crystalline regions. Reprinted with kind permission of Springer[2].

IV.2.5 Conclusion§

In summary, including all data from WAXS, RS, L-AFM and TEM the multiphasic nature of MACS was demonstrated together with the ability to change the intrinsic amount of crystalline cellulose. Already evident from the fabrication process or visual appearance of the corresponding specimen (see Figure IV-6c), the dissolution limit of Avicel in BMIMICl was shown by WAXS (see Figure IV-7b).

§ Section IV.2.5 is reprinted from [2] with kind permission from Springer[2]. Reference style is adapted.

Here, an increase of C1b associated peaks could be observed after exceeding a mixing ratio of 12 wt%. This is in good agreement with dissolution limits from literature[4,6,7]. Closer analysis of amorphous substrates between MACS-4 and MACS-8 showed evidence for a minor contribution of C2[22]. For further clarification RS was used to acquire spatially resolved information. RS revealed that cellulose of allomorph I_β was found in larger crystalline particles (Figure IV-9b, c) and amorphous cellulose in the surrounding matrix. L-AFM investigations for high concentrated MACS further showed nano-sized fibers in the amorphous matrix (see Figs. 5, 6) in accordance to recent studies[1,9]. MACS fabricated with concentrations lower than 12 wt% seemed to have no or minor quantity of fibers. These findings are supported by TEM analysis, which showed the increasing density of such fibers going from lower to higher concentrations of Avicel (see Figure IV-12). Although fibrous structures were demonstrated by AFM and TEM, the crystalline allomorph of these fibers can only be concluded by WAXS and Raman data. With the missing evidence for $C1_\beta$ in the amorphous part of the substrate by Raman investigations and evidence from WAXS, fibers are therefore most likely of allomorph II. The deliberate incorporation of crystalline features in the amorphous material allows investigations on substrates with a mixed amorphous–crystalline character as shown in recent studies[1,9]. Even though natural sources in their native state are structurally more complicated in respect to additional lignin and hemicelluloses, MACS offers the possibility to emulate the multiphase character of such substrates to a certain extent. With this, valuable information may be gained especially concerning systems of cellulases acting in a synergistic way on structurally diverse substrates. In addition, the applied preparation protocol allows RMS values below 10 nm, which is extremely important for any high resolution investigation to improve our understanding of enzymatic cellulose degradation as a key method in carbohydrate research.

IV.3 Tunable Semi-Crystalline Cellulose Substrate for High-Resolution, *In-Situ* AFM Characterization of Enzymatic Cellulose Degradation

IV.3.1 Publishing Information

This *chapter* contains the results as summarized in the manuscript *"Tunable Semi-Crystalline Cellulose Substrate for High-Resolution, In-Situ AFM Characterization of Enzymatic Cellulose Degradation"* [2] which was submitted in October 2015 and was accepted in ACS Applied Materials & Interfaces (American Chemical Society) on the 30th of November 2015. Thomas Ganner**, Stephanie Roŝker**, Manuel Eibinger, Johanna Kraxner, Jürgen Sattelkow, Johannes Rattenberger, Harald Fitzek, Boril Chernev, Werner Grogger, Bernd Nidetzky, and Harald Plank†† are the involved authors. Concept and idea for the manuscript was from HP and TG. TG and SR conducted the AFM experiments. TG and SR performed WAXS experiments and data analysis. TG, SR and JS prepared the substrates. TG and SR made all figures and captions. JK performed TEM investigations and HP and WG was responsible for TEM data analysis. HF and BC performed Raman experiments while data was analyzed by TG and SR. Biochemical experiments were designed by ME and BN while data analysis was conducted by ME. TG and HP wrote the paper including the revision with the help of ME and BN. In brief, the manuscript includes a comprehensive demonstration of a novel thin film cellulose substrate which without elaborate preparation includes polymorphism, flatness and reproducibility. Again multiple methods were applied to analyze the substrate by AFM, Scanning Electron Microscopy (SEM), Transmission Electron Microscopy (TEM), Raman microscopy and Wide Angle X-ray Scattering methods.

IV.3.2 Introduction

Cellulose hydrolysis by enzymes is a highly promising concept for the utilization of the world's most abundant biopolymer for energy production.[23–25] However, the recalcitrance of cellulose causes hydrolytic degradation processes triggered by enzymes (cellulases) to be rather inefficient. Optimization requires a fundamental understanding of localized activities for individual cellulases[17,26,27]. For several decades, visualization was predominantly performed via optical or electron microscopy with either low resolution or inappropriate environmental conditions, respectively[16,28–30]. In recent years Atomic Force Microscopy (AFM) in liquids attracted increasing attention for the investigation of enzymatic cellulose breakdown due to high spatial resolution, easier handling and faster imaging speeds down to the sub-second range[31,32]. In particular, this technology complements state-of-the-art biochemical experiments, which can only provide convoluted data with information on the micro- and nanoscale. Hence, the combination of AFM and biochemical experiments becomes increasingly important as it enables a deep and comprehensive insight into bio-materials and dynamic processes. So far, AFM experiments for the *in-situ* visualization of enzymatic cellulose decomposition often used substrates with homogeneous

---

** Equally contributing authors.
†† Corresponding author.

composition of either crystalline or amorphous cellulose, which usually restricts analysis and is not representative of natural celluloses where these morphologies are found side-by-side.[21] Not surprisingly, the morphological complexity (polymorphism) is influencing the degradability of differently composed substrates as demonstrated in various studies.[16,27,33] It is this interdependence between individual enzymes and a specific substrate morphology which is known to play a significant role in so called synergistic activities of multi-cellulases cocktails,[1,9,34,35] which simply describes higher combined activities of the latter compared to the sum of individual enzyme activities. To unravel these interdependencies, an ideal substrate would be desirable which provides nanoflat topology for high-resolution imaging as well as a tunable di-morphism to study structure-to-activity relationships side-by-side. A recent study by the authors provided a first mixed amorphous-crystalline cellulose substrate (MACS) which was successfully applied to synergism investigations of the well-known model cellulase system of *Hypocrea jecorina (*former *Trichoderma reesei).*[1,9,16] However, MACS required an elaborate preparation, lacked a fixed reference for the determination of absolute degradation rates, led to strongly increased surface roughness during experiments, and, most strikingly, did not allow one to control the size and spatial distribution of cellulose crystals which has further implication on local activities.

The main aspect of this study is the introduction of a cellulose substrate with tunable polymorphism. Here, homogeneously sized cellulose nano-crystals are embedded in an amorphous cellulose matrix revealing a nanoflat surface topology and tunable layer thickness. In more detail, we combine the cellulose precursor (trimethylsilyl-cellulose, TMSC) with fully crystalline cellulose whiskers via simple protocols and prepare thin films via spin-coating, followed by regeneration into cellulose[36–40]. Such substrates are not only easy and fast to fabricate but also reveal very high reproducibility which is essential for consecutive experiments. This study is divided in two thematic parts, starting with a comprehensive material analysis using Wide Angle X-Ray Scattering (WAXS), Raman spectroscopy, *in-situ* AFM, and Electron Microscopy (Scanning, SEM; Transmission, TEM). The second part of the study aims on a practical test of the substrate during enzymatic degradation via *in-situ*, high-speed AFM in liquid environments. Here, individual and combined cellulases from *Hypocrea jecorina* are used as this organism is well-known. Both parts together, in-depth material analyses and feasibility experiments, confirm that the substrate is highly suited for high-resolution AFM studies with particular suitability on unraveling synergetic effects between different enzyme species for a deeper understanding of biological processes.

IV.3.3 Experimental Procedures

IV.3.3.1 Materials

All used materials and chemicals have been purchased at the highest available purity unless otherwise stated. Pre-cut silicon wafers (10×10 mm^2) with 3 nm SiO$_2$ were kindly provided by AMS AG (Unterpremstätten, Austria).[41] Glass vials (4 mL, Ø 15mm, Rotilabo) and slides, tetrahydrofuran, 2-propanol, ethanol (analytical grade, not denatured), sulfuric acid and xylol were purchased from Carl Roth (Karlsruhe, Germany) while Whatman® No. 1 filter paper was purchased from Sigma-Aldrich (St. Louis, MO, USA). Trimethylsilyl-cellulose (TMSC, DP = 2.8) was purchased from Thüringisches Institut für Textil- und Kunstoff-Forschung (TITK e.V, Rudolfstadt, Germany). Uranyl acetate was purchased from Christine Gröpl (Tulln, Austria).

IV.3.3.2 Nano-Crystalline Cellulose (NCC)

Nano-cellulose was prepared according to protocols from the literature.[42] Briefly, 40 g of Whatman® No. 1 qualitative filter paper was incubated in Millipure® water for 24 h and mechanically processed afterward, yielding a wet cellulose pulp. Bound water was determined by microweighting and acid solution was prepared to obtain 700 mL of 64 wt.% sulfuric acid after combination with the pulp. Both, acid and pulp were individually heated to 45°C, then mixed, and kept for 45 minutes at the same temperature for hydrolysis. Thereafter, reaction was stopped by dilution with Millipore® water in a ratio of 10:1, and solution was further processed by multiple iterations of centrifugation and dilution steps until pH is 1.5 or higher. Please note, the low pH value is required to fully stabilize the colloidal solution as reported in the literature[42,43]. Finally, the colloidal solution was separated from the centrifuge supernatant and sodium azide (0.05 wt. %) was added to prevent microbial growth and stored in capped vials at 4 °C until further use. Concentration of the solution was determined with 7.5 g L^{-1} by weighing of the dry mass and is further denoted as NCC-stock-solution. Prior to further use, stock was again treated with an ultrasonic bar (Sonoplus HD2200, Bandelin electronic GmbH & Co. KG, Berling, Germany) for at least 10 min at 52 % power (P_{max}=200 W) while being cooled in an ice bath to ensure a colloidal dispersion of NCC.

IV.3.3.3 Thin Films

Preparation was executed in analogy to literature protocols by the use of different solvents.[37,39,44] For nano crystalline thin film cellulose (NCTFC), NCC-stock-solutions were diluted (1:10) with deionized water prior to spin-coating. For amorphous thin film cellulose (ATFC), TMSC (5, 10, 15 mg) was dissolved in xylol (1 mL) further denoted as $xylol_{(XX)}$ (with XX equal to the concentration in mg L^{-1}). For semi-crystalline thin film cellulose (SCTFC), TMSC (5, 10, 15 mg) solutions were prepared in tetrahydrofurane (THF, 1 mL) according to its miscibility with water (NCC stock solution). In all cases, TMSC was dissolved assisted by ultrasonic treatment (Transsonic T560, Elma Schmidbauer GmbH, Singen, Germany) until the absence of a solid phase in the vials. For SCTFC, NCC stock was diluted (1:10) and added (5, 10, 15 µl) to the TMSC solutions (1 mL). These mixtures are then denoted as $THF_{(XX / YY)}$ with XX (mg L^{-1}) and YY (µl mL^{-1}) indicating the TMSC and NCC concentrations, respectively.

IV.3.3.4 Spin coating

Prepared solution (100 µl) was carefully dropped on pre-cleaned Si-SiO$_2$ substrates (acetone wiping, CO$_2$ spraying, isopropanol wiping, CO$_2$ spraying, 15 min. isopropanol ultrasonic bath, and immediate CO$_2$ spraying), followed by immediate spin-coating with 3500 rpm for 45 seconds.

IV.3.3.5 Regeneration

Cellulose thin films were obtained according to protocols from the literature.[37] Briefly, spin coated specimens were transferred to a desiccator at an elevated position with HCl (25 mL, 2M) solution below. The desiccator was connected to a water vacuum pump and continuously evacuated for 15 minutes thereby forming a reaction environment of saturated water - HCl vapor. The regeneration progress can be followed by color change of the film due to loss of trimethylsilyl-groups and corresponding reduction of film thickness according to previously reported mechanisms.[37,39,44] After

15 min, specimens were removed, thoroughly rinsed with deionized water, and dried for one hour at 60°C before further use. Please note that films before regeneration are denoted as TMSC while regenerated layers are named ATFC throughout the article.

IV.3.3.6 Enzymes

*Hj*Cel7A was purified via a modified ion exchange protocol from the complete *Hypocrea jecorina* cellulase pool as described elsewhere in more detail.[45] *Hypocrea jecorina Hj*Cel6A was obtained via heterologous expression in *Pichia pastoris.*[46] β-Glucosidase from *Aspergillus niger* was purchased from Megazyme (Dublin, Ireland). Concentrations of individual enzyme preparations were determined via absorption spectroscopy at 280 nm with a DeNovix DS-11+ Spectrophotometer (Silverside, USA). Molar extinction coefficients for individual enzymes in solution were determined from the protein sequence from UniProt using ProtParam.

IV.3.3.7 Enzymatic Reaction (AFM)

AFM experiments were conducted in duplicates using sodium acetate buffer (50 mM, pH 5.0) in a laboratory built liquid cell at room temperature. A single silicon wafer coated with cellulosic material was used as substrate. *Hj*Cel7A and *Hj*Cel6A were sequentially added with a total enzyme loading (800 µg) for each individual enzyme.

IV.3.3.8 Enzymatic Reaction (Biochemical)

Released glucose was measured utilizing either ATFC or NCC as substrate. Experiments were conducted as duplicates at 50 °C in a water bath with mild agitation. 50 mM sodium acetate buffer, pH 5.0 was used in a total reaction volume of 2 mL in glass vials. A single ATFC or NCTFC coated silicon wafer was used as substrate. Cellulosic material was equilibrated in buffer for 30 minutes prior to the addition of enzyme.

The respective enzymes (*Hj*Cel7A or *Hj*Cel6A) were present either alone or combined at a concentration of 10 µg mL^{-1} per enzyme. β-Glucosidase was added to a concentration of 1 µg mL^{-1} to all reaction to promote the conversion of cellobiose to glucose. Negative controls did not contain enzymes except for β-Glucosidase. Sampling was performed at suitable time points. Briefly, 180 µL of the supernatant were withdrawn and mingled with 20 µL 1 M NaOH to stop the reaction. Subsequently, the samples were centrifuged (9 300 g, 1 min) and the cleared supernatant was subjected to sugar analysis.

IV.3.3.9 Atomic Force Microscopy

Investigations (Figure 6) were carried out on a Dimension 3100 microscope using a XYZ Hybrid scan head (Bruker AXS, Santa Barbara, California/USA), operated by a Nanoscope IVa controller and AC240TS cantilevers with a nominal spring constant of 2 N m^{-1} (Olympus Probes, Tokyo, Japan). Dynamic liquid measurements were conducted in a laboratory build liquid cell at air conditioned temperatures (22 °C). High-speed, *in-situ* AFM experiments (Movie S5) were performed on a Fastscan Bio AFM microscope (Bruker AXS, Santa Barbara, California/USA) equipped with a Nanoscope V

controller, a capped liquid cell (Bruker AXS, Santa Barbara, California/USA) and Fastscan D cantilevers (Bruker AXS, Santa Barbara, California/USA) with a nominal spring constant and a tip radius of 0.3 Nm^{-1} and 8 nm, respectively. The capped cell was pressed on the substrate, filled with buffer and investigated by continuous imaging. After several reference images, the enzymes were injected via laboratory build injection system and continuous imaging was applied. Nano-mechanical mapping was performed on the Fastscan Bio AFM by the use of Scanasyst-Air cantilevers (nominal spring constant k = 0.2 N m^{-1}). In order to produce a reference to the underlying substrate, films were in all experiments carefully scratched with sharp tweezers. Setpoints, scan rates and controlling parameters were chosen carefully to ensure lowest possible energy dissipation to the sample and to exclude tip driven artifacts. Multiple images were recorded on each spot to cross-check the results and give statistical relevant information.

IV.3.3.10 Wide angle X-ray Scattering (WAXS)

Analysis was performed on a Siemens D 5005 diffractometer (Siemens, Munich, Germany) using CuK$_\alpha$ radiation at 40 kV (0.154 nm) and 40 mA. Source slit was variable (V20 Option) to give constant area illumination (2 × 2 cm^2) throughout the measurements. All samples were characterized in coupled Θ/2Θ mode from 10 ° to 60 ° (2Θ) with an angle increment of 0.05 ° every 6 sec. In order to achieve higher signal-to-noise ratios, multiple single films (N = 15) were first prepared via spin-coating on glass substrates. Glass slides are then immersed slowly in deionized water to delaminate the individual films from the glass, thus producing free floating films. Films were collected, regenerated, if required, and placed on a zero diffraction silicon crystal holder (Bruker AXS, Santa Barbara, California/USA). Other specimens (TMSC powder, regenerated TMSC powder, cellulose-II powder and Filterpaper) were analyzed by putting small amounts directly on the same holder. Data analysis was performed using Origin 9 (OriginLab cooperation, Northampton, USA).

IV.3.3.11 Raman Spectroscopy

Measurements were conducted on a confocal Horiba Jobin Yvon LabRam 800 HR spectrometer, equipped with a He-Ne laser, emitting at 633 nm, a grating with 300 l mm^{-1} and an Olympus BX41 microscope. The objective used was x100 (NA = 0.9)* Olympus (Objektiv MPlan N). The used 1024 x 256 CCD was Peltier-cooled for low noise performance. Si-SiO$_2$ substrates were, prior to spin coating, coated via low dose PVD in an EM ACE 600 (Leica, Vienna, Austria) with 200 nm of gold to eliminate superposition of cellulose and Si bands. Again, multiples films (N = 10) with xylol$_{20}$ were produced on one gold substrate by repeated spin-coating and regeneration steps to achieve higher signal-to-noise ratios. Powder specimens (TMSC powders, cellulose-II powder, and filterpaper) were directly placed on similar Si-SiO$_2$-Au substrates. Data analysis was performed using Origin 9 (OriginLab cooperation, Northampton, USA).

IV.3.3.12 Transmission Electron Microscopy (TEM)

Experiments were carried out on a Tecnai T12 and Tecnai F20 TEM (FEI, Eindhoven, The Netherlands) equipped with a thermionic source under 120 kV and a Schottky emitter under 200 kV acceleration voltages, respectively. For TEM investigations, thin films on glass were pre-cut in squares (2 × 2 mm^2)

via a scalpel, followed by immersion into deionized water to get free floating films in analogy to XRD specimens. The respective fragments could then easily be collected via nickel TEM grids (200 mesh). Prior to TEM investigations, the films were regenerated on the grid as described above and dried overnight (T = 50 °C) in a desiccator with silica beads. NCC films were prepared by dropping a diluted (1:10) NCC stock solution on carbon-Formvar® coated TEM copper grids (200 mesh) and excessing liquid was carefully removed after 1 min by side-wall contact with filter paper. Subsequently, specimens were stained in a droplet of uranyl acetate solution (2 wt.%) for 2 minutes. Excess solution was washed thoroughly with deionized water and dried for 24 hours (T = 50°C) in a desiccator with silica beads. TEM investigations were done on several films and on multiple spots with lowest possible dose conditions to prevent electron induced material damage.

IV.3.3.13 Scanning Electron Microscopy (SEM)

Investigations were carried out on a ULTRA 55 (ZEISS, Oberkochen, Germany) microscope with primary energies below 3 keV and the highly sensitive in-lens SE / BSE detector to enable low dose inspection. NCC films were prepared by spin coating a diluted (1:4) NCC-stock-solution with the same parameter as described above. Prior to SEM investigation, specimens were coated with an Ir Layer (10 nm) via low dose PVD in an EM ACE 600 (Leica, Vienna, Austria) to achieve electric surface conductivity for SEM imaging.

IV.3.4 Results and Discussion

So far, a variety of substrates were applied to study the hydrolytic activity of different cellulases. The special requirements of AFM operation usually require elaborate preparation routines to gain a sufficiently flat topology. In particular, high crystalline bacterial, cotton[47,48], or pretreated amorphous celluloses [38,47–50] are extensively used. Although impressive results were obtained, a controllable and laterally distinguishable polymorphism is difficult to obtain by these substrates. The approach presented here uses preparation protocols from literature [36,40,42,51] concerning TMSC solutions further expanded by the careful addition of so called nano-crystalline-cellulose (NCC) whiskers in different concentrations. As will be shown, the narrow size distribution and highly crystalline NCC character (cellulose I$_\beta$) in combination with the miscibility by the introduced protocols, enables the fabrication of truly semi-crystalline cellulose substrates with variable and controllable crystallinity. Beside the key element of a side-by-side arrangement of crystalline and amorphous cellulose areas, the flat topology allows high-resolution and high-speed AFM imaging with quantifiable degradation rates. In the following, we start with a detailed characterization of individual substrate components which are further used to fabricate the semi-crystalline-thin-film-cellulose (SCTFC) substrate.

IV.3.4.1 Characterization of semi-crystalline thin film

Thin films of TMSC as well amorphous-, nano-crystalline and semi-crystalline thin film celluloses (TMSC, NCTFC, ATFC, SCTFC) were initially analyzed via WAXS and Raman spectroscopy for morphological and chemical details. Figure IV-13a shows the results for the crystalline (NCTFC; top, red) and amorphous (ATFC; bottom, green) part which later are used within the semi-crystalline

substrate. Corresponding reference patterns for cellulose I$_\beta$ and amorphous cellulose are also shown (see indications). For NCTFC the diffraction pattern corresponds to the crystalline cellulose-I$_\beta$ reference (top, black) which proves the intended crystallinity of nano-crystalline thin films. The diffraction patterns for ATFC (green) shows two main features: **1)** a broad diffuse peak around 20° consistent with an amorphous structure (reference)[52,53]; **2)** a minor peak around 12.2° which correlates to the (1$\bar{1}$0) diffraction-peak of cellulose II (blue)[10,14,36,54]. Although, this indicates a predominantly amorphous nature of the film, the additional diffraction peak may indicate an ordering in the film. Detailed AFM investigations revealed some fibrillary structures reminiscent of ordered celluloses (see Figure IV-14). We want to emphasize that similar structures were already observed in previous studies by Kontturi et al. as well as Notley and Wågberg[55,56] who attributed this effect to the well-known cellulose hornification tendency after full drying. We observed similar structures on substrates not fully dried which may suggest that the structures are the result of the fabrication process itself and that drying of films has an reinforcing effect in terms of fibrillation[37]. In summary, regenerated ATFC cellulose films show ordered cellulose reminiscent structures on the surface but prove to be predominately of the amorphous allomorph (see WAXS data). No correlation to TMSC patterns further confirms full regeneration to cellulose by the presented protocol. Therefore, we can deduce that NCTFC and ATFC films result in highly crystalline (cellulose-I$_\beta$) and mainly amorphous cellulose as intended.

Complementary chemical information was obtained by Raman spectroscopy summarized in Figure IV-13b. The direct comparison of NCTFC and cellulose-I$_\beta$ (top, red) reveals, as expected, identical spectra, without evidence of impurities[15,57]. Here, it is noteworthy, that sulfuric acid treatment of cellulose results in sulfonic ester groups which are present on the surface of the crystallites. However, corresponding to the Raman results, the concentration is below the limit of detection which is supported by earlier studies using conductometric titration and EDS which revealed an atomic sulfur content of 0.24% which is considerably low[58].

For amorphous ATFC layers (Figure IV-13; bottom, green), the direct comparison reveals full conformity with the amorphous reference spectra (orange) in good agreement with literature and confirms the successful regeneration to pure cellulose[12,15]. Characteristic peaks are indicated for crystalline (+) and amorphous cellulose (--). In summary, the presented Raman and WAXS data reveal NCTFC and ATFC as fully crystalline and amorphous materials from a chemical and morphological point of view, respectively.
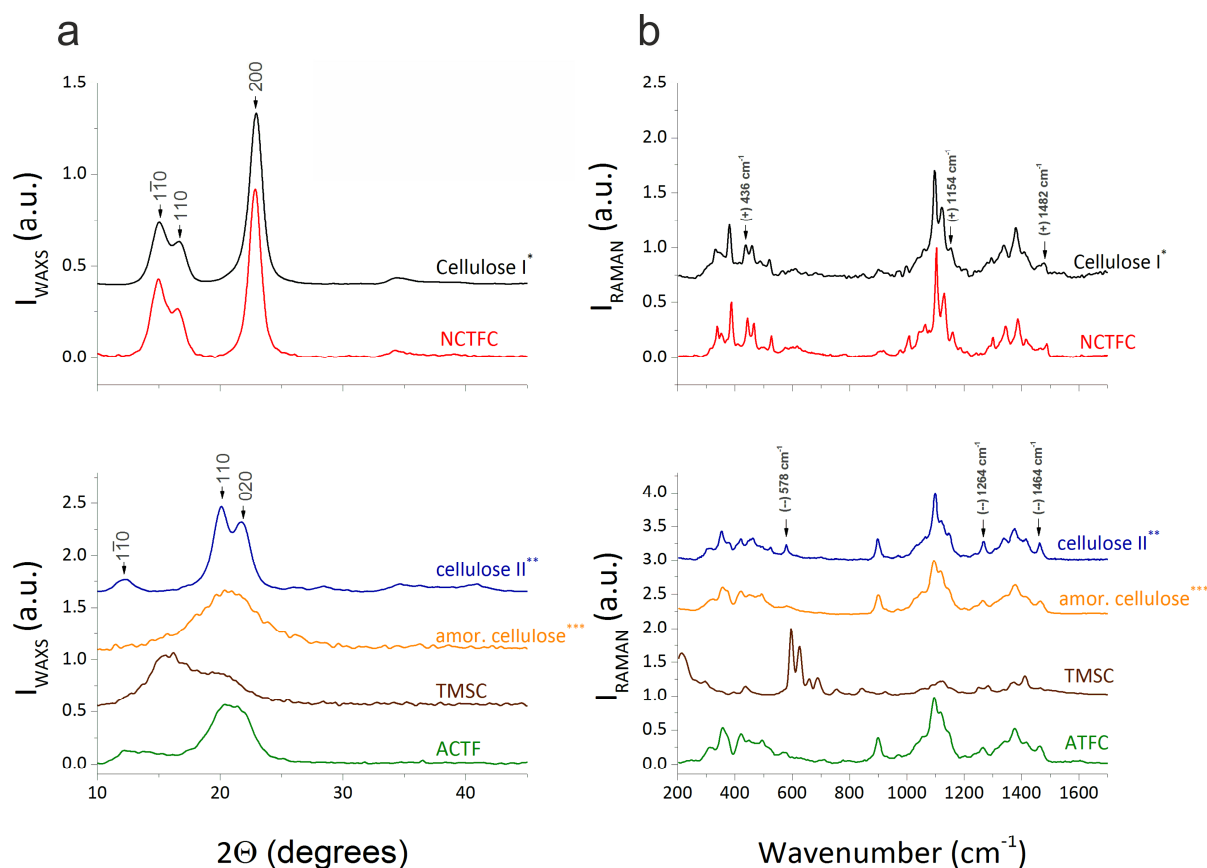
Figure IV-13: (a) WAXS diffraction patterns of NCTFC (red), TMSC (brown) and ATFC (green) with the corresponding reference patterns for cellulose-I_β(black),–II (blue) and amorphous cellulose. Cellulose I_β was from Whatman No.1 filter paper (*), Cellulose II from mercerized Avicel PH-101 (**) and amorphous cellulose (orange) from a regenerated cellulose produced by solvation in 1-Butyl-3-methylimidazolium chloride according to the protocol from the literature[2]. NCTFC films show the same diffraction pattern as cellulose-I_β (upper panel) demonstrating the successful transfer from Whatman No. 1® filter paper into nano-crystalline thin films. ATFC shows a predominantly amorphous characteristic with low indications of cellulose-II and no correlation to the TMSC source material (lower panel). (b) Raman spectroscopy of NCTFC (red), TMSC (brown) and ATFC (green) in comparison to that of cellulose-I_β (black), -II (blue) and amorphous reference spectra. In accordance to WAXS data, NCTFC and ATFC reveal the same chemical signatures as those for crystalline and amorphous reference materials which confirm the preparation protocols as successful. Characteristic bands are highlighted for amorphous (--) and crystalline (+) cellulose.
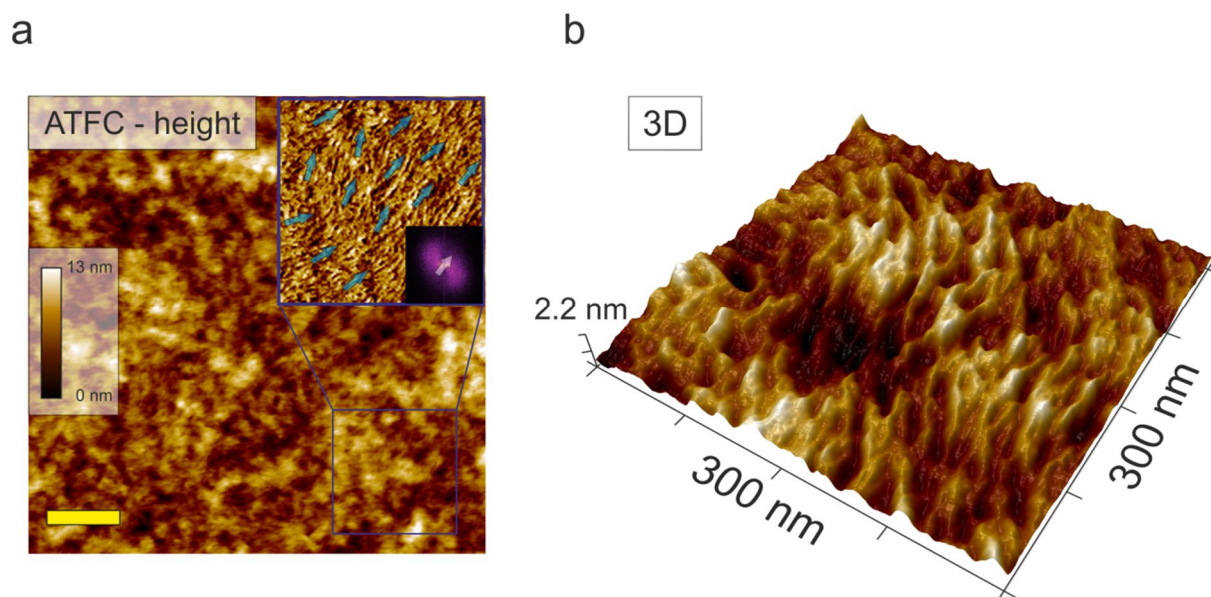
a

b

Figure IV-14: AFM images of amorphous cellulose surfaces showing fibrillary structures. (a) AFM height image of ATFC topography showing the usually observed non-structured surface. High resolution phase contrast imaging of the highlighted area (inset) allows however to distinguish clearly between individual fibrillary structures and shows a preferred direction (blue arrows). A FFT map of the whole image demonstrates a specific preferred direction of the fibers most likely introduced by the spin-cast process (white arrow). (b) 3D high resolution AFM image of a similar ATFC film. Scale bar represents 200 nm.

Besides morphological and chemical properties, surface structure is of significant importance for high-resolution, *in-situ* AFM as step edges, pin holes or protrusions may induce unwanted convolution effects in the imaging. Furthermore, small holes, obstacles and available surface area are strongly influencing enzymatic hydrolysis and should therefore be known.[1,28,50] Figure IV-15a shows a representative 3D AFM height image (left) together with a high-resolution image of an ATFC film (right) confirming the homogeneous and compact surface morphology. Roughness analyses revealed root mean square (RMS) values of less than 2 nm over an area of $10 \times 10 \ \mu m^2$ in good agreement with literature[36] which justifies the notation "nanoflat". Figure IV-15b summarizes the layer thickness as a function of TMSC concentration at fixed spin-coat process parameters for dry (red diamonds) and fully water swollen films (blue circles). The first thing to notice is the controllable film thickness which scales almost linearly with TMSC concentrations for the studied range between 20 nm and 100 nm in dry conditions. Full swelling in buffer solution causes a 100 % increase of film thickness (blue circles) without significant increase of RMS values.
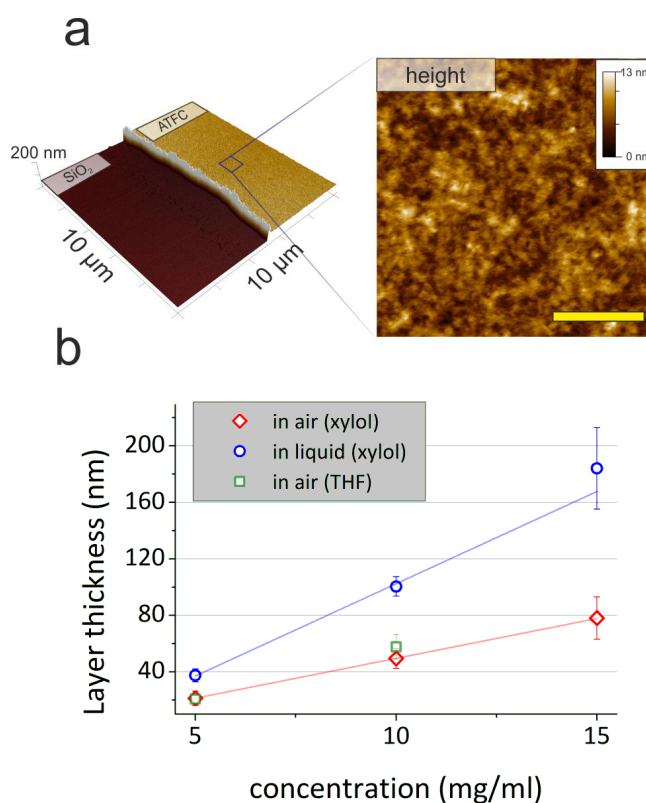
Figure IV-15: (a) AFM height images (3D; left) and in high resolution (2D; right) of ATFC films which reveal a crack-free and compact surface morphology (scale bars are 200 nm) with an RMS roughness below 2 nm over areas of 10 x 10 µm². The step at the left side has been made via careful scratching via tweezers which enable absolute thickness and volume loss determination. (b) ATFC film thickness in dry and liquid conditions as a function of TMSC concentrations for constant spin-cast parameters and varying solvents.

For NCTFC we extended our investigation to electron microscopy methods to obtain comprehensive knowledge on crystal size and shape. Figure IV-16a shows morphological results obtained via AFM (top), TEM (bottom left) and SEM (bottom right) imaging. As expected NCC whiskers show an elliptical shape [40,59] and form partly covered layers. To get statistically relevant data, more than 200 particles were characterized on different specimens via each technique as summarized in Figure IV-16b for their lengths (left) and widths (right). Direct comparison reveals, in good agreement with literature, average lengths and widths of 127±45 nm and 17±6 nm, respectively [40]. Please note, while the lengths are in good agreement for all techniques, the width analyses via AFM is prone to tip convolution effects by the finite size and shape of the probe apex and the opening angle explaining a broader distribution in the same range as the tip radius (~ 10 nm). Furthermore, the partly stacked NCC layers also prevented reliable AFM height measurement of individual particles. Hence, to avoid convoluted AFM data we have used TEM based widths (Figure IV-16b, green) as the most reliable value for NCC widths specified above. SEM data on width are also not included due to the metallic surface coating (>10 nm) which convolute the derived data.

In summary, the sole ATFC and NCTFC substrates are suitable for *in-situ* AFM experiments and show the required properties by means of crystallinity, purity and nanoflat topology. As a final step the combination of both components is anticipated to achieve the desired semi-crystalline substrate for advanced studies on the synergistic activity of different types of cellulases.
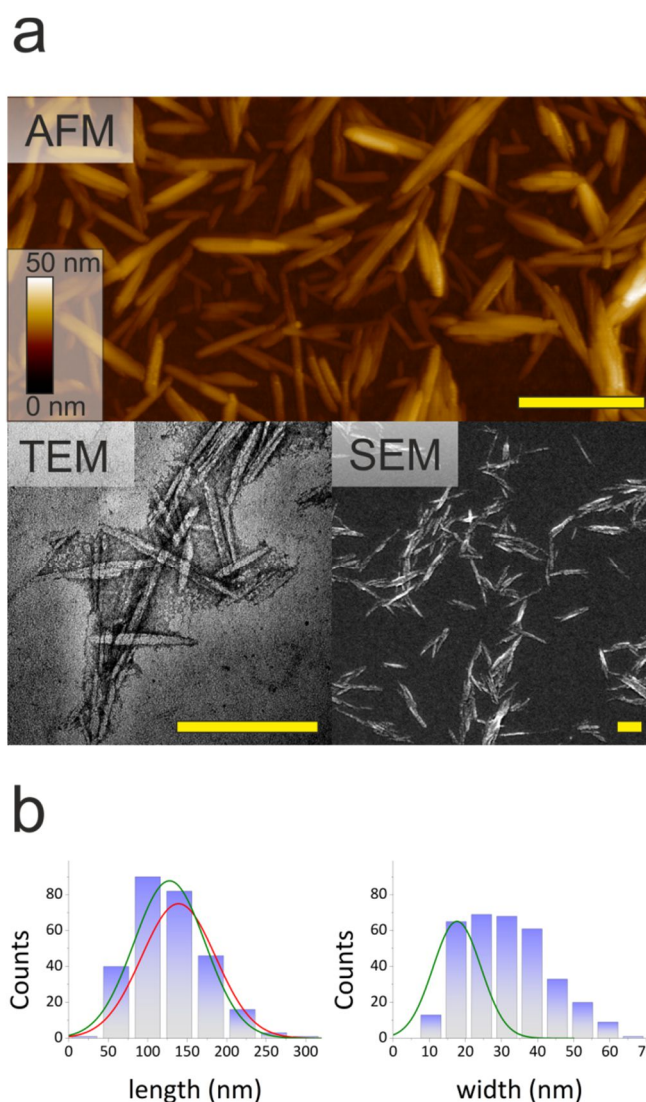
Figure IV-16: (a) AFM height (top), SEM (bottom right) and TEM images (bottom left) of crystalline thin films which confirm the elongated needle shape of NCCs as expected (scalebars are 200 nm). (b) Statistical analyses by AFM (blue bars), SEM and TEM methods with a size distribution revealing 127 ± 45 nm of 17 ± 6 nm in length and width. Histogramm data was fitted as normal distribution (red, SEM; green, TEM) and mean values were taken from TEM results. Please note, while lenghts are very similar for all techniques (upper panel), AFM based results for the particle width are shifted to higher values due to tip convolution effects.

IV.3.4.2 Characterization of semi-crystalline thin film

As a first step, we aimed our analysis on typically used non-polar solvents [49,59] which are poorly suited for a combination with water based NCC stock solutions. Tetrahydrofuran (THF) which is used in the production of TMSC [55,60] was used to overcome this problem. Preparation of films is identical to ATFC films with the exception that after full dissolution of TMSC varying quantities of NCC stock were added. In a first experiment, 5 µl of NCC stock were dissolved in THF_{10} and dispersed for about 30 seconds in an ultrasonic bath. Films were spin-coated and transferred to TEM grids, cured in HCl and imaged via AFM and TEM to access surface and projected bulk information, respectively. As shown by a TEM bright field image in Figure IV-17a, SCTFC proves to be constituted of well dispersed crystallites (dark) in the amorphous cellulose matrix (bright). However, occasionally occurring

agglomerations cannot be entirely avoided. Correlated AFM experiments revealed minor increase of RMS (2 nm → 4 nm; data not shown) compared to $Xylol_{10}$ without significant change in film thickness (see Figure IV-19).

To exclude the possible surface confined agglomeration of NCC particles, Figure IV-18 shows the results of nano-mechanical AFM experiments (PeakForce Tapping®) on SCTFC. The image shows the film in proximity of a scratch (dark area at the left) which was produced as described in the experimental section. The three insets at the left represent the zoom area in the large image with morphology (top), stiffness (center) and surface deformation (bottom). Nano-crystals are found on (white arrows) and below the surface (gray arrows) consistent with higher stiffness and lower deformation information. Moreover, a direct comparison between the NCC crystal densities on the surface (AFM) and the bulk (TEM) confirms that only a small fraction is found on the surface which further confirms a spatial distribution of NCC within the SCTFC film.

Finally, to prove the tunable contents of cellulose crystals, additional experiments were conducted with different NCC-to-TMSC ratios at constant total TMSC concentrations to provide identical film thicknesses. Figure IV-17b gives the TEM based summary derived from several samples and multiple imaging areas on each to provide reasonable statistics. As can be seen, there is an almost linear increase of NCC particles for the range of 5 µl mL^{-1} - 15 µl mL^{-1} NCC stock solutions in THF_{10}. Furthermore, correlated AFM characterizations revealed constant film thickness and surface roughness of 49±4 nm and 6±0.2 nm, respectively. The latter is attributed to a higher number of protruding nano-crystals as shown later. Please note, even higher NCC concentrations would be possible but viscosity is increased by addition of higher amounts of NCC and smooth films are thereby difficult to achieve. It may be noteworthy that higher ratios may be achieved by using an alternative protocol with alternating spin coating of crystalline and amorphous layers.
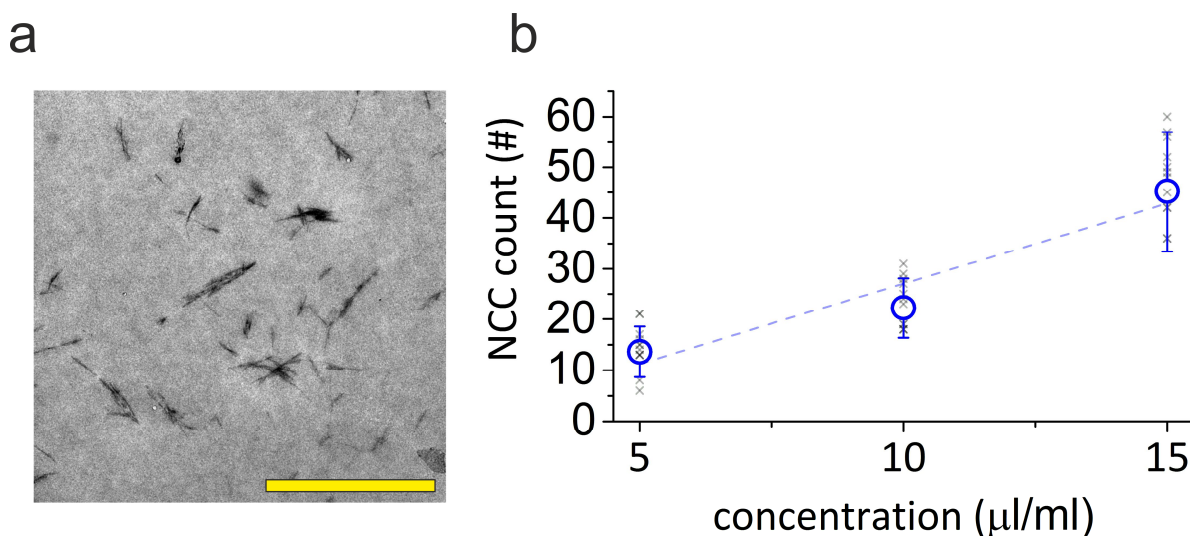

Figure IV-17: (a) TEM bright field image of a 50 nm thick SCTFC film revealing the well dispersed character of NCC (dark) within the bulk matrix (scalebars are 2 µm). (b) Plot of the number of NCC particles in 6 x 6 µm² images confirming the controllable crystallinity of the presented semi-crystalline model substrate.

In summary, the combined investigations prove that the mixing of crystalline and amorphous compounds (TMSC and NCC) is possible to fabricate the desired semi-crystalline-thin-film-cellulose (SCTFC) substrates. TEM and AFM characterizations show evenly distributed crystallites within an amorphous matrix, as desired. In the following the substrates, in particular, the semi-crystalline substrate, is tested to demonstrate the proposed feasibility for AFM studies on the degradability of polymorphous substrates by various cellulases.
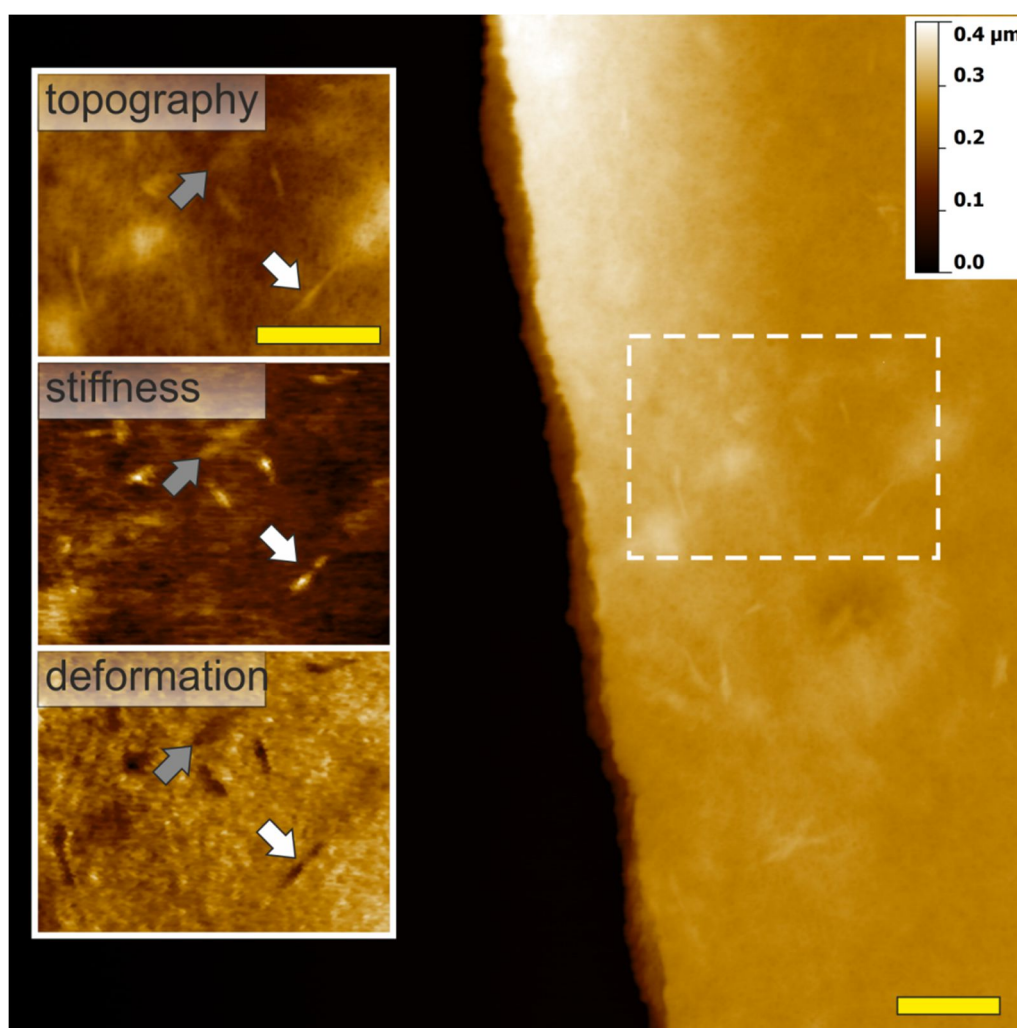

Figure IV-18: AFM height image of a SCTFC layer (large image) with a scratch at the left. The three insets give a topography close up (top) and correlated stiffness (center) and deformation (bottom) information via PeakForce tapping®. The analysis shows that crystallites are found on the surface (white arrows), but also below the surface (gray arrows) where a buried crystallite is shown by a positive stiffness and negative deformation singnal but no crystallite in the topography. As expected, NCCs show higher stiffness values and lower deformation depths further confirming TEM data (scalebars are 1 µm).
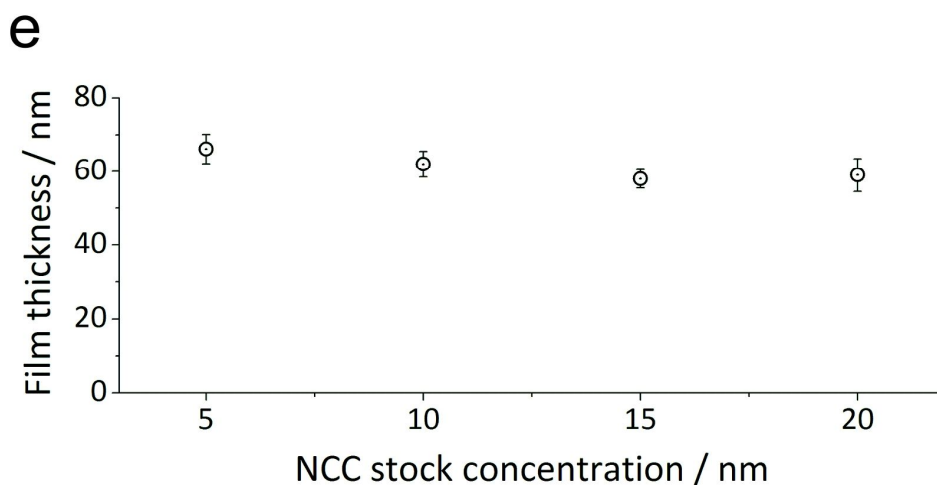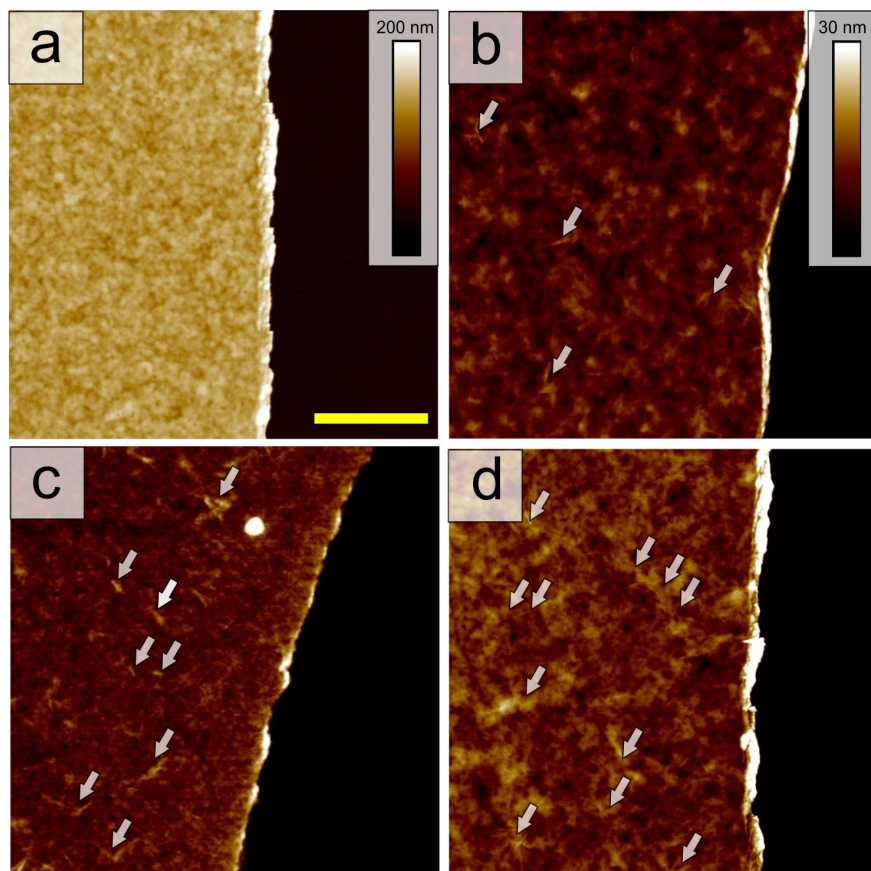
Figure IV-19: AFM topography of THF$_{10/5}$ (a), THF$_{10/10}$ (b), THF$_{10/15}$ (c), and THF$_{10/20}$ (d) prepared SCTFC films after curing. (a) Full height image (200nm) of a thin film with 5 µl NCC stock incorporated nano-crystallites. For (b-d) a smaller height scale was chosen in order to visualize surface bound nano-crystallites (white arrows). Please note that the crystallites are small and thus not well resolved. The concentration on the top surface, in accordance with TEM data, is gradually increased. To exclude thickness biased counting in TEM images (Figure IV-17), we have measured the thickness of each film (d). Here the thickness variation is within 5 nm. Scale bar represents 1 µm.

IV.3.4.3 Application of semi-crystalline films in in-situ AFM experiments

After the comprehensive material analyses in agreement with previous literature, we subjected the SCTFC substrates to a feasibility study via dynamic, *in-situ* AFM experiments to confirm its suitability with respect to the intended purpose. For that, we first exposed SCTFC substrates to full cellulase cocktails of *Hpocrea jecorina (*former *Trichoderma reesei*) with its typical major components *Hj*Cel7A, *Hj*Cel6A and *Hj*Cel7B[1,9,47,61]. As shown by the supplementary Movie S9, SCTFC substrates are fast and entirely degraded by the enzyme cocktail. In agreement with literature and recent results of cellulose degradation by cellulases[1,9,47,61,62], amorphous parts of the substrate are primarily degraded, which leads to excavated cellulose crystals. Following excavation these are then attacked by the ablative activity of exo-glucanase activity. These first investigations confirm the suitability of SCTFC materials for high-resolution, *in-situ* and high-speed AFM experiments to unravel the cellulolytic activity of cellulases. Another unique aspect of such SCTFC layers is the absolute determination of degradation rates which can be achieved by a preliminary scratch which introduces a non-affected silicon dioxide reference level. This is of particular interest in the sequential application of different cellulases to study the specific synergistic activities[1,48]. In one of our earlier studies[1] we have observed that *Hj*Cel6A shows significant affinity for amorphous cellulose. Briefly, *Hj*Cel6A seems to initially attack the amorphous matrix material, thus uncovering the crystalline cellulose. As a consequence free chain ends get available and are slowly degraded by *Hj*Cel6A. The resulting bi-specific activity turns out to be of significant importance on small crystalline features[1]. The combination with *Hj*Cel7A is of interest as significant synergism is expectable simply by the fact that now available chain ends boost its processive and ablative activity[31,32]. We therefore have chosen the exo-exo synergism between *Hj*Cel7A and *Hj*Cel6A as a representative example. Figure IV-20 summarizes the sequential incubation by *Hj*Cel6A and *Hj*Cel7A on SCTFC substrates (THF$_{15/5}$) demonstrating local cellulolytic events by AFM image analysis (a) and complementary automated and quantitative determination of degradation rates (b). As shown in Figure IV-20a (upper row), *Hj*Cel6A activity leads first to a gradual removal of amorphous substrate material. Thereby, cellulose crystallites are excavated (indicated by arrows in 1 – 4) and slowly degraded which is in conformity to our recent results[1,9]. Adding *Hj*Cel7A yields similar results, however, with much higher degradation rates of crystalline areas as indicated by the white arrows in the lower row of Figure IV-20a. From a quantitative point of view, we found a significantly faster overall volume loss after injection of *Hj*Cel7A (*Hj*Cel6A: 0.06 ± 0.01 nm min^{-1}; *Hj*Cel6A + *Hj*Cel7A: 0.31 ± 0.02 nm min^{-1}) as evident by the linear interpolation in Figure IV-20b. The corresponding time scales to remove a crystalline feature are highlighted in Figure IV-20b by blue and red arrows for *Hj*Cel6A and *Hj*Cel6A + *Hj*Cel7A, respectively. The time resolved evaluation of RMS surface roughness[63] reveal a slow increase during *Hj*Cel7A exposure followed by strong increase after adding *Hj*Cel7A which correlates well with localized AFM results and volume loss data (Figure IV-20) due to the synergistic activity (see Figure IV-21).
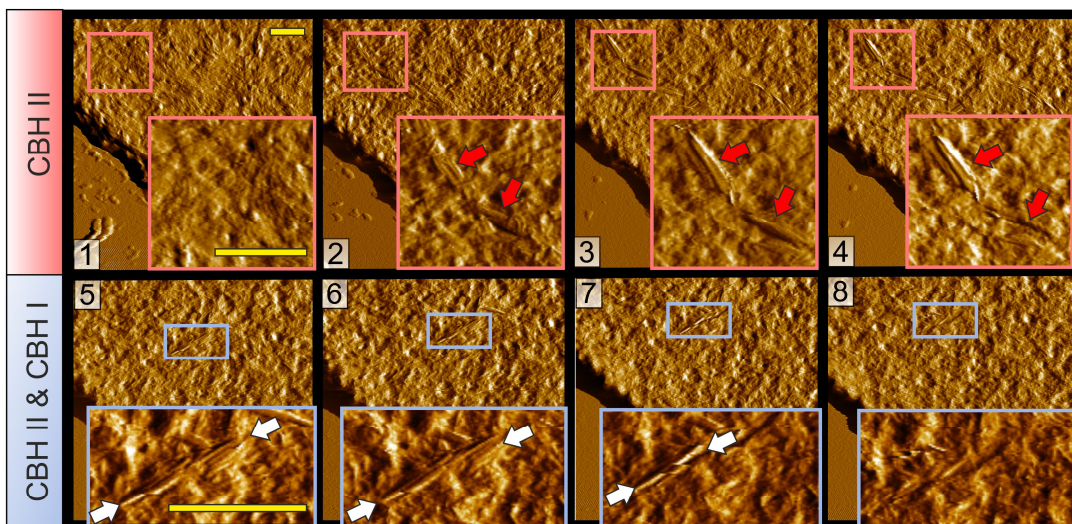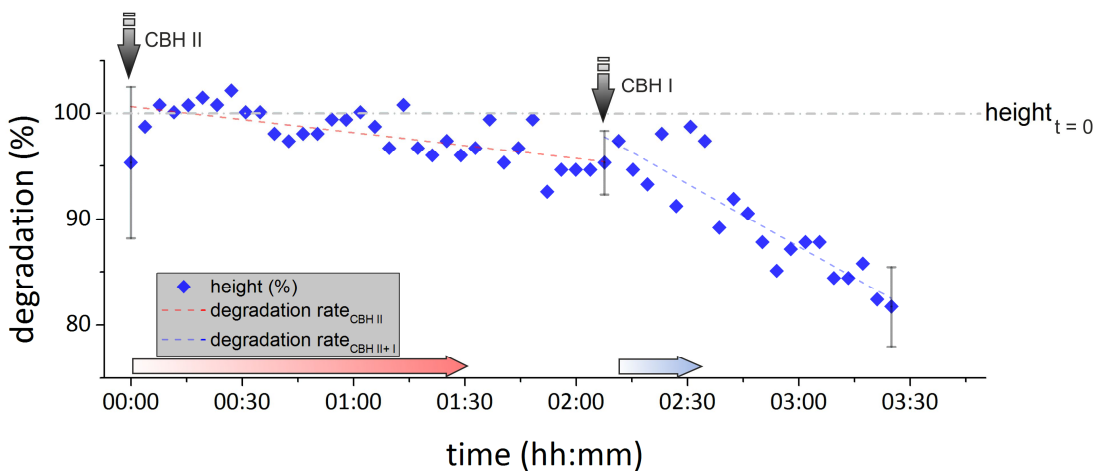
Figure IV-20: (a) AFM amplitude images of an in-situ experiment of SCTFC degradation by attack of HjCel6A showing a gradual removing of amorphous material covering crystallites, followed by slow degradation of the crystallites (1-4; red insets; crystallites are highlighted by arrows). Addition of HjCel7A shows two effects: The volumetric degradation speed is increased (b) and more crystallites appear and are removed by the combinational attack at faster rate (5-8; blue insets; prefereed direction of degradation: white arrows). (b) Corresponding degradation in percent of the maximum film thickness showing a rate of 0.06 ± 0.01 nm and 0.31 ± 0.02 nm per minute for HjCel6A and HjCel6A plus CBH-I, respectively. Grey arrows indicate the time HjCel6A and HjCel7A were added and red and blue arrows correspond to the time in images above (a) for CBH-II (1-4) and HjCel6A & HjCel7A(5-8), respectively. Errorbars were calculated from three independent measurment methods of the layer height (height distribution, section analysis, bearing analysis). Scale bars are 200 nm.
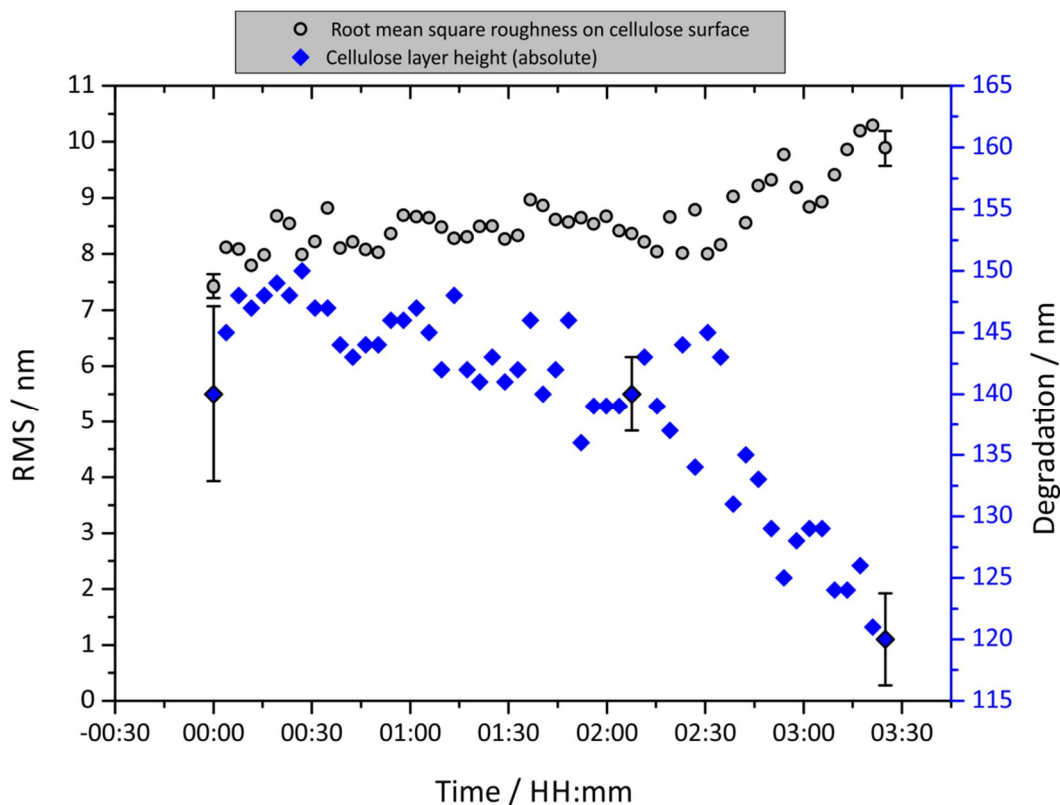
Figure IV-21: RMS (left ordinate, grey circles) analysis during the hydrolytic activity of HjCel6A (00:00 – 02:10) and HjCel6A plus HjCel7A (02:10-03:27). At first, a weak RMS increase is observable triggered by the hydrolytic activity of HjCel76A and the corresponding removal of amorphous material together with the excavation of crystalline features. After addition of HjCel7A (02:20), the RMS increases again which is in agreement with synergistic activity of the cellulases in combination.

To allow a comparison to biochemical data, we conducted the same experiments on ATFC and NCC as the representative allomorphs contributing to the decomposition of SCTFC. For ATFC (Figure IV-22), a comparable and synergistic activity for the individual and combined cellulases is found, respectively. On MACS[1,2], we have observed higher rates for *Hj*Cel6A against *Hj*Cel7A which resulted from the bi-specific activity. On SCTFC, it is feasible to assume an influence of the higher ordering in the film which we observed by WAXS and AFM analysis (Figure IV-13 and Figure IV-14). A higher ordering of the cellulose must result in larger mean free paths for *Hj*Cel7A, thus boosting activity and higher degradation rates on SCTFC. On NCC films (Figure IV-22, NCC), the total amount of released reducing sugars is close to the limit of detection (less than one monolayer of crystallites on the silicon dioxide substrate; Figure IV-16) which renders analysis to be difficult. Here, no expected synergism is observable and individual activities are close to equal. To account for this problem, we performed the same experiment on free dispersed NCCs in solution (see Figure IV-23). Here, the expected predominance of *Hj*Cel7A and the corresponding synergism is demonstrated. The resulting cyclic mechanism by removal of crystallite covering amorphous material and following crystallite degradation seems to be a characteristic feature on the exo-exo synergism of *Hj*Cel7A and *Hj*Cel6A. A similar study by Kontturi and coworkers[43] using QCM-D showed a less prominent effect of exo-glucanases on ATFC. The authors compared the activity of *Hj*Cel7A (exo) and *Hj*Cel7B (endo) on a to ATFC similar substrate by monitoring the frequency and dissipation change over hydrolysis time. While *Hj*Cel7B was effective in degrading the amorphous cellulose, *Hj*Cel7A was not over 60 minutes

after incubation. In contrast, the data presented in Figure IV-20 shows that exo-glucanase activity is degrading SCTFC. However, despite the fact that *Hj*Cel7A was not observed alone in the here presented AFM experiment, we applied longer timescales (Figure IV-20). A comparison of glucose release obtained in Figure IV-22 for *Hj*Cel7A and *Hj*Cel6A allows the conclusion that degradation rates are close to equal on ATFC. Thus considering the volume loss in Figure IV-20 for *Hj*Cel6A allows concluding that *Hj*Cel7A on ATFC may show similar hydrolytic activity which results in a volume loss of approximately 3-5% which is in good agreement with the study performed by Kontturi and coworkers [43]. Furthermore by setting *Hj*Cel7A activity equal to *Hj*Cel6A, a synergism of approximately 2.5 for the exo-exo system may be derived from Figure IV-20 which is in well agreement with literature[35,64].
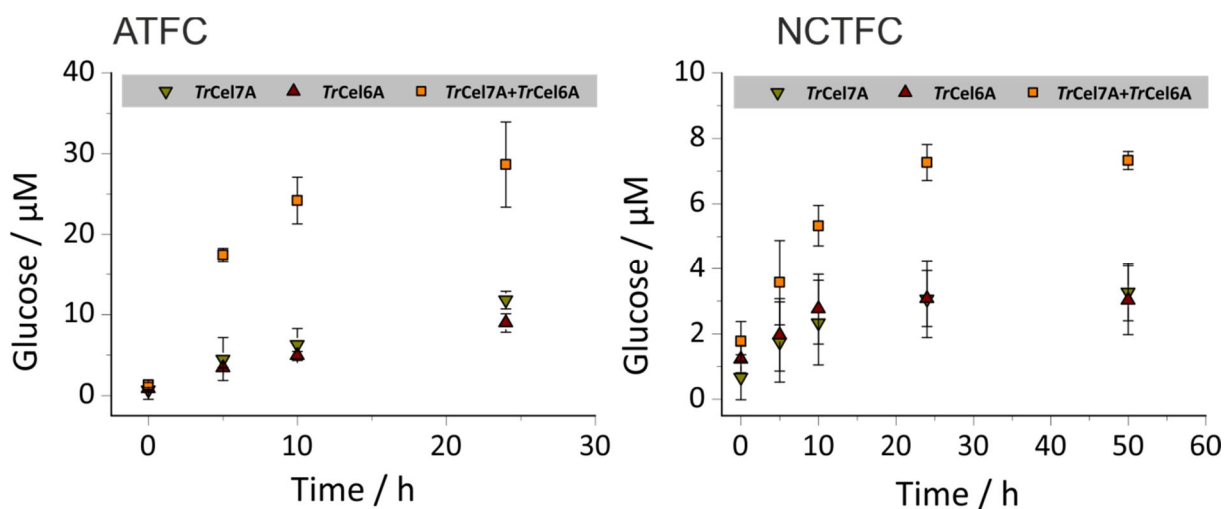

Figure IV-22: Synergy between HjCel7A and HjCel6A on ATFC (a) and NCTFC (b) determined over 24 hours and 50 hours incubation, respectively. On ATFC, HjCel7A shows slightly higher activity compared to HjCel6A which can be attributed to a higher ordering of cellulose chains in the amorphous films as seen in Figure IV-13. On NCC films (NCTFC) with a relative low amount of degradable material, the released sugars are too low for detectable synergism (Synergism is within error bars). To account for this problem we have performed complementary experiments on free NCCs as demonstrated in Figure IV-23.

In conclusion, during this feasibility study of SCTFC substrates, it is again confirmed that the surface morphology strongly influences enzymatic cellulose hydrolysis in agreement with previous literature[1,65]. These experiments prove that SCTFC is a well suited, standardized cellulose model substrate which is tailored to fit the requirements for easy and successful AFM operations and the common nature of cellulose as a polymorphous substrate. By that, analysis of enzymatic cellulose degradation is possible in real time via high speed AFM experiments with the additional possibility to quantitatively analyze the degradation rate on the fixed silicon dioxide reference. By the combination with biochemical data comprehensive information of cellulolytic activity of different cellulases is available from an integral and a nanoscale point of view which essentially expands the insight in biomaterial and related dynamic processes.
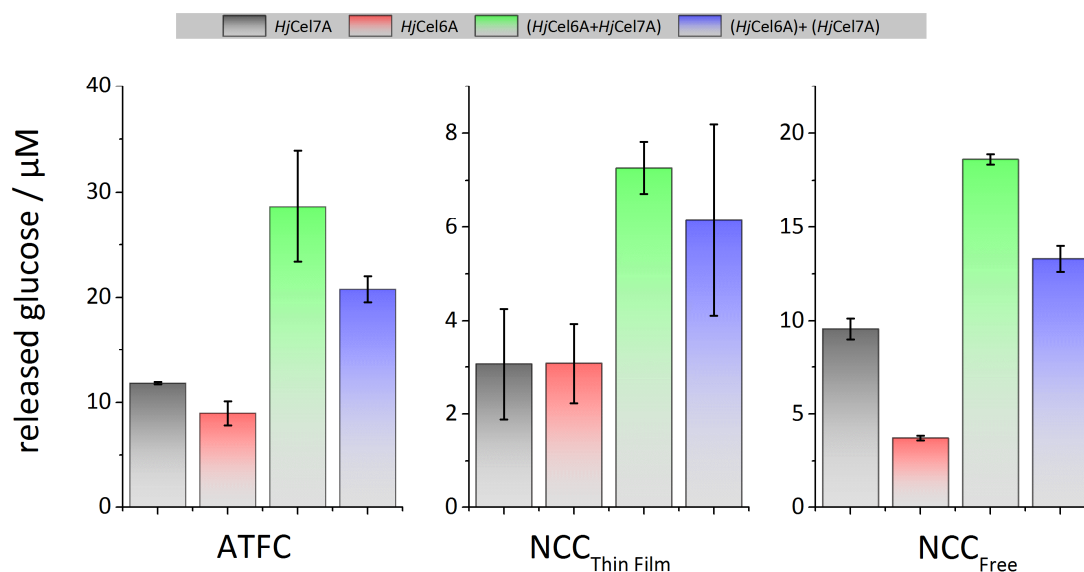
Figure IV-23: Release of reducing sugars for ATFC, NCTFC (NCC_Thin Film) and free NCC (NCC_Free) after 24 hours of incubation. Black, red and green bars show released glucose in µM for HjCel7A, HjCel6A and the combination of enzymes, respectively, against the theoretical calculated sum of both release activities in blue. On ATFC individual cellulase activities are comparable while being synergistic in combination. On spin-cast NCC films, the relative low degradable amount of substrate and high recalcitrance of crystalline cellulose are exacerbating analysis (detectable synergism is within error bars). Complementary experiments using free dispersed NCC (18.75 mg L^{-1}) clearly indicate the expected higher activity for HjCel7A and synergism. Experiments were performed in duplicates at 50°C. Liberation of glucose was assayed via high pressure liquid chromatography (spin-cast substrates) or colorimetrically with glucose oxidase and peroxidase (free NCC)[16].

IV.3.5 Conclusions

In this study, a semi-crystalline-thin-film-cellulose (SCTFC) substrate is introduced which unifies several demands on a cellulose model substrate: **1)** fast, simple and reproducible preparation, **2)** polymorphic character with tunable contents of homogeneously sized cellulose nano-crystals embedded in an amorphous cellulose matrix, and **3)** a nanoflat topology. While the former is of high relevance concerning the reliability in consecutive experiments and provides an ease-of-use character, the latter point is essential for high scan speeds and high spatial resolution during *in-situ* AFM experiments. The most striking aspect, however, is the tunable polymorphism which can unravel synergistic effects of different enzyme species on different cellulose phases in a side-by-side fashion. This not only provides entirely new capabilities for fundamental insights concerning elementary effects on nano-crystalline cellulose and amorphous phases in between as well as synergism but also can be used for application oriented optimization once the local processes are unraveled.

IV.4 Chapter Summary

The here introduced concepts to fabricate appropriate model substrates featuring an adjustable degree of polymorphism (crystalline/amorphous) are a good basis for further conducted AFM experiments. MACS and SCTFC showed both, high feasibility in AFM experiments, as well biochemically conducted experiments, which offers a valuable tool to compare results obtained with both techniques. Although both substrates are well suited, there are significant differences in between. While SCTFC was designed for high-speed AFM measurements at highest available resolution, MACS offers a broader range of crystallite sizes which proved to be of significant influence for the degradation activity (see next *chapter*). SCTFC included nano-cellulose which is thought to represent the smallest crystalline unit in cellulose fibers. These highly crystalline needles are highly recalcitrant to hydrolysis and state a major obstacle for enzymes. It is thus highly interesting to visualize effects on these entities. In contrast, MACS offers small and large crystals and allows the analysis of both on one substrate. In both cases, a common feature is the mixture of amorphous matrix with crystalline celluloses. This combination is interesting, because clear separation of phases is available which in most natural cellulose sources is difficult to achieve or visualize. An advantage of SCTFC may be the readily preparation and flat character from the beginning, while MACS requires long preparation times and elaborate processes to gain absolute flat specimens. Summing up SCTFC features: An **easy preparation and flat topology** with small and evenly distributed nano-crystallites; an **extremely well defined reproducibility with a fixed reference** (silicon substrate). MACS features: **Larger and smaller crystallites** with a disadvantage of **elaborate preparation**, however, the possibility to **prepare large quantities at once**. **Both** show **tunable polymorphism** as a key requirement for our further investigations of synergistic cellulase activity. Combining advantages and disadvantages of both, we may state that the substrates feature a complementary set of standardized substrates, which may be used well in dedicated and comprehensive experimental setups to unravel complex interdependencies between cellulases and substrate morphologies.

IV.5 References

[1]   T. Ganner, P. Bubner, M. Eibinger, C. Mayrhofer, H. Plank, B. Nidetzky, *J. Biol. Chem.* **2012**, *287*, 43215.

[2]   T. Ganner, T. Aschl, M. Eibinger, P. Bubner, A. Meingast, B. Chernev, C. Mayrhofer, B. Nidetzky, H. Plank, *Cellulose* **2014**, *21*, 3927.

[3]   C. Graenacher, *Cellulose Solution*, **1934**, US Patent 1934176.

[4]   J. Vitz, T. Erdmenger, C. Haensch, U. S. Schubert, *Green Chem.* **2009**, *11*, 417.

[5]   R. P. Swatloski, S. K. Spear, J. D. Holbrey, R. D. Rogers, *J. Am. Chem. Soc.* **2002**, *124*, 4974.

[6]   P. Mäki-Arvela, I. Anugwom, P. Virtanen, R. Sjöholm, J. P. Mikkola, *Ind. Crops Prod.* **2010**, *32*, 175.

[7]   M. Zavrel, D. Bross, M. Funke, J. Büchs, A. C. Spiess, *Bioresour. Technol.* **2009**, *100*, 2580.

[8]   P. Bubner, J. Dohr, H. Plank, C. Mayrhofer, B. Nidetzky, *J. Biol. Chem.* **2012**, *287*, 2759.

[9]   M. Eibinger, P. Bubner, T. Ganner, H. Plank, B. Nidetzky, *FEBS J.* **2014**, *281*, 275.

[10]   S. Park, J. Baker, M. Himmel, P. Parilla, D. Johnson, *Biotechnol. Biofuels* **2010**, *3*, 10.

[11]   A. D. French, *Cellulose* **2014**, *21*, 885.

[12]   H. Wiley, R. H. Atalla, *Carbohydr. Res.* **1987**, *160*, 113.

[13]   K. Schenzel, S. Fischer, *Cellulose* **2001**, *8*, 49.

[14]   U. P. Agarwal, R. S. Reiner, S. a. Ralph, *Cellulose* **2010**, *17*, 721.

[15]   K. Schenzel, S. Fischer, E. Brendler, *Cellulose* **2005**, *12*, 223.

[16]   M. Eibinger, T. Ganner, P. Bubner, S. Rošker, D. Kracher, D. Haltrich, R. Ludwig, H. Plank, B. Nidetzky, *J. Biol. Chem.* **2014**, *289*, 35929.

[17]   M. E. Himmel, S.-Y. Ding, D. K. Johnson, W. S. Adney, M. R. Nimlos, J. W. Brady, T. D. Foust, *Science* **2007**, *315*, 804.

[18]   V. Kocherbitov, S. Ulvenlund, M. Kober, K. Jarring, T. Arnebrant, *J. Phys. Chem. B* **2008**, *112*, 3728.

[19]   G. Chinga-Carrasco, *Nanoscale Res. Lett.* **2011**, *6*, 417.

[20]   L. M. J. Kroon-Batenburg, B. Bouma, J. Kroon, *Biomacromolecules* **1996**, *9297*, 5695.

[21]   D. Klemm, B. Heublein, H.-P. Fink, A. Bohn, *Angew. Chem. Int. Ed. Engl.* **2005**, *44*, 3358.

[22]   D. Fengel, H. Jakob, C. Strobel, *Holzforschung* **1995**, *49*, 505.

[23]   A. E. Farrell, R. J. Plevin, B. T. Turner, A. D. Jones, M. O'Hare, D. M. Kammen, *Science* **2006**, *311*, 506.

[24]   E. M. Rubin, *Nature* **2008**, *454*, 841.

[25]   D. Graham-Rowe, *Nature* **2011**, *474*, 6.

[26]   U. Bornscheuer, K. Buchholz, J. Seibel, *Angew. Chem. Int. Ed. Engl.* **2014**, *53*, 10876.

[27]   C. M. Payne, B. C. Knott, H. B. Mayes, H. Hansson, M. E. Himmel, M. Sandgren, J. Ståhlberg, G. T. Beckham, *Chem. Rev.* **2015**, *115*, 1308.

[28]   J. M. Moran-Mirabal, N. Santhanam, S. C. Corgie, H. G. Craighead, L. P. Walker, *Biotechnol. Bioeng.* **2008**, *101*, 1129.

[29]   P. Bubner, H. Plank, B. Nidetzky, *Biotechnol. Bioeng.* **2013**, *110*, 1529.

[30]   H. Chanzy, B. Henrissat, R. Vuoung, *FEBS* **1984**, *172*, 193.

[31]   K. Igarashi, T. Uchihashi, A. Koivula, M. Wada, S. Kimura, T. Okamoto, M. Penttilä, T. Ando, M. Samejima, *Science* **2011**, *333*, 1279.

[32]   K. Igarashi, A. Koivula, M. Wada, S. Kimura, M. Penttilä, M. Samejima, *J. Biol. Chem.* **2009**, *284*, 36186.

[33]   M. Hall, P. Bansal, J. H. Lee, M. J. Realff, A. S. Bommarius, *FEBS J.* **2010**, *277*, 1571.

[34]   B. Henrissat, H. Driguez, M. Schülein, *Nat. Biotechnol.* **1985**, *3*, 722.

[35]   B. Nidetzky, W. Steiner, M. Hayn, M. Claeyssens, *Biochem. J.* **1994**, *298*, 705.

[36]   E. Kontturi, et al., *Biomacromolecules* **2011**, *12*, 770.

[37]   T. Mohan, S. Spirk, R. Kargl, A. Doliška, H. M. A. Ehmann, S. Köstler, V. Ribitsch, K. Stana-Kleinschek, *Colloids Surfaces A Physicochem. Eng. Asp.* **2012**, *400*, 67.

[38]   G. Cheng, Z. Liu, J. K. Murton, M. Jablin, M. Dubey, J. Majewski, C. Halbert, J. Browning, J. Ankner, B. Akgun, C. Wang, A. R. Esker, K. L. Sale, B. A. Simmons, M. S. Kent, *Biomacromolecules* **2011**, *12*, 2216.

[39]   E. Kontturi, T. Tammelin, M. Osterberg, *Chem. Soc. Rev.* **2006**, *35*, 1287.

[40]   W. Bai, J. Holbery, K. Li, *Cellulose* **2009**, *16*, 455.

[41]   B. Geier, C. Gspan, R. Winkler, R. Schmied, J. D. Fowlkes, H. Fitzek, S. Rauch, J. Rattenberger, P. D. Rack, H. Plank, *J. Phys. Chem C* **2014**, *118*, 14009.

[42]   C. D. Edgar, D. G. Gray, *Cellulose* **2003**, *10*, 299.

[43]   M. Suchy, M. B. Linder, T. Tammelin, J. M. Campbell, T. Vuorinen, E. Kontturi, *Langmuir* **2011**, *27*, 8819.

[44]   E. Kontturi, P. C. Thüne, J. W. Niemantsverdriet, *Polymer (Guildf).* **2003**, *44*, 3621.

[45]   J. Medve, D. Lee, F. Tjerneld, *J. Chromatogr. A* **1998**, *808*, 153.

[46]   A. Mellitzer, R. Weis, A. Glieder, K. Flicker, *Microb. Cell Fact.* **2012**, *11*, 1.

[47]   A. Quirk, J. Lipkowski, C. Vandenende, D. Cockburn, A. J. Clarke, J. R. Dutcher, S. G. Roscoe, *Langmuir* **2010**, *26*, 5007.

[48]   J. Wang, A. Quirk, J. Lipkowski, J. R. Dutcher, A. J. Clarke, *Langmuir* **2013**, *29*, 14997.

[49]   T. Mohan, R. Kargl, A. Doliška, H. M. A. Ehmann, V. Ribitsch, K. Stana-Kleinschek, *Carbohydr. Polym.* **2013**, *93*, 191.

[50]   S. Ahola, X. Turon, M. Osterberg, J. Laine, O. J. Rojas, *Langmuir* **2008**, *24*, 11592.

[51]   S. Elazzouzi-Hafraoui, Y. Nishiyama, J.-L. Putaux, L. Heux, F. Dubreuil, C. Rochas, *Biomacromolecules* **2008**, *9*, 57.

[52]   T. Paakkari, R. Serimaa, H.-P. Fink, *Acta Polym.* **1989**, *40*, 5.

[53]   D. Ciolacu, F. Ciolacu, V. I. Popa, *Cellul. Chem. Technol.* **2011**, *45*, 13.

[54]   C. F. Macrae, I. J. Bruno, J. A. Chisholm, P. R. Edgington, P. McCabe, E. Pidcock, L. Rodriguez-Monge, R. Taylor, J. van de Streek, P. A. Wood, *J. Appl. Cryst.* **2008**, *41*, 466.

[55]   E. Kontturi, P. C. Thüne, a. Alexeev, J. W. Niemantsverdriet, *Polymer (Guildf).* **2005**, *46*, 3307.

[56]   S. M. Notley, L. Wågberg, *Biomacromolecules* **2005**, *6*, 1586.

[57]   J. J. Cael, K. H. Gardner, J. L. Koenig, J. Blackwell, *J. Chem. Phys.* **1975**, *62*, 1145.

[58]   F. Jiang, Y. Lo Hsieh, *Carbohydr. Polym.* **2013**, *95*, 32.

[59]   R. J. Moon, A. Martini, J. Nairn, J. Simonsen, J. Youngblood, *Chem. Soc. Rev.* **2011**, *40*, 3941.

[60]   S. Köhler, T. Liebert, T. Heinze, *J. Polym. Sci. Part A Polym. Chem.* **2008**, *46*, 4070.

[61]   J. Wang, A. Quirk, J. Lipkowski, J. R. Dutcher, C. Hill, A. Mark, A. J. Clarke, *Langmuir* **2012**, *28*, 9664.

[62]   T. Imai, C. Boisset, M. Samejima, K. Igarashi, J. Sugiyama, *FEBS Lett.* **1998**, *432*, 113.

[63]   K. Takeda, T. Uchihashi, H. Watanabe, T. Ishida, K. Igarashi, N. Nakamura, H. Ohno, *PLoS One* **2015**, *10*, 1.

[64]   E. Hoshino, M. Shiroishi, Y. Amano, M. Nomura, T. Kanda, *J. Ferment. Bioeng.* **1997**, *84*, 300.

[65]   P. Bansal, B. J. Vowell, M. Hall, M. J. Realff, J. H. Lee, A. S. Bommarius, *Bioresour. Technol.* **2012**, *107*, 243.

Chapter V The Direct Visualization of Enzymatic Cellulose Degradation

200 nm
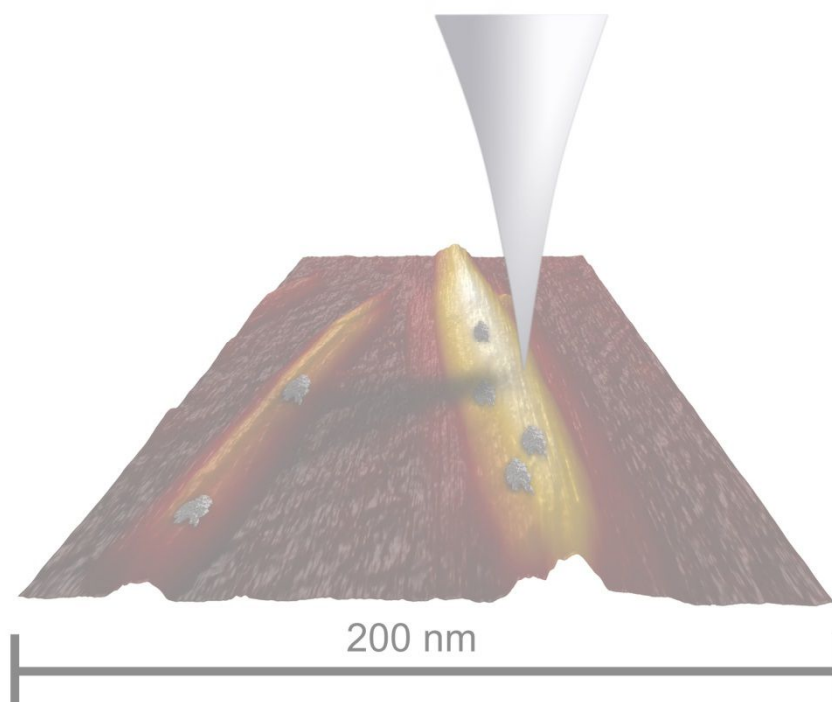
V.1 Introduction

After the introduction to AFM, cellulose, enzymes and the discussion of the availability of standardized cellulose substrates for enzymatic cellulose degradation, we now can focus on the visualization of the enzymatic activity. Direct visualization of enzymatic or molecular processes has been striven since the invention of high-resolution microscopy. However, most of these methods were limited to *ex-situ* investigations with no or limited information on the real-time behavior of the corresponding system. This originates from the fact that most high-resolution microscopy methods are based on electron microscopy with its requirement on high vacuum conditions. Direct visualization, however, is absolutely required as complex interdependencies are not fully accessible by sole biochemical methods. As AFM can provide today *in-situ* and high-resolution measurements at sub-second frame rates, it developed into a state-of-the-art method in enzymology. AFM in liquid is currently the only method with real-time topographic investigations of enzymatic activity on the lower nanoscale. In this *chapter,* the work of more than 3 years of research focused on the visualization of enzymatic cellulose degradation will be summarized. The *chapter* will be divided into 3 main topics, concerning each of the enzymatic systems presented in *chapter* III and the corresponding visualization via AFM methods. The commonalities are the two novel substrates, presented in *chapter* IV, which were the pivotal point for the following experiments and conclusions. As a starting point, the well-known model system of the *Hypocrea jecorina* (mutant SVG 17) will be used to demonstrate the remarkable capabilities of AFM methods in the analysis of enzymatic cellulose degradation. Here, AFM methods will be combined with biochemical methods to demonstrate this beneficial approach. Based on these results, the system will be expanded using recently discovered and so called lytic polysaccharide monooxygenases (LPMOs) to reveal new and so far unknown information on this particular synergistic system. As a last part, the concept of synergism will be evaluated on compact multi-enzyme machineries which are denoted as cellulosomes used by bacterial organisms like *Chlostridium thermocellum*. Each topic was already published in peer reviewed journals or is currently under submission. A publication summary will be given at the beginning of each section and includes author information and a short abstract. In difference to the former *chapter* all presented sections are summaries of the corresponding papers without permitted reprints. Figures will be reprinted with kind permission of the respective journals unless otherwise stated. Style of figure captions was adapted to fit the style of the thesis.

V.2 *Hypocrea Jecorina* Cellulase System: Strain SVG 17

V.2.1 Background

As described in *chapter III,* efficient enzymatic degradation usually requires a set of specific cellulases which form a synergistic system. Synergism is given, if the combined activity of a cellulase system is higher than the sum of the individual activities on the same substrate. So far, the understanding of enzymatic activity is based on biochemical and electron microscopy methods. To show real time information, AFM based methods are anticipated and more appropriate. The enzymes used in this study are, as described in *chapter III, Hj*Cel7A, *Hj*Cel6A and *Hj*Cel7B, which correspond to CBH I, CBH II and EG, respectively. We have used the substrate MACS-15[1] for the experiments, as it shows first

a polymorphic nature and – is from this point of view – the closest substrate to usually applied Avicel. The reason to use MACS instead of Avicel, is simply that Avicel cannot be prepared accordingly to feature a nanoflat surface required for AFM operation. The experimental idea is now as follows: Using the whole cellulase cocktail, a first AFM experiment should show the principle behind synergistic activity by direct visual and sequential analysis of images. The governed information should than be used to design a dedicated set of experiments pointing at the activities of the individual cellulases. Thus, the role of each cellulase should be studied and later reconstructed to a final and new model. In a last step, another sequential experiment where enzymes are injected at different times to the reaction chamber should prove the conclusions drawn before. An outline of the experimental procedure is given in Figure V-4.

V.2.2 Publishing Information

The following sections (V.2.3 & V.2.4) were topic of the paper *"Dissecting and reconstructing synergism: in-situ visualization of cooperativity among cellulases"*[2] in the Journal of Biological Chemistry (American Society of Biochemistry and Molecular Biology), submitted in September, 2012. The paper was published in October 2012 and authors were Thomas Ganner[*], Patricia Bubner[*], Manuel Eibinger[*], Claudia Mayrhofer, Harald Plank[†] and Bernd Nidetzky[‡]. Concept and idea of the manuscript were from HP, BN and PB; AFM experiments were performed by TG and ME; AFM Data analysis was performed by TG and HP; ME performed enzyme purification, biochemical experiments and analysis of the latter; CM performed Ultramicrotomy preparation and helped with the fabrication of MACS-15; TG and ME produced the figures; TG, ME, PB, HP and BN wrote the paper including the revision.

Section V.2.5 was topic of the paper *"Surface structural dynamics of enzymatic cellulose degradation, revealed by combined kinetic and atomic force microscopy studies"*[3] in FEBS Journal (Federation of European Biochemical Societies), submitted in July, 2013. The paper was published in October 2013 and authors were Manuel Eibinger[*], Patrica Bubner[*], Thomas Ganner, Harald Plank and Bernd Nidetzky[†]. Concept of the manuscript was from ME and BN; ME and PB performed biochemical experiments and ME performed analysis. TG and HP performed AFM experiments and analyses. ME and BN wrote the paper including revision with the help of HP and TG.

For consistency, *T. reesei* is substituted with *H. jecorina*. Please note, although organisms are identical, *H. jecorina* is the modern accepted notation. Reference style and figure captions were adapted for the thesis.

V.2.3 Experimental Procedures

Visualization of enzymatic activity is a considerable and complicated task as applied forces, energy dissipation by the cantilever and liquid environment have to be carefully controlled. Therefore, the experimental details for such experiments are important. In the following, a comprehensive overview over applied methods will be given.

---

[*] Equally contributing authors
[†] Corresponding author
[‡] Co-corresponding author

V.2.3.1 Substrates

MACS-15 was chosen as cellulose substrate and prepared as described in c*hapter IV*. The specimens were first analyzed via light microscopy to ensure homogeneous surface features. As a result of the high mixing ratio (15 wt.%), the substrate shows distinctive polymorphic features as demonstrated in Figure V-1. Therefore, the effect of enzymatic activity can be studied on crystalline and amorphous cellulose side-by-side offering a fully and more comprehensive insight into synergism. In Figure V-1, the light microscopy image and the schematic 3D structure are depicted. The entire background of MACS materials can be found in *chapter IV* and *II*.
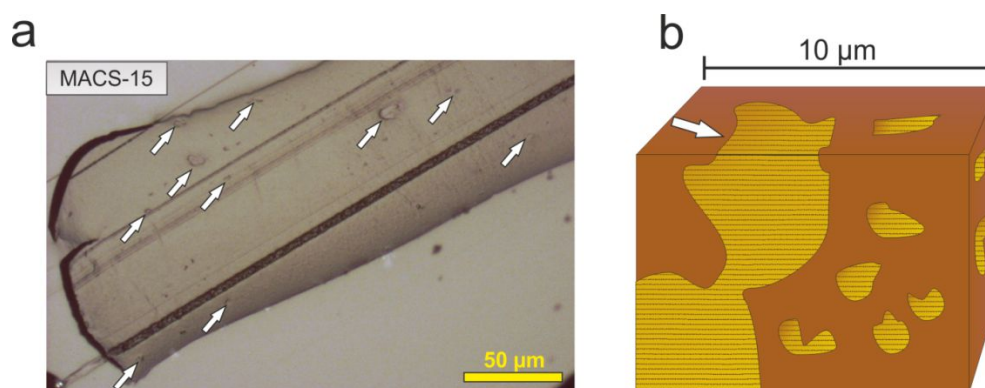

Figure V-1: (a) A MACS-15 substrate visualized in the light microscope shows a flat surface with some grooves originating from knife defects. White arrows indicate larger crystalline residues forming polymorphous substrates. (b) 3-D presentation of the substrate with larger crystallites (white arrow) and smaller ones not accessible by light microscopy (< 500 nm) but demonstrated by AFM analysis (see chapter IV)

V.2.3.2 Enzymes

The supernatant (with major activities of *Hj*Cel7A, *Hj*Cel6A and *Hj*Cel7B) from *Hypocrea jecorina* mutant was produced as described previously[4]. Individual cellulases were either purchased from Megazyme (Dublin, Irland) or provided from collaborators. See Table 1 for corresponding data.

Purity and absence of enzymatic cross contamination was verified by MUF-cellobioside assays[5]. Concentrations of enzymes in solution was determined according to a procedure introduced by Bradford[6] using Roti®-Quant and Roti®-Nanoquant (Carl Roth, Karlsruhe, Germany) assays standardized by BSA. The concentrations applied later in the experiments are summarized in Table 2.

Table 1: Cellulases for experiment 1 (individual incubation). T. longibrachiatum is closely related to H.jecorina and cellulases are structurally analogous. (BGL, β-glucosidase (a cellobiose degrading enzyme)).

Enzyme	Expressing organism	Description	Supplier
*Hj*Cel7A	*T. longibrachiatum*	Enzyme analogous to *H. jecorina*	Megazyme
*Hj*Cel6A	*H. jecorina*	Heterologous expression	Anton Glieder (TU Graz)
*Hj*Cel7B	*T. longibrachiatum*	Enzyme analogous to *H. jecorina*	Megazyme
BGL	*Aspergillus niger*	Cellobiose degrading enzyme	Megazyme

Table 2: Applied enzymatic concentrations in experiments 1 & 2. Note, concentration for HjCel6A was enhanced for the AFM experiments as preliminary data showed low activity levels. Note, BGL was added to prevent inhibition by cellobiose (natural inhibitor of cellulases).

Enzymatic system	Concentration (mg$_{enzyme}$/g$_{substrate}$)
Complete cellulase (BGL)	3,6 (1 unit[§])
*Hj*Cel7A (BGL)	36 (1 unit)
*Hj*Cel6A (BGL)	1300 (1 unit)
*Hj*Cel7B (BGL)	36 (1 unit)

V.2.3.3 In-situ Atomic Force Microscopy

The used instrument was a Dimension 3100 AFM equipped with a liquid probe holder and a Nanoscope IVa controller (Bruker AXS, Santa Barbara, USA). Experiments were conducted in a home-made liquid cell[**] with a total reaction volume of about 3 ml (Figure V-2). Operating software was Nanoscope 6.13 (Bruker AXS, Santa Barbara, USA) and images were analyzed using Gwyddion[7] (Gwyddion 2.25) or NanoScope Analysis 1.20 (Build R1Sr3.64571).

The liquid probe holder was operated with TR400 PSA cantilevers (Olympus Probes, Tokyo, Japan) in Tapping Mode, unless otherwise stated. AFM Experiments were performed according to the following protocol: The specimen was removed from buffer solution, positioned in the liquid cell and immediately immersed with buffer. Specimen, buffer and liquid cell were allowed to equilibrate at air conditioned temperatures (22°C) in the AFM laboratory for at least 30 min, followed by coupling to the AFM stage. AFM experiment was started by acquiring a set of reference images to ensure homogenous substrate composition around a crystalline residue. Observation position was then chosen in proximity of a crystalline residue to cover the polymorphous nature during the experiment. Subsequently, enzymes were injected by pipettes in above given concentrations and continuous imaging was started. Scan rates and amplitude set-points were chosen to ensure highest possible image quality at lowest energy dissipation. Image position was carefully controlled during imaging to compensate the drift. For experiment 3 (concept and naming is demonstrated in Figure V-4), the same procedure was applied. However, enzymes were injected at sequential time points starting with *Hj*Cel7B (9 mg$_{enzyme}$ / g$_{substrate}$) followed after 175 minutes with *Hj*Cel6A (320 mg$_{enzyme}$ / g$_{substrate}$) and finalized after further 85 minutes with 9 mg$_{enzyme}$ /g$_{substrate}$ *Hj*Cel7A. The reduced concentration was chosen in respect to the expected high activity after full combination (synergism).

[§] 1 unit ist the amount of enzyme which is required to catalyze 1 mM of substrate per minute @ standard conditions (25°C and optimal pH value).
[**] Thomas Ganner, Enzymatic cellulose degradation via atomic force microscopy in liquid environments, Master thesis, Graz University of Technology, (2012)
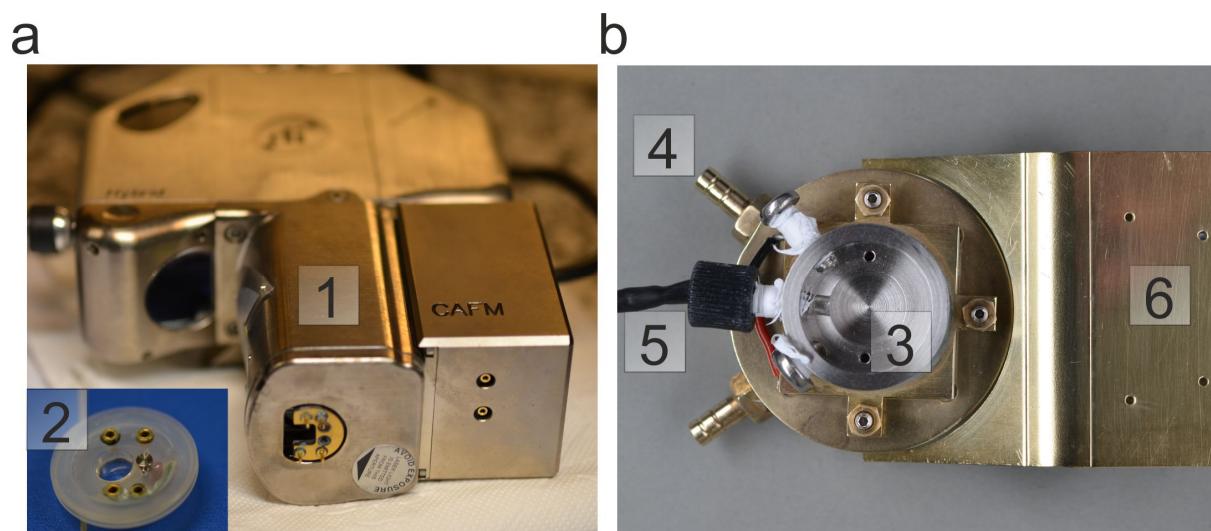
Figure V-2: (a,1) x-y-z Hybrid scan head of the Dimension 3100 AFM with the corresponding liquid probe holder (a,2). The holder is required as waterproof element to ensure no contact of liquid with the piezoelectric elements of the scan head. (b,3) The home-made AFM liquid cell (total volume: 3 ml) and a drilled hole for specimen fixation. (b,5) Electrical connection to the Peltier element for heating and cooling of the sample and (b,4) cooling valves for a water heat sink during specimen cooling. (b,6) A connection to the AFM stage allowing accurate positioning of the specimen.

V.2.3.4 Image Analysis and Data Recording

Recorded images were post-processed only if necessary to compensate for scan and tip related artifacts. As described above larger crystallites were present in all images. These crystallites – due to their resistance against hydrolytic degradation – represented fixed height markers for the post-analysis of the degradation progress. Thus, absolute quantification of the degradation speed via AFM techniques is available. This procedure is feasible as preliminary experiments proved that the crystalline surface of larger crystallites (µm range) is resistive to enzymatic degradation. Plane-fitting (first order, see Figure V-3) was conducted due to the following reason: To ensure a consistent orientation of timely separated images, the cross face of the crystallites are aligned perpendicular to the z-direction as described in Figure V-3. Thereby, quantitative information can be recorded on the degradation rate in z-direction. Data points were drawn after plane fitting by measuring the depth difference between the crystallite and a specific point on the surface. Thereby, recorded data gives quantitative degradation information in z-direction which directly can be fitted to volumetric degradation rates. Data analysis was performed using Origin Lab 9.0 (OriginLab Corp., Northampton, US). A schematic representation of the plane fit process is shown in Figure V-3.

To calculate the average z-degradation rate, statistical analysis was applied by using a histogram analysis of the measured velocities (between images) and the non-linear fit tool in Origin 9.0 was used to fit Gaussian functions to the data.
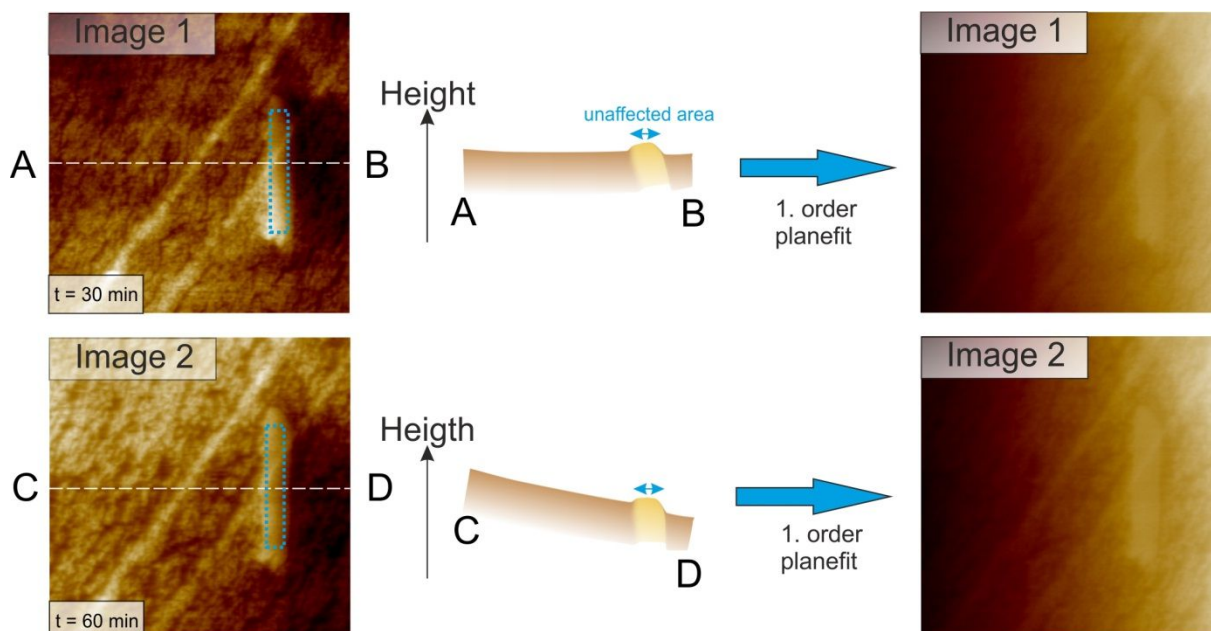
Figure V-3: Image processing to gain quantitative degradation rate results. After the first order plane fit of the not degraded cellulose crystallite (blue dotted rectangle), image planes are aligned consistently for all images. By this process, depth measurements can be taken from the crystallite as reference to any point on the surface. Image 1 (t = 30 min) and image 2 (t = 60 min) are depicted as representative examples. Image distortion, most likely introduced by interference with the liquid, causes different tilts. To correct for this tilt only flat and stable areas are appropriate. This is the case for larger crystallites, due to their resistivity against hydrolytic degradation. Flat areas on these crystallites are shown by dotted blue rectangles and first order fitting align consecutive images for data extraction. Original images (left) with white dotted section line, which schematically is shown in the middle. The result of this procedure is seen on the right site.
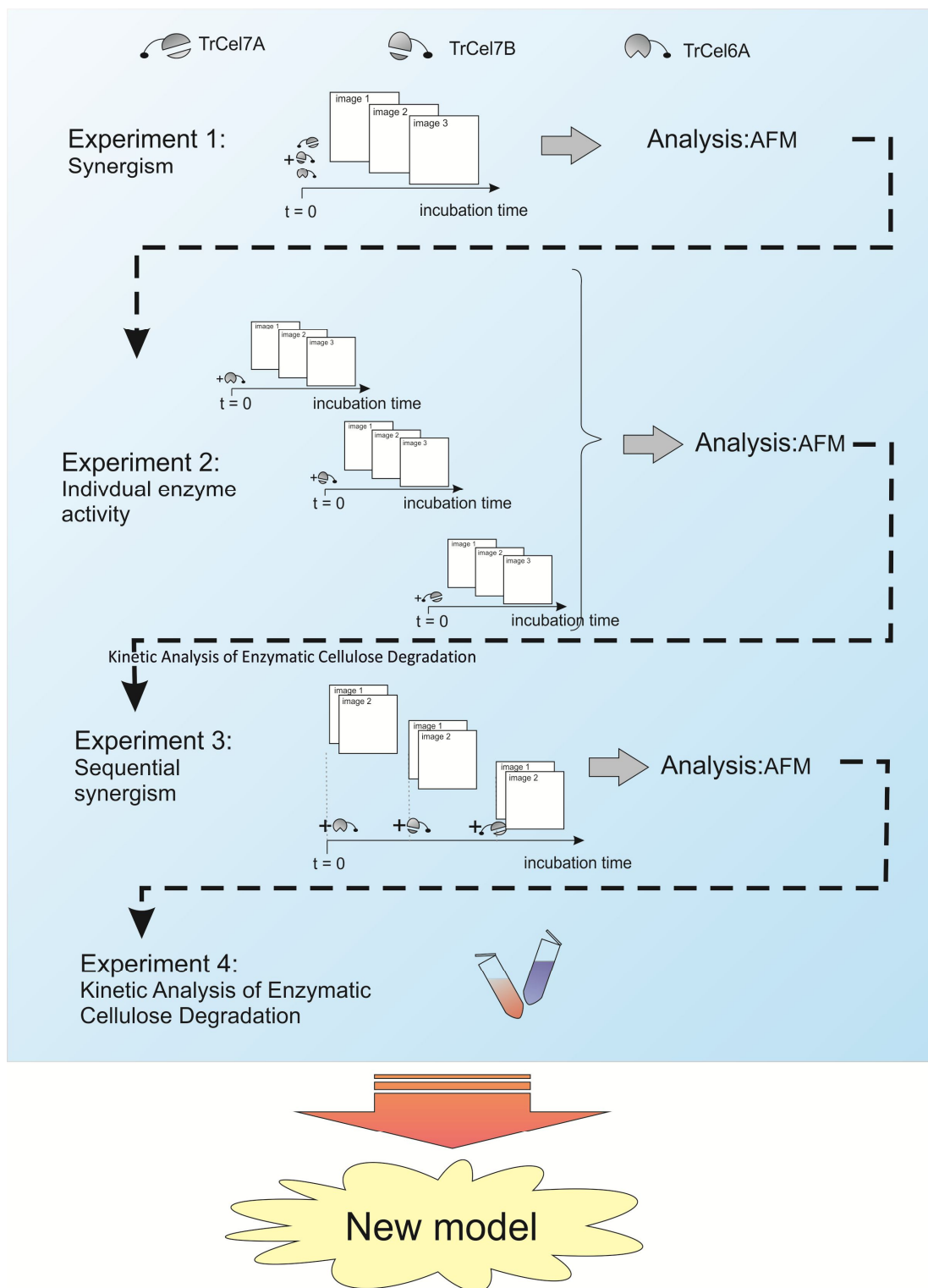
V.2.3.5 Experimental Strategy

Figure V-4: Experimental outline of enzyme visualization of Hypocrea jecorina cellulases on MACS. The setup is divided into four parts covering an analysis of synergistic activity followed by comprehensive analysis of degradation mechanisms. The gathered information is used to establish another set of experiments pointing at individual enzymatic activities, and finally a sequential approach – where enzymes are injected at different time points to unravel the individual synergistic contributions – is applied. Finally, biochemical experiments are conducted to validate the data. The complete dataset is used to construct the final refined model.

V.2.4 Results and Discussion

V.2.4.1 Experiment 1: Synergism of the Complete Supernatant of H. Jecorina

In a first experiment, the synergism of the complete cellulase system was investigated to show its behavior on MACS. The reason for this first approach was that *in-situ* and real time investigation – both only possible in a liquid cell – were still missing on MACS[4]. In the earlier study, a sequential approach was chosen, where cycles of incubation and drying combined with AFM investigation were applied[4]. First results of the *in-situ* approach are shown in Figure V-5.

Considering the data (Figure V-5; supplementary Movie S1) two main conclusion can be drawn: *1)* **Large, crystalline** residue particles (see Figure V-1) **are resistive to degradation** due to their size as mentioned and demonstrated in preliminary experiments; and *2)* Degradation is observable and **surface roughness is increased significantly** (Figure V-6)**.** For the latter, the following conclusion is feasible: Although the main part of MACS is amorphous, it is conceivable and propped by WAXS and RAMAN evidence that the amorphous matrix is not homogenously amorphous. As already mentioned in *chapter IV*, MACS-15 includes a considerable amount of crystalline phases. It is thus likely that the increase of surface roughness stems from this inhomogeneity. It is inevitable, that the near ordering and binding of cellulose chains affects the local degradation thus producing an increasing surface roughness over time.
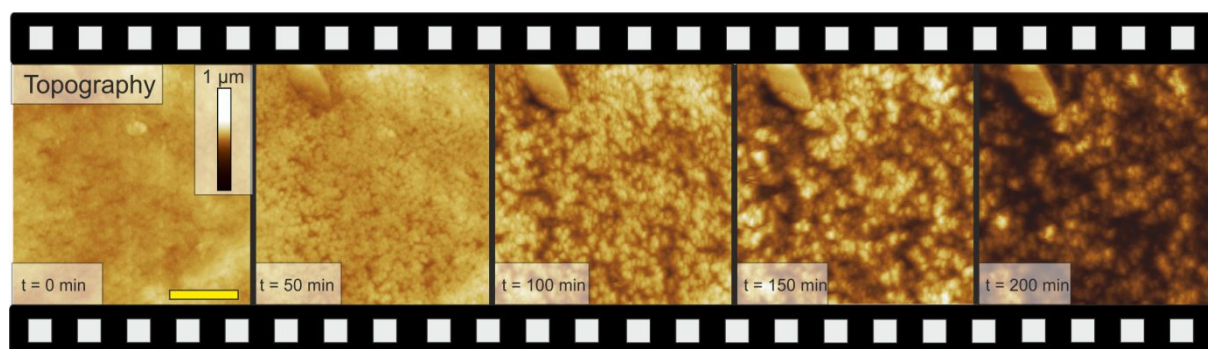

Figure V-5: In-situ AFM investigation of synergistic degradation of a MACS-15 surface. The particle in the upper left corner is a crystalline residue and thus not affected. Data scale is fixed to this particle and degradation proceeds approximately 400 nm in z-direction over a time frame of 200 min. Characteristic features are an increasing roughness (Figure V-6) of the surrounding cellulose material which by earlier analysis (chapter IV) shows an inhomogeneous distribution of crystallinity. Scale bar represents 4 µm.

To test this hypothesis, we performed dedicated experiments focusing at higher resolutions to resolve the morphological differences. Again, a MACS-15 substrate was imaged under the same conditions as visualized in Figure V-5. Figure V-7 directly shows and proves the previous conclusions.

First, we see similar behavior in the low-resolution mode, if compared to Figure V-5, where no degradation of the larger (white arrow) crystallite is visible together with increasing surface roughness in the amorphous matrix (Figure V-6).
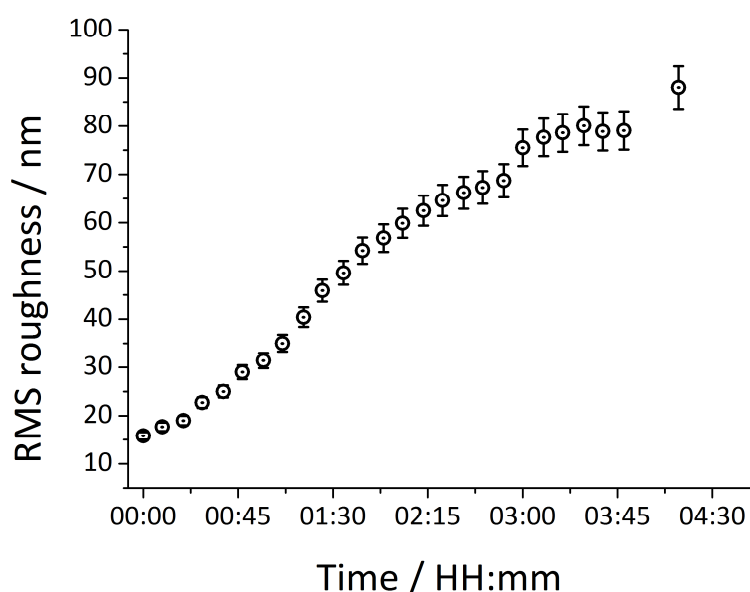
Figure V-6: Roughness increase due to synergistic activity of the full cellulase cocktail of H. jecorina. RMS data was calculated without the large crystallite in Figure V-5.

Medium-resolution already provides the proposed evidence of local fibrillary structures in MACS. This difference is even more pronounced if imaged with high-resolution, where single fibers are visible (approx. 7 nm in width) correlating with elementary fibrils of cellulose. These fibers are degraded at obviously different speeds compared to the surrounding material. **It is now clear from here demonstrated data (Figure V-5 & Figure V-6), that the increase in surface roughness stems from a non-homogenous crystallinity of the amorphous matrix.** Although we know that the substrate is responsible for different degradation rates, we know little about the enzymes contributing to this morphology depending degradation. To gain statistical relevant data on the divalent degradation rates, we analyzed the experiment further. Aligning the crystallite as seen in Figure V-3 allows measurement of the degradation in z-direction. We used 10 points and followed the degradation for 18 images (120 minutes). Measurement of the z-position of individual points on subsequent images allows the quantification of the degradation in z-direction (per image and point). Correlation with the image recording time results in a degradation rate in z-direction per minute or second which can be used for statistical analysis. The data in Figure V-8 nicely demonstrates the capabilities of this approach. While biochemical data would yield averaged data (see Figure V-8a, green shading), AFM analysis allows the specification of local activities. Interestingly, in this case, the two velocities yield directly the observed increase in surface roughness but also show that two processes are observable. Correlation of data and statistical analysis demonstrates that the faster velocity can be attributed to small nano-crystalline material and the slower one to the amorphous matrix. It is conceivable that the higher ordering and short distance from one end to the other facilitated faster degradation of the small crystallites. Here, the endo-glucanase *Hj*Cel7B may be able to produce new chain ends which efficiently are used by exo-glucanases *Hj*Cel7A and *Hj*Cel6A, which remove the crystallite quickly. Note that this is the current understanding of the process as depicted in *chapter III*. Nonetheless, there is the problem that larger crystallites are only weakly attacked. The cause of this problem is speculative, but may be attributed to a tighter packing of elementary fibrils

and an intermingling with each other causing multiple obstacles. Thereby, exo-glucanases get stuck further obstructing degradation.

However, from this analysis we cannot attribute specific cellulases to the divalent rates due to: *1)* although lateral resolution is sufficient to resolve individual cellulases, we **lack the appropriate imaging speed**[8,9]; and *2)* with appropriate image speed we are **not able to distinguish different cellulase** as individual cellulase dimensions are in the same range. Therefore, we applied a set of experiments focusing on the individual activities to get a more comprehensive insight into these processes.
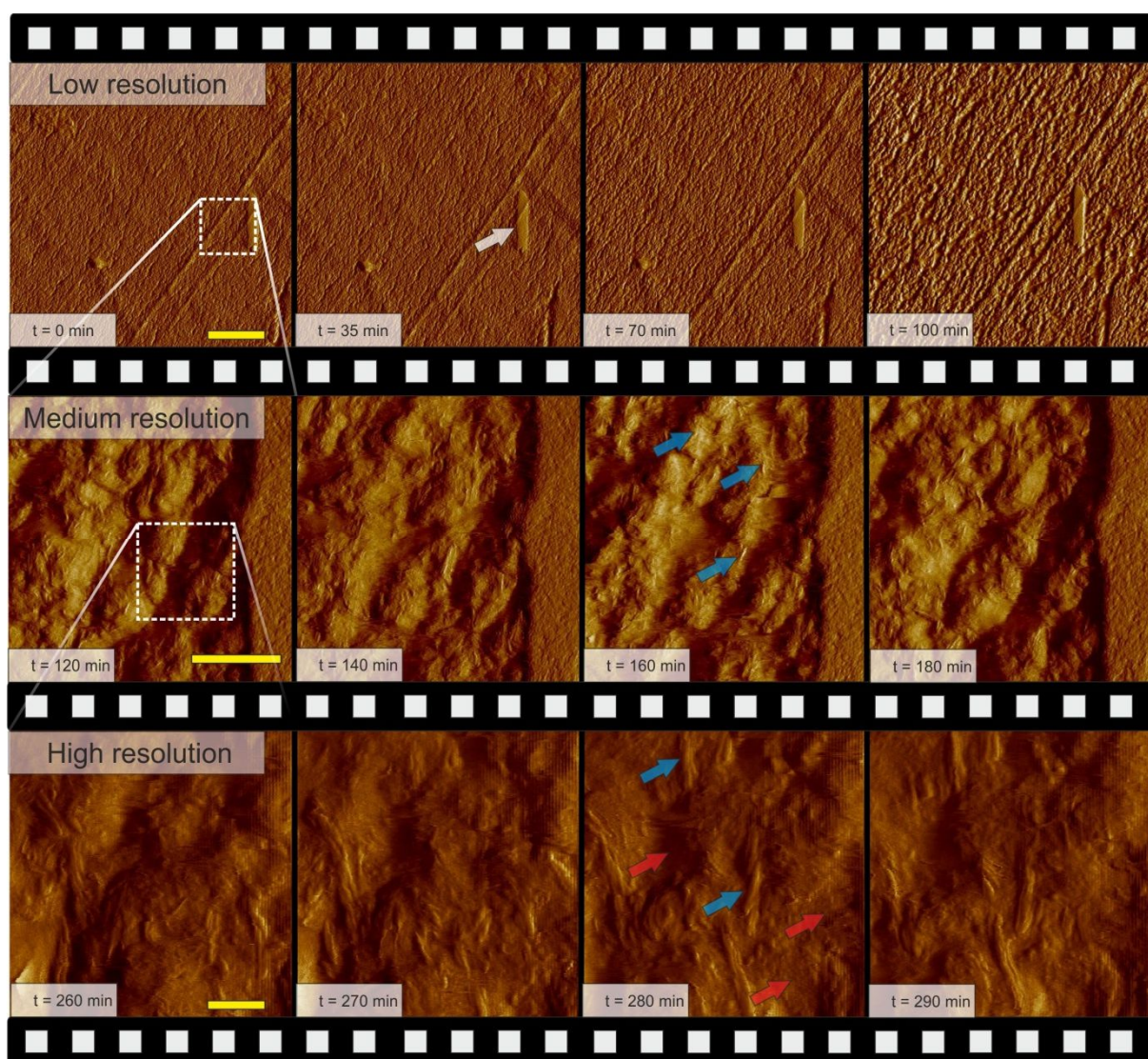

Figure V-7: Amplitude AFM images of MACS-15 degradation by SVG-17 supernatant enzymes. Images were recorded in low-, medium- and high-resolution to unravel otherwise elusive information on the morphology dependent degradation. Arrows point at distinctive features: The large crystallite is indicated by a white arrow; Fibrillar crystalline morphologies are highlighted by blue arrows and amorphous unordered cellulose is indicated by red arrows. Time frames of the experiments are indicated in the lower left corner. Scale bars are from top to down: 2 µm, 500 nm and 100 nm for low-, medium- and high-resolution, respectively.
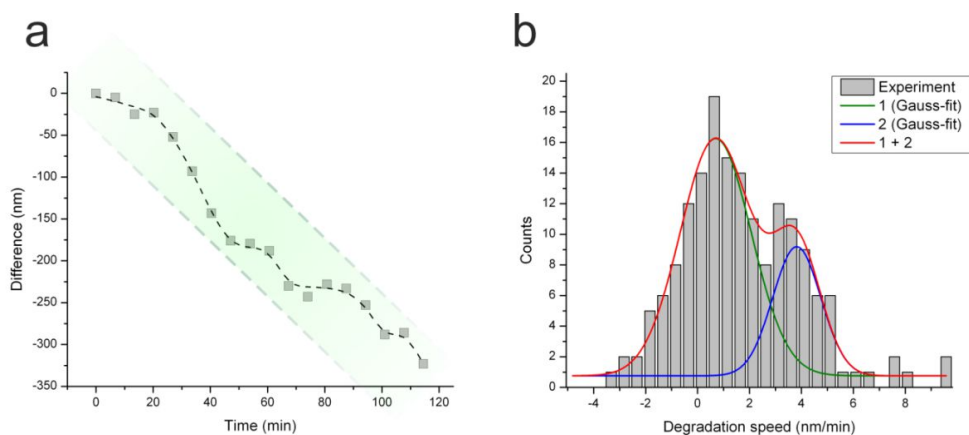
Figure V-8: (a) Degradation observed for one specific point on the substrate over 120 minutes. Clearly, the presence of different degradation speeds is observable. (b) Statistical analysis of 10 of such points with the corresponding histogram. Fits by Gaussian functions reveal two velocities for the degradation: the slow degradation rate is (0.7 ± 0.2) nm/min; the fast degradation is (3.8 ± 0.2) nm/min. Correlation with image data reveals that the fast velocity is achieved on small crystalline features. In (a) the green shading shows what conventional biochemical data would yield which once more emphasizes the need of AFM imaging.

### V.2.4.2 Experiment 2: Individual Cellulase Experiments on MACS

In order to understand the following conclusions and the experimental data, it is feasible to repeat the current paradigm of synergistic activity (see also c*hapter III*). In Figure V-9, a schematic representation in similarity to c*hapter III i*s given. The synergism is characterized through different individual affinities for cellulose morphologies. Cellobiohydrolases (**CBHs;** *Hj*Cel7A and *Hj*Cel6A) are thought to prefer crystalline cellulose due to structural reasons. The tunnel located catalytic site of the enzyme confines the activity to the processive movement of the enzymes on ordered and parallel aligned cellulose. In contrary, the outside pointing active site of endoglucanases facilitates degradation of more accessible chains, which usually are found in amorphous regions.
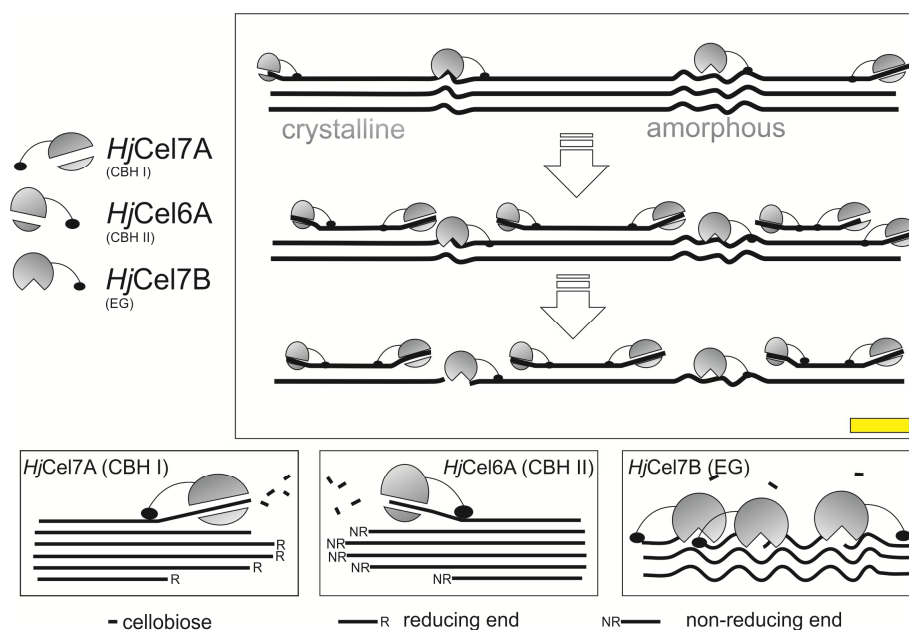
Figure V-9: Current paradigm of cellulose degradation by the enzymatic system of the fungus H. jecorina. The activity of endo-glucanases (e.g. HjCel7B) yields a higher number of accessible chain ends for CBHs and thus boosts degradation. Single activities are thought to comprise the following: While HjCel7A requires a reducing end to load the cellulose chains HjCel6A requires the non-reducing end. HjCel7B, if incubated individually, should only affect amorphous cellulose, as here accessibility and weak coupling allow complete disruption of chains. On crystalline regions HjCel7B is also active; however, no visible results are expected due to the small changes in morphological structure. Scale bar represents 20 nm.

Cellobiohydrolase *Hj*Cel7A:

The degradation of *Hj*Cel7A is shown as movie-strip in Figure V-10 where minor degradation can be visualized in the time course of 240 minutes. The observed effects are consistent with the current understanding of *Hj*Cel7A as crystalline preferring cellulase. The fact that only crystalline or fibrillary material is affected is clearly visible. Surrounding material is completely unaffected.
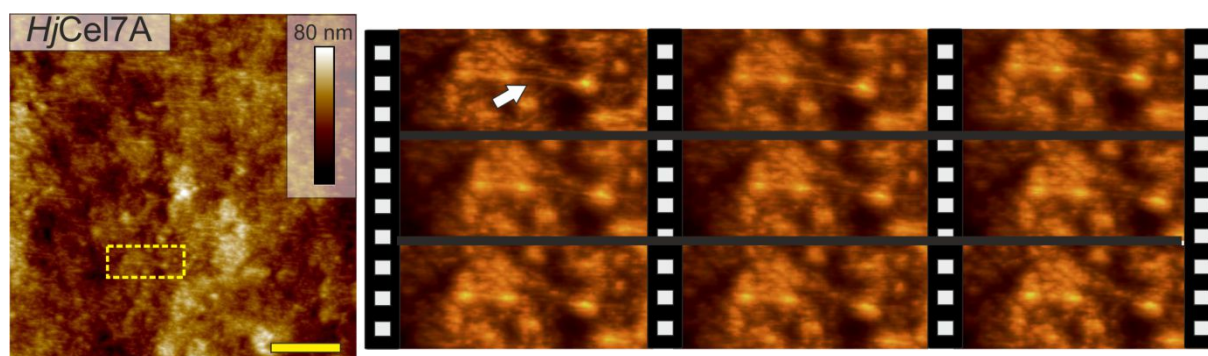
Figure V-10: Topography AFM images of HjCel7A degradation on MACS-15 substrate. The highlighted area (white dotted rectangle) in the low resolution image is used for the movie (Movie S2). Experiment time on the movie strip is 240 minutes from the first image to the last image (approx. 27 min / image). It is clearly visible that material degradation is extremely low and only visible on smaller fibers as indicated by the white arrow. This is consistent with the current paradigm stating a preferential degradation of crystalline and ordered material for HjCel7A. Scale bar represents 1 µm.
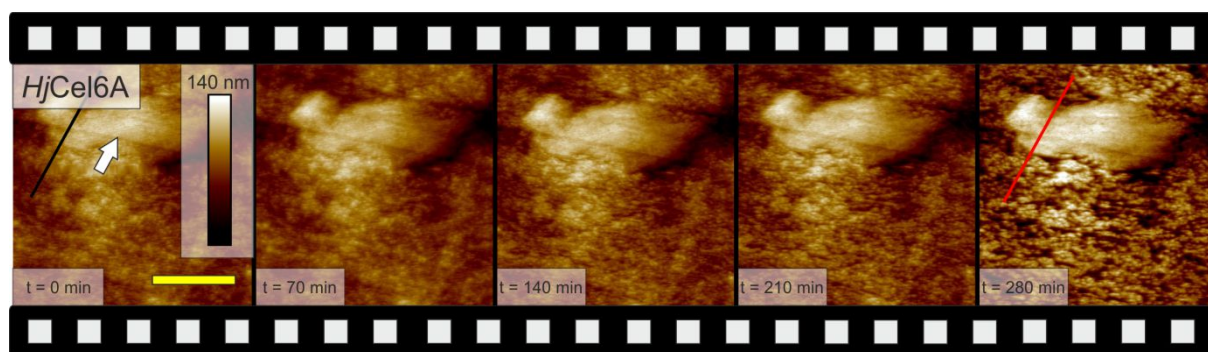
Cellobiohydrolase *Hj*Cel6A:

Figure V-11: HjCel6A degradation visualized in the in-situ AFM (Movie S3). The crystallite is again marked by a white arrow. Degradation proceeds at localized areas and leaves other areas unaffected. Thereby deep holes appear. At t = 0 min (black line) and t = 280 min (red line) section lines as depicted in Figure V-12 are shown. Scale bar represents 1 µm.
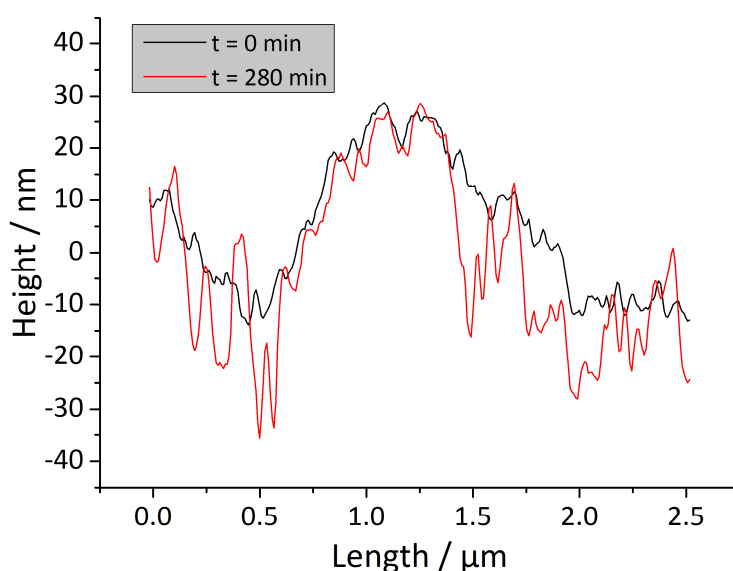

Figure V-12: Section profiles as drawn in Figure V-11. Note the primary appearing deep holes while other areas seem to be not affected at all.

In Figure V-11 degradation of *Hj*Cel6A activity provides direct visualization of preferred degradation on specific parts of the surface. First, it is evident that surface roughness (Figure V-13) is again increased by the formation of deep holes (Figure V-12) and that the large crystalline residue (white arrow; Figure V-11) is unaffected. Now, considering the former conclusion that the amorphous material in MACS (see *chapter IV*) is interspersed by highly ordered fibrils, the origin of this degradation may result from the preferential attack of this fibers. Nevertheless, higher resolution images are required to test this hypothesis (Figure V-14). By the data seen in Figure V-14 we can prove that despite the given model, the majority of the degradation takes place on **amorphous areas** resulting in the excavation of the crystalline features. **This is a remarkable result**, as by recent knowledge, *Hj*Cel6A is classified as pure exo-glucanase, which should facilitate degradation of

crystalline material. However, we see from additional experiments that crystalline material is attacked after this cleaning of amorphous material. This only allows one conclusion: Although in recent studies classified as pure exo-glucanase[10,11], *Hj*Cel6A shows strong bi-specificity for amorphous and crystalline parts.
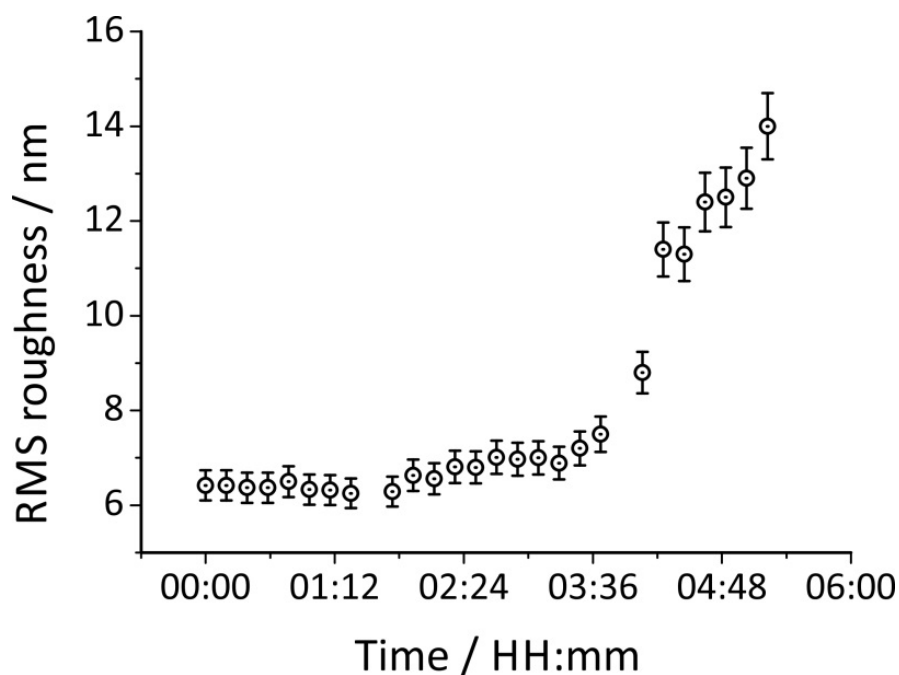

Figure V-13: Full RMS profile for the data shown in Figure V-11. The data shows after an onset of about 1 to 2 hours that RMS increase is significantly enhanced. This behavior was seen in all experiments using our home-made liquid cell and is attributed to diffusion of enzymes. After all enzymes adsorb to the substrate the RMS increase shows the strong hydrolytic activity of HjCel6A. Primarily this effect is caused by cleaning and removing of amorphous structures (see Figure V-14).
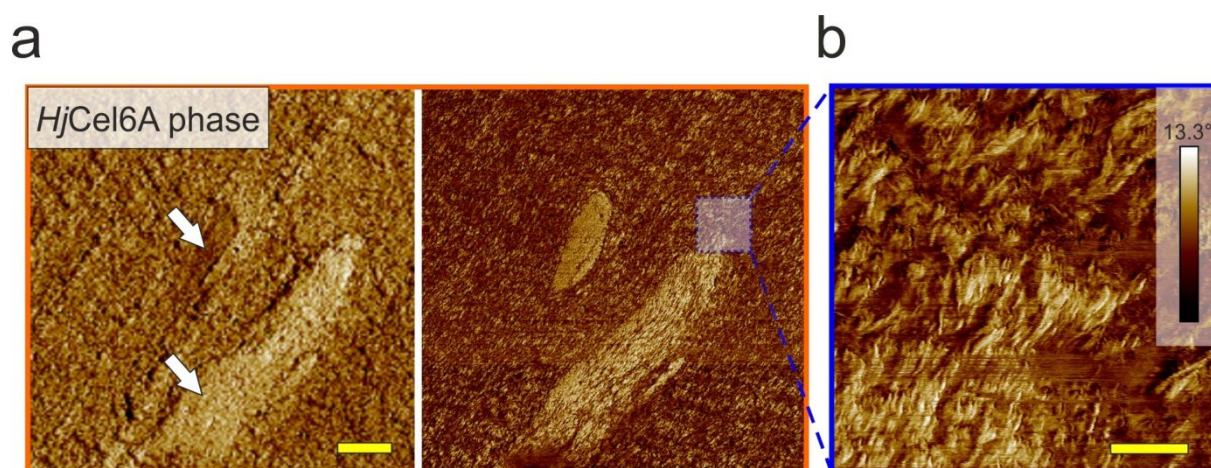
Figure V-14: (a) AFM phase images of MACS area before and after 240 min of degradation by HjCel6A. White arrows indicate larger crystalline residues. Correlation of height data and phase information shows that bright features correlate to higher features in Figure V-11. Darker features correlate to degraded material. It is evident from the phase image that bright regions resemble to fibrillary structures (b). A comparison to the crystalline material (white arrows) proves that the remaining structures are predominantly crystalline (bright phase color

*corresponds). This means that although HjCel6A should facilitate crystalline degradation the **majority of removed material stems from amorphous areas**. Scale bar represents (a): 1 µm and (b): 200 nm.*

Thereby we conclude: Although *Hj*Cel6A is classified as mono-specific enzyme, which is thought to primarily attack crystalline cellulose, **we observe strong degradation on amorphous material** parts. Furthermore the combined activity on crystalline material resulting in fiber sharpening and further degradation shows that a **new mechanism is unraveled by the direct AFM evidence**. Thus *Hj*Cel6A seems to clean crystalline features from amorphous debris and later degrades also the crystalline fibers. To test this hypothesis we primarily focused on crystalline features with amorphous material on top as depicted in Figure V-15.
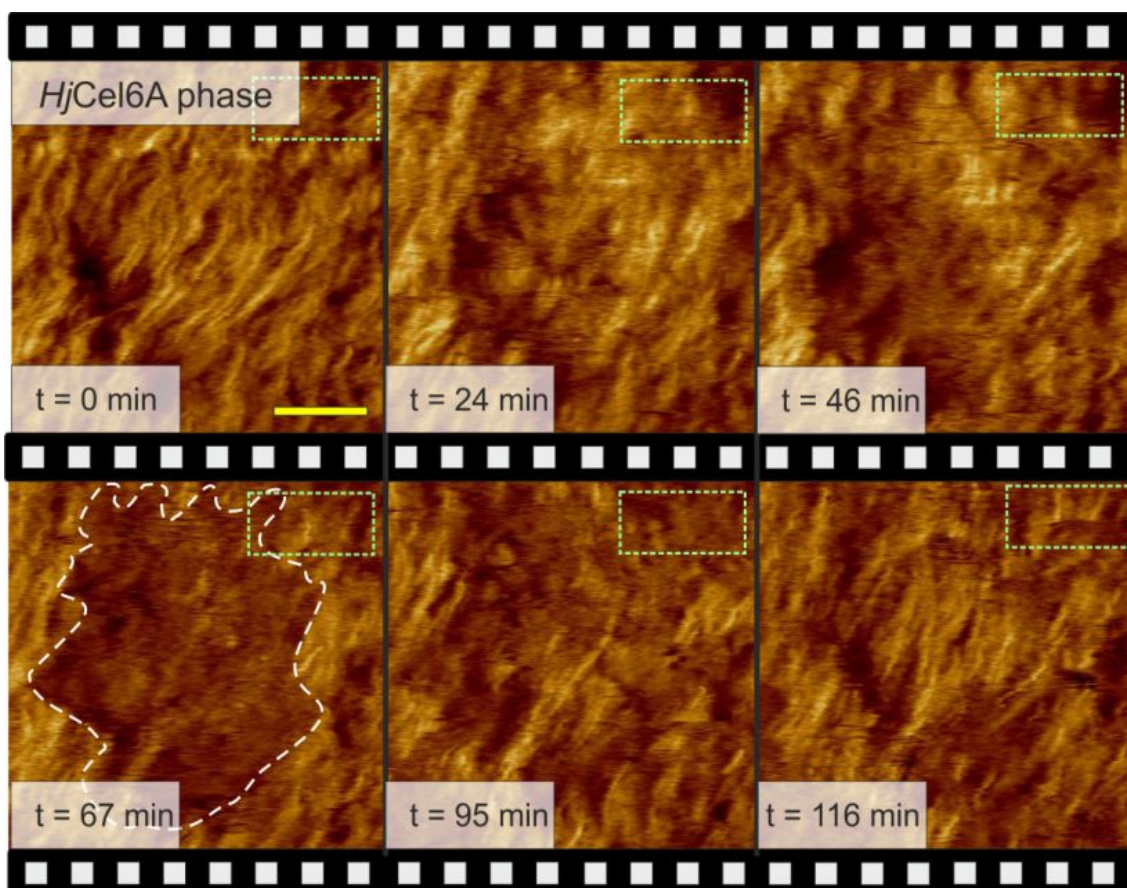

Figure V-15: HjCel6A activity on larger crystallites visible through parallel aligned fibers (center of image at t = 0). The phase contrast shown over 116 minutes is characterized through strong dynamics by appearing and moving darker regions (see representative white dashed envelope curve at t = 67 min; darker phase). As no other components are included in the buffer, the clouds must stem from HjCel6A particles in an agglomerated state. Once clouds disappear, new ordered structures are visible in conformity with the cleaning effect of HjCel6A (green dotted rectangle). Scale bar represent 200 nm. See also: Supplementary movie S4.

The first thing to notice are the cloud-like structures shortly after incubation as indicated in Figure V-15 (t = 67 min; white dashed envelope curve; Movie S4). These structures are highly dynamic which is consistent with enzymatic activity. The result of this activity is an apparent cleaning of crystalline surface structures, which was hypothesized in literature[12,13] but has never been directly observed (Figure V-15; green dotted rectangle).

An explanation for this obviously contradictory behavior may be found in the structure of the enzyme. The relative short tunnel of *Hj*Cel6A (2 nm for *Hj*Cel6A against 5 nm for *Hj*Cel7A) formed by two protein loops may be flexible enough to allow small structural changes which render the enzyme capable to perform cuts in an endo-type fashion (e.g. *Hj*Cel7B; Figure V-9). Thus evidence for the bi-specific nature is also covered from a structural point of view.

Even more, this special activity may be a pivotal aspect of synergistic cellulose degradation, where the cleaning of covered crystalline material and the ability to also degrade highly ordered material makes this enzyme to a flexible counterpart to the monospecific *Hj*Cel7B and *Hj*Cel7A. However, so far, we have not tested the EG *Hj*Cel7B for its specific activity on MACS. We therefore proceeded by the same experiment as for *Hj*Cel7A and *Hj*Cel6A.

Endoglucanase (*Hj*Cel7B):

EGs like *Hj*Cel7B are long known and have already proven to be relatively monospecific for amorphous cellulose. On MACS-15, we found the expected behavior in similarity to *Hj*Cel7A. Both enzymes seem to feature a dedicated affinity for either amorphous or crystalline material, respectively.

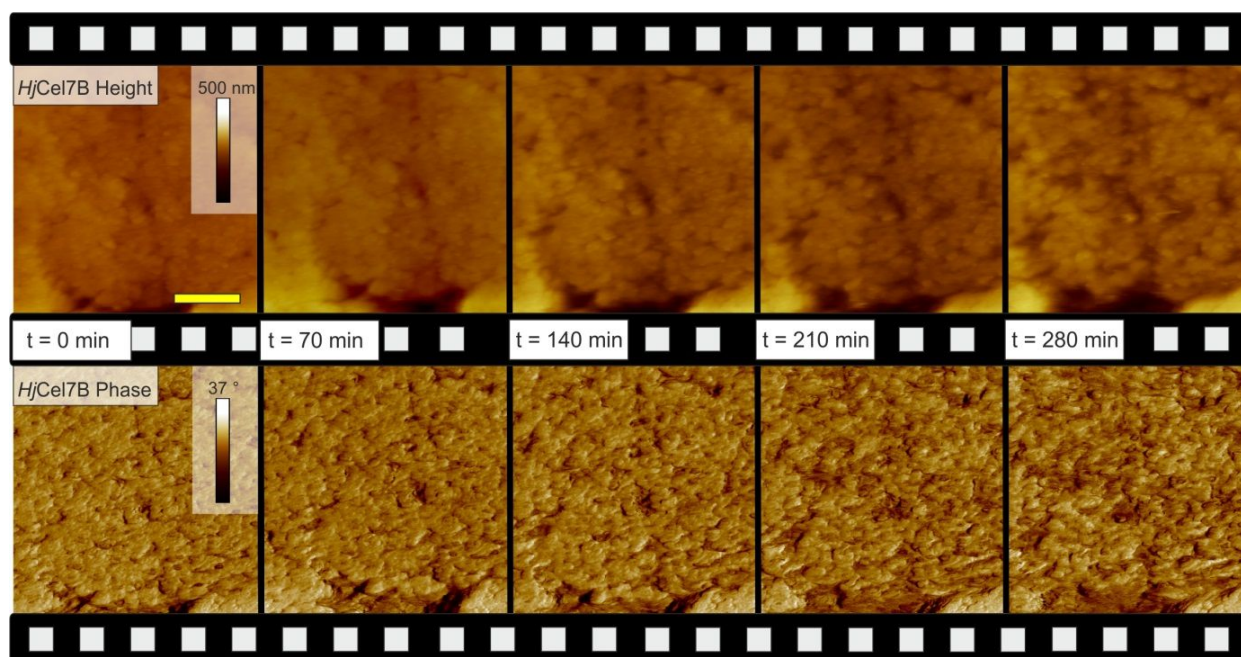*Figure V-16: Endoglucanase HjCel7B activity on MACS in the in-situ AFM. Areas of primarily unordered structure are attacked by the cellulase until activity starts to stall (t = 210 minutes to 280 minutes). In the left and right lower corner a crystalline residue is visible. The scale bar represents 500 nm.*
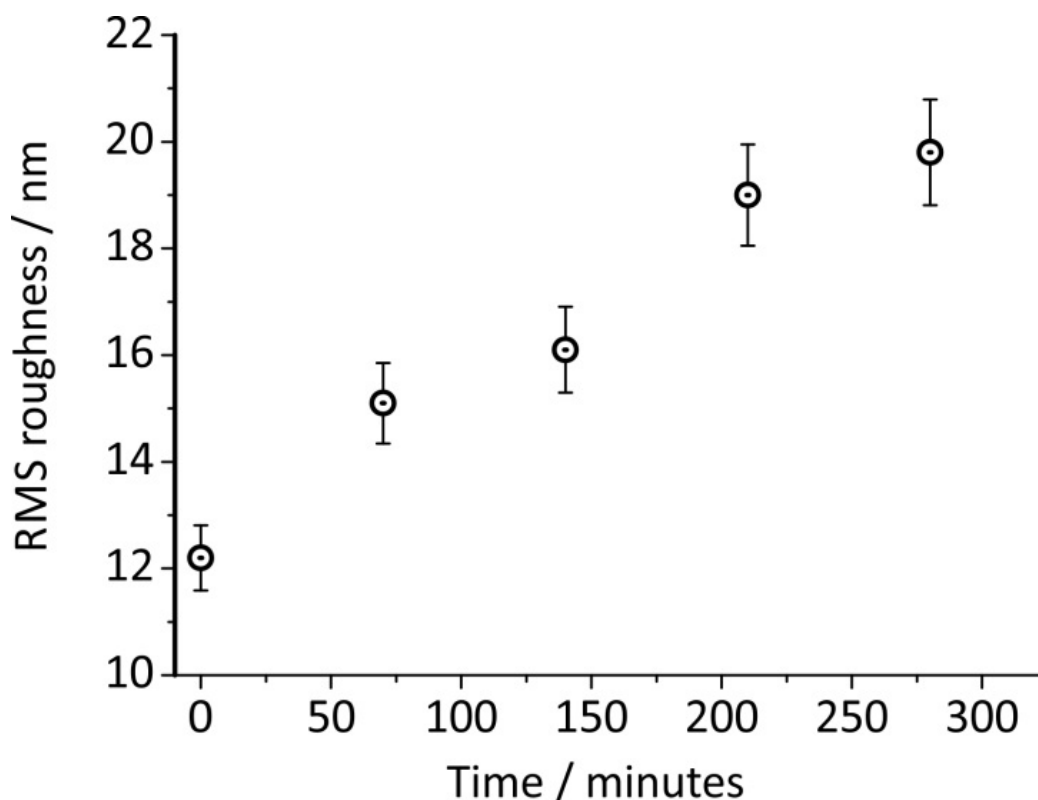
Figure V-17: Increase of RMS over incubation time as seen in Figure V-16 demonstrating the hydrolytic activity of HjCel7B on the MACS substrate. The increase is caused by attack of the amorphous allomorph concentrated mainly in the matrix surrounding the larger crystallites.

Data shown in Figure V-16 is in agreement with the current understanding of an amorphous affine cellulase, where the activity is the following: Accessibility of primary disordered amorphous cellulose results in multiple cleavages and shorter oligosaccharides which then are dissolvable in the buffer (the only form of EG ablative activity). On crystalline areas, tighter packing and reduced accessibility (active site is located in a cleft) impedes efficient degradation. Thus, amorphous areas are degraded by ongoing degradation, which results in holes and cavities [2,3].

With this basic analysis of individual activities, we now can study the synergism in more detail. We therefore incubated MACS once more by sequential addition of the individual enzymes, thus forming the synergism step by step.

V.2.4.3 Experiment 3: Sequential Synergism

Before the following experiment, it is feasible to summarize experiment 2: Specific activities of *Hj*Cel7B and *Hj*Cel7A are pointing at degradation of amorphous material and crystalline material, respectively. Activity of *Hj*Cel6A, is however, of a more general case: removal of amorphous material and thus **cleaning of crystalline cellulose** yields crystalline-rich surfaces. Thereby, the following model is plausible: The monospecific activity of *Hj*Cel7B and *Hj*Cel7A is important for the effective

degradation of fully amorphous and crystalline cellulose, respectively. *Hj*Cel7B further opens new chains on crystalline cellulose, which accounts for the often seen endo-exo synergism. In contrast, the activity of *Hj*Cel6A covers a broader range and fills the gap between fully amorphous and crystalline materials. It is noteworthy that by this model a long controversy of the exo-exo synergism may be resolved. It is complicated to understand exo-exo synergism by full processive (exo) activity of both cellulases, as collision events are inevitable on especially cellulose I (see *chapter II*, parallel alignment of chains). However, by the bi-specific activity of *Hj*Cel6A this enzyme may not only provide the processive activity needed for crystallite degradation, but it also may form new chain ends in an endo-manner for the fully processive *Hj*Cel7A. Moreover, by the increased proposed flexibility it may be the case that – in the case of collision – *Hj*Cel6A de-complexes with the cellulose thus allowing *Hj*Cel7A to proceed. Strong evidence for such behavior was found by Igarashi and coworkers[9].

To test this hypothesis, the following sequential approach was chosen: In the case, that *Hj*Cel7B is applied to the surface, a cleaning of amorphous material should be the result, **but** no degradation of crystalline material. Addition of *Hj*Cel6A in a next step should not only lead to crystalline cellulose decomposition, but also to an increase in amorphous cellulose degradation which is – if only processive movement is assumed – not compatible. Finally, addition of *Hj*Cel7A should boost the system to its full synergism in conformity with the results from experiment 1. Figure V-18 shows the specified experiment by a series of amplitude AFM images of MACS-15 during degradation with sole *Hj*Cel7B, combined *Hj*Cel7B & *Hj*Cel6A and with the full system (*Hj*Cel7B & *Hj*Cel6A & *Hj*Cel7A).

Detailed analysis of all images confirms that the suggested behavior is responsible for synergism. The activity of *Hj*Cel7B alone leads to cleaning of amorphous cover-material which stalls after no more accessible amorphous cellulose is available. Adding *Hj*Cel6A leads to fiber shortening and additional degradation of amorphous material. The final addition of *Hj*Cel7A boosts the reaction to its maximum, which is reflected by strong degradation activities and clear indication that even highly crystalline regions (in the center of the image) are degraded. This yields the first evidence of synergism if reconstructed artificially by sequential mixing. Although already clear from the AFM images, a comprehensive analysis requires biochemical prove to exclude tip driven interference with the degrading system.
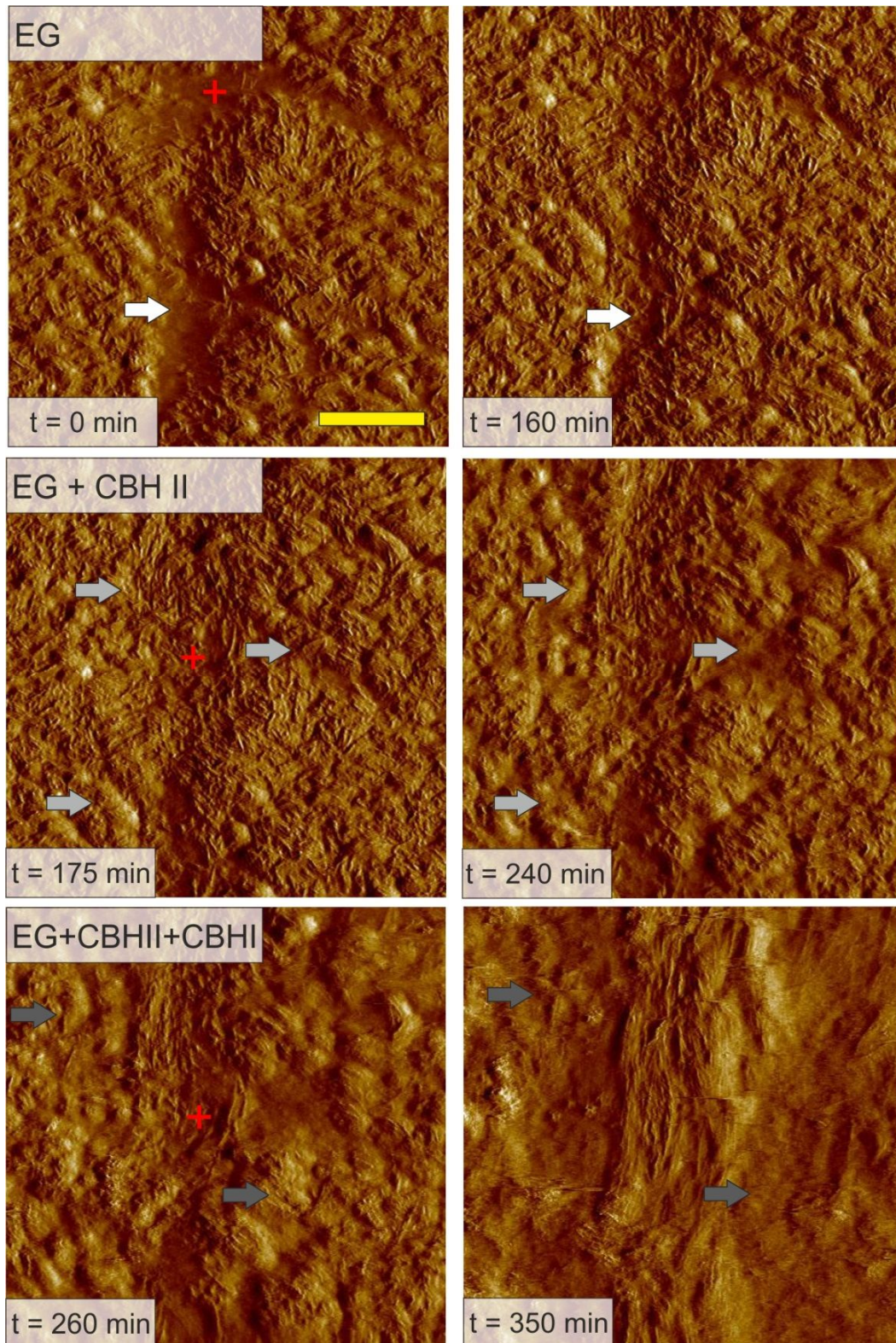
Figure V-18: Amplitude images of a sequential synergism experiment on MACS-15. The red crosses point at the same position in all images. HjCel7B cleans, as expected, amorphous material debris which is probably introduced by preparation (highlighted by white arrows). After 175 min HjCel6A is added which results in pronounced shortening of fibers and stronger degradation of amorphous material (highlighted by light gray arrows). Finally, after 260 min HjCel7A is added and boosts the activity to its maximum (highlighted by dark gray arrows). The scale bar represents 1 µm.

Measurement of quantitative data shown in Figure V-19 was performed by simultaneous biochemical analysis using the same substrates. The rate of sugar release by incubation with *Hj*Cel7B was, as expected, considerably low. Addition of *Hj*Cel6A accelerates the conversion rate by a factor of 4. This stems from the combined and synergistic activity. Final boost in hydrolysis rate is achieved by addition of *Hj*Cel7A, thus producing a further 6-fold increase (or 24-fold increase compared to the initial *Hj*Cel7B activity). This demonstrates the importance of the cooperative activity and proves that *Hj*Cel7B alone is rather ineffective. *Hj*Cel6A and *Hj*Cel7B already show synergism by achieving shortening of crystalline fibers and stronger amorphous cellulose degradation. Final addition of *Hj*Cel7A yields strong volumetric loss of material and high dynamics, which results in fast and complete removal of smaller fibers in the amorphous matrix and notably strong increase in roughness as expected (see Figure V-20).
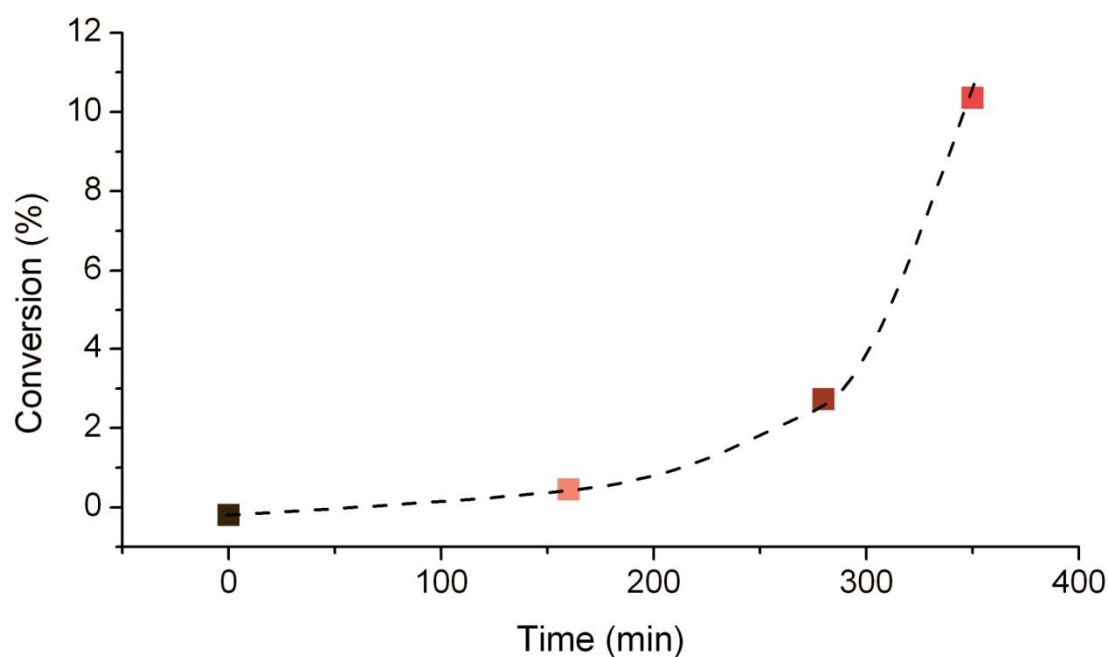
Figure V-19: Sugar release rate (conversion) measured for the blank substrate without enzymes (t = 0 min), HjCel7B (EGI; t = 175 min), HjCel7B + HjCel6A (EGI + CBH II; t = 260 min) and HjCel7B + HjCel6A + HjCel7A (EGI + CBH II + CBH I; 350 min). A 4-fold increase in hydrolysis rate is observed for the endo-exo system of EG and CBH II. Full system yields further increase by the factor of 6 demonstrating the astonishing capabilities.
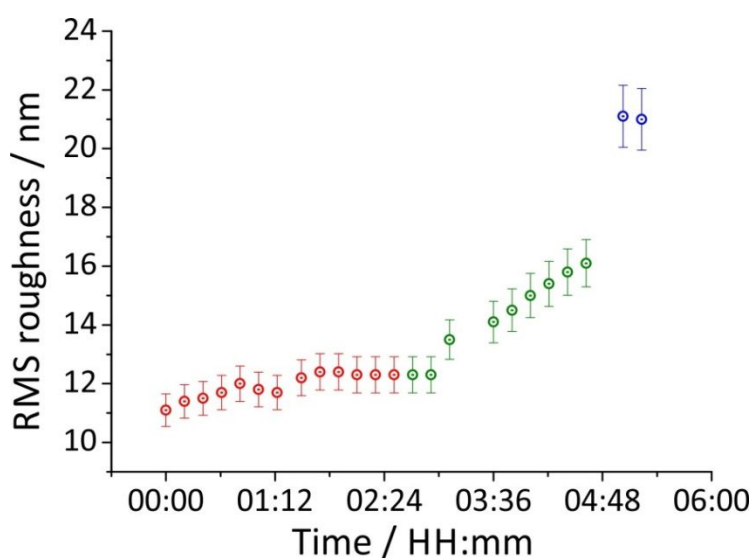
Figure V-20: Roughness increase measured for all images as shown in Figure V-18 and Figure V-19 shows a similar trend as from the biochemical data (Figure V-19) thus reflecting a strong increase of the hydrolytic activity from HjCel7B (red) to HjCel7B + HjCel6A (green) and finally to the full synergism for HjCel7B + HjCel6A + HjCel7A (blue).

V.2.5 Kinetic Analysis of Enzymatic Cellulose Degradation

V.2.5.1 Background

So far applied analyses were focused on the interpretation of AFM results and their correlation with known studies on enzymatic cellulose degradation. Although we have provided proof for the decisive role of synergism in cellulolytic systems, we still lack corresponding biochemical data. Hereon, of particular interest are specific enzyme adsorption (E_ads) and specific activities (R_ads) which supply data on bound enzyme mass per mg of substrate and the hydrolyzed amount (µmol) per mg substrate and per hour, respectively. These values are important factors, as correlation offers to specify the ratio of active and bound enzyme. This is important because enzymatic cellulose hydrolysis is characterized through fast rate retardation of glucose release[14,15], which represents one of the major limitations concerning efficient cellulose hydrolysis. It is fact that cellulose, in particular if chemically pretreated, constitutes a highly irregular topography with fissure, cracks and obstacles[3]. Here, the overall complex structure (see *chapter II*) and the dissolution of other compounds (lignin, hemicellulose) are responsible for. From an enzymatic point of view, these pores may seem advantageous as the surface area is increased. Although this is the case, these pores and fissures may also represent obstacles where cellulases may get trapped, rendering them as unavailable for further degradation. The complexity of usual applied substrates as Avicel with its high amount of surface area limits investigation to conventional biochemical methods. Herein, MACS offers a valuable alternative, as these substrate related effects may be compared to important characteristic degradation parameters. To complete the herein shown effects of enzymatic cellulose hydrolysis we aimed this study[3] on a correlation of kinetic (biochemical) and surface related effects (AFM) on MACS to give an even subtler understanding of enzymatic cellulose disintegration. Methods and experimental details correlate largely with section V.2.3 or may be found in the literature[3].

V.2.5.2 Specific Enzyme Absorbance Related to Structural Dynamics

In the following, we again applied cellulases *Hj*Cel7A, *Hj*Cel6A and *Hj*Cel7B individually or in combination on MACS and compared results to similar experiments on Avicel. For the complete system we found for E_ads and R_ads the parameters depicted in Figure V-21.
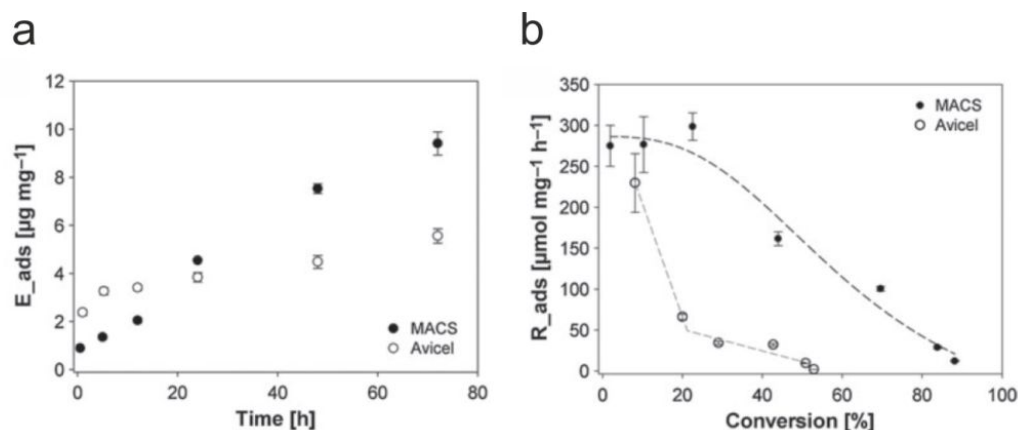

Figure V-21: Specific enzyme adsorption (a) and specific enzyme activity (b) of the complete cellulases system on MACS and Avicel. (a) Specific adsorption on MACS is increasing over hydrolysis time on MACS and Avicel. (b) Specific activity for the full cellulase cocktail shows decreasing trend for Avicel and MACS. On MACS a slower decrease is observed. Adapted and reprinted with kind permission from FEBS Journal[3].

Specific binding or adsorption of enzyme in the full system is increased over time as synergistic activity causes an increase in roughness over time (see Figure V-5 and Figure V-6). In contrast, specific activity diminishes over hydrolysis time which has two implications: **1)** Although **more enzymes** are **bound to the substrate** due to the increased surface area, more and more of these **enzymes are catalytically inactive.** **2)** The reduction appears well ahead of the full depletion of amorphous cellulose (MACS-14 has typically 10-20% crystallinity; see *chapter* IV) and thereby shows that the rate limitation usually observed in enzymatic cellulose hydrolysis may be associated by factors not in conjunction with the substrate's crystallinity. Again, we investigated the individual roles of each cellulase to unravel specific contributions to this behavior. The data of E_ads of *Hj*Cel7A, *Hj*Cel6A and *Hj*Cel7B on MACS and Avicel are shown in Figure V-22.
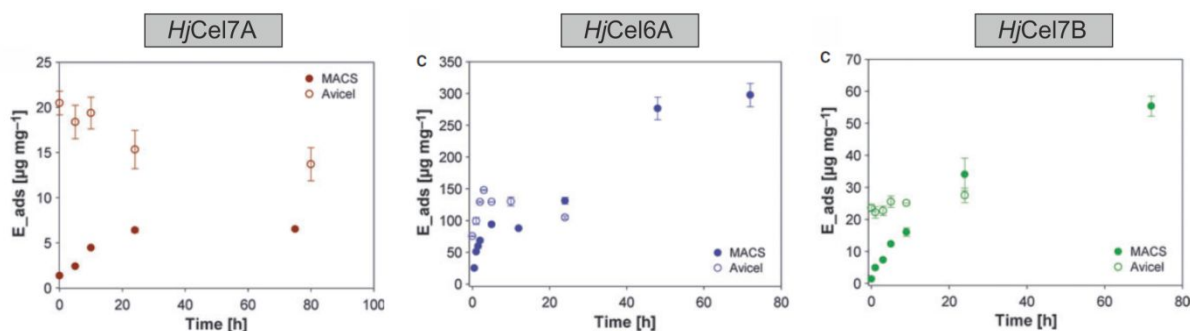
Figure V-22: E_ads of HjCel7A, HjCel6A and HjCel7B. Upward trend is observed for all cellulases except HjCel7A which is in good agreement with the overall substrate composition. On MACS, a rather high amount of degradable fibrils is available for HjCel7A. However, once degraded, the missing activity on amorphous parts of the substrate does not allow the enzyme to excavate more degradable material. Thereby, specific adsorption is reduced. The ability of HjCel6A and HjCel7B to hydrolyze amorphous cellulose allows the generation of more degradable material with time and leads to increasing trends. Reprinted with kind permission from FEBS Journal[3].

Individual activities of cellulases show – in good agreement with AFM data – that specific adsorption of *Hj*Cel7A follows a decreasing trend on Avicel, whereas an increasing trend is observed on MACS. This observation is in absolute coincidence with AFM data. While at the beginning, enough crystalline surface features are available (larger crystallites and smaller fibers), the following degradation leads to a depletion. As *Hj*Cel7A is rather inefficient on amorphous cellulose (Figure V-10), no new fiber material is excavated and specific adsorption stays at one point constant. This happens because *Hj*Cel7A requires a free end for full complexation which in this state is not available as all fibers were already degraded. On Avicel, the situation is different due to the following fact: In strong contrast to MACS, Avicel constitutes of significant high amounts of crystalline fibers (Crystallinity between 60-90 %[16]). For *Hj*Cel6A and *Hj*Cel7B we observe the opposite. While on Avicel rather decreasing (or only slightly increasing) trends are observed, both cellulases show strong increasing trends on MACS. Here, the ability of *Hj*Cel7B to primarily hydrolyze less ordered amorphous celluloses – in coincidence with AFM data (Figure V-16, Figure V-17) – yields increasing surface roughness and thus larger surface areas for *Hj*Cel7B to bind. Please note, *Hj*Cel7B may complex also on crystalline cellulose where chains are opened but no degradation is visible (due to the stronger binding the fragments do not dissolve that easily). The same is true for *Hj*Cel6A but even more pronounced. Here, the bi-specific activity of the enzyme not only increases surface roughness (see Figure V-13) but also allows to excavate and degrade crystalline cellulose which acts also as substrate for *Hj*Cel7A. This and the increasing surface area are a good explanation of the increasing E_ads. On Avicel, there is a peak in the specific binding which then diminishes over time. This may result from activity on amorphous cellulose. Once degraded, almost all surface area is crystalline. These structures are rather hard to degrade and may lead to a constant E_ads as observed. R_ads shows – in coincidence with Figure V-21 – a decreasing trend over time as depicted in Figure V-23. The decline in R_ads for the individual cellulases is, if compared to Figure V-21 b even more pronounced. A simple explanation is the missing synergism. Here, this missing effect leads to significantly higher reduction rates of the specific activity. Here missing effects from the other cellulases may lead to more inactively bound cellulases.
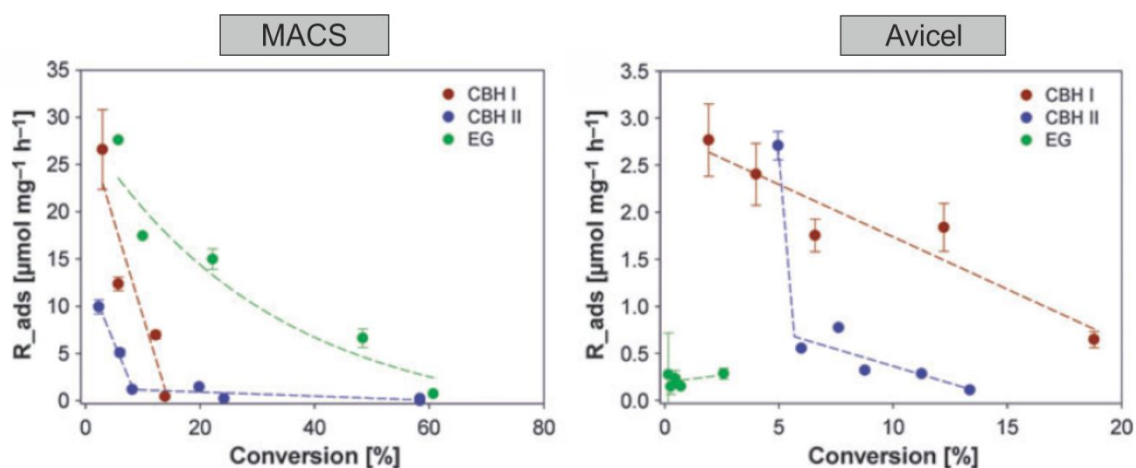
Figure V-23: R_ads of individual cellulases on MACS and Avicel. Dashed lines are guides to the eye. Reprinted with kind permission from FEBS Journal[3].

Interpretation of this data is difficult as the decline does neither correlate with the increase of surface roughness (which appears already after very short time; see Figure V-5 and Figure V-6) nor by the full depletion of amorphous material (the crystallinity of MACS-14 is as low as approx. 20 %). This

means that if the crystal structure itself would be responsible for the decline in R_ads, we at least should see no decline until 80% of the substrate is degraded. Concluding, rate retardation is neither dependent on the substrates crystallinity nor the increase of surface roughness. However, again we proved that substrate-conversion-dependent decline of R_ads is a characteristic feature, also for MACS. A comparison of E_ads and R_ads offers the assumption that – although adsorption is enhanced more and more – enzymes are bound inactively. Here, cellulases may increasingly encounter cellulose which is not available for hydrolysis. This may be at chains which are crystalline but intertwined in a complex manner or any other sort of obstacles. Furthermore, we hypothesize that these cellulases then itself represent additional obstacles, which lead to an accumulating circle of non-active cellulase. In conclusion, we showed that the rate limitation is a significant factor in enzymatic cellulose degradation and that correlation of this data with AFM results offered us to exclude possible reasons. So far, there is no indubitable prove of the causes which lead to inactive binding of enzymes. Further investigations have to be performed to unravel the reason.

V.2.6 Conclusion

Synergistic cellulases activity on polymorphic substrates is characterized via morphology dependent degradation rates – First AFM experiments revealed a strong increase in surface roughness (Figure V-6) which can be linked to two separable velocities. The different rates of degradation stem from heterogeneous morphology of MACS, where regions of higher crystallinity are found to be intermixed with amorphous cellulose. These morphologies are strongly influencing the degradability of the localized substrate, which was statistically demonstrated in Figure V-8. Correlation with image data in Figure V-7 allows the assignment of the fast velocity to small but crystalline areas. On first sight the results are not consistent if larger crystalline residues, which are hardly degraded at all and smaller crystallites which even show faster degradation than amorphous celluloses are considered. However, keeping in mind that larger crystallites show part of the cell wall structure, which includes a strong and complex integration and intertwining of fibers, we may conclude that this result is not conflicting. On larger crystallites, simply the intense number of obstacles and reduced accessibility of free chain ends must lead to a reduced degradability. In strong contrast, smaller fibers are, if not covered by amorphous material, comparable to small highways for cellobiohydrolases (*Hj*Cel7A & *Hj*Cel6A), which must result in faster degradation against amorphous material parts where the processive movement of CBHs is again obstructed by a large quantity of obstacles. So in conclusion, AFM showed that substrate composition is of significant influence to the degradability of celluloses.

The underlying mechanism is characterized through the synergistic cooperation of mono-specific and bi-specific cellulases – While the current paradigm suggests mono-specific activities for CBHs and EG, which in term of *Hj*Cel7A and *Hj*Cel7B could be demonstrated, we interestingly see differences to the current model for *Hj*Cel6A. For *Hj*Cel7B and *Hj*Cel7A, we showed that substrate degradability goes hand-in-hand with either amorphous or crystalline cellulose, respectively. However, we provided the first proof that *Hj*Cel6A takes a more general role by providing activity on amorphous and crystalline parts, which allows the notation of a bi-specific cellulase. Earlier investigations by Igarashi and coworkers already showed that the picture of *Hj*Cel6A as fully processive exo-glucanase may not be fully true[9]. Benefits of such a bi-specific strategy may be seen in the morphological structure of cellulose. In general fully crystalline or fully amorphous areas are coupled by areas of intermediate

ordering in between. Thus, by providing two highly specific cellulases (*Hj*Cel7A & *Hj*Cel7B) and one flexible one as *Hj*Cel6A, cellulose disintegration may be tuned to a maximum.

Analysis of individual cellulases activities allows attribution to morphology dependent synergism – The monospecific activity of *Hj*Cel7A as demonstrated in Figure V-10 shows that this cellulase is not – or only weakly – involved in the degradation of amorphous material. Thus, the removal of amorphous material is mainly achieved by the endo-exo synergism between *Hj*Cel7B and *Hj*Cel6A. Their activity uncovers smaller crystalline features until free ends get accessible for *Hj*Cel7A. At this point the fibers are quickly removed by the synergism of the endo-exo and exo-exo system where *Hj*Cel7B and *Hj*Cel6A are opening new chain ends in consistency with Figure V-9 while *Hj*Cel7A removes the remaining short fragments. Hence, if we now combine bi-specificity for *Hj*Cel6A and mono-specificity for *Hj*Cel7A and *Hj*Cel7B with the corresponding substrate, we see that synergism **is a complex interdependency between individual cellulases and their substrates.**

Direct observation of the cellulose degradation allows improving the current understanding of cellulose degradation – By combining all data collected so far, we now are able to propose a new model as depicted in Figure V-24. Here, *Hj*Cel6A and *Hj*Cel7B attack in combination the amorphous material, thus uncovering the crystalline features. Once accessible, *Hj*Cel7A quickly removes the crystalline features with the help of *Hj*Cel6A and *Hj*Cel7B (opening of new chain ends). Although simple in principle, we showed that the substrate is pivotal for synergism and that the current understanding of cellulases may not in any case be complete. To test these hypotheses we focused on the analysis of biochemical data.

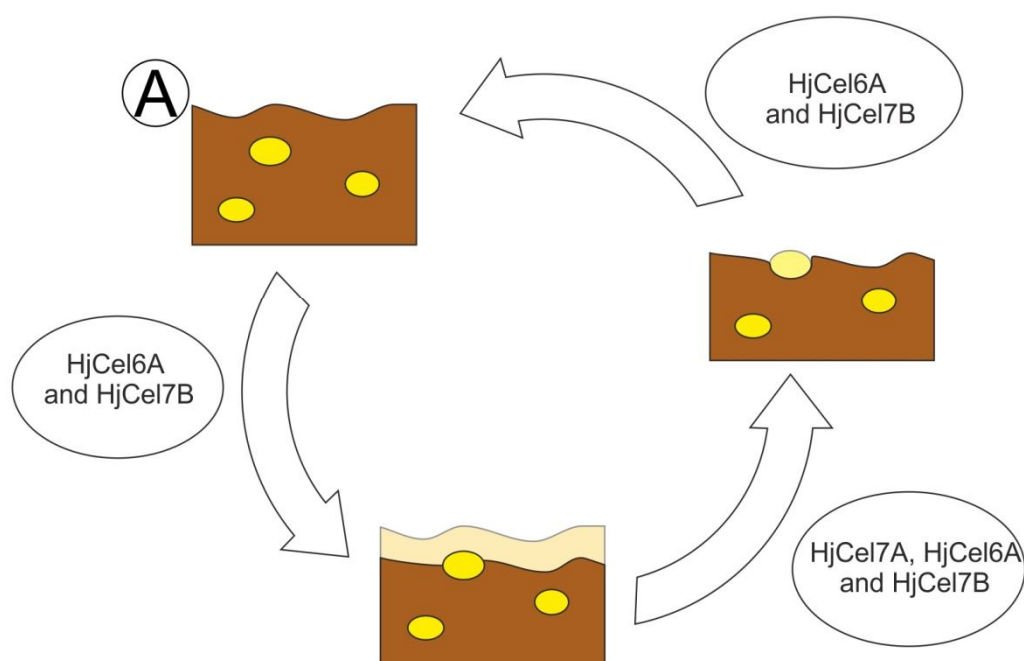*Figure V-24: The model depicted from the observed data. HjCel6A and HjCel7B are responsible for the preparation of the substrate for HjCel7A. Crystalline features are uncovered and quickly degraded by HjCel7A with the help of HjCel7B and HjCel6A (chain opening). After removal of crystalline material the process is repeated from position A forming the two step statistics (Figure V-24).*

Kinetic analysis and confrontation with AFM data excludes surface topology or crystallinity related decline in specific activity and adsorption of enzymes – The fact that the decline in R_ads is not caused by the increase of surface roughness or crystallinity in MACS, which at least should play a significant role after approximately 80% conversion, supports the hypothesis of inactively bound enzymes. This is different to enzymes locked in, e.g., a deep hole. Here at least after a certain time where others degrade the surface, this enzyme would be freed again. However, as E_ads is increasing for the full cellulase cocktail as well individual cellulases except HjCel7A eliminates this possibility. Therefore, it is rather likely, that enzymes bound irreversibly to non-degradable parts of the substrate. Although most likely low in number at the beginning, such obstacles have an accumulating effect on cellulases by leading to traffic jams[9].

In conclusion this showed that the combination of AFM techniques, substrate preparation techniques and biochemical methods allows comprehensive analysis of enzymatic cellulose hydrolysis. In this section, we have focused on the system of *H. jecorina.* We showed that the principle activities are explainable by AFM analysis and that synergism can be unraveled. However, we also showed that AFM data alone may be prone to misinterpretation. Measurements at longer timescales (biochemical data) show again that rate limitations are not caused by the increase in roughness seen in AFM. Here, the exact cause is still not fully clear but most likely caused by inactivation of enzymes on obstacles in the substrates. There may be ways to remove these obstacles by different enzymes. Therefore, we took a look at different cellulosic systems to probably overcome the observed rate limitation. The next section will deal with a novel and important enzyme, which comprises a completely novel form of cellulose disintegration.

V.3 Lytic Polysaccharide Mono-Oxidase – LPMO

V.3.1 Background

As discussed in *chapter III*, cellulose structures are usually characterized by more or less densely packed cellulose fibers on which cellulases have to act. By the results from the previous section (V.2) this is of predominant relevance, if we consider larger crystalline structures as found in MACS. The recalcitrant nature of these cellulose structures can be explained by the high crystallinity but also by the higher entanglement of fibers compared to small crystalline regions. It is likely that nature provides additional enzymatic activities or factors which help to disrupt the crystalline network of these fibers, thus leading to higher accessibility for exo- and endo-glucanases. In 2010, a discovery provided strong evidence for this hypothesis and was classified in a new family of biomass-degrading enzymes further denoted as lytic polysaccharide monooxygenases (**LPMOs**)[17,18]. The reported mechanisms differ completely[19] from so far known cellulase strategies to degrade cellulose. Structural analysis revealed a relatively small enzyme exhibiting a metal binding site on a flat surface and it was shown that removal of the metal yields a loss in observed performance[20]. Furthermore, it was reported that the enzymatic activity depends fully on electron donors which may be a small molecule or a partner redox protein[17,21,22]. The reported activities are characterized through synergistic activity, if combined with exo- and endo-glucanases as presented in the former *chapter*. Incubated without any other sort of cellulase, LPMO yields only minor amounts of released and oxidized sugars. So oxidation is thought to be primarily happening in between still not dissolvable cellulose chains as found on crystalline areas. By that, the oxidation, which can be occur on the C1 or C4 side of the glycoside, is causing a local disruption of the crystalline network thus enhancing degradability by other enzymes. This current understanding has been demonstrated by biochemical evidence of a slow release of oxidized cello-oligosaccharides and still requires immediate and direct observation on a solid surface. In order to achieve this goal, we used the same procedures as in section V.2 and show the synergistic activity on MACS together with the complete cellulase of *H. jecorina*. The experiments are supported by fluorescence dye absorption microscopy and biochemical experiments to show the unique activities associated with this highly interesting enzyme.

V.3.2 Publishing Information

[††] Equally contributing authors
[‡‡] Co-corresponding author
[§§] Corresponding author

TG and ME; DK, DH and RL provided the enzyme and preliminary experimental data and information; ME, TG, HP and BN wrote the paper including the revision.

V.3.3 Experimental Procedures

Substrate preparation (MACS) and AFM and data analysis corresponds, if not otherwise stated, to the respective sections V.2.3.1 and V.2.3.4 . All AFM experiments were conducted at 22 °C in liquid unless otherwise stated.

V.3.3.1 Enzymes

Purification protocols and protein determination for the complete *H. jecorina* correspond to methods described in section V.2.3.2 . Purified LPMO was prepared according to protocol from the literature[24] from *Neurospora crassa* (LPMO gene product; NCBI accession number XP_955892). Enzymatic reactions were conducted in 1 mg / ml cellulose in 50 mM sodium phosphate buffer, pH 6.0 and a total volume of 500 µl. Storage tubes were sealed with oxygen permeable Parafilm® to allow constant exchange of oxygen, consumed in the oxidizing reaction. Reduction agent for LPMOs was L-ascorbic acid at 7.5 µM. Enzyme loadings are summarized in Table 3.

Table 3: Applied enzymatic concentrations for LPMO, complete cellulase and specific mixtures. Note BGL was added to prevent inhibition by cellobiose (natural inhibitor of cellulases) and L-ascorbic acid was present in LPMO mixtures as reducing agent in a concentration of 7.5 µM.

Enzymatic system	Concentration ($mg_{enzyme}/g_{substrate}$)
Complete cellulase (BGL)	25 (5)
LPMO (BGL)	9 (5)
***Hj*Cel7A, *Hj*Cel6A and *Hj*Cel7B (BGL), respectively**	100 (5)
LPMO & *Hj*Cel7A (BGL)	9 & 100 (5)
LPMO & complete cellulase (BGL)	9 & 25 (5)

V.3.3.2 Fluorescence Dye Adsorption by Confocal Laser Scanning Microscopy (CLSM)

Staining buffer (2.5 mM MgCl2·6H2O, 16 mM (NH4)2SO4, 67 mM Tris-HCl) with pH 8.4 was prepared without or with 5 µM SYTO-62 (Invitrogen). SYTO-62 is a small fluorescent probe which binds to carboxyl groups thus visualizing enzymatic activity of LPMO[25].

Thin slices of MACS were incubated with LPMO for 12 hours. Thereafter, enzyme was removed by repeated and careful rinsing with absolute ethanol and Milli-Q water. Samples were then equilibrated in staining buffer for 2 hours and subsequently transferred to aluminum foil covered Eppendorf tubes with 10 mL of fresh staining buffer and the fluorescent probe. Staining was

performed at 4°C for 12 hours and finished by extensive rinsing with staining buffer. Samples were used for the experiment within 4 hours and stored in aluminum foil covered Eppendorf tubes. The negative controls were prepared in the same manner without LPMO or with LPMO missing L-ascorbic acid (electron donor). The samples were analyzed using a Leica TCS SPE confocal laser microscope (Leica Microsystems, Wetzlar, Germany) with an exciting laser at 635 nm and an emitted light detection at a range between 645-709 nm. Transmission images were recorded at 488 nm. A Leica ACS APO x 63 OIL CS objective was used for the recording of the confocal stacks. Image analysis was performed in Image J version 1.40 (rsbweb.nih.gov).

V.3.3.3 Analytics

Soluble products in excess solution after incubation were determined via colorimetry using glucose oxidase and peroxidase according to presented protocols in literature[26]. Higher oligosaccharides including cellobiose, as well as the oxidized products, were analyzed using high performance anion exchange chromatography (HPAEC-PAD) with pulsed-amperometric detection (Dionex BioLC, Thermo Fisher Scientific, Waltham, MA) as described in literature[3].

V.3.3.4 Experimental strategy
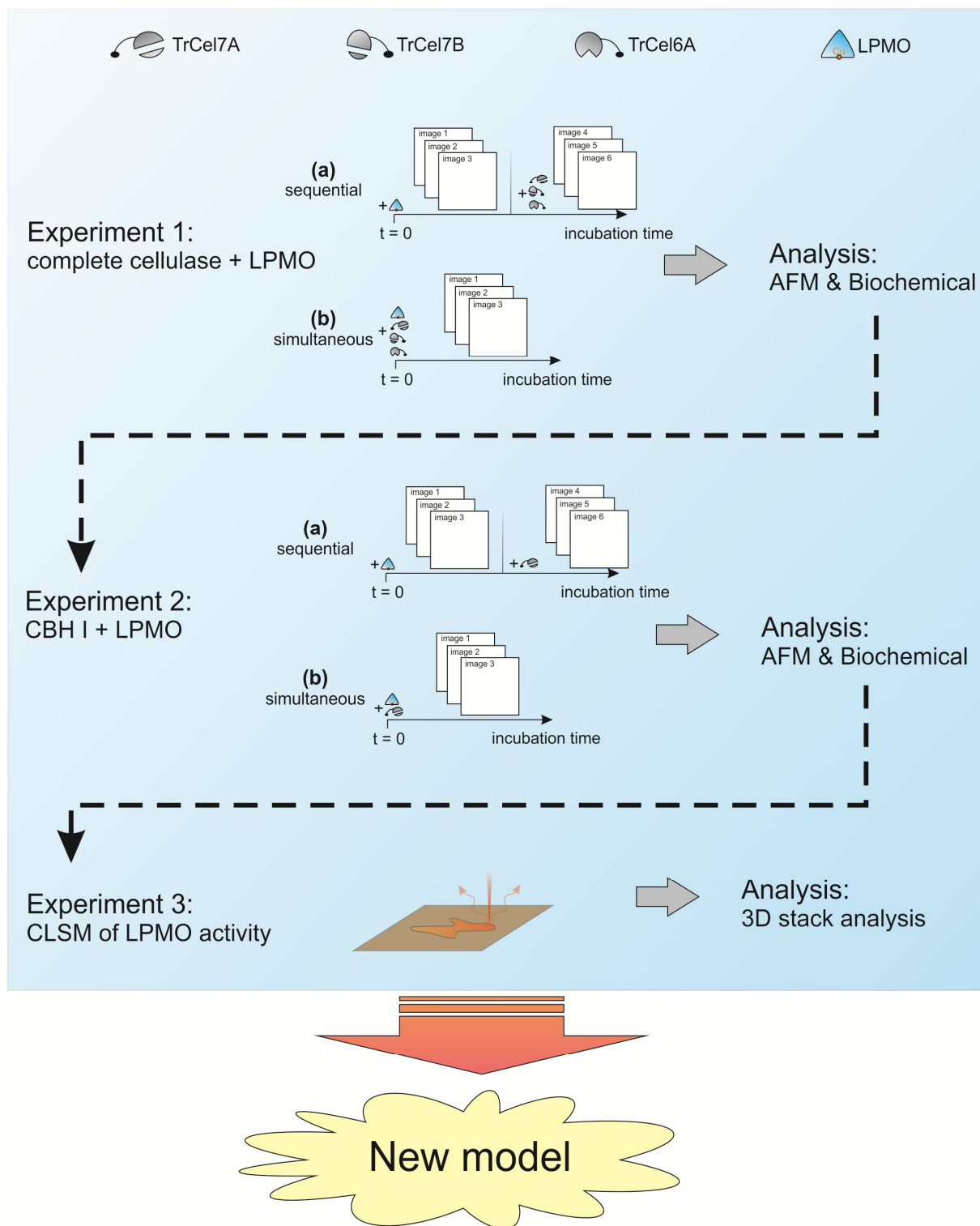
Figure V-25: Experimental procedure for visualization of LPMO activity and corresponding degradation mechanisms. In total 3 dedicated experiments were conducted. First (experiment 1) was designed to investigate the LPMO proposed activity with a full enzymatic cellulase cocktail (H. jecorina). The second experiment is based on the former and the assumption that LPMO – due to its activity – should facilitate HjCel7A degradation. The last CLSM experiment is used to demonstrate the primary attacking site of LPMO by fluorescence dying of carboxyl groups.

V.3.4 Results and Discussion

V.3.4.1 Experiment 1: Synergism of H. Jecorina Cellulase Cocktail with LPMO
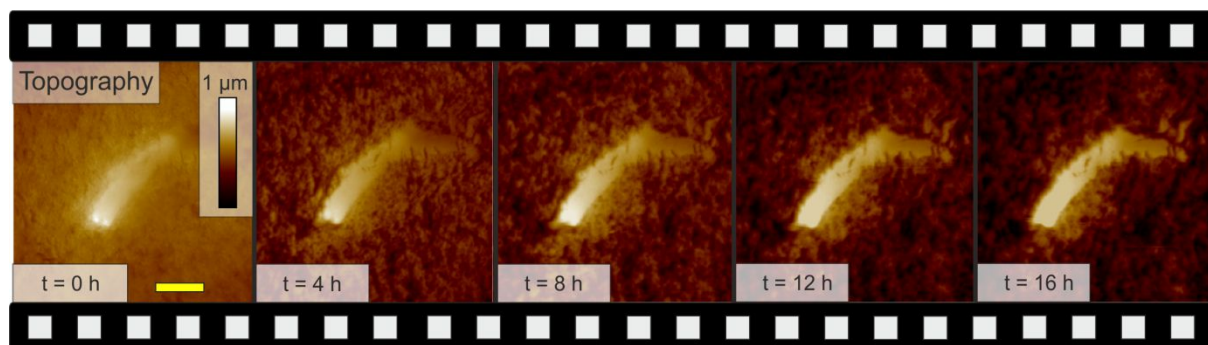
Figure V-26: AFM height images of synergistic degradation of the complete cellulase cocktail of H. jecorina with the C1 oxidizing LPMO of N. crassa. In the center of the image, a crystalline residue is observable, showing again higher resistance than the surrounding predominantly amorphous material. However, in contrast to our previous findings without LPMO we observe slow but significant degradation resulting in crack-formation and degradation from the side (see Figure V-28). Scale bar represents 2 μm.
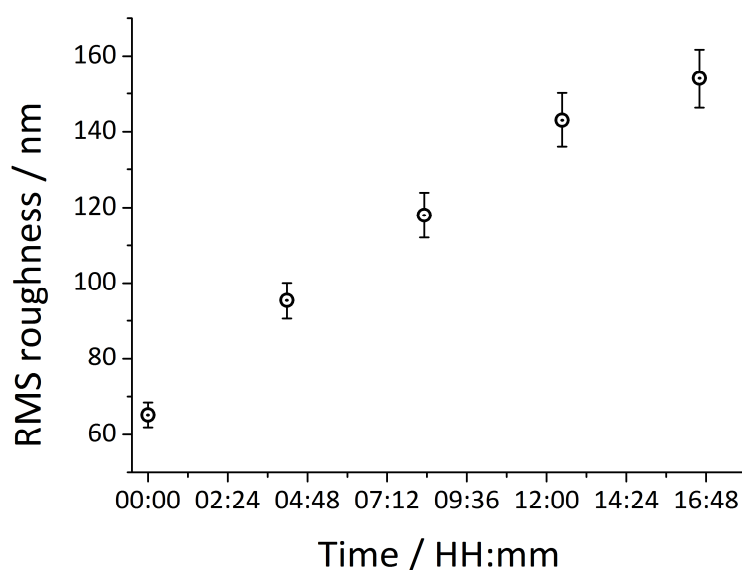
Figure V-27: Roughness increase due to the activity of the LPMO-SVG cellulase system. Note, RMS was recorded on areas excluding the crystalline residue.

The combined activity of LPMO and complete cellulase is reflected, in accordance to our previous study, by a strong degradation of surrounding amorphous matrix material (see supplementary Movie S5, S6 & S7). The observed loss of material in z-direction is approximately 500 nm within 16 hours. Surrounding matrix material is degraded similar to SVG incubation alone (see Figure V-5 and Figure V-6) and produces a significant increase in surface roughness (Figure V-27). The crystalline residue is again more resistant to degradation, however, with a significant difference: While the system lacking LPMO is not able to degrade the crystallite in sufficient timescales at 22°C, we here observe considerable degradation for the system with LPMO (Figure V-26). A closer examination of the crystallite structures reveals that cracks are enlarged, and the whole block face of the crystallite gets thinned (Figure V-28, supplementary Movie S6 & S7). The corresponding section analysis reveals a

thinning of the crystallite and a deepening and widening of cracks (Figure V-28b). As this process was not observed for the complete cellulase system of *H. jecorina* without LPMO, the cracking can be clearly attributed to this enzyme and its synergistic activity with cellulase from *H. jeroncia*. This remarkable result is in coincidence with the current paradigm concerning LPMO action. However, we provided the first visual proof for this behavior. Here LPMO indubitable seems to attack the highly crystalline regions of a substrate[19,27], thus producing new chain ends and local disruption of the hydrogen bonding network. By this, accessibility for processive enzymes *Hj*Cel7A and *Hj*Cel6A must be increased. Please note, to test the primary attack of LPMO on crystalline phases we provide CSLM data later in this chapter (Figure V-33). The reason that this effect is mainly acting on the larger crystallites may be understandable by considering the mode of action. The oxidation of the cellulose chain causes a distribution of the hydrogen bonding network not only at the oxidation but also within a small radius affecting more chains. This is in strong contrast to e.g. *Hj*Cel7B activity, where only the chain is terminated. Thereby, the accessibility is increased for cellobiohydrolase (e.g. *Hj*Cel7A and *Hj*Cel6A) and their increased activity thus yields the distinctive observed synergism[28]. Supplementary experiments provided proof that without LPMO or LPMO without L-ascorbic acid, degradation of larger crystallites is not observable. Thereby first visual proof is given that LPMO is synergistically active with a complete cellulase cocktail of *H. jecorina*. However, from these experiments, it is not clear whether LPMO is interacting with the complete system or individual cellulases of the mixture (*Hj*Cel7A, *Hj*Cel6A and *Hj*Cel7B).
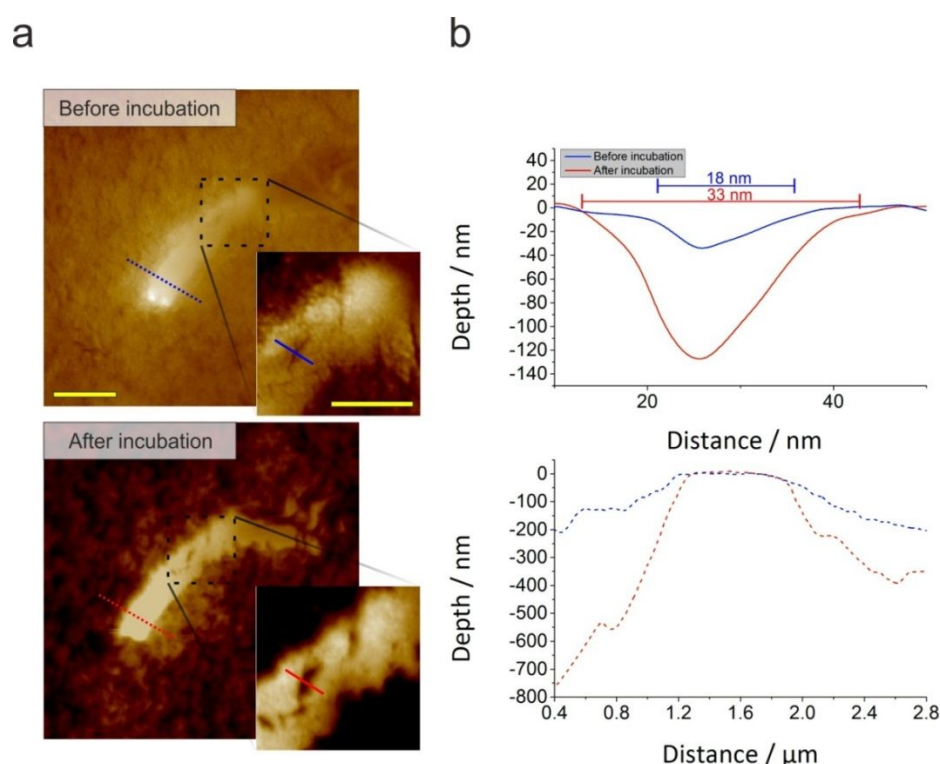
Figure V-28: AFM images providing proof for the significant crystallite degradation by synergistic activity of LPMO and complete cellulase of H. jecorina. (a) The images show the situation before (t = 0 h) and after (t = 16 h) of incubation with sections and enlarged areas (black dashed rectangle) as inset. (b) Section analysis of the areas indicated in (a) showing a deepening and widening of cracks and a clear thinning of the crystallite. The width of the crack is increased from 18 nm (before; blue line) to 33 nm (after; red line) while increasing the depth by a factor of 4. The width of the crystallite decreases from former 800 nm (blue dotted line) to 610 nm (red dotted line). Scale bars represent 2 µm in the overview images and 1 µm in the insets.
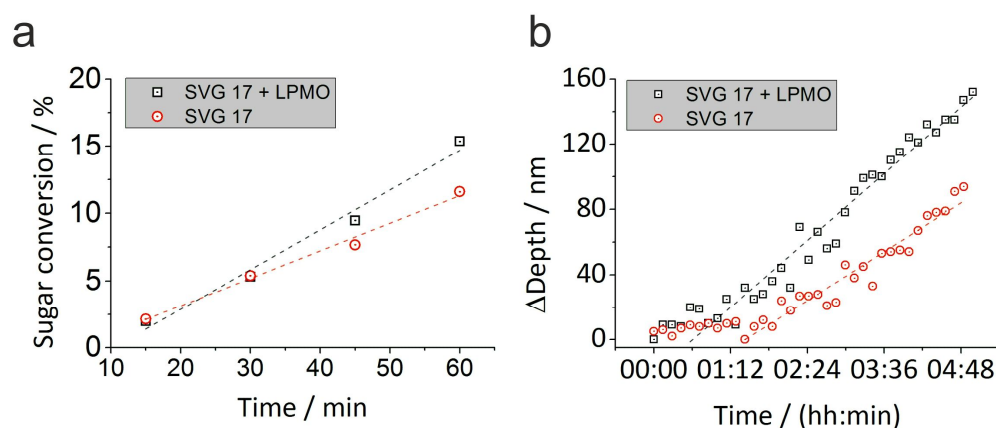
Figure V-29: Activity of complete cellulase (SVG 17; HjCel7A + HjCel7B + HjCel6A) without (red) or with LPMO (black) on MACS measured by biochemical methods (a) and AFM techniques (b). The results suggest a synergism in the range of 1.2 if calculated via the slopes of the linear fits. This is expectable concerning the relative low concentration of larger crystallites on MACS. On substrates featuring predominately crystalline phases (Avicel ~ 60-70%) synergism shows larger factors[28].

In order to get quantitative results, we performed similar AFM experiments as described in section V.2.3.4 and additionally characterized the volume degraded by the enzymatic system. Related data are shown in Figure V-29 and clearly confirm synergistic activity on MACS. The enhancement factor of 1.2 is comparable low considering the low spatial density of larger crystallites in MACS. Investigation of the degrading mechanism on the surrounding matrix shows a comparable activity in comparison to previous experiments without LPMO. This is further evidence that the predominant synergism between LPMO and other cellulases is most relevant on the crystalline phases. We already showed that *Hj*Cel7A is the primary factor in the degradation of crystalline material. Therefore, further investigations were mainly focused on the synergism between LPMO and *Hj*Cel7A.

V.3.4.2 Experiment 2: Synergism of LPMO with Cellulases HjCel7A, HjCel6A and HjCel7B

Although previous data suggests a predominant effect of LPMO in combination with *Hj*Cel7A, for completeness we also performed the same experiments with *Hj*Cel6A and *Hj*Cel7B. However, in coincidence with the discussion on the previous experiment, we did not see any significant boost in activity for *Hj*Cel6A and *Hj*Cel7B within the first hours of the experiment (data not shown as no variation was found). We therefore focused the investigation on the specific synergism between *Hj*Cel7A and LPMO as the most probable cause of the observed synergism in Figure V-29.
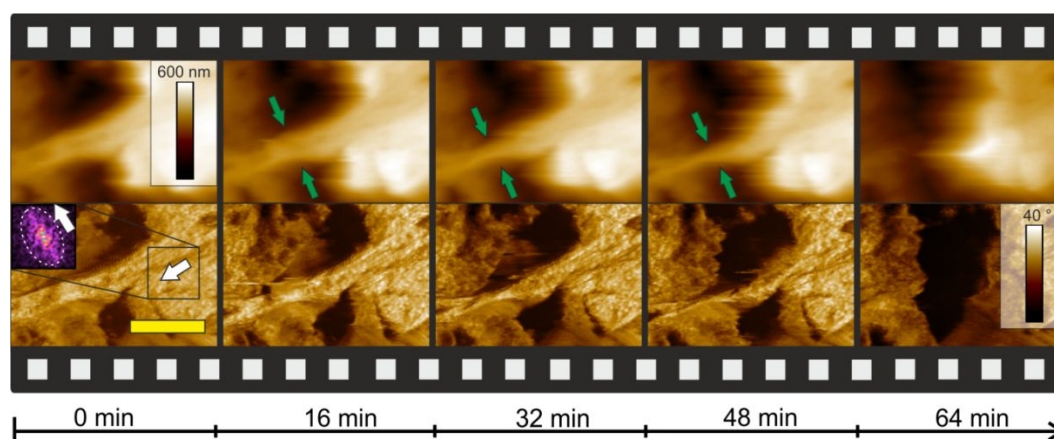
Figure V-30: AFM height (top) and phase (bottom) images showing the degradation of crystalline parallel oriented fibers over a timescale of 64 minutes. Note that the preferential form of fiber decomposition originates from a side wall attack of the fibers (green arrows). The orientation is highlighted by a FFT map (phase image; 0 minutes; black square) showing an ellipsoidal orientation corresponding to the 90° tilted fiber orientation (white arrow). After 64 minutes the fiber bundle, approximately 150 nm in width is completely degraded by the combined activity of CBH I and LPMO. Scale bar represents 300 nm. Adapted and reprinted with kind permission from ADBMB/JBC [23].

As evident in Figure V-30 (see supplementary Movie S7), the combined activity of *Hj*Cel7A and LPMO results in pronounced degradation of crystalline material, followed by complete removal of a fiber bundle of initially 150 nm in width. Again, we have to emphasize that this type of degradation is not observed in the complete cellulase system (*H. jecorina*; SVG 17) alone and proves to be specific for this synergism. The observed fiber thinning is in conformity with the processive movement of the exo-glucanase while LPMO acts as chain opening and crystallite disrupting enzyme.

This is a remarkable result, as **we provided the first proof** of the unique role of LPMO in a "classical" synergistic system. The role of morphology dependent synergism has to be emphasized once again as LPMO and *Hj*Cel7A rely on crystalline cellulose for full deployment of activity. Considering the fact that MACS is mainly constituted of rather disordered matrix material, the synergism observed in biochemical studies must be low. This is already true if we compare the data from Figure V-29. Now doing the same for *Hj*Cel7A and LPMO, we observe a controversial result (see Figure V-33).

Biochemical data, shown in Figure V-33, confirms synergism for NCC and Avicel but rather inhibiting effects on MACS. Considering the main difference of MACS, if compared to NCC and Avicel, we find that the majority of the cellulose in MACS is amorphous with multiple smaller crystalline fibers embedded (*chapter IV*) and sparse larger crystallites. From AFM data and confocal laser scanning microscopy experiments (see Figure V-33) we know that LPMOs primarily attack the crystalline part of the substrate. Thus, apart from the larger crystallites which show a significant and positive synergism, we have either amorphous cellulose which in previous experiments was found to be widely inaccessible for *Hj*Cel7A and smaller crystalline fibers. It is conceivable that LPMO action on such small fibers leads to a de-polymerization and -crystallization that renders the morphological properties to a point, where *Hj*Cel7A is no longer effective. For instance, multiple de-polymerization steps on smaller crystalline fibers may alter the structure to a point were fragments of the individual chains get so short that *Hj*Cel7A can no longer proceed efficiently along chains. This is important as chain complexation and de-complexation – that is merging or removing of chains – takes a certain

amount of time. Thus, the time span to degrade the former short but crystalline small fiber is extremely increased. On larger crystallites, the opposite is the case: As chains are longer, more intermingled and inaccessible, LPMO activity provides beneficial effects.
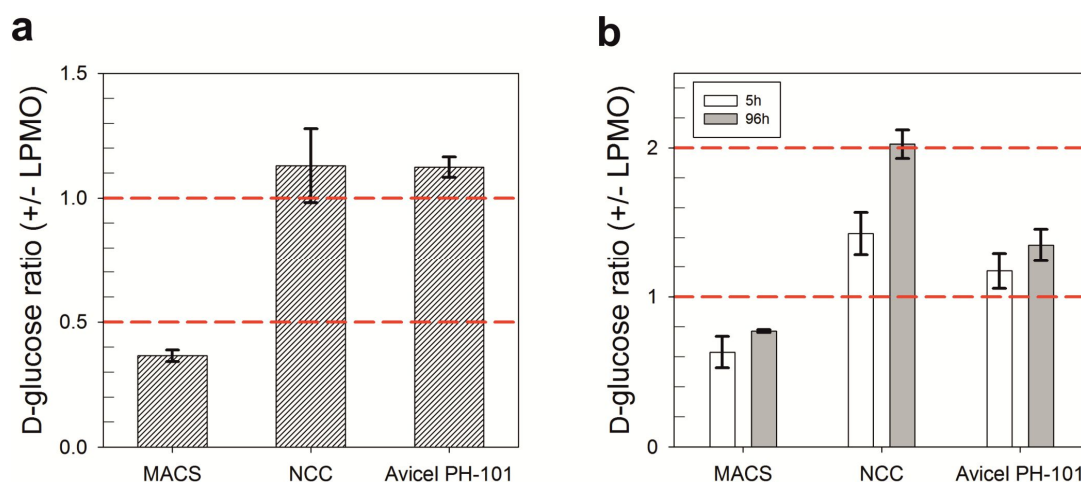

Figure V-31: Biochemical analysis of HjCel7A – LPMO synergism on different substrates for the sequential (a) and simultaneous approach (b). Bars correspond to the observed synergism. For MACS we see a negative synergism in both cases which is in contradiction to the observed AFM data. However, considering a low ratio of crystalline cellulose in MACS compared to amorphous cellulose, these effects may stem from alternative mechanisms. For nano-crystalline cellulose (NCC), we observe in both cases the highest synergism while on Avicel PH-101 weak synergistic activity is revealed. Reprinted with kind permission from ADBMB/JBC [23].

This is clear if we consider NCC and Avicel where we have the situation that in both cases primarily crystalline cellulose is present. For these substrates, we see the facilitated synergism between both enzymes. Interestingly, we observe a quite strong synergism for NCC in the simultaneous approach (Figure V-31 b) which is even higher than for Avicel. An explanation is that LPMO activity and entailed formation of carboxyl groups leads to charged particles which are beneficial for colloidal stability. NCCs, as described in *chapter II,* are present in a liquid phase and the colloid is stabilized through electrostatic interactions. Increasing the number of charged moieties on the surface of the nano-crystallites must therefore further stabilize the colloid which is beneficial for *Hj*Cel7A as all the crystallites stay accessible. To sum up: On MACS, the relative low number of nano-crystalline particles and the activity of LPMO most likely form highly disrupted surfaces which are no longer a good substrate for *Hj*Cel7A. In strong contrast, this effect is – due to longer elementary fibrils and a larger surface area – not problematic on larger crystallites. Here activity of LPMO increases the degradability by disrupting the otherwise recalcitrant surface for *Hj*Cel7A. Now, the same must be true for Avicel, as these crystallites are closely related to the larger ones in MACS. For NCCs, which are more likely related to the nanocrystallites in MACS, we see however, in contradiction positive synergism. But, the surface area is huge due to the high surface-to-volume ratio, which does not apply for nano-crystallites embedded in MACS. Furthermore, the introduction of charged moieties is beneficial for colloidal stabilization and renders the crystallites more accessible for *Hj*Cel7A degradation.

Therefore, the effect of LPMO in this case produces another form of synergism where the specific activity stabilizes the crystallite in solution, thus making it more accessible for *Hj*Cel7A activity. It has

to be emphasized that this is a good example, how synergism can be related to either enzyme-enzyme or enzyme-substrate or enzyme-substrate-solution interdependencies.
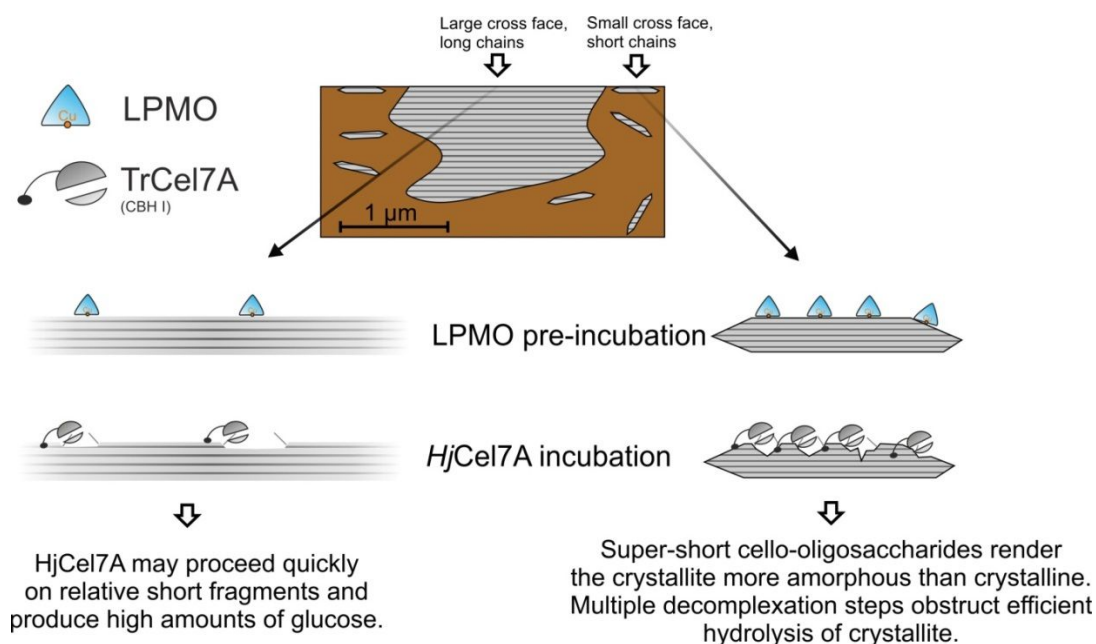
Figure V-32: Schematic model of MACS-15 decomposition of the cooperative activity between LPMO and HjCel7A. On larger crystallites the corresponding larger cross face and longer chains yield a situation where LPMO produces relative short fragments, which are well suited for HjCel7A processive activity (HjCel7A may proceed relative long chain segments without obstacles). On shorter crystallites LPMO activity leads to very short fragments which render the crystallite more amorphous than crystalline. The relative short free path length slows hydrolysis by HjCel7A considerably down.

V.3.4.3 Experiment 3: Confocal Laser Scanning Microscopy to Unravel the Individual Role of LPMO on Polymorphous Substrates

Concluding data revealed by AFM analysis and biochemical analysis (Figure V-26 till Figure V-31), we now can specify the individual role of LPMO without any other enzyme. As already mentioned in the beginning, LPMO deploys only negligible cellulose degradation if incubated alone, but should strongly alter the surface by forming oxidized cellulose products. In order to visualize the oxidation of cellulose, we must state that AFM techniques are not appropriate. The reason is that the chemical sensitivity of the phase signal is often too low for reliable single molecule detection.

Here, the method of choice is confocal laser scanning microscopy (CLSM), as the small fluorescent probe, which binds to carboxyl residues introduced by oxidization, can be mapped efficiently. It must be emphasized that the resolution of CLSM is less than for AFM, but if significant oxidation can be assumed, the mean signal of regions with preferential attack of LPMO is easy detectable.

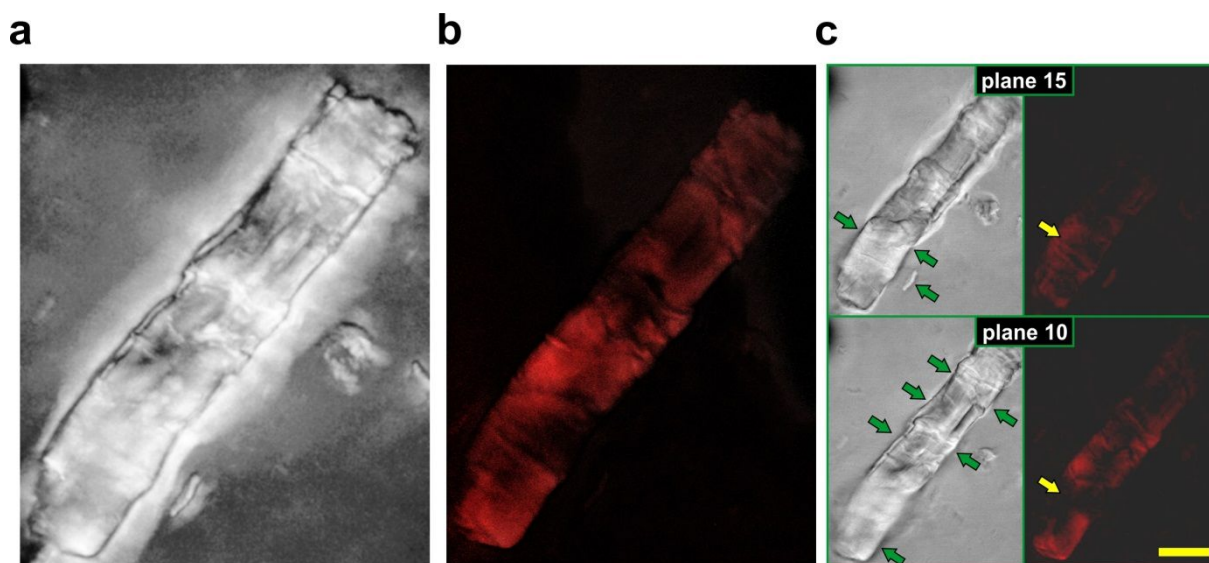*Figure V-33: (a) Light microscopy image in transmission showing MACS with a residual crystallite similar to AFM experiments. (b) CLSM image of the same regions showing the fluorescence of the SYTO-62 probe, bound to carboxyl groups. Interestingly, the majority of oxidized cellulose products are found on the crystallite supporting preferential attack of ordered regions by LPMO. Stacks (c) showed that the oxidation is limited to the surface of the crystallite demonstrating a negligible degradation by LPMO. (c) Demonstration of the surface confinement of carboxyl groups. The green arrows point at regions in focus which are fluorescent in the CSLM image. Areas not in focus do show no fluorescence. In the case that in-depth carboxylation or degradation is resulting from LPMO activity, the plane inside the crystallite (which is in focus at that plane) must show fluorescence. However, there is none as shown in plane 10 by the yellow arrow which means that the activity of LPMO is limited to the surface. Scale bar represents 10 µm. Adapted and reprinted with kind permission from ADBMB/JBC [23].*

Results obtained by CSLM experiments (Figure V-33) reveal the preferential activity and preliminary binding of LPMO to crystalline cellulose parts. Most likely, the specific binding to highly ordered cellulose parts may be addressed to the LPMO structures exposed on the flat planar surface which are similar to carbohydrate binding modules (family 1; CBMs) as proposed by Harris coworkers[20]. Furthermore, we observe a surface confined oxidation of the cellulose particle which allows the conclusion of no in-depth degradation (see Figure V-33 c; plane 15 & plane 10) as already observed in the AFM experiments. Concluding, LPMO is active on crystalline cellulose and not or only in a minor extent on the amorphous matrix of MACS. The primary form of synergism is confined to crystalline structures and is thus closely related to *Hj*Cel7A activity.

V.3.5 Conclusion

By the combination of CSLM, AFM and biochemical methods the following characteristics of synergistic LPMO activity could be revealed.

Cellulase cocktail from H. jecorina shows synergism with LPMO from N. crassa on polymorphous MACS – Quantitative biochemical data (Figure V-29) reveals a weak, but clear synergism on MACS. *In-situ* visualization in Figure V-26 provides evidence that LPMO activity boosts crystallite degradation by the *H. jecorina* system. Further proof is given by quantitative AFM analysis concerning crystallite thinning and crack opening, where we could show that ongoing activity for 16 hours results in a 25 % thinning of the crystalline block face and crack deepening / widening of 400 % and 200 %,

---

respectively (see Figure V-26). As a matter of fact, we could not observe this behavior by incubation without LPMO. In conclusion these results suggest a strong interdependency with *Hj*Cel7A which, in the case of the cellulase cocktail of *H. jecorina,* is responsible for crystallite degradation.

Crystallites are degraded by synergistic HjCel7A and LPMO activity by pronounced thinning of fiber bundles – AFM investigations of LPMO - *Hj*Cel7A interdependency show the attack of an approximately 150 nm wide fiber bundle resulting in complete removal (Figure V-30). It is noteworthy that *Hj*Cel7A alone, as shown by previous experiments, is only able to degrade smaller fragments embedded in the amorphous matrix. Therefore we once more showed that the specific de-polymerization and -crystallization activity of LPMO is preparing crystallites for efficient *Hj*Cel7A activity.

LPMO – HjCel7A activity on MACS shows rather inhibiting effects than synergism – Biochemical results (Figure V-31) clearly reveal a decrease in synergism for sequential and simultaneous exposure on MACS. Explanation for this – on first sight – contradictory result is the polymorphic nature of MACS. While LPMO shows synergism on crystalline features as demonstrated by AFM (Figure V-26, Figure V-28 and Figure V-30) and biochemical data on Avicel and NCC, synergism is obstructed by LPMO activity on the shorter crystallites in MACS. It is conceivable, that limited binding sites on the smaller crystallites and possible irreversible binding of LPMO or strong de-polymerization of these short fragments renders fibers inaccessible by *Hj*Cel7A (see Figure V-32). Please remember, for the complete cocktail, synergism, although low, is present which can be easily understood. In this case, small fiber de-polymerization which renders them inaccessible for *Hj*Cel7A is not problematic as these areas are now suited for *Hj*Cel6A and *Hj*Cel7B. Here, the weak synergism (factor of 1.2) presumably results from the increased degradation of larger crystalline material.

LPMO primarily oxidizes areas with crystalline orientation without in-depth degradation – CLSM data provided the final evidence for the above given conclusions. The activity could be visualized by the use of a small fluorophore (SYTO-62) which binds to the carboxyl groups. In Figure V-33, clear indication is given that the activity is confined to the surface of these crystallites and that no major degradation takes place on the amorphous surroundings. It is therefore clear, that LPMO prepares crystalline areas by depolymerizing long cellulose chains, thus producing docking sites for *Hj*Cel7A.

LPMO proves to be a highly interesting enzyme which shows indeed synergism with *Hj*Cel7A. This is interesting, as form of activity is completely different to usually observed endo-active enzymes. Again the combined implementation of biochemical and AFM methods supported by CLSM showed a deeper insight into enzymatic activity which otherwise would be strongly masked or elusive.

V.4 Cellulosomes - Multi-Enzyme Complexes

V.4.1 Background

The results obtained via *in-situ* AFM techniques on the synergism of the cellulase complex of *H. jecorina* and its interaction with rather recently discovered LPMO of *N. crassa* demonstrates the importance of cooperative activity. Secreted by the corresponding organism as free enzyme, interdependencies rely on a sequential binding on specific substrate morphologies (as the case for LPMO and *Hj*Cel7A) or on a simultaneous attack (*Hj*Cel6A with *Hj*Cel7B). One may speculate that a

limitation of the degree of freedom of these interacting enzymes may optimize the synergism in complex systems. Not surprisingly, nature has encountered for this possibility by producing multi-enzyme complexes found in bacterial and fungal organisms. Here CBMs usually associated with the glucosidases are substituted by dockerin molecules, which strongly bind to cohesion proteins aligned on a scaffolding protein[29,30] (see Figure V-34). The scaffolding usually contains the CBM required for binding. It is not hard to imagine the advantages of this strategy. While free enzymes are oblique to thermodynamically driven diffusion to cooperate with each other, the cellulosome combines the relevant enzymes in spatial proximity to each other. However, proof that the strategy of linking different cellulases in spatial proximity to each other is beneficial (synergistic) has been given rather recently by Fierobe and coworkers[31]. They used artificially complexed cellulosomes and compared these to a cellulase system including the exact same enzymes. A huge variety of cellulases, xylanases, pectinases and hemicallulases in different organisms depicts that cellulosomes are highly flexible nano-machines used for the degradation of cellulose and other polysaccharides. Not surprisingly, the scientific interest in diverse types of cellulosomes, genetic sequencing, the catalytic components, regulation, assembly and the cellulosome function[29,30,32] is given and new approaches for a deeper understanding are absolutely required. Ding and coworkers emphasized in 2008 the possibility to use AFM for the investigation of cellulosome-cellulose interaction and its assembly as well as binding[33]. However, to the best of our knowledge direct *in-situ* visualization was, so far, not achieved by AFM techniques. Although recent TEM studies showed that the current paradigm for cellulosome activity has to be reconsidered[34,35], we want to point out that beside the remarkable obtained results, direct visualization is inevitable for a full picture. TEM investigation requires staining and treatment of the reaction product, which could give rise to artifacts. Furthermore, the analysis can only show endpoint results of the ongoing degradation mechanism and is thus not sufficient for a full proof of the accompanying and undoubtedly complex coherencies. In this section, we show the first successful attempts of cellulosome visualization on highly crystalline nano-cellulose whiskers which were immobilized on highly ordered pyrolytic graphite. However, preliminary experiments showed that cantilevers and cellulosomes interact and thus obstruct imaging. Most likely some part of the flexible structure may bind to the silicon or silicon-nitride tip which obstructs stable imaging significantly. **By tip-modification,** we were able to account for this problem and study cellulosome **interaction *in-situ* for the first time**. We apply specific studies on the degradation damage on individual crystallites and demonstrate a non-processive degradation mechanism leading to a new paradigm of cellulosome degradation.
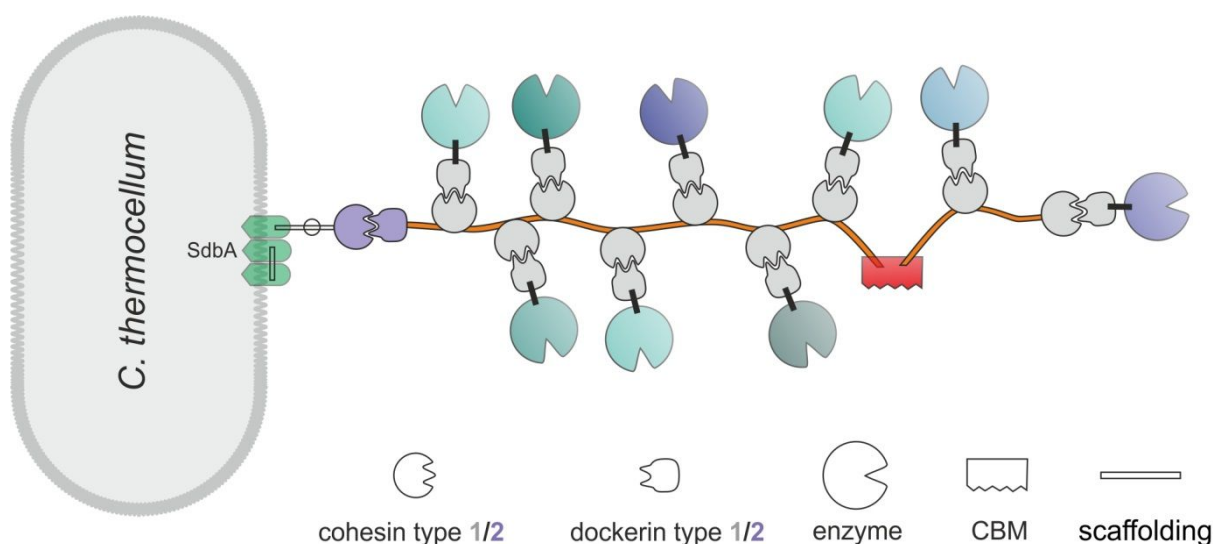
Figure V-34: Schematic representation of the cellulosome. The scaffolding (orange) and the cohesins act as linker between multiple cellulases which have substituted their binding modules with dockerins. Each cellulosome features an additional CBM connected to the scaffolding.

V.4.2 Publishing Information

The following section is a preliminary draft for a publication in a peer reviewed journal on the degradation of cellulose by cellulosomes. The alphabetically ordered authors are: Timothy Aschl, Manuel Eibinger, Thomas Ganner, Bernd Nidetzky and Harald Plank. Concept and Idea was from TG, ME, BN, and HP; AFM experiments were conducted by TG, TA and ME; *C. thermocellum* cultivation and cellulosome purification were from ME; biochemical experiments were from ME; text and images in this draft are from TG.

V.4.3 Experimental Procedures

V.4.3.1 Sample Preparation

Nanocrystalline cellulose was prepared by sulfuric acid treatment according to protocol from literature[23,36]. Resulting colloidal solution was complemented by 0.05% sodium azide to prevent microbial growth and stored at 4°C in capped vials. Cellulose mass concentration was determined by multiple weighting of the dry mass with 7.5 mg/ml. Precursory to AFM experiments, the solution was sonificated with an ultrasonic bar (Sonoplus HD2200, Bandelin electronic GmbH & Co. KG, Berling, Germany) for at least 5 min at 52 % of the maximum power (200 W) while cooled in an ice bath. Solution was than diluted 1:10 to achieve a suitable concentration of nano-crystallites.

For liquid investigations highly ordered pyrolytic graphite (**HOPG**), ZYB grade (Bruker AXS, Santa Barbara, California/USA), was prepared by cleavage with the scotch tape method[37]. Immediately after, approximately 300 µl of NCC solution was suspended and evenly distributed on the freshly cleaved HOPG followed by resting for 3 minutes. Thereafter, solution was carefully removed by rinsing with Milli-Q water and stored in buffer until the experiment.

For pre-/post-incubation experiments an alternative substrate was chosen as the result of the special preparation routine. To allow specific conclusion on cellulosome activity we had to ensure to investigate the same crystallites before and after incubation. We therefore prepared silicon wafers with a 3 nm oxide layer by focused ion beam (**FIB**) milling to form 2 x 2 μm^2 gratings with 4 individual segments (see Figure V-35). Silicon wafers were carefully cleaned (lens paper, isopropanol and CO_2 spray drying) and mounted in the FIB (FIB Nova 200, FEI Company, The Netherlands). Gratings were milled into the substrate at positions (3 mm, 3 mm) and (7 mm, 7 mm) with primary ion beam energies and beam currents of 30 kV and 30 pA, respectively. An appropriately adapted bitmap image (Figure V-35, b) was used for milling the pattern with 1024 x 1024 pixels, a pixel dwell time of 100 μs via a single pass. Thereafter, specimens were removed and 300 µl of NCC solution was suspended on the substrates for again 3 minutes and removed after 3 minutes by careful rinsing with Milli-Q water. Specimens were dried at 50 °C for about 6 hours and then used for investigation.
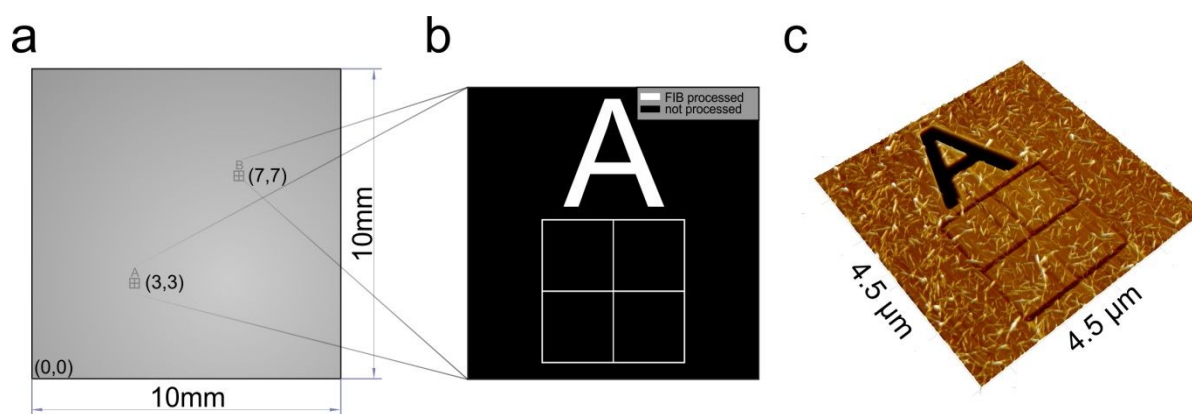

Figure V-35: Schematic drawing of the FIB preparation protocol for the silicon specimens. (a) Specimens have dimension of 10 x 10 mm^2 and are FIB milled at position (3,3) and (7,7) with the in (b) shown pattern (white areas processed; black areas not processed). Parameters were chosen in a way that the 4 segment grid has dimensions of 2 x 2 μm^2 and processing was done at primary beam energies of 30 kV and 30 pA current. In total 1024 x 1024 pixels were scanned at dwell times of 100 μs and with one pass. (c) AFM image of (b) on the processed silicon substrate with already adsorbed NCC particles.

V.4.3.2 Atomic Force Microscopy

AFM images were collected on a Bruker Fastscan Bio AFM operated by a Nanoscope V controller and the Nanscope 9.1 imaging software (Bruker AXS, Santa Barbara, California/USA). Measurements were conducted either *in-situ* at elevated temperatures or *ex-situ* under ambient conditions in a pre-/post-incubation manner.

A liquid cell with a total volume of 60 µl, an injection system (Bruker AXS, Santa Barbara, California/USA) and a home-made double syringe injection valve was used for *in-situ* studies. Experiments were conducted using Fastscan D cantilevers with spring constants between 0.25 N/m and 0.4 N/m, resonance frequencies around 110 kHz in liquid and nominal tip radii of approximately 8 nm (supplier specifications). Temperatures were controlled using a Peltier-element driven heating plate (Bruker AXS, Santa Barbara, California/USA) operated by a Lake Shore 331S temperature controller (Lake Shore Cryotronics Inc., Westerville, OH). Prior to approach, stage and sample were heated to 50°C followed by 5 minutes of temperature equilibration. The liquid cell was filled with buffer, carefully engaged and flushed with 300 µl of buffer to remove air bubbles. Temperature

equilibration was repeated for 5 minutes. Appropriate positions were chosen according to flat clean areas and a set of reference images covering the micro to nanoscale (2 x 2 μm^2 to 0.1 x 0.1 μm^2) was recorded. Incubation was started by flushing 200 μl of a 25 μg / mL cellulosome buffer solution through the liquid cell followed by continuous image recording.

Pre- and post-incubation experiments were conducted using Fastscan C cantilevers with a nominal spring constant of 0.4 N/m, resonance frequencies around 200 kHz and tip radii of approximately 5 nm (supplier specifications). Images were recorded prior to incubation at each quadrant of the grating followed by incubation (see V.1.1.4 for details).

In all experiments, scan rates, set points and gains were chosen to ensure lowest possible energy dissipation to the sample and imaging was constantly evaluated to exclude tip induced artifacts.

V.4.3.3 Tip Functionalization

AFM tips were cleaned prior to modification according to a protocol derived from literature[38] and specified in more detail in Table 4. Subsequently an octadecyltrichlorosilane (OTS) monolayer was deposited on the AFM tips using the workflow described in Table 5.

Table 4: AFM Si3N4 tip cleaning process flow[38]

1.	Washed with C_2H_5OH and ddH_2O
2.	Dried in oven for 10 min at 120°C
3.	Rinsed with ddH_2O
4.	Immersed in 0.5 M NaOH solution for 20 min, in 0.1 M HCl for 10 min, and in 0.5 M NaOH solution for 10 min
5.	Washed with 0.1 M HCl and ddH_2O
6.	Dried in oven for 10 min at 120°C
7.	Transferred into a glovebox and dried in a nitrogen stream for at least 30 min at room temperature

Table 5: The process flow of AFM Si3N4 tip modification with and OTS monolayer[38]

1.	Immersed in 2 mM solution of OTS in toluene at room temperature in a nitrogen atmosphere
2.	Washed thoroughly with toluene, C_2H_5OH and ddH_2O
3.	Dried in oven for 30 min at 120°C

V.4.3.4 Cultivation and Purification of *C. thermocellum*

C. thermocellum ATC 27405 was grown in GS-2 media1 on 5 g/L Avicel PH-101 as sole carbon source in a volume of 50 mL. Fermentation was conducted at 60 °C with shaking (100 rpm) in 100 mL bottles. The fermentation broth was harvested after the complete dissolution of Avicel PH-101 and solids were removed by centrifugation (5000 rpm, 30 min). The cleared supernatant was filtered through 0.2 µm disposable syringe filter (Sartorius, Germany) and the buffer was exchanged and concentrated using a disposable Vivaspin® (Sartorius, Germany) ultrafiltration device with a 300 kD molecular weight cut off to 30 mM MOPS pH 7.0, 100 mM NaCl and 10 mM $CaCl_2$.

To isolate the cellulosomes from the secretome a GE FPLC equipped with a HiLoad® 16/60 Superdex 200 prep grade (GE Healthcare, UK) size exclusions column was applied with buffer containing 30 mM MOPS pH 7.0, 100 mM NaCl and 10 mM $CaCl_2$. Fractions containing cellulosomes were pooled, concentrated and stored at 4°C. Protein concentration was measured using a commercial BSA kit (Thermo scientific, USA).

V.4.3.5 Activity of *C. thermocellum* cellulosome

All experiments were conducted in 30 mM sodium acetate pH 5.5 buffer containing, 100 mM NaCl, 10 mM $CaCl_2$, 10 mM cysteine and 2 mM EDTA. Overnight experiments were conducted as duplicates at 50 °C in a water bath with mild agitation in a total reaction volume of 2 mL in glass vials. A single silicon wafer coated with cellulosic material was utilized as substrate. Cellulosic material was equilibrated in buffer for 30 minutes prior to the addition of enzyme. Concentration of enzyme (either *H. jecronica* SVG17 supernatant or *C. thermocellum* cellulosome) was 7.5 µg/mL. β-Glucosidase was added to a concentration of 1 µg/mL to all reaction to promote the conversion of cellobiose to glucose. The reaction was stopped by removing the reaction buffer, rinsing the silicon wafer with ddH_2O and drying it for one day at 70 °C. Negative controls did not contain enzymes except for β-Glucosidase.

Prior to AFM experiments, a Fastscan C cantilever was cleaned and modified according to a protocol from literature to improve imaging. All experiments were conducted at 50 °C in 30 mM sodium acetate pH 5.5 buffer containing, 100 mM NaCl, 10 mM $CaCl_2$, 10 mM cysteine and 2 mM EDTA. AFM experiments were either conducted on silicon wafers, previously structured according to Figure V-35, in ambient pre-/post-incubation conditions or on HOPG substrates in liquid. Enzyme was added in a total amount of 5 µg in the AFM cell via a home-made syringe system.

V.4.4 Results and Discussion

The visualization of cellulosome activity on highly crystalline cellulose fibers (NCC) and in particular on elementary crystalline entities by AFM offers a deeper and subtler understanding of the recently demonstrated paradigm by Resch and coworkers[34,35]. Here, we present the application of AFM methods on cellulose nano-whiskers as substrate. As recently[39] demonstrated, these crystallites are identified as an elementary part of the fibril structure of cellulose and thus constitute an significant part of degradable material in cellulosic materials. Moreover, cellulosomes, as shown recently, are primarily effective on crystalline celluloses and thus should be investigated on these elementary crystalline entities. A needle-like apex and approximate dimensions of 200 nm and 20 nm in length

and width, respectively, are further arguments to use such nano-crystalline whiskers for AFM applications as flat topology is guaranteed.

V.4.4.1 Preliminary Investigations

As a first step, we performed preliminary investigations, pointing at the interaction of the enzymatic complex with the AFM probe. It is expectable that *in-situ* AFM investigations of cellulosomes in liquid are considerably harder to achieve than for e.g. free fungal cellulases, notably if we consider the presumably soft and flexibly structure of such an enzymatic complex in such an environment. We therefore performed preliminary experiments using "as purchased" probes which yielded in any case similar unsatisfactory results as shown in Figure V-36. Shortly after incubation with cellulosomes, AFM imaging became unstable showing significant streaks in images and a general tendency to lose contact with the specimen which rendered experiments as impracticable. A corresponding image series with these effects is shown in Figure V-36.
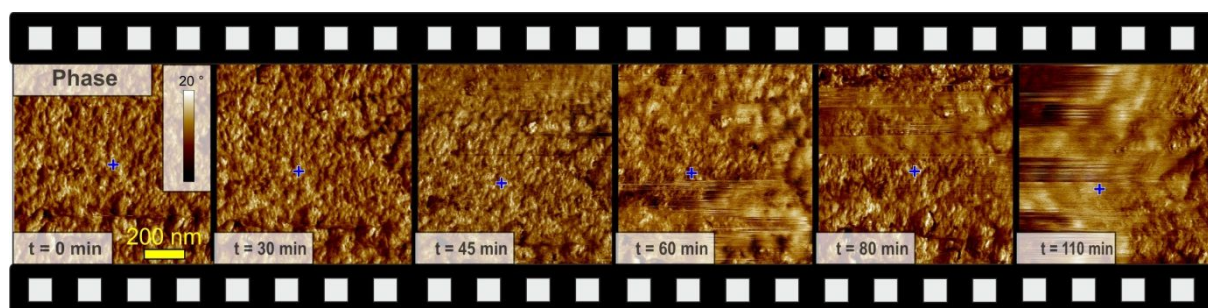

Figure V-36: AFM-Phase image series of cellulosome incubation on a polymorphic cellulose substrate (MACS)[1] over a timescale of 110 minutes. Incubation starts at 0 minutes and shows a well resolved fibrillary structure on MACS as specified in earlier studies [2,3,23]. After 45 minutes, streaks appear in the image and unstable imaging is observed. Over the following 55 minutes image quality is reduced constantly and multiple "loss of contact" events were observed. It is noteworthy that this experiment was conducted with an extreme low concentration of cellulosomes and previous experiments with higher concentrations showed these effects already shortly after incubation. The blue crosses indicate the image centers in respect to incubations start. Scale bar represents 200 nm.

In order to address this problem we performed a series of different measures: At first we **reduced the cellulosome concentration** which proved to be successful in a way that image instabilities are delayed. It is also possible to maintain at least partly stable imaging for longer time periods but nevertheless this proves to be extremely challenging and requires permanent parameter adjustments. However, a low concentration correlates to less surface activity of the multi-enzyme complex. As this is not practicable, we alternatively **changed the surface parameters of the probe** by functionalizing it with octadecyltrichlorosilane (OTS) dissolved in Tulol or ethanolamine dissolved in dimethyl sulfoxide (DMSO) in order to gain hydrophobic and hydrophilic AFM tips, respectively (procedure can be found in section V.4.3.3). As the tip in general is hydrophilic, we expected changes for the hydrophobic system. In fact, the first test showed that streaks or unstable imaging are no longer present and furthermore individual cellulosomes may be visualized. We therefore can conclude that the interaction of the hydrophilic tip and the cellulosome is responsible for the unsatisfactory effects in the previous experiments. It is conceivable that at least part of the complex interacts with the tip, which presumable produces the streaks in the images. Here, by adhering to the tip, a significant change in tapping amplitude is expectable thereby accounting for the loss of contact

events (cellulosome-cellulose-tip complex and thereby reduced tapping amplitude). All following *in-situ* experiments use therefore hydrophobic probes as achieved by the protocol presented in section V.4.3.3 for OTS.

V.4.4.2 In-Situ and Ex-Situ Cellulosome Investigation

First of all, we focused on the visualization of the cellulosome activity on highly crystalline NCC nano-whiskers. *In-situ* experiments were conducted in a liquid cell at physiological conditions (50°C). Multiple experiments (N ≥ 3) revealed a similar behavior: After incubation with the cellulosome buffer, **particles** approximately **50 nm in diameter appear on the HOPG surface and NCC cellulose**. It is needless to say, that the size of the cellulosome which correlates with data from literature[40], and immediate appearance after incubation demonstrates the binding of the cellulosome complex to the HOPG support and the crystalline NCC areas. A corresponding time series of the binding is shown in Figure V-38 (as well as in supplementary Movie S8). Here, a gradual increase of bound cellulosomes is observed over time (Figure V-37, blue circles) and a steady state appears after approximately 10 minutes. Interestingly, the prevalent binding of cellulosomes takes place initially on the HOPG support followed by diffusive motion. Then, the cellulosome is eventually reaching a cellulose crystallite and appears to be bound from that point on. Nevertheless, additional experiments revealed that besides the strong binding of the cellulosome to the crystallite, a significant part of the structure stays flexible. This is conceivable, by considering the scaffolding protein which presumably shows a high grade of flexibility. A demonstration of this behavior is shown in Figure V-38. Furthermore, the binding doesn't seem to correlate with either reducing or non-reducing ends of the cellulose crystallite. This should lead to agglomeration at these sites. This is a significant difference to previous studies on fungal cellulases where processive exo-glucanases are in particular dependent on the free ends to bind to the cellulose. The rather distributed binding of cellulosomes over the crystal could also be observed in real-time *in-situ* AFM series (see supplementary Movie S8). To strengthen the latter hypothesis we conducted complementary experiments by analyzing pre-incubated substrates by high-resolution imaging in air. The results of such an experiment are presented in Figure V-39 and provides clear evidence for the latter hypotheses. Here, numerous features which presumably reveal the elementary structures of the cellulosome are located almost entirely around the crystallites. The observed minimum resolution is estimated below 3 nm and allows identification of individual features. We are well aware that the structures in Figure V-39 do not represent a native state, however, can be considered as frozen state of the dynamic cellulosome incubation.
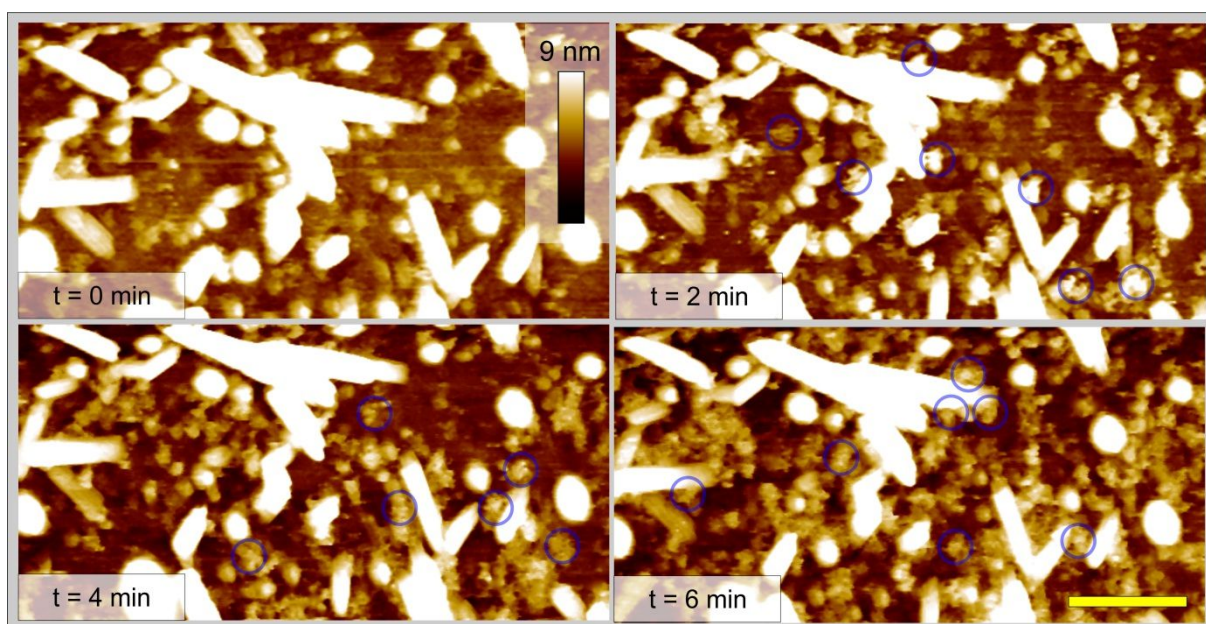
Figure V-37: In-situ AFM topography observation of cellulosome binding to crystallites and HOPG substrate (see supplementary movie S8). The time series reveals a fast binding of cellulosomes to the substrate and the crystallite over a timeframe of 6 minutes. For better visibility of the smaller cellulosomes, color scale is adjusted to lower values (crystallites are oversaturated). Blue circles highlight particles which are not present in the former image. Images were processed by 3 x 3 pixels median filter. Scale bar represents 200 nm.
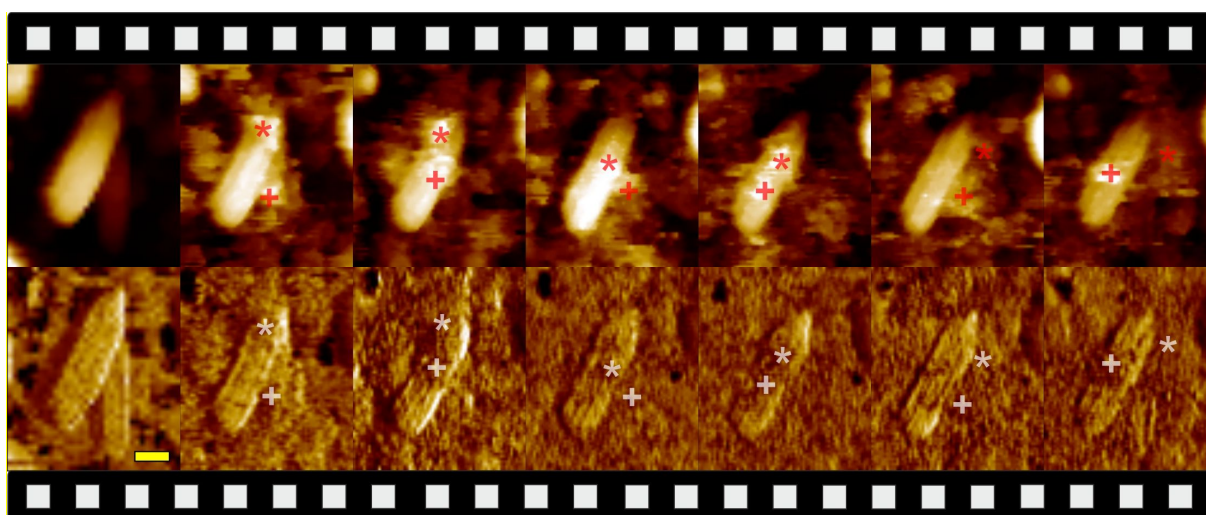
*Figure V-38: AFM high speed image series demonstrating the binding of two cellulosomes to the crystalline surface. The cellulosomes are highlighted in red (Celluosome 1: *; Cellulsome 2: +) in the topography data (top) and in white in the phase data (bottom), respectively. Although bound to the surface, still high flexibility is observed in coincidence with the flexible nature of the scaffolding. Subsequent images are shown at 10 minutes time intervals. Scale bar represents 25 nm.*
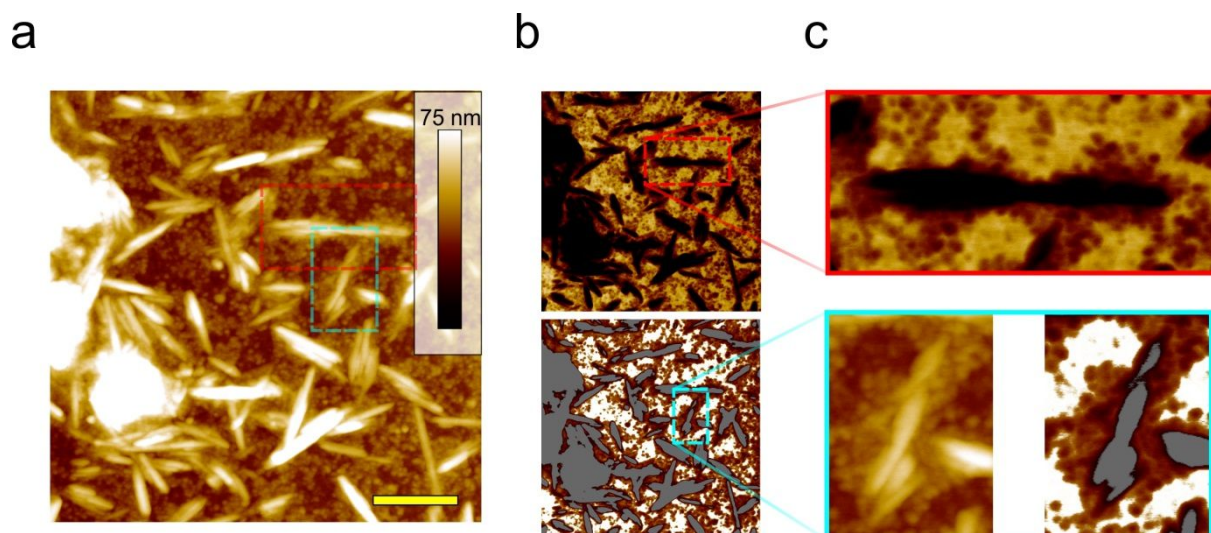
Figure V-39: AFM height images of cellulosome incubated nano-crystallites analyzed after incubation and in a dry state in ambient conditions. (a) Nanocrystalline cellulose evenly distributed on the surfaces is surrounded by small multi-component features. These agglomerates are concentrated around crystallites which are highlighted in (b) by providing a negative of (a) with removed crystallites (b, upper panel) and also removed silicon-dioxide surface (b, lower panel). (c) Highlighted areas from (a & b). Areas are indicated in (a) and (b) by dashed rectangles in red (c; upper panel) and cyan (c; lower panel). These images (c) demonstrate the concentration of particles around crystallites. The absence of other enzymatic components in the incubation solution allow to conclude, that the seen features represent, due to the removal of buffer, cellulosomes. Scalebar represents 200 nm.

V.4.4.3 Analysis of Cellulosome Activity

Corresponding to the dislocated binding of cellulosomes on the surface of crystallites, we observe – as expected – inter-crystalline degradation (see Figure V-40). This is not surprising, considering the fact that endo- and exo-type cellulases are found to be bound to the cellulosomal scaffolding[41]. Moreover, we found evidence for this behavior not only in real-time experiments but also in analyzing cellulosome hydrolyzed nano-crystallites. A summary of these experiments can be seen in Figure V-40 where *in-situ* experiments give the first direct proof of the endo-type reminiscent activity of cellulosomes. The activity of two nearby sitting cellulosomes, and its mutual displacement, allows investigation of the attacked crystallite (see Figure V-40, white arrows; section profile as inset). In fact, the activity seems to generate cavities in between the parallel aligned cellulose chains. It is known from previous experiments on fungal cellulases[2,19] that this mechanism is important for the efficient degradation of crystalline cellulose which is reflected in the presences of inter-crystalline endo-active cellulases in complete cellulase cocktails. These mechanisms are known to significantly boost synergistic activity in such systems. Concerning cellulosomes and its efficient degradation on crystalline substrates, it is not surprising that we see a similar behavior. In fact, recent work by Resch and coworkers[34,35] already provided proof for the synergism between fungal cellulases and cellulosomes. However, so far it was not possible to access the inter-cellulosomal synergism via direct visualization methods. Hence, to the best of our knowledge, **we here provide the first reported evidence for the endo- and exo- reminiscent activity of a multi-cellulases system**. In order to exclude the possibility that the damage to the crystallites was present before, we designed additional experiments providing a more statistical relevant proof of this behavior. We used FIB milled silicon dioxide substrates to generate a fixed grating on predefined positions as discussed in

the experimental section (section V.4.3.1). The grating was chosen to fit the size of 2 x 2 µm which is in respect to the crystallite size and the AFM resolution the best compromise (see Figure V-35). By that we are able to follow the changes introduced by the cellulosomal activity even without *in-situ* experiments, which proved to be extremely challenging exceeding time scales of 4 hours. The reason is simply that the formation of gas bubbles in the liquid cell limits the observation time significantly (Note, the AFM is operated at 50°C cell temperature.). By the use of the gratings we are able to compare the pre- and post-incubation results which we further denote as the **sequential experiments**. In order to gain a reference to a well-known cellulose degrading enzymatic system we used the cocktail of the fungus *H. jecorina*. Complementary experiments using the blank buffer including beta-glucosidase excluded the influence of buffer related changes on the crystallites (data not shown due to not existing effects).
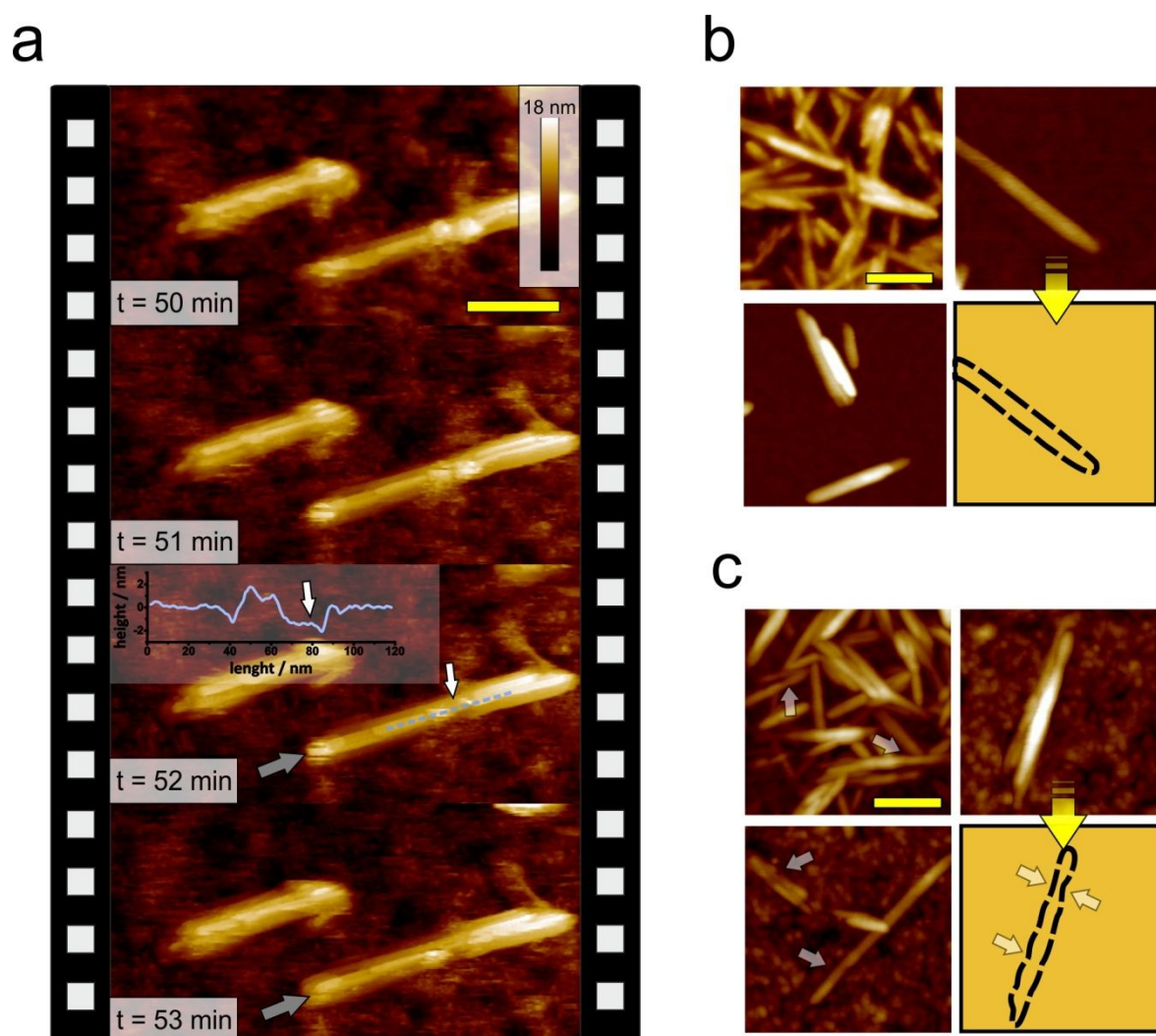
Figure V-40: In- and ex-situ AFM experiments reveal endo- and exo-type activity of the cellulosomal complex on highly crystalline nano-cellulose. (a) In-situ experiments performed at 50°C show two cellulosomes attacking the crystallite in the middle. At time t = 52 minutes after the incubation start one cellulosome is desorbed (white arrow) from the surface and exposes an approximate 2 nm deep trench in the crystallite (see section analysis, light blue dotted line). Small grey arrows point at positions at the end of the crystallite compatible with exo-type activity. (b,c) Ex-situ experiments reveal the strong contrast between fungal cellulases (b) and cellulosomes (c). For cellulosomes, crystallites apparently show multiple kinks in one crystallite stemming from the in (a) shown hydrolytic activity. (b) In conformity with the major ablative activity of the fungal system crystallites appear rather smooth and straight. Scale bars represent 100 nm.

Figure V-40 b & c do allow concluding that cellulosome and free cellulase activity differ primarily in their capability to remove singular chain segments of the crystallite in an ablative manner. However, there is no real proof that the necking of crystallites, although unlikely, was not present before incubation. To exclude this possibility, we aimed to find the same crystallites before and after incubation. As already described, we used FIB milling to form 2 x 2 µm patterns which are large enough to be found by light microscopy which allows defined repositioning of the AFM cantilever prior and after incubation. To even allow finer distinction we additionally introduced a 2 x 2 grating with areas of 1 x 1 µm which then can be separately compared (Figure V-35). The experiments were started by a careful analysis of crystallites at highest possible resolution. The following incubation was performed at optimal conditions at 60°C over a time period of 30 hours. After this period, the same analysis as performed before incubation was repeated.
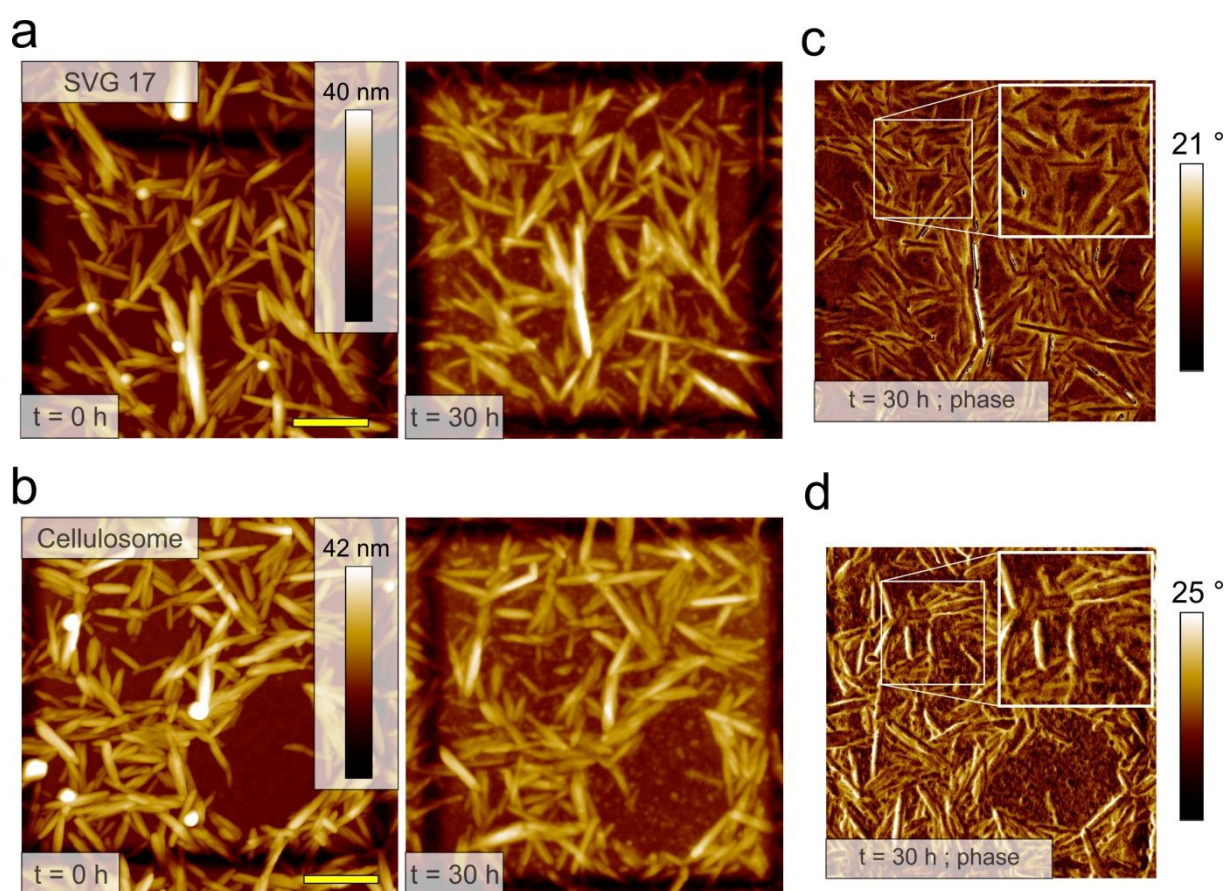
Figure V-41: AFM topography (a,b) and phase images (c,d) of pre- and post-incubated cellulose substrates. (a) H. jecorina (SVG 17) incubated nano-crystallites before and after 30 hours of incubation and (b) from the cellulosome solution before and after 30 hours of incubation. Comparing (a) and (b) reveals that activities differ significantly. This is evident be looking at the phase information (see c & d, white zoom rectangles). For cellulosomes, crystallites show – compared to SVG – rather irregular shapes. In particular SVG crystallites seem thinned after incubation which is in consistency with the ablative activity of HjCel7A and HjCel6A (see section V.2) [8,9]. Scale bars represent 200 nm.

There are significant differences, as already proposed, when the effects of free cellulases (fungal cellulase cocktail; SVG 17) and cellulosomes are compared. The resolution in Figure V-41 is clearly not sufficient to see individual changes on the crystallite as seen in Figure V-40. Nevertheless, a first observable is readily seen by comparing the phase images of the incubated substrates. While the

crystallites appear pointed and thin for the fungal cellulase cocktail, crystallites appear dull and thicker with rougher edges and surfaces (see Figure V-41; phase information a & b; white zoom rectangles or Figure V-43 and Figure V-44). It is noteworthy that both images were recorded with the same probe which excludes tip driven broadening of images due to the different end radii. We therefore are confident that this, as already proposed, can be attributed to the different mechanisms upon hydrolysis of crystalline cellulose. The free fungal system includes exo- (*Hj*Cel7A, *Hj*Cel6A) and endo-glucanses (*Hj*Cel7B) in concentrations of 60 wt.%, 20 wt.% and 12 wt.% for the major enzyme content. Exo-activity of *Hj*Cel7A in particular is reflected in ablative peeling of crystallites as demonstrated in recent studies[2,8,9]. It is therefore expectable that the main outcome is a thinning of crystallites with a smooth surface topology. In contrast the results for cellulosome activity allow us to propose a different paradigm of cellulose hydrolysis: Here, the cellulosome binds to different docking sites of the crystallite which are rather evenly distributed and initially opens chains by endo-catalytic hydrolysis if cellulose. Once inter-chain cleavage by endoglucanases is achieved, on site exo-specific cellulases may widen the produced hole and thus form the observed trenches (Figure V-40; section analysis). It is however rather difficult to see the corresponding topological changes on individual crystallites. We therefore performed additional high-resolution experiments to further strengthen this hypothesis.
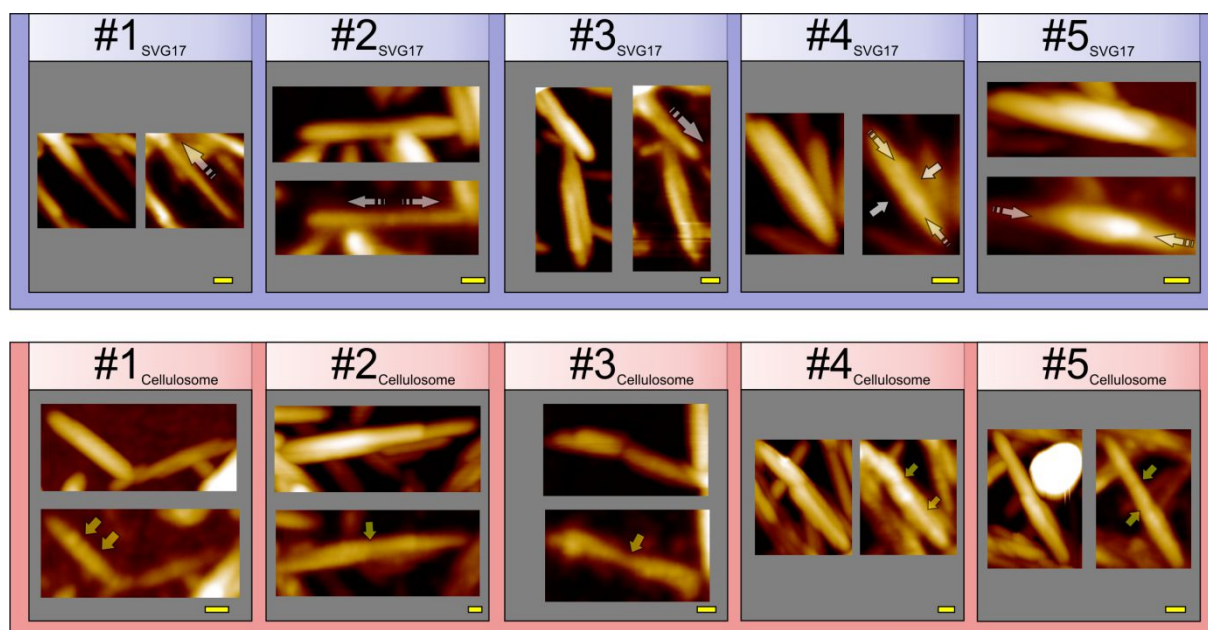
Figure V-42: Close up analysis of individual crystallites visualized before (either left or top) and after (either right or bottom) 30 h incubation with SVG 17 (blue, upper panel) and Cellulosomes (red, lower panel). In total 5 particles are analyzed for each system and show that for SVG 17 ablative activity is prevalent. Degradation results in thining (#2SVG17, #3SVG17, #4SVG17) and shortening of fibers (#5SVG17, #1SVG17) indicated by white arrows. For cellulosome activity, we see roughened surfaces and intrusions compatible with the hypothesis of inter-crystalline hydrolysis by endo-glucanases and following widening by exo-glucanases. Note, the particle seen in #5Cellulosome is most likely associated with contamination and not a cellulosome (specimens were thoroughly washed). Scale bars represent 20 nm.

In Figure V-42, the former proposed hypothesis is once more supported. While for SVG 17, where we rather see smooth crystallites (#1$_{SVG17}$ - #5$_{SVG17}$), cellulosome incubation yields more disrupted crystallites (see yellow arrows (#1$_{Cellulosome}$ - #5$_{Cellulosome}$). Activity by the SVG system is rather ablative (white arrows) which is in coincidence with the ablative activity of cellulases *Hj*Cel7A and *Hj*Cel6A. To support the data depicted in Figure V-42, we also performed section analysis of crystallites before and after incubation with cellulosomes (Figure V-43) and SVG enzymes (Figure V-44).

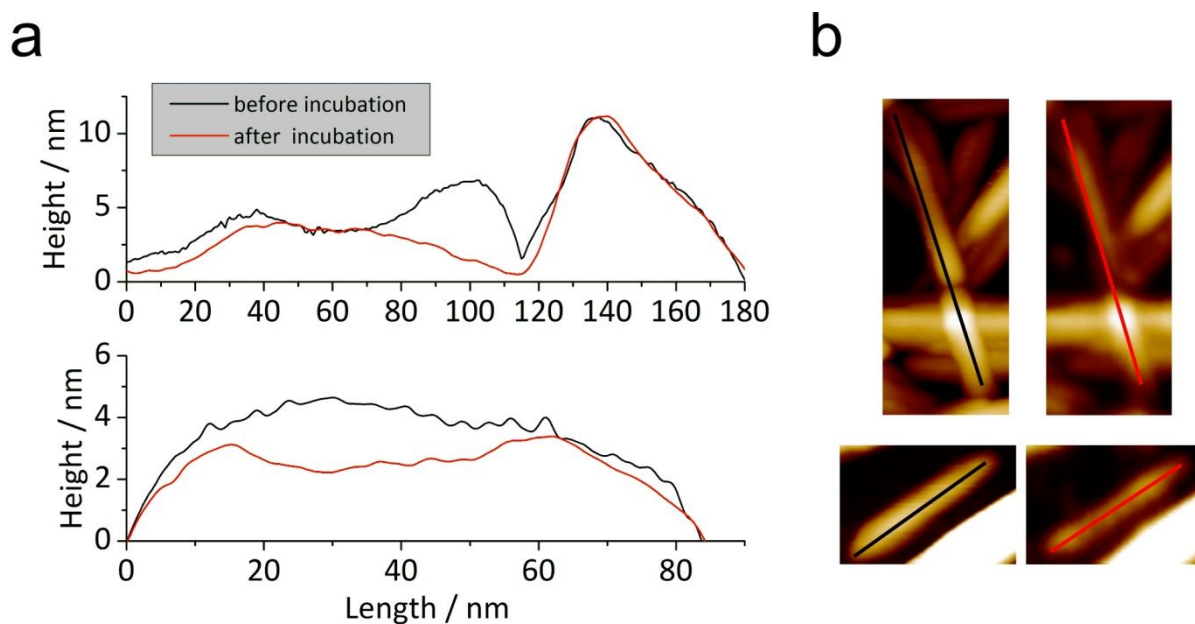*Figure V-43: A section analysis (a) of a cellulosome hydrolyzed nano-crystallites. Please note the thinning of crystallites in between (in particular for the bottom crystallite).*
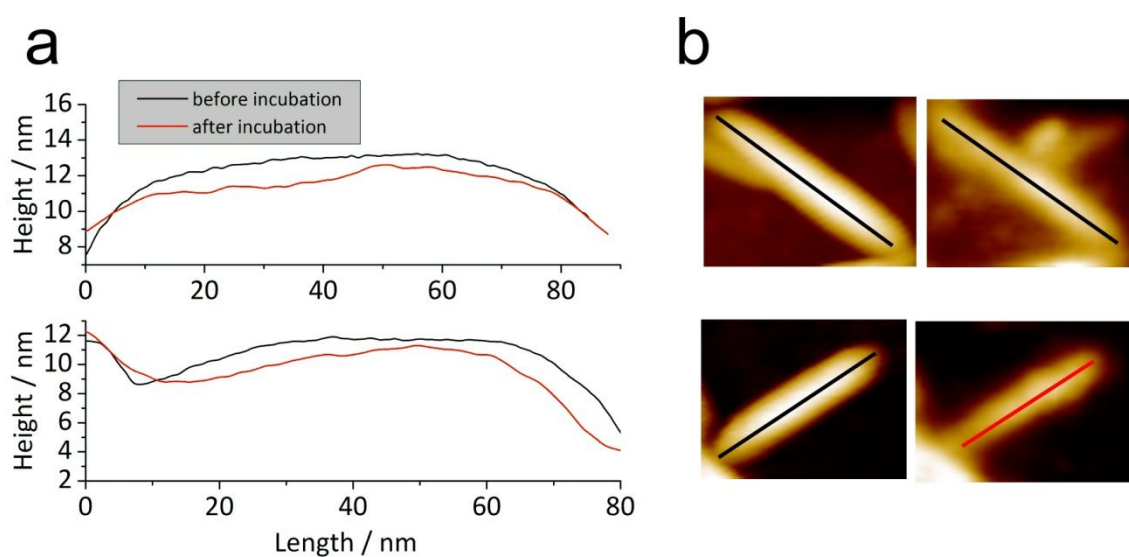

Figure V-44: A section analysis (a) of a SVG hydrolyzed nano-crystallites. Please note the thinning of the crystallites and rather ablative activity which is in coincidence with the current understanding of a full cellulase system of H. jecorina.

All in all, we may state that the cellulosome features a completely different activity as the full cellulases cocktail of *H. jecorina*. This is on the one hand not surprising as cellulosomes stem from completely different organisms. However, from enzymatic view the participating enzymes are very similar. It is therefore evident that the differences in activity stem from the confined state of the cellulosome. As mentioned before, the scaffolding protein is responsible for a confinement of relevant enzymes on a rather small area which may be of advance when degrading highly crystalline material. A simple summary may say: If for example a processive cellulase encounters an obstacle associated with e.g. in-degradable amorphous cellulose, nearby endo-active cellulases are on the spot to remove it and vice versa. This most likely also results in rather disruptive activity as seen in Figure V-41 and Figure V-42.

V.4.5 Conclusion

Reconsidering the structure of the cellulosome and its anchoring to the bacterial cell surface[30,42,43], it is actually not a surprising result that the degradation paradigm differs significantly from the one of free cellulases. Here, the size of the complex, a multi-enzyme system, with its different affinities for different celluloses, hemicelluloses and lignin and the anchoring to the cell wall may render processive activity rather needless. Clearly, we are confident that exo-glucanases which are part in the cellulosomal complex of *C. thermocellum* (glucosidase family 48 (www.cazy.org)[34]) do contribute significantly to the overall performance of the cellulosome, however, in certainly different way as for processive free exo-glucanases. The results obtained in *in-situ* (Figure V-40) and *ex-situ* experiments (Figure V-42) suggest that the cellulosome activity can be seen as follows: At first, cellulosomes bind to the crystalline cellulose substrate and further remain fixed. However, the overall structure maintains it flexibility (Figure V-38). This is not surprising as the scaffolding protein was shown to be highly flexible[44,45]. This flexibility allows the individual cellulases to move freely in the range of the scaffolding. The data obtained by *in-situ* and *ex-situ* analysis (Figure V-40 to Figure V-42) reveals not only a considerably more structured cellulose surface for the cellulosome compared to free cellulases, it also shows a pronounced necking (Figure V-42) within the crystallites. Now, it is conceivable that once bound to the cellulose surface, endo-glucanases start to open up chains which in turn are now available to exo-glucanases within the enzymatic complex. These widen the gap by processive moving in the range of the scaffolding radius. In turn, new chains are now accessible which then can again be opened by the endo-glucanases and so on. A schematic illustrating this model is provided in Figure V-45. While the ablative activity of the free cellulases produces narrower crystallites and less structured cellulose surfaces, the special activity of cellulosomes with endo-glucanases, exo-glucanases and other polysaccharide degrading enzymes produces local disruptions within the cellulose fiber. This paradigm on the elemental basis of the cellulose fiber disintegration by cellulosomes is consistent with recent findings by Resch and coworkers[34] but proved here via direct visualization for the first time. Resch and coworkers observed that cellulosomal activity produces splayed ends on electron transparent Avicel particles. These ends were confined to one end of the crystallite. Accounting for the fact that in smaller crystallites parallel arrangement of chain ends is feasible (as already shown in chapter II) this hypothesis is feasible. Furthermore, they also suggested that the cause of the endpoint specific activity may be associated with glucosidase family 48 cellulases (reducing end specific exo-glucanase; www.cazy.org) which exist in the cellulosomal system of *C. thermocellum.* We are confident, that this may play a significant role if cellulosomes bind

to the end of crystallites which we have observed in consistency with the work by Resch and coworkers. However, we also showed by high-resolution imaging and direct evidence that the cellulosomal complex may produce inter-crystalline protrusions with the help of endo-glucanases which may further lead to the observed splaying. It is clear that protrusions, if appearing in sufficient number, would lead to separation of individual fibers and in turn to a higher accessibility for free cellulases as observed by Resch and coworkers[34]. In conclusion, the subtler analysis due to *in-situ,* high-resolution AFM methods allowed us to refine the paradigm of a non-processive multi-enzyme complex. Moreover, the increased number of free chain ends is further advantage for exo-glucanases which are numerously present in the cellulase cocktail of *H. jecorina*.
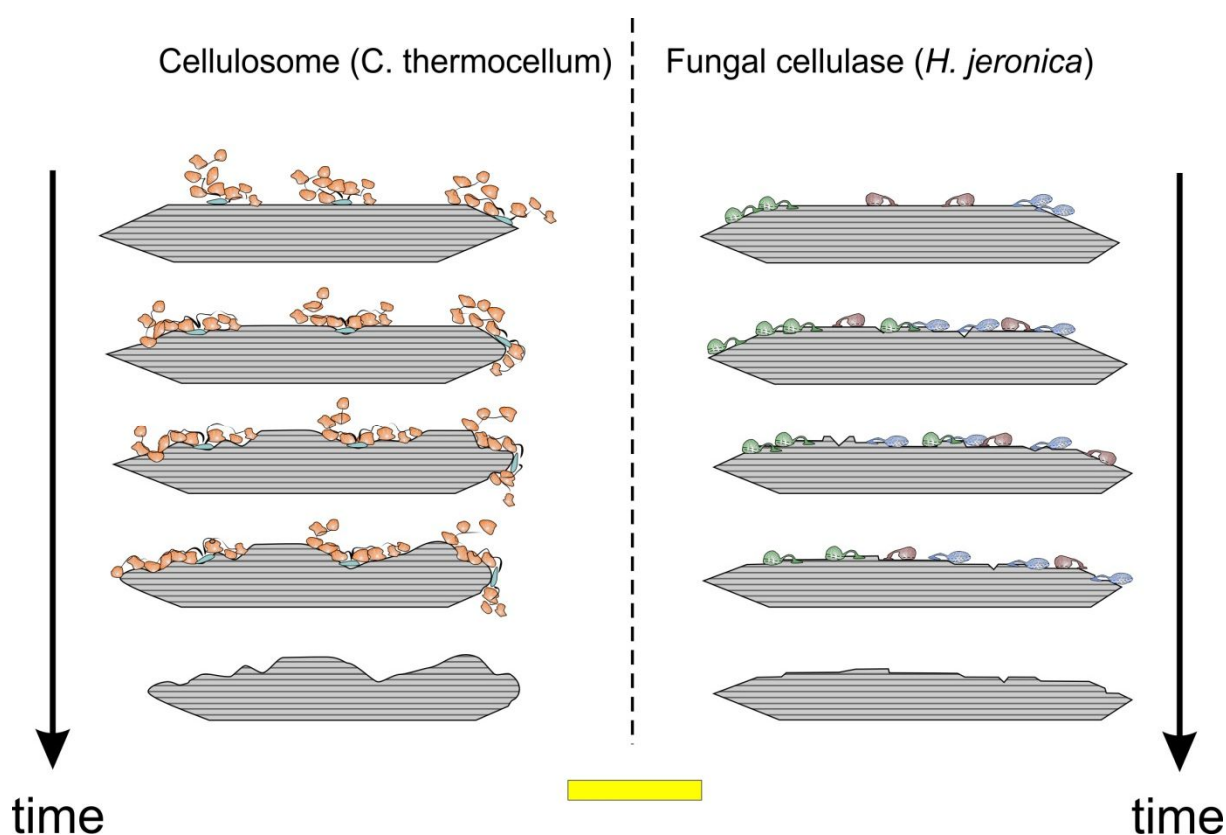
Figure V-45: Schematic model oft he obtained data for cellulosomes from C. thermocellum and the free cellulases cocktail of H. jecorina. Upon binding of the cellulosome to the crystallite, most of the cellulosome is still flexible. Binding was observed on crystallite ends and in between. After binding, endo-glucanase activity produces free chain ends which subsequently are available to exo-glucanases which are confined in the complex. The flexible scaffolding allows exo-glucanases to process along the chain at a certain distance, thus widening the hole. As a result, new chains are again accessible and used by endo-glucanases to again open chains. By that a cyclic activity of endo- and exo-glucanases produces the observed structured and necked crystallites, which in contrast to free cellulases show rather rough topology. Free cellulases – as a result of their ablative activity – produce thinner crystallites. Scale bar represents 50 nm.

V.5 Chapter Summary

In this *chapter,* we have now shown how to implement our developed model substrates into the AFM experiment. The dedicated character of a multiphase substrate, with crystalline and amorphous areas in between, allowed us to unravel so far unknown effects during hydrolysis of different cellulose degrading enzymes. First of all, we showed that the substrate composition is of extreme importance for degradation. Here, we may emphasize that a simple consideration of crystalline vs. amorphous material is far from complete. It is also the size of the crystallites which significantly contribute to the degradability. While larger crystallites showed that they are rather resistive, smaller once were degraded quite fast. It is clear from fundamental considerations that larger crystallites will encounter a larger amount of intermingled elementary fibrils, while smaller crystallites do not. Thus, the ablative activity of processive cellulases must be enhanced. However, it is rather unlikely that nature is not accounting for this problem. In a second part of this *chapter* we introduced the concept of LPMOs which feature completely different mechanisms of degradation. While from an empirical view the activity seems to be rather equivalent to endo-glucanases, we must emphasize that underlying mechanisms are completely different. This is already evident from the name lytic polysaccharide mono-oxidase which already states that the chemical mechanism is not comparable to classical hydrolysis. Here, oxidation of the C1 or C4 atom leads to a destabilization of the β-glycosidic bond which after the reaction results in chain cleavage. Furthermore it is believed that this oxidation also leads to a destabilization of surrounding cellulose chains which further reduces the tight crystalline packaging. Thus, other hydrolytic cellulases may easier degrade the crystallite. We showed that this is of extreme relevance on larger crystallites, where the tight binding and intermingling of fibers may be disturbed. It is astonishing to see this in the AFM, and it once more states the importance of this tool for the investigation of such processes. For the last concept, we introduced the cellulosome which also features a complete different strategy to depolymerize cellulose. Quantitative data by AFM showed that the degradation is rather local and in-depth compared to the ablative one form the free cellulases system (e.g SVG17 of *H. jecorina*). This was so far, never seen *in-situ*. We must once more emphasize that this results were only possible by providing hydrophobic tips. In other cases we observed that imaging was impossible, most likely through interaction with the scaffolding of the cellulosome. For all topics we have provided a new and refined model which was based and supported by quantitative data from the AFM and biochemical methods. We showed in any case that the combination of both methods has an enormous potential to encounter the difficulties still observed in the understanding of such processes. Now at the end of this *chapter* it must be once more stated that the family of cellulose degrading enzymes is immense and that further work has to be done to encounter the effects of each one. We here have only provided the tool-box with corresponding substrates and a development of the relevant techniques which will be of use for future science in this field.

V.6 References

[1]   T. Ganner, T. Aschl, M. Eibinger, P. Bubner, A. Meingast, B. Chernev, C. Mayrhofer, B. Nidetzky, H. Plank, *Cellulose* **2014**, *21*, 3927.

[2]   T. Ganner, P. Bubner, M. Eibinger, C. Mayrhofer, H. Plank, B. Nidetzky, *J. Biol. Chem.* **2012**, *287*, 43215.

[3]   M. Eibinger, P. Bubner, T. Ganner, H. Plank, B. Nidetzky, *FEBS J.* **2014**, *281*, 275.

[4]   P. Bubner, J. Dohr, H. Plank, C. Mayrhofer, B. Nidetzky, *J. Biol. Chem.* **2012**, *287*, 2759.

[5]   M.-C. Marx, M. Wood, S. . Jarvis, *Soil Biol. Biochem.* **2001**, *33*, 1633.

[6]   M. M. Bradford, *Anal. Biochem.* **1976**, *72*, 248.

[7]   D. Nečas, P. Klapetek, *Open Phys.* **2012**, *10*, 181.

[8]   K. Igarashi, A. Koivula, M. Wada, S. Kimura, M. Penttilä, M. Samejima, *J. Biol. Chem.* **2009**, *284*, 36186.

[9]   K. Igarashi, T. Uchihashi, A. Koivula, M. Wada, S. Kimura, T. Okamoto, M. Penttilä, T. Ando, M. Samejima, *Science* **2011**, *333*, 1279.

[10]   J. Medve, J. Ståhlberg, F. Tjerneld, *Biotechnol. Bioeng.* **1994**, *44*, 1064.

[11]   E. Hoshino, M. Shiroishi, Y. Amano, M. Nomura, T. Kanda, *J. Ferment. Bioeng.* **1997**, *84*, 300.

[12]   M. Kurasin, P. Valjamae, M. Kurašin, P. Väljamäe, *J. Biol. Chem.* **2011**, *286*, 169.

[13]   A. Varrot, S. Hastrup, M. Schülein, G. J. Davies, *Biochem. J.* **1999**, *337 (Pt 2*, 297.

[14]   M. Monschein, C. Reisinger, B. Nidetzky, *Bioresour. Technol.* **2013**, *128*, 679.

[15]   B. Nidetzky, W. Zachariae, G. Gercken, M. Hayn, W. Steiner, *Enzyme Microb. Technol.* **1994**, *16*, 43.

[16]   S. Park, J. Baker, M. Himmel, P. Parilla, D. Johnson, *Biotechnol. Biofuels* **2010**, *3*, 10.

[17]   C. M. Phillips, W. T. Beeson, J. H. Cate, M. A. Marletta, *ACS Chem. Biol.* **2011**, *6*, 1399.

[18]   F. Mba Medie, G. J. Davies, M. Drancourt, B. Henrissat, *Nat. Rev. Microbiol.* **2012**, *10*, 227.

[19]   C. M. Payne, B. C. Knott, H. B. Mayes, H. Hansson, M. E. Himmel, M. Sandgren, J. Ståhlberg, G. T. Beckham, *Chem. Rev.* **2015**, *115*, 1308.

[20]   P. V Harris, D. Welner, K. C. McFarland, E. Re, J.-C. Navarro Poulsen, K. Brown, R. Salbo, H. Ding, E. Vlasenko, S. Merino, F. Xu, J. Cherry, S. Larsen, L. Lo Leggio, *Biochemistry* **2010**, *49*, 3305.

[21]   S. J. Horn, G. Vaaje-Kolstad, B. Westereng, V. G. Eijsink, *Biotechnol. Biofuels* **2012**, *5*, 45.

[22]   G. R. Hemsworth, G. J. Davies, P. H. Walton, *Curr. Opin. Struct. Biol.* **2013**, *23*, 660.

[23]   M. Eibinger, T. Ganner, P. Bubner, S. Rošker, D. Kracher, D. Haltrich, R. Ludwig, H. Plank, B. Nidetzky, *J. Biol. Chem.* **2014**, *289*, 35929.

[24]   R. Kittl, D. Kracher, D. Burgstaller, D. Haltrich, R. Ludwig, *Biotechnol. Biofuels* **2012**, *5*, 79.

[25]   S. Rödiger, M. Ruhland, C. Schmidt, C. Schröder, K. Grossmann, A. Böhm, J. Nitschke, I. Berger, I. Schimke, P. Schierack, *Anal. Chem.* **2011**, *83*, 3379.

[26] P. Wildberger, C. Luley-Goedl, B. Nidetzky, *FEBS Lett.* **2011**, *585*, 499.

[27] W. T. Beeson, V. V. Vu, E. a. Span, C. M. Phillips, M. a. Marletta, *Annu. Rev. Biochem.* **2014**, *84*, 150317182619002.

[28] J. Hu, V. Arantes, a Pribowo, *Energy Environ. Sci.* **2014**, *7*, 2308.

[29] C. M. G. A. Fontes, H. J. Gilbert, *Annu. Rev. Biochem.* **2010**, *79*, 655.

[30] E. A. Bayer, J.-P. Belaich, Y. Shoham, R. Lamed, *Annu. Rev. Biochem.* **2004**, *58*, 521.

[31] H. P. Fierobe, E. A. Bayer, C. Tardif, M. Czjzek, A. Mechaly, A. Bélaïch, R. Lamed, Y. Shoham, J. P. Bélaïch, *J. Biol. Chem.* **2002**, *277*, 49621.

[32] A. L. Demain, M. Newcomb, J. H. D. Wu, A. L. Demain, M. Newcomb, J. H. D. Wu, **2005**, *69*, 124.

[33] S. Y. Ding, Q. Xu, M. Crowley, Y. Zeng, M. Nimlos, R. Lamed, E. A. Bayer, M. E. Himmel, *Curr. Opin. Biotechnol.* **2008**, *19*, 218.

[34] M. G. Resch, B. S. Donohoe, J. O. Baker, S. R. Decker, E. A. Bayer, G. T. Beckham, M. E. Himmel, *Energy Environ. Sci.* **2013**, *6*, 1858.

[35] M. G. Resch, B. S. Donohoe, P. N. Ciesielski, J. E. Nill, L. Magnusson, M. E. Himmel, A. Mittal, R. Katahira, M. J. Biddy, G. T. Beckham, *ACS Sustain. Chem. Eng.* **2014**, *2*, 1377.

[36] C. D. Edgar, D. G. Gray, *Cellulose* **2003**, *10*, 299.

[37] K. S. Novoselov, A. K. Geim, S. V. Morozov, D. Jiang, Y. Zhang, S. V. Dubonos, I. V. Grigorieva, A. A. Firsov, *Science (80-.).* **2004**, *306*, 666.

[38] Z. Q. Wei, C. Wang, C. L. Bai, *Surf. Sci.* **2000**, *467*, 185.

[39] R. J. Moon, A. Martini, J. Nairn, J. Simonsen, J. Youngblood, *Chem. Soc. Rev.* **2011**, *40*, 3941.

[40] E. A. Bayer, E. Morag, R. Lamed, *Trends Biotechnol.* **1994**, *12*, 379.

[41] T. W. Dror, A. Rolider, E. A. Bayer, R. Lamed, Y. Shoham, *J. Bacteriol.* **2005**, *187*, 2261.

[42] E. A. Bayer, L. J. Shimon, Y. Shoham, R. Lamed, *J. Struct. Biol.* **1998**, *124*, 221.

[43] E. A. Bayer, R. Lamed, *J. Bacteriol.* **1986**, *167*, 828.

[44] Y. J. Bomble, G. T. Beckham, J. F. Matthews, M. R. Nimlos, M. E. Himmel, M. F. Crowley, *J. Biol. Chem.* **2011**, *286*, 5614.

[45] A.-L. Molinier, M. Nouailler, O. Valette, C. Tardif, V. Receveur-Bréchot, H.-P. Fierobe, *J. Mol. Biol.* **2011**, *405*, 143.

Chapter VI Novel Concepts for Nano-scale Structuring of Cellulose
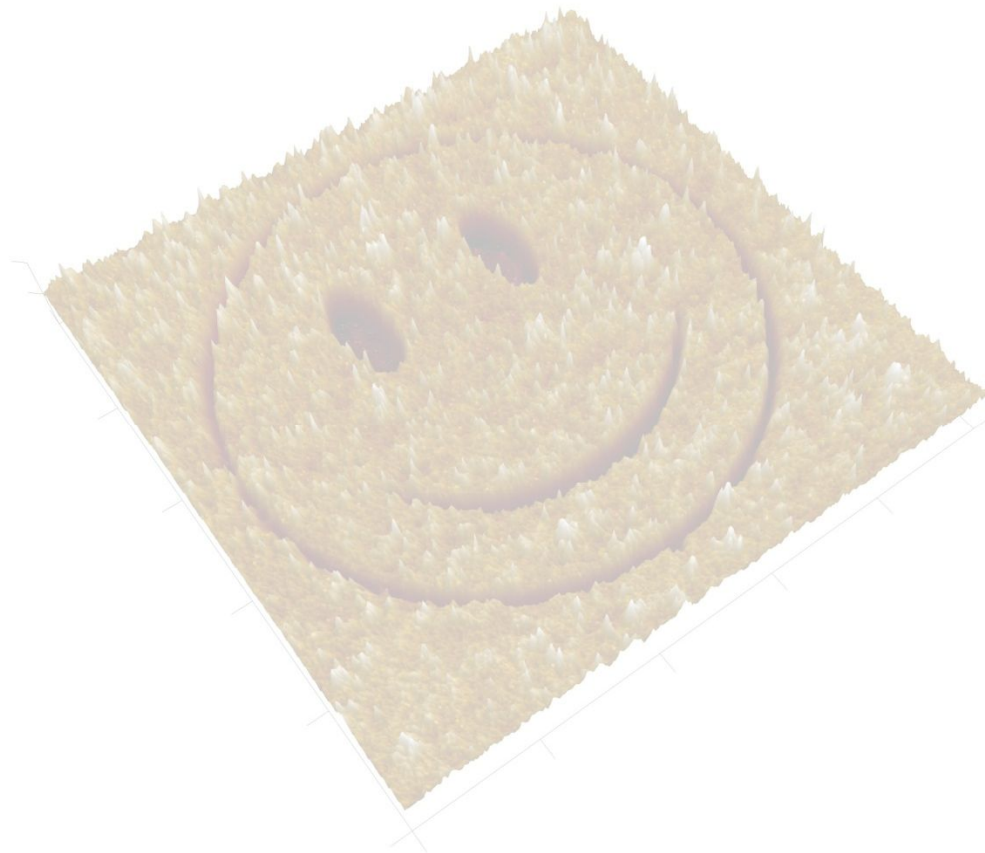
VI.1 Introduction

So far we have focused our research on the understanding of cellulose structures (*chapter II*) and corresponding fabrication of model substrates for AFM investigations (*chapter IV*) and the analysis of enzymatic hydrolysis of the latter (*chapter V*). The combination of AFM methods and biochemical analysis showed to be a favorable strategy to give light to some enigmas still encountered with enzymatic cellulose decomposition. However, cellulose is not only interesting as degradable material, it also states a promising material in the nano-sciences for biodegradable coatings[1], supporting materials for semiconductors[2] or medical products[3]. As a consequence, notable effort is put into the investigation of cellulose structures with a defined shape. First efforts included the investigation and characterization of cellulose thin film substrates as used in this thesis[4–8]. Not surprisingly, ongoing research focused on the possibility to **structure** such films by using e.g. photolithographic methods[3,9,10]. Kargl and collaborators used an interesting approach to do so: By blending small amounts of photo-acid generators into the TMSC solution and further into the film, photolithographic methods were applicable to regenerate TMSC to cellulose only at specific regions. So far, resolution by this method was limited to approximately 500 nm. Other methods used prior produced structuring masks or PDMS molds to regenerate TMSC to cellulose by covering and protecting specific regions from the regenerating HCl gas. Advantages of these methods include high production throughput or parallel fabrication ability. Disadvantages include low resolution or the presence of photoacid generator within the film. We therefore have focused on an alternative method by using electron induced regeneration of TMSC. At first sight, this approach may rather seem to be impossible as the regeneration of TMSC to cellulose at least would require a protonated species to substitute the TMS residue. However, preliminary investigations soon showed that electrons are well suited to regenerate the material. It is most probable that the accelerated electrons lead to multiple cleavage events within the TMSC film, thus producing a broad range of radicals which further catalyze the regeneration reaction. This is analogous to the well-known method of focused electron induced deposition of different precursor gases to fabricate metal compounds on any given substrate[11]. A decisive unknown factor is the ratio of cellulose regeneration or the possible presence of unwanted by-reactions. We therefore applied parameter scans to evaluate the optimal electron dose for the electron induced regeneration of TMSC films. By using multiple methods we show that the main product is cellulose and that it is degradable by enzymes. We apply a dedicated set of experiments to approach the absolute limit of resolution and show that this method is superior in this manner against other photolithographic methods. Moreover, the method is ultimately fast for even rather large structures and gives the researcher a tool to fabricate almost any given structure on any given substrate.

VI.1.1 Publishing Information

VI.2 Experimental Procedures

VI.2.1 Materials

All used materials and chemicals have been purchased in highest available purity unless otherwise stated. Pre-cut silicon wafers (10 × 10 mm^2) with 3 nm SiO_2 were kindly provided by AMS AG (Unterpremstätten, Austria).[12] Glass vials (4 mL, Ø 15mm, Rotilabo) and slides, tetrahydrofuran, 2-propanol, ethanol (analytical grade, not denatured) and xylol were purchased from Carl Roth (Karlsruhe, Germany) while Whatman® No. 1 filter paper was purchased from Sigma-Aldrich (St. Louis, MO, USA). Trimethylsilyl-cellulose (TMSC, DP = 2.8) was purchased from Thüringisches Institut für Textil- und Kunstoff-Forschung (TITK e.V, Rudolfstadt, Germany).

VI.2.2 Preparation of Trimethylsily-Cellulose Films

Cellulose films were prepared according to protocols from literature[13] or *chapter IV*. Briefly, 20mg ml^{-1} of TMSC were dissolved in xylol and transferred to a sonification bath (Transsonic T560, Elma Schmidbauer GmbH, Singen, Germany) and treated until no residual particles were observable (typically 15 min). The resulting solution was drawn into a syringe and filtered through a nitro-cellulose filter with a nominal pore size of 5 μm into a new capped glass vial. In a next step, silicon wafers (AMS AG, Unterpremstätten, Austria) were carefully removed in a flow box to prevent contamination with dust and transferred to the spin-coater (Laurell ws-650-S7-6NPP/LITE, Laurell Technologies Corporation, North Wales, USA). Approximately 200 μl of solution were pulled up into a glass pipette and transferred onto the silicon specimen which was followed by immediate spin-coating. Parameters were: An acceleration period of 4 seconds to 3600 rpm, followed by constant spinning for further 25 seconds to ensure complete evaporation of the solvent. Specimens were removed from the coater and stored until further use in Parafilm® sealed petri-dishes.

VI.2.3 Focused Electron Beam Induced Conversion

TMSC thin film specimens were positioned on a conventional SEM holder (Ø 10 mm) by double sided adhesive carbon tape. A FIB Nova 200 microscope (FEI, Hillsboro, OR, USA) was used for the patterning of the TMSC thin films. Optimal parameter range was analyzed according Table VI-1 and Figure VI-1. Here U_{Beam}, I_{Beam}, DT and P where varied to find a set of optimal patterning parameters. Once optimal parameters were available, the patterning was performed as follows: For each structure, conventional drawing tools (CorelDraw X6, Corel Corporation, Ottawa, CANADA) were used to design a black/white bitmap image with the corresponding non-patterend/patterned points, respectively. The image was then processed by the recently introduced SIL engine to gain a corresponding stream file[14]. Briefly, this engine was specially designed to allow lowest possible temperature introduction to in particular polymers. Patterns were then structured into the specimens by the FIB patterning engine. Please note that the structuring was applied in "blind" mode as each electron would lead to regeneration effects. After patterning, specimens were removed from the vacuum chamber and stored in Parafilm® capped petri-dishes for further characterization or further processing.

Table VI-1: Used electron acceleration voltages (U_{Beam}) and beam currents (I_{Beam}) in the parameter scan experiments. Each value of U_{Beam} and I_{Beam} is further coupled to a Dwelltime (DT) and Multiplication variation seen in in Table S2. The point-pich (PP) was defined by a 50% beam overlap accounting for the fact that beam profiles change with voltage and current. Thereby, easier dose comparability is given (see equation 1 and 2).

	U = 2 kV	U = 5 kV	U = 10 kV
I_1 (pA)	210	400	540
I_2 (pA)	53	98	130
I_3 (pA)	13	25	33
I_4 (pA)	2.5	5	7.5

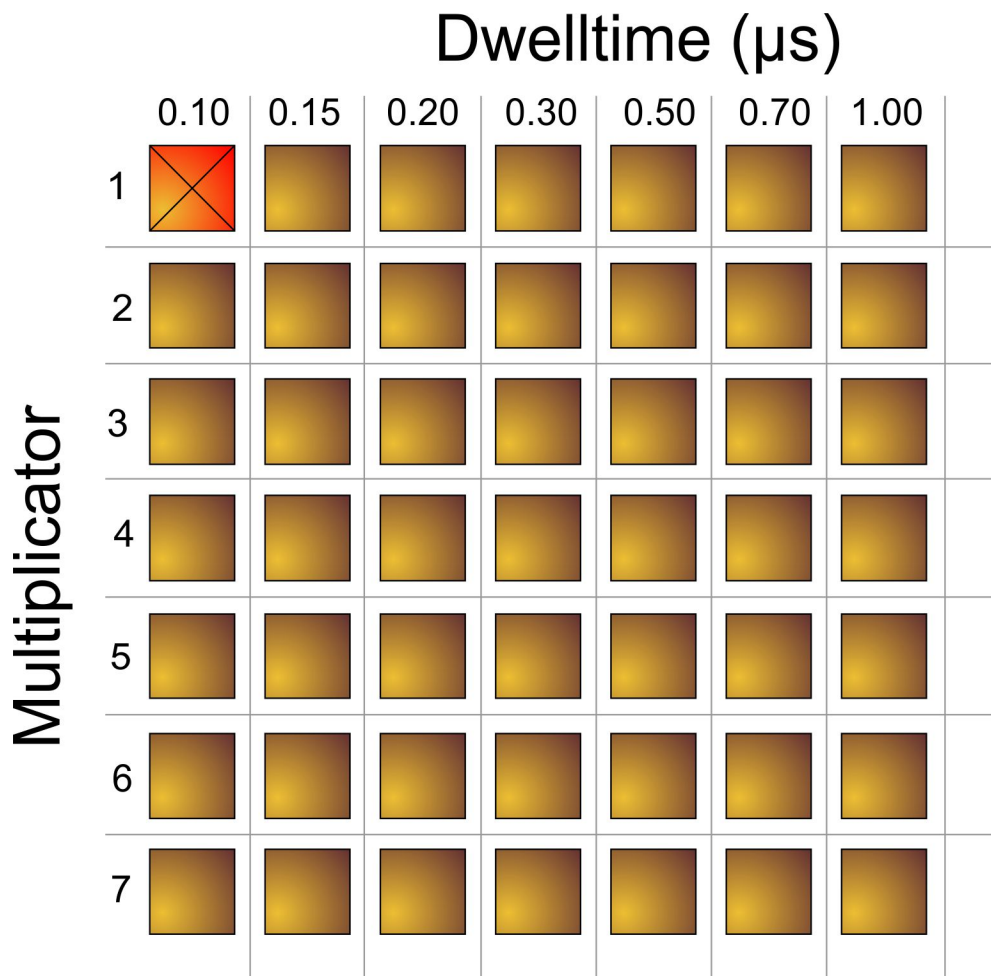Figure VI-1: Dwelltimes (DT) and multiplication values used for each acceleration voltage and beam current as specified in Table S1. The obtained pattern therefore is representative for different introduced electron doses (see equation 1 and 2). Note, preliminary investigations already defined roughly the borders between DTs of 0.1-7 µs. The red square is patterned at DT 4 µs and acts as synchronization and positioning pad.

VI.2.4 Enzymatic Hydrolysis

Complete cellulase system of *Hypocrea jecorina* mutant SVG 17 was prepared according to protocol from literature[15]. All hydrolysis experiments were performed using 2 ml of 50 mM sodium citrate buffer (pH 5.0) and 300 μl of the cellulase supernatant. Hydrolysis was performed at ambient temperature and for 24 hours to ensure complete conversion of degradable material. Afterwards, specimen was carefully rinsed with deionized water for 5 minutes, followed by CO_2 spray drying.

VI.2.5 Infrared Light Spectroscopy

For FTIR experiments, silicon wafer specimens were preliminary covered with a 10 nm layer of chromium followed by 100 nm of gold. TMSC films were then prepared and structured according to the procedures above. For FTIR experiments an area of approximately 100 x 100 μm^2 was fully regenerated by the electron beam at the optimal parameters (U = 2kV; I = 54pA; DT = 1600ns; P = 1; $PP_{@50\%overlap}$ = 10.4 nm). FTIR spectra were recorded on a Perkin Elmer Spectrum One instrument with a spectral range of 850 - 4000 cm^{-1} and an resolution of 1 cm^{-1} in reflection mode.

VI.2.6 Atomic Force Microscopy

AFM investigations were carried out using a FastScan Bio AFM microscope (Bruker AXS, Santa Barbara, CA/USA) operated by a Nanoscope V controller. For all investigations FastScan C cantilevers (Bruker AXS, Santa Barbara, California/USA) with nominal spring constants of 0.4 N/m and a tip radius of 5 nm were used. Experiments were conducted under ambient conditions and at an air conditioned temperature of 22°C. Films were analyzed in negative or positive structured manner, i.e. with still present TMSC layer or without, respectively. In order to produce the positive structures, films were preliminary to the AFM investigations immersed in xylol for 2 minutes followed by careful rinsing with xylol in order to remove the TMSC. For negative structured films, carful scratching with ultra-sharp tweezers allowed a reference to the underlying silicon for height measurements. Setpoints, scan rates and controlling parameters were chosen carefully to ensure lowest possible energy dissipation to the sample and to exclude tip driven artifacts. Data analysis of images was performed using Nanoscope Analysis.

VI.2.7 Calculation of the Electron Dose

The electron dose introduced by the beam may be calculated by equation (6.1) and (6.2). The overall dose is defined by the current I_{Beam} times the dwell time (DT) times the number of passes per area. For simplicity, we approximated the Gaussian beam profile by a square one. Now, if in equation (6.2) the beam diameter (A_{Beam}) is taken, we have to multiply by four as each quadrant of the beam area is passed four times by the beam due to the 50% beam overlap. As alternative, we may take the area spanned by the PP which is one fourth of the beam area. Please note that we are aware that edge patterning points would require a different treatment with different multiplication factors. However, given the fact that a pattern with total area of 4 μm^2 yields between 5000 and 20000 points depending on the beam diameter, we treat edge patterning points as negligible.

$$D \cdot A = I \cdot t \tag{6.1}$$

$$D = \frac{I \cdot t}{A} = 4 \cdot \frac{I_{Beam} \cdot DT \cdot P}{A_{Beam}} = \frac{I_{Beam} \cdot DT \cdot P}{A_{POP}} \tag{6.2}$$

VI.3 Results and Discussion

VI.3.1 Preliminary Experiments

At first, we performed preliminary investigations to gain a rough understanding of the usable parameter regime. It is noteworthy that first results were performed in an environmental scanning electron microscope, as we suspected the need of H_2O vapor to provide H^+ for successful re-substitution of TMS. We performed simple experiments using high vacuum (HV) conditions or low vacuum (LV) conditions (ESEM mode) with 10 Pa primarily H_2O atmosphere. Accelerating voltage was 5 kV at 400 pA with an approximate point pitch of 5 nm. The patterns generated hereby are shown in Figure VI-2 for both conditions before and after enzyme treatment. Visual analyses via optical microscopy reveals clear differences between both approaches. First of all, there are significant changes before and after cellulase treatment which suggests considerable regeneration processes, notably on the LV patterns. However, despite stronger changes, the patterns in LV mode are far from sharp and reaching small structures is most likely impossible. On the other hand, the HV patterns show sharp edges, however, less prominent change after cellulase treatment. Nevertheless, electron interaction yields considerable changes in film thickness which is evident from the change in interference color. Here, the dark blue suggests thinner films after patterning. Additionally, a change from blue to rather black patterns from 1 to 32 passes is observable in the HV patterns suggesting prominent changes in film properties. This is further reflected after enzyme treatment, where we could only observe considerable changes for the 1 and 2 frame patterns but not for the higher ones. In contrast, LV patterns show in all cases considerable changes after enzyme treatment. Here, after primary patterning, patterns change from dark blue to greenish which suggests also changes in film thickness. Additionally, for multi-pass patterns a considerable curtaining effect is visible. The reason is the water vapor present in the vacuum chamber causing multiple electron-water collisions and thus broadening of the beam profile. As a consequence, fewer electrons are to be found in the primary beam which in turn reduces the local dose. This is the reason why multi-pass patterns show degradability up to 4-8 passes, while in HV mode degradability is seen only for 1-2 passes. Furthermore, it states that regeneration seems to not rely on H_2O vapor as we see regeneration in the HV mode experiment. Thereby, we have proof for the following: Although we suggested H_2O as essential, we see regeneration in HV as well LV mode. As a consequence of the curtaining effect patterns in the LV mode get widened rendering high-resolution structures as impossible. Furthermore we see considerable changes with the introduced electron dose. At high doses, the degradation of the structures by enzymes seems again impossible which suggest considerable beam material damage. In the following, we state this obviously damaged cellulose structure and TMSC as non-degradable (ND) material.
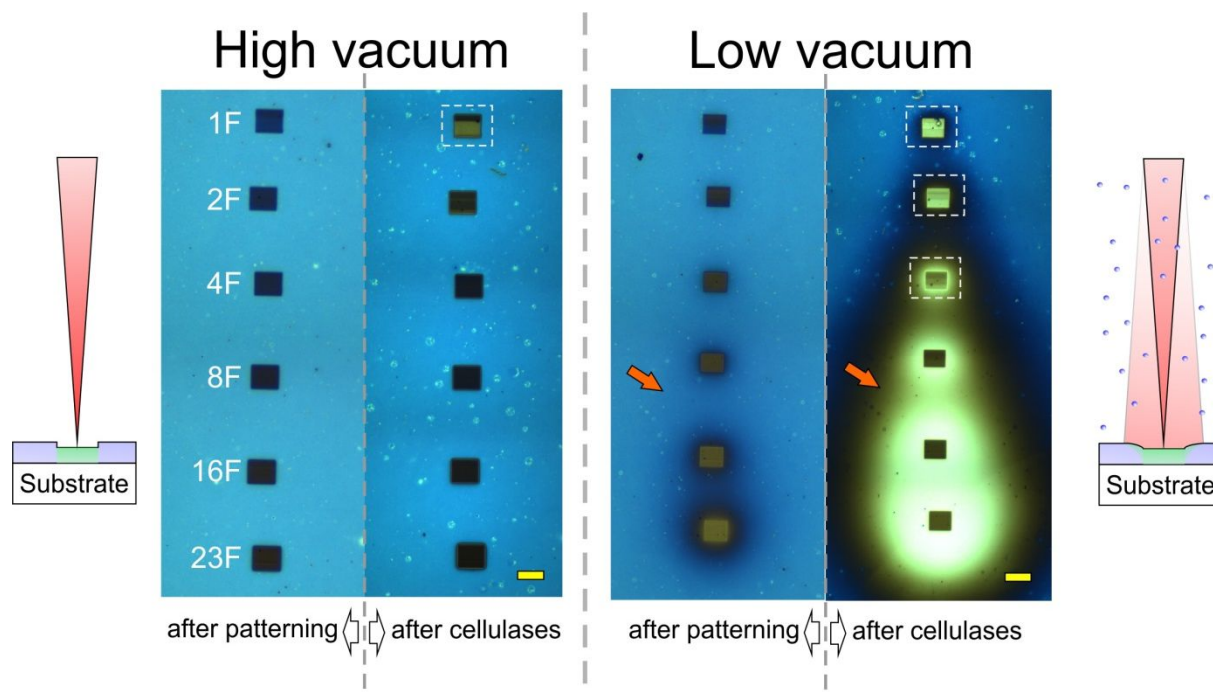
*Figure VI-2: Light microscopy images of patterns generated by the ESEM. On the right, a schematic depicts the beam shape in high vacuum (**HV**) conditions and on the left in low vacuum (10 Pa; **LV**) conditions with water present. Beam current and voltage is 400 pA and 5 kV, respectively. Patterns from top to down were generated by 1,2,4,8,16 and 32 frame imaging. Light microscopy was performed before (after patterning) and after 24 hours of enzyme treatment (after cellululases; see experimental procedures). Scale bars represent 10 µm.*

In order to evaluate the structure between different multi-pass images, we performed AFM analysis for HV patterns as demonstrated in Figure VI-3. The differences between AFM images shown in Figure VI-3b is a doubling of the electron dose. Section profiles provide proof for the obvious: An increase in electron dose – at least for these parameters yields – less degradable substrates. So far, this is an important result as it suggests that the electron dose is an important factor in the regeneration of TMSC to cellulose by electron beams. The difference in Figure VI-3 b (Section profiles) shows that the height difference with 2 passes is 61 ± 1 nm and with 4 passes only 46 ± 1 nm. This is a significant reduction which has to be considered and is further evidence that successful regeneration to cellulose depends on a specific parameter window which still has to be evaluated.
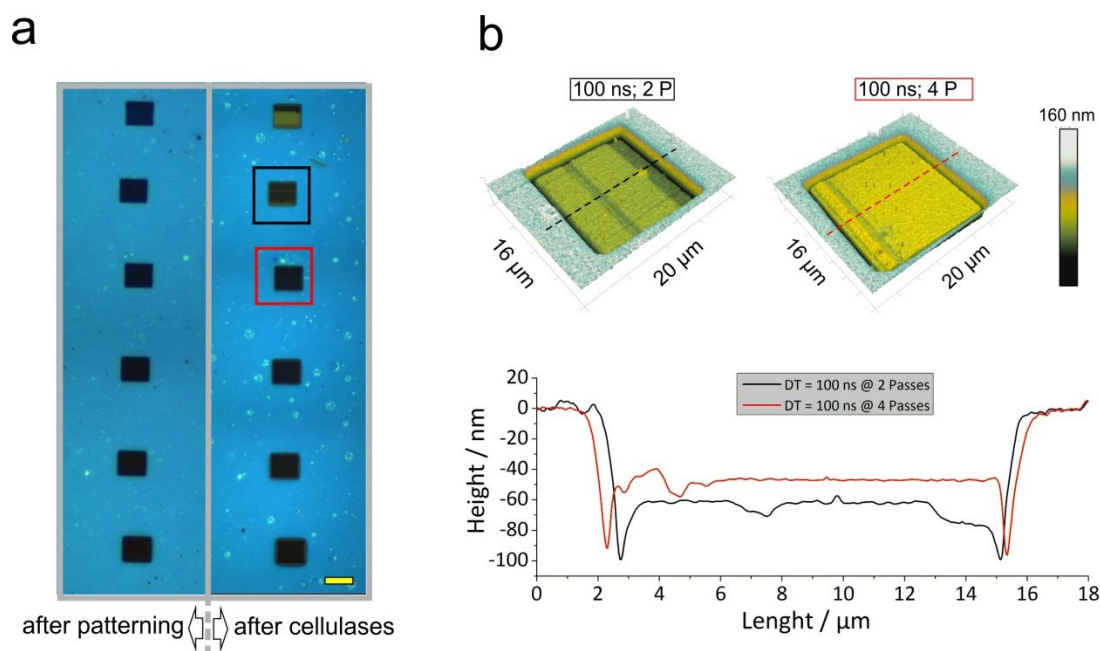
Figure VI-3: AFM analysis of two cellulase treated patterns for 2 and 4 passes. (a) Light microscopy images as shown in Figure VI-2 and AFM analysis in (b) with section profiles. Colors correlate with the square in (a) and the 3D images in (b) as well as the sections. Dashed lines show the position of the recorded section profiles. At 2 passes and 4 passes, we observe a height difference between TMSC and exposed areas of 61 ± 1 nm and 46 ± 1 nm, respectively, suggesting different material's properties. Scale bar represents 10 µm.

A full analysis of all patterns in HV and LV conditions showed that optimal parameters are to be found between DTs of 100 and 7000 ns. To scan a broader range of voltages and currents – which increase either the penetration depth or the dose – we have chosen the values specified in Table VI-1 and transferred the analysis to a dual-beam instrument (NOVA 200, FEI, The Netherlands) which provides a high-performance patterning engine for precise control of process parameters. To get a full data set we used the pattern strategy shown in Figure VI-1.

VI.3.2 Parameters Space

For all patterns we used the following strategy: First, patterns were structured into thin films and subsequently removed. All patterns were analyzed by AFM imaging and then placed in enzyme solution as described in the experimental section. Immediately after 24 hours of cellulase treatment, specimens were carefully rinsed and again imaged in the AFM. It is noteworthy that rinsing with water should be performed with great care as films are easily delaminated after such long times in liquid solution. Patterns are then measured and compared to each other to show the degraded material. In Figure VI-4, 3D AFM images demonstrate our chosen approach. By consideration of the patterns after enzyme treatment, we can support our hypothesis of an optimal regime in the patterning parameters. Furthermore, we see two regimes of the electron induced regeneration. While at low doses, an overall deficiency of electrons yields only partly regenerated structures, we observe, at high doses, a similar effect, however, with different origin. Here, an overall excess of electrons most likely damages the former regenerated cellulose substrate, thus rendering it once again non-degradable. In Figure VI-4 (after enzyme) two high-resolution scans undermine this thesis: Here, at low doses (left, black dashed square, image magnified) we see a similar depth as for high doses (right, red dashed square, image magnified) while at intermediate doses the color scale shows

almost full degradation (green, diagonal from top corner to bottom corner). At high doses, we see that the volume of the structure is once more increased which suggests the generation of non-degradable material after generation of cellulose. Therefore, optimal doses are to be found in between these applied doses.
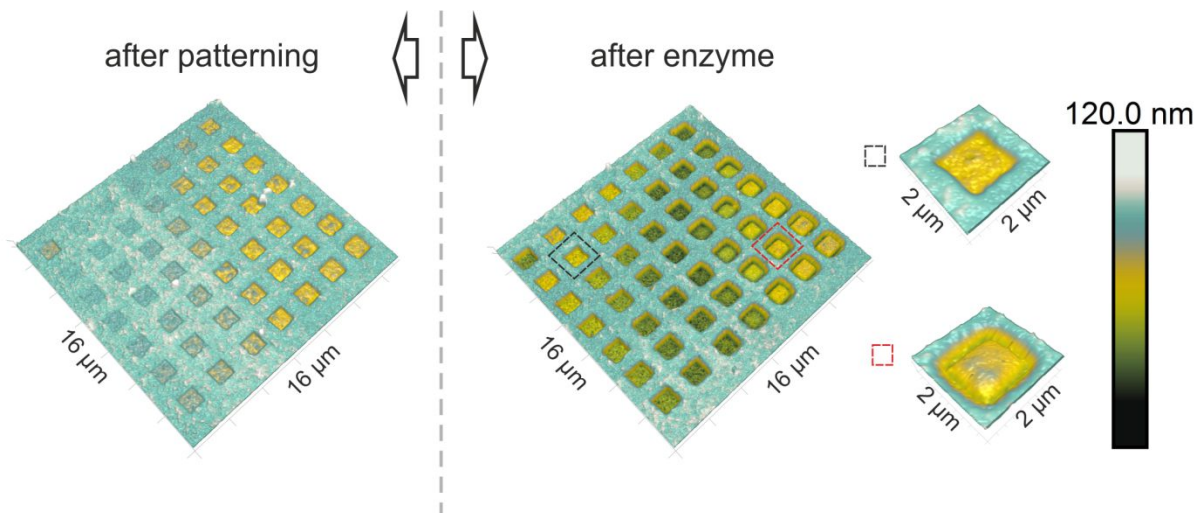
Figure VI-4: 3D AFM images of "as patterned" structures and after 24 hours enzyme treatment revealing again the presence of two opposing effects. At the left site we observe a deficiency of electrons (low doses) which leads to incomplete regeneration. At the right site we see an excess of electrons (high doses) which causes damage to the former cellulose material. In the middle (from the upper to lower corner; after cellulases) the optimal pattern parameters yield maximum conversion to cellulose.

We have shown by enzymatic degradation that most of the structure is cellulose as otherwise enzymes would not be able to degrade it. On the other hand, Spirk and collaborators as well as Reese have shown that cellulose with a degree of substitution below 0.5 is still degradable by cellulases [10,16]. We therefore used Fourier transformed infrared spectroscopy (FTIR) to access spectroscopic data to exclude the possibility of incompletely regenerated TMSC.

VI.3.3 FTIR Spectroscopy

A full spectrum was recorded on pads formerly introduced on a gold substrate as specified in the experimental section. The recorded spectrum is shown in Figure VI-5. Here, the spectrum shows in full conformity with literature pure cellulose[9,17]. We here have chosen the optimal parameters as already determined from Figure VI-4. If we consider spectra obtained on TMSC[9], we see no evidence for it. However, we know that higher doses again yield non-degradable material. To unravel the optimal dose, we measured each pad in Figure VI-4 and analyzed the relative loss of height after enzyme treatment.
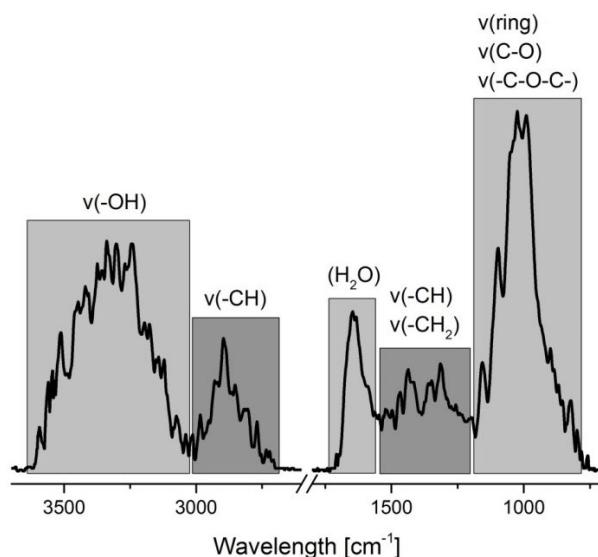
Figure VI-5:FTIR spectrum recorded on electron regenerated cellulose films. The spectrum is in full conformity with spectra in literature[9,17] and shows pure cellulose without peaks from TMSC. Thus, the regeneration step indeed leads to cellulose as the main product.

VI.3.4 Dose dependency

By using the following procedure, we were able to find a model for the here shown behavior during structuring: The TMSC film height corresponds to 100% non-degradable (ND = 100%, [ND] = 1) material. By measuring the depth after enzymatic degradation, we get again the residual ND material. By using this value as a relative amount we get graphs shown in Figure VI-6 and Figure VI-7.

Performing the above depicted procedure and by the use of equation (6.2), we were able to analyze each pad towards its remaining non-degradable material and to calculate the corresponding dose. The result for 2 kV electrons is shown in Figure VI-6 and provides and important finding. The data shows unequivocally that the electron dose is the only parameter of interest for the patterning strategy. This is extremely important as it states that structuring may be achieved in a wide range of parameters as long as the optimal dose is considered. At higher currents, we also may conclude that the structuring is exceptionally fast. Here, optimum doses allow dwell-times of less than 800 ns. Needless to say, that these short DTs are rather challenging for the patterning engine. Nevertheless, as a wide range is available, currents may be reduced to increase the DT. Another important aspect is that in all cases non-degradable material (Figure VI-6) was observed even for optimum parameters. A closer analysis reveals that there is a steep decrease ($0 - 0.5$ C/m^2; Figure VI-6 green dashed line) which corresponds with mainly regeneration effects. After approximately 0.5 C/m^2, a second reactions seems to start significantly contributing, thus increasing once again the non-degradable material ($0.5 - 5$ C/m^2; Figure VI-6 red dashed line). The superposition of both leads to the observed minimum at approximately 0.8 C/m^2. The opposing character of the relevant chemical reactions is described in the next section.
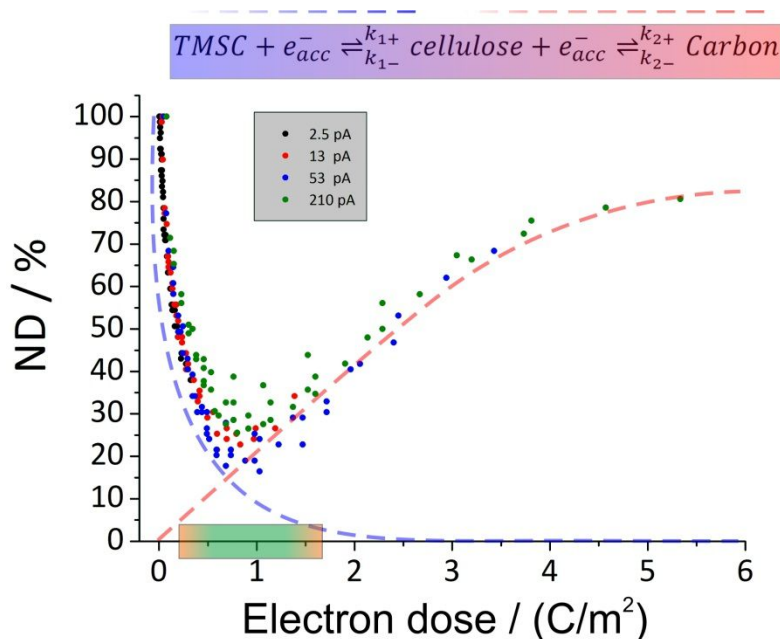
Figure VI-6: Non-degradable (ND) material as a function of the electron dose at 2 kV. Currents are shown in the legend. Here, a clear indication is given that the structuring is only dependent on the dose and not on the beam current. Additionally the contributions of reaction (6.3) are indicated by a green and red dashed line, respectively. Additionally, the optimal regime is indicated on the dose axis as green to orange bar (Green: optimal; orange: threshold value).

In the following, a dedicated model for the here observed model is provided resulting in fitting functions which may be used to derive valuable information from the graphs and most importantly to validate the hypotheses drawn here.

VI.3.4.1 Model of FEBIC - Regeneration

The interaction of electrons with the TMSC and further its regenerated products may be described by chemical formalisms as depicted in equation (6.3). We have demonstrated by FTIR and indirect enzymatic degradation that cellulose is an intermediate product. However, we also observed the generation of non-degradable material with ongoing dwell-times (DTs) which most likely results from electron induced damage of the cellulose backbone. It is so far not clear which products are generated, but it is feasible to assume that the main portion is carbon. We therefore may write the chemical reaction as follows:

$$TMSC + e_{acc}^- \rightleftharpoons_{k_{1-}}^{k_{1+}} cellulose + e_{acc}^- \rightleftharpoons_{k_{2-}}^{k_{2+}} Carbon \tag{6.3}$$
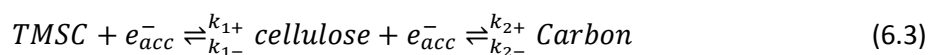
Here, e_{acc}^- is representative for the accelerated electrons which contribute to the reactions. At first, it is feasible to neglect k_{1-} and k_{2-} as these reactions are rather unlikely. From here on k_{1+} and k_{2+} will be denoted as k_1 and k_2, respectively. Each partial reaction, first from TMSC to cellulose (green dashed line in Figure VI-6) and from cellulose to carbonized products (red dashed line in Figure VI-6) follows second order chemical kinetics. However, by assuming a constant flow of electrons which is the case, at least for the dwell-time, we obtain the situation of pseudo first order chemical reactions (see equation (6.4) with $B_{(t)}$ = constant). In fact, our analysis to unravel the regeneration from TMSC to

cellulose and further to carbonized and non-degradable material represents the corresponding reaction kinetics and here derived formalisms must account for that. By finding appropriate equations, we may be able to fit the functions and derive important parameters in addition to the optimal dose. Further, it would prove our hypothesis derived in equation (6.3). The following formalism is a concise summary of the theoretical background behind the used model. In the following variables summarized in Table VI-2 will be used.

Table VI-2: Summary of the in equation (6.4) to (6.13) used variables.

Parameter	Variable	Description
[TMSC]	$A_{(t)}$	Concentration of TMSC
$[e^-_{acc}]$	$B_{(t)}$	Concentration of electron: $B_{(t)} = B$ = constant
[Cellulose]	$C_{(t)}$	Concentration of pure cellulose: $C_{(t)} = (A_0 - A_{(t)}) - D_{(t)}$
[Carbon]	$D_{(t)}$	Concentration of carbon rich, beam damaged material
[ND]	$\gamma_{(t)}$	Concentration of non-degradable material: $\gamma_{(t)} = A_{(t)} + D_{(t)}$

For the concentration of TMSC over time, equation (6.4) is immanent:

$$-\frac{dA_{(t)}}{dt} = k_1 \cdot A_{(t)} \cdot B \tag{6.4}$$

Reorganization and integration yields:

$$A_{(t)} = A_0 \cdot e^{-k_1 \cdot B \cdot t} \tag{6.5}$$

As experimental curves denote the non-degradable material we must have a look at $C_{(t)}$ which is:

$$-\frac{dC_{(t)}}{dt} = k_2 \cdot C_{(t)} \cdot B - k_1 \cdot A_{(t)} \cdot B = k_2 \cdot C_{(t)} \cdot B - k_1 \cdot B \cdot A_0 \cdot e^{-k_1 \cdot B \cdot t} \tag{6.6}$$

If we use the expression for $C_{(t)}$ and $\gamma_{(t)}$ as depicted in Table VI-1, we may write:

$$\frac{d\gamma_{(t)}}{dt} = k_2 \cdot A_0 \cdot B - k_2 \cdot \gamma_{(t)} \cdot B - k_1 \cdot B \cdot A_0 \cdot e^{-k_1 \cdot B \cdot t} \tag{6.7}$$

This is an ordinary linear differential equation of $\gamma_{(t)}$ and thus of the concentration of non-degradable material. A solution to equation (6.7) may easily be found by using a variation of parameters ansatz. Here, the homogenous part of the equation may be easily derived in similarity to equation (6.4).

$$\frac{d\gamma_{(t)}}{dt} + k_2 \cdot \gamma_{(t)} \cdot B = 0 \quad \Rightarrow \gamma_{h_{(t)}} = C_h \cdot e^{-k_2 \cdot B \cdot t} \tag{6.8}$$

A variation of constant ansatz now is:

$$\gamma_{p(t)} = C_{h(t)} \cdot e^{-k_2 \cdot B \cdot t}$$ (6.9)

Straightforward differentiation and substitution to equation (6.7) yields:

$$C_{h(t)} = \int (k_2 \cdot A_0 \cdot B - k_1 \cdot A_0 \cdot B \cdot e^{-k_1 \cdot B \cdot t}) \cdot e^{k_2 \cdot B \cdot t} dt = \cdots$$

$$= A_0 + A_0 \cdot \frac{k_1}{k_1 - k_2} e^{-k_1 \cdot B \cdot t} + C_p \cdot e^{-k_2 \cdot B \cdot t}$$ (6.10)

With homogenous and particular solution we can now find a general solution to equation (6.7):

$$\gamma_{(t)} = \gamma_{h(t)} + \gamma_{p(t)} = A_0 + A_0 \cdot \frac{k_1}{k_1 - k_2} e^{-k_1 \cdot B \cdot t} + C_{p+h} \cdot e^{-k_2 \cdot B \cdot t}$$

To solve for C_{p+h} we now have to find a boundary condition of equation (6.7). Needless to say, the equation must satisfy

$$\gamma_{(0)} = A_0 = A_0 + A_0 \cdot \frac{k_1}{k_1 - k_2} + C_{p+h}$$ (6.11)

or

$$C_{p+h} = A_0 \cdot \frac{k_1}{k_2 - k_1}$$ (6.12)

The final solution to this problem is therefore as follows:

$$\gamma_{(t)} = A_0 + A_0 \cdot \frac{k_1}{k_1 - k_2} e^{-k_1 \cdot B \cdot t} + A_0 \cdot \frac{k_1}{k_2 - k_1} \cdot e^{-k_2 \cdot B \cdot t}$$ (6.13)

By substitution of the general terms in equation (6.13), we then get the fitting function with parameters a_1, a_2, b_1 and b_2.

$$[ND] = a_1 + a_2 \cdot (e^{-b_1 \cdot t} - e^{-b_2 \cdot t})$$ (6.14)

Furthermore a_2 may be expressed by a_1, b_1 and b_2, which yields the final fitting function with 3 parameters:

$$[ND] = a_1 + a_1 \cdot \frac{b_1}{b_1 - b_2} (e^{-b_1 \cdot t} - e^{-b_2 \cdot t})$$ (6.15)

Please note, as these reactions are dependent in time and not on the dose we had to fit the data to curves showing ND in dependency of the DT. Once the optimal DT is known from the fits, we simply use equation (6.2) to recalculate the optimal dose. In Figure VI-7, a representative fit for the analysis

of the 2kV at 210 pA pattern is shown. A similar fit was performed for each curve and the tabulated values may be found in Table VI-3. It is noteworthy that all fits showed exceptional agreement with experimental data. Further graphs may be found in supplementary images S1-S3.
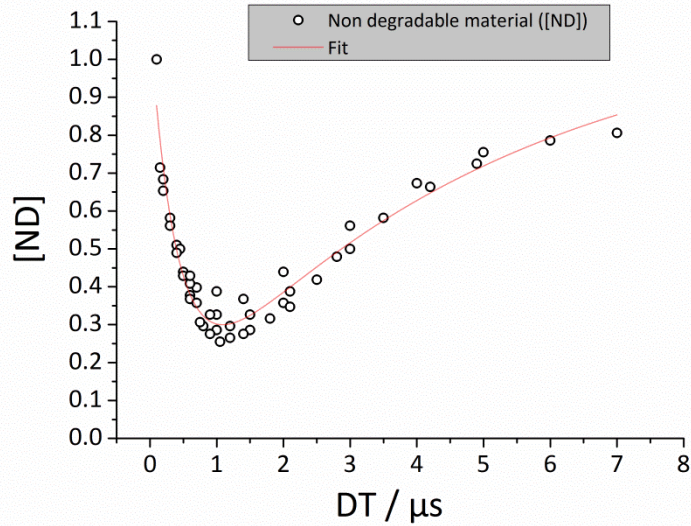

Figure VI-7: Non-degradable (ND) material for patterning parameters of 2 kV at 210 pA and with varying dose as specified in Figure VI-1 and Table VI-1. The fit in red is in exceptional good agreement with the experimental data. Thereby valuable information as the optimal dose and other reaction relevant parameters can be derived. The tabulated values for the optimal dose can be found in Table VI-3.

Table VI-3: Fitted optimal dwell times ($DT_{opt.}$) which corresponds to each minimum for each pattern at the specified parameters of U_{Beam}, I_{Beam} and the corresponding point-pitch (PP). The optimal dose ($Dose_{opt.}$) was calculated by equation (6.2).

U_{Beam} (kV)	I_{Beam} (pA)	PP (nm)	$DT_{opt.}$ (µs)	$Dose_{opt.}$ (C/m^2)
2	2.5	7.4	6.1 ± 7.5	0.3 ± 0.4
	13.0	8.1	3.9 ± 0.2	0.7 ± 0.1
	53.0	10.4	1.6 ± 0.1	0.8 ± 0.1
	210	16.6	1.0 ± 0.1	0.8 ± 0.1
5	5.0	4.0	3.2 ± 1.8	1.0 ± 0.6
	25.0	4.9	1.0 ± 0.2	1.1 ± 0.2
	98.0	7.4	0.7 ± 0.1	1.3 ± 0.1
	400.0	13.5	0.6 ± 0.1	1.3 ± 0.1
10	7.5	2.7	1.7 ± 1.5	1.7 ± 1.5
	33.0	3.6	0.7 ± 0.1	1.9 ± 0.2
	130.0	5.8	0.6 ± 0.1	2.2 ± 0.1
	540.0	11.0	0.5 ± 0.1	2.1 ± 0.1

By the here shown data (Figure VI-2 to Figure VI-7 and Table VI-3), we now can state: The optimal patterning strategy to regenerate TMSC to cellulose depends only on the introduced dose and an optimal minimum can be found for each voltage. For each voltage the dose shows a constant value ((0,7 ± 0,2) C/m^2 for 2 kV; (1.2 ± 0,2) C/m^2 for 5 kV and (2.0 ± 0,4) C/m^2 for 10 kV)) for varying currents. Hereby, we also see that the cross section of reaction is reduced with increasing acceleration voltage which is expectable (higher accelerated electrons are less likely to interact with the TMSC moieties). Now with this data at hand, we proceeded by evaluating the maximum attainable resolution.

VI.3.5 Downscaling

To do so, we designed as specified in the experimental section different patterns by simply using black and white bitmaps. A dedicated program to produce stream files out of this bitmaps was used to feed the FIB patterning engine with the optimal evaluated doses. To unravel the maximum resolution, we used a sun structure as depicted in Figure VI-8. The reason is: *1)* the pattern is rather simple and *2)* the reducing line width of the individual rays of the sun towards the center of the image shows immediately the maximum attainable resolution. The data in Figure VI-8 shows considerably that a resolution of below 100 nm is easily achieved. In detail, by taking section profiles we see that a FWHM resolution of 70 nm is attainable. We found, that at even closer separations (center) neighboring sun branches start to overlap most likely due to proximity effects which limit the resolution below 70 nm. It further is conceivable that individual cellulose- or TMSC-chains start to exceed the maximal resolution at one point making regeneration once more complicated. However, we can state that electron induced regeneration is available to fabricate extremely fine structures of cellulose which so far have not been possible by any other technique.

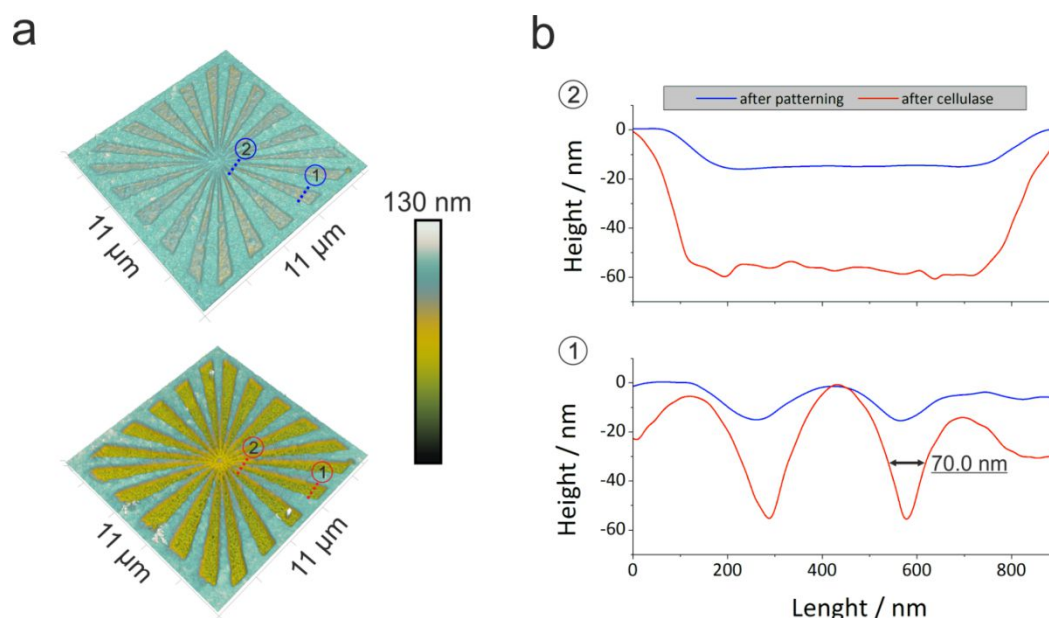*Figure VI-8: (a) Patterned sun structure with a total area of 10 x 10 µm^2 before (top) and after cellulase treatment (bottom). Two sections where taken on the outer site (1) and close to the center (2). Both sections before (blue) and after cellulase treatment (red) are shown in (b). A measurement of the FWHM width of one sun branch shows that a resolution of 70 nm is reachable.*

VI.4 Chapter Summary

The method of electron beam induced regeneration of TMSC to cellulose has so far not been demonstrated. A carful and comprehensive analysis of the underlying processes showed that we are able to produce cellulose without any help of acidic components as usually used to regenerate TMSC to cellulose[4–7]. It is clear from fundamental considerations that electrons will lead to cleavage of the TMS-C bond but also will interact with cellulose, once regenerated. We have seen already early in the investigations that the electron dose is the important parameter (Figures VI-2 and VI-3). Therefore, we used a dedicated patterning strategy by using matrices of pads with different dwell times. Here, the point pitch (PP) was fixed to a 50% beam overlap which eased the calculation of the electron dose. We answered the important question of the main regeneration product after electron irradiation by using FTIR. Here, we indubitable showed that the resulting material is cellulose. However, the optimal dose was so far only known for 2 kV at 53 pA (DT = 1600 ns; see experimental section, FTIR). To unravel it for each current and accelerating voltage, we used the in Figure VI-1 depicted strategy. After measuring the non-degraded material (after cellulase treatment), we could find curves similar to that in Figure VI-6. It is immediately evident from Figure VI-6 that the optimal patterning is only dependent on the dose. This is extremely valuable as current and DT may be altered to the desired needs for each machine. As a last step, we aimed on a demonstration of the ultimate resolution. Here, we showed again without doubt that a resolution of 70 nm is easily achieved. This is a significant reduction compared to photolithographic methods as demonstrated by Wolfberger and collaborators [9,10]. Here, limitations are in the range of 500 nm. To conclude electron based regeneration of TMSC to cellulose is a versatile tool to fabricate extremely small cellulose structures on any given surface. Moreover, we showed that the patterning is extremely fast which must be considered as a significant advantage. The impressive capabilities may be once more demonstrated in Figure VI-9.
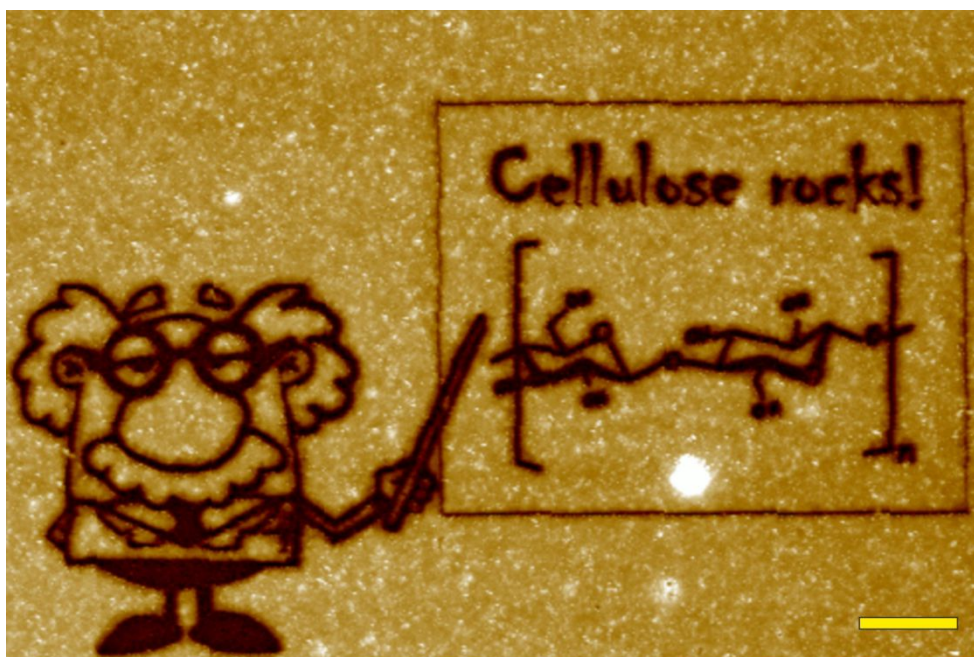

Figure VI-9: AFM image of a regenerated TMSC film (brown – cellulose; yellow – TMSC) after cellulase treatment, patterned with 5 kV, 25 pA and a DT of 1.2 µs. Scale bar represents 3 µm.

VI.5 References

[1]   R. N. Tharanathan, *Trends Food Sci. Technol.* **2003**, *14*, 71.

[2]   J.-H. Seo, T.-H. Chang, J. Lee, R. Sabo, W. Zhou, Z. Cai, S. Gong, Z. Ma, *Appl. Phys. Lett.* **2015**, *106*, 262101.

[3]   R. Kargl, T. Mohan, S. Köstler, S. Spirk, A. Doliška, K. Stana-Kleinschek, V. Ribitsch, *Adv. Funct. Mater.* **2013**, *23*, 308.

[4]   T. Mohan, S. Spirk, R. Kargl, A. Doliška, H. M. A. Ehmann, S. Köstler, V. Ribitsch, K. Stana-Kleinschek, *Colloids Surfaces A Physicochem. Eng. Asp.* **2012**, *400*, 67.

[5]   E. Kontturi, P. C. Thüne, J. W. Niemantsverdriet, *Polymer (Guildf).* **2003**, *44*, 3621.

[6]   E. Kontturi, T. Tammelin, M. Osterberg, *Chem. Soc. Rev.* **2006**, *35*, 1287.

[7]   E. Kontturi, et al., *Biomacromolecules* **2011**, *12*, 770.

[8]   E. Kontturi, P. C. Thüne, a. Alexeev, J. W. Niemantsverdriet, *Polymer (Guildf).* **2005**, *46*, 3307.

[9]   A. Wolfberger, R. Kargl, T. Griesser, S. Spirk, *Molecules* **2014**, *19*, 16266.

[10]   A. Wolfberger, A. Petritz, A. Fian, J. Herka, V. Schmidt, B. Stadlober, R. Kargl, S. Spirk, T. Griesser, *Cellulose* **2014**, 717.

[11]   R. Winkler, A. Szkudlarek, J. D. Fowlkes, P. D. Rack, I. Utke, H. Plank, *ACS Appl. Mater. Interfaces* **2015**, *7*, 3289.

[12]   B. Geier, C. Gspan, R. Winkler, R. Schmied, J. D. Fowlkes, H. Fitzek, S. Rauch, J. Rattenberger, P. D. Rack, H. Plank, *J. Phys. Chem C* **2014**, *118*, 14009.

[13]   T. Ganner, S. Rosîker, M. Eibinger, J. Kraxner, J. Sattelkow, J. Rattenberger, H. Fitzek, B. Chernev, W. Grogger, B. Nidetzky, H. Plank, *ACS Appl. Mater. Interfaces* **2015**, *7*, 27900.

[14]   A. Orthacker, R. Schmied, B. Chernev, J. E. Fröch, R. Winkler, J. Hobisch, G. Trimmel, H. Plank, *Phys. Chem. Chem. Phys.* **2014**, *16*, 1658.

[15]   P. Bubner, J. Dohr, H. Plank, C. Mayrhofer, B. Nidetzky, *J. Biol. Chem.* **2012**, *287*, 2759.

[16]   E. T. Reese, *Appl. Microbiol.* **1955**, *4*, 39.

[17]   D. Ciolacu, F. Ciolacu, V. I. Popa, *Cellul. Chem. Technol.* **2011**, *45*, 13.

Thesis Summary

The purpose of this thesis was to introduce liquid AFM techniques to enzymatic systems. The process of enzymatic cellulose disintegration is now known for almost one century and still poses unanswered questions. Although microbiology gave answer to most of the questions related with enzymatic degradation of cellulose, it failed in providing sufficient direct visualization. This is not surprising, as cellulases show average sizes in the range of a few nanometer. We have shown here that atomic force microscopy is suited to visualize effects associated with enzymes on a local basis. We also showed that the success of such experiments is dependent on the substrate used. The reason is that natural celluloses feature a polymorphism which has significant influence on the degradability. We therefore showed the preparation of artificial substrates featuring an adjustable polymorphism, high reproducibility, purity and an overall flat topology. We aimed the development and focus of the thesis to imply the successful application of fluid experiments, the availability of long time analysis, the visualization of enzymatic effects on a micrometer basis, the visualization of individual enzymes and the availability of real time investigation in the AFM. In the next paragraphs, a concise summary of each chapter will once more conclude the important findings.

In *chapter I,* a basic introduction to atomic force microscopy has demonstrated its advantages as a minimally invasive high resolution microscopy method to raster the topography of various substrates reminiscent to our tactile sense. It was shown that additional signals generated during operation may be used to characterize the substrate further. Here, of particular interest is phase imaging as it also provides the basis for more advanced methods like MFM or EFM. Basic theoretical considerations as the point mass model may be seen as a good and valid basis to understand AFM operation. Furthermore, as one of the most stunning capabilities, fluid AFM imaging was introduced. Here, different forces as the solvation force and the double layer force were concisely and comprehensively described. Furthermore, by a short introduction to the theory behind it, it was shown that the double layer force is only dependent on the solvent and its ionic interaction with the tip. It means that by **adjusting the pH of a solution the resolution of the image may be optimized**. The point mass model in fluid showed further the basic response of the tip cantilever system in fluid far away from the surface. The fact that interaction with the surface in liquid are considerable more complicated as in air or vacuum excluded a deeper theoretic introduction. *Chapter I* also gave a quick overview over substrate preparation as it states a considerably harder task on the researcher as in air or vacuum. The reason is simply that in liquid otherwise immobile particles usually are liberated from the surface, thus introducing problems during imaging. Therefore the most common substrates to ensure fixation were shown. The last section dealt with the forces excreted on in particular biological specimens during imaging. This is important as most of the time liquid AFM is used to analyze biological or living material and minimal invasive also includes minimal forces. Here, proof is given that forces in liquid can be considerably high which should be considered in experiments.

Chapter II gave a basic overview over cellulose structures, their origin and chemical appearance. The complexity of celluloses found in nature was comprehensively described by showing that the structure is **highly heterogeneous with polymorphous nature**. Here, **crystalline and amorphous areas are found side-by-side** in complex arrangements. Associated crystal morphologies – from whom only cellulose I and II are of relevance – were furthermore introduced. The understanding of

these structures is important on later concepts of enzymatic synergism where the cooperative activity of different cellulases was investigated (e.g. parallel C1 and antiparallel C2). Furthermore this *chapter* laid the foundation to basic analytical methods used during this thesis as wide angle X-ray scattering and Raman microscopy. Also the basic chemistry behind cellulose is introduced and how cellulose may be dissolved. This is extremely important for *chapter IV* where model substrates were produced artificially to provide reasonable reproducibility and purity.

In *chapter III,* an introduction to enzymology is given which may be seen as foundation for the further understanding of the later introduced models and bio-chemical methods (*chapter V*). Here, fundamental considerations provided insight into the kinetics and associated concepts (e.g. Michaelsen-Menten kinetics). Following this introduction, the enzymes used in this thesis are shortly described with the so far known understanding of their action on polymorphous celluloses. Here, cellulases of the well-known **model organism *Hypocrea jeronica*** (former *Trichoderma reesei*) were introduced. A second non-hydrolytic and strongly investigated enzyme, the **lytic polysaccharide mono-oxidase or LPMO** was introduced. Here, the specific features of this completely different enzyme were introduced. As a last system **cellulosomes or complex multi-enzyme systems** usually used by bacterial organisms were introduced. All cellulolytic systems are based on natural cellulase systems, however, with different mechanisms which we unraveled in *chapter V*. However, to be able to compare activities in consecutive experiments standardized substrates which emulate natural celluloses are necessary.

In *chapter IV* two such model substrates were introduced. The first one – denoted **as mixed amorphous crystalline cellulose substrate or MACS –** featured an **adjustable crystallinity** and **high reproducibility**. Further features are that the substrate may be produced in high quantities, however relies on **elaborate preparation** to achieve sufficient smooth topologies. Nevertheless enzymes of H. jeronica and the LPMO were investigated on these substrates in *chapter V*. The advantages of the substrate include that large crystallites with a complex structure reminiscent to natural cellulose may be investigated alongside smaller elementary crystallites ranging from a few nanometer to micrometers. Although the high variability of crystal sizes may be seen advantageous in large scale imaging**,** small-scale and high-speed measurements are difficult to achieve. The reason is that during enzymatic hydrolysis a strong increase of the surface roughness is observable due to the different degradation velocities on large, small crystalline and amorphous cellulose. We therefore introduced a second concept, the **semi-crystalline thin film cellulose (SCTFC)** which includes **elementary crystallites as the basic crystalline building block** of cellulose and amorphous thin films. Both combined again yield a tunable crystallinity, however, with **flat topology from the beginning**. Furthermore, nano-crystallites are the basic unit of an elementary cellulose fibril and may be seen as the smallest and highly crystalline entity which every enzyme encounters during degradation. Thus, **small scale and fast imaging** are available to unravel the mechanisms on a molecular basis. These substrates were used in *chapter V* for the cellulosome, however, in its pure crystalline form. Both concepts have in common that the reproducibility and purity is absolutely given.

We proceeded with analyzing the synergistic and individual effects of different cellulases. Here, we showed for the extensively investigated model organism H. jeronica that the understanding is far from complete. So far most researches took *Hj*Cel6A as an enzyme that, similar to *Hj*Cel7A, is solely processively active on crystalline cellulose. Direct evidence on MACS, however, revealed that the enzyme shows a **bi-specific activity** by also degrading amorphous cellulose at even higher rate. This

means that the enzyme is capable of cleaning crystalline parts from the amorphous top layer and further to degrade it with its ablative activity. While this effect on its own is impressive, we showed that it is even more pronounced in synergism with *Hj*Cel7A and *Hj*Cel7B. By sequential incubation with the corresponding cellulases we could reconstruct the synergism and provide a new understanding and model. The knowledge of this approach was then used to unravel the kinetic mechanisms by the help of biochemical methods. By that, the astonishing advantage of the combined techniques could be shown. Keeping a similar routine we proceeded by adding LPMO to this system. This was interesting because **LPMO is thought to strongly cooperate with *Hj*Cel7A** which mainly acts on crystalline cellulose. We could provide the **first direct evidence that the hypothesis** based on biochemical data is **indeed true** and may be used to further boost enzymatic conversion of cellulose to glucose. As a last part, we have focused on cellulosomes which are multi-enzyme systems which are thought to primarily act on crystalline cellulose. Via direct visualization methods we showed that the basic mechanism can be identified on the smallest crystalline entity the cellulose nano-crystallite. Here is of particular interest, that the **form of activity is significantly different** to that of free cellulases like the here used *H. jeronica* ones. While the **latter show ablative activity**, **cellulosomes seem to disintegrate the crystallites more statically** but with stronger in-depth de-polymerization. This form of degradation was postulated before from TEM and biochemical data but not shown on such a small scale directly and with this resolution. Again this data led to the development of a new model and a deeper understanding. With these 3 systems, the enzymatic part of this thesis is completed and shows that AFM based investigation is absolutely recommended to unravel otherwise elusive information.

The last *chapter* of this thesis (*chapter VI*) has to be seen in the concept of future prospects and research activities which will be applied after this thesis. **We showed for the first time that celluloses may be structured by electron beam induced regeneration**. This is remarkable as the regeneration of Trimethylsilyl-cellulose usually requires acidic environments. However, here only electrons interact with TMSC and transform it to cellulose. By this strategy small cellulose structures on any given surface may be generated. We provided a comprehensive analysis of the optimal pattering parameters and showed that regeneration is only dependent on the used dose. Moreover, line widths of **below 100 nm are easily achieved** which is almost an order of magnitude less compared to those reached by lithographic methods. This states a fully new field of investigation as this may be comparable to those used for the investigation of enzymatic cellulose degradation by providing standardized volume blocks or by the implantation into bio-degradable and bio-active sensors.

To conclude, this thesis was designed as fundamental research in the field of enzymatic cellulose degradation by the use of AFM techniques but further provided important strategies for standard polymorphic cellulose substrates and further structural celluloses. With this, the basis for ongoing research in the field of enzymatic cellulose degradation and bio-sensor research is laid.